KU LEUVEN

ARENBERG DOCTORAL SCHOOL
Faculty of Engineering Science

# Characterization of passive acoustic dampers with orifices using linear and nonlinear numerical models

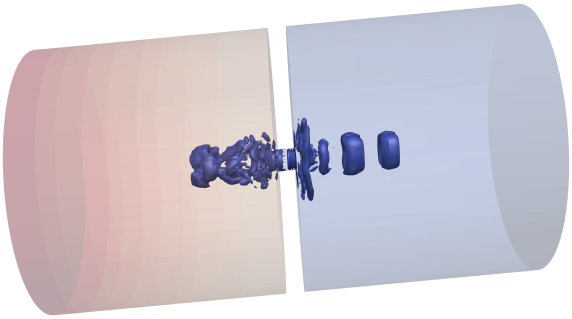

**Jonathan Tournadre**

Dissertation presented in partial
fulfillment of the requirements for the
degree of Doctor of Engineering Science (PhD):
Mechanical Engineering

January 2018

# Characterization of passive acoustic dampers with orifices using linear and nonlinear numerical models

**Jonathan TOURNADRE**

Examination committee:
Prof. dr. ir. O. Van der Biest, chair
Prof. dr. ir. W. Desmet, supervisor
Dr. ir. W. De Roeck, co-supervisor
Dr. ir. P. Martínez-Lera, co-supervisor
(Siemens Industry Software NV)
Prof. dr. ir. E. Reynders
Dr. ir. M. Vanierschot
Prof. dr. ir. H. Bodén
(KTH Royal Institute of Technology)
Dr. ir. G. Gabard
(Université du Maine)

Dissertation presented in partial fulfillment of the requirements for the degree of Doctor of Engineering Science (PhD): Mechanical Engineering

January 2018

# Preface

*Not everything that can be counted counts,*
*and not everything that counts can be counted*
- William Bruce Cameron

After some intensive months working on this dissertation, it is now time for me to put the final touch on it by writing this note of thanks. Looking back to the journey that brought me to this moment, I can safely say that it has been a period of great learning for me, not only in the scientific arena, but also on a personal level. I would like to reflect on the people who have supported and helped me so much throughout this time.

Of course, this work would not have been possible without financial supports. This research has been mostly funded by the European Commission under call FP7-PEOPLE-ITN-2012 via the Marie Curie Initial Training Network "Thermoacoustic and Aeroacoustic Non-linearities in Green combustors with Orifice structure" (TANGO), Grant Agreement 316654, coordinated by Professor Maria Heckl from the Keele University (United Kingdom). The work has been carried out partly in the offices of Siemens Industry Software in Leuven, Belgium, and at the division *Production engineering, Machine design and Automation* (PMA) of the Mechanical Engineering Department of the KU Leuven, Belgium. During the time spent at the KU Leuven, the research has been financially supported by the Research Fund KU Leuven, as well as the European Commission through the FP7 Collaborative Project IDEALVENT (GA 314066).

Consequently, I would particularly like to acknowledge my supervisors, Professor Wim Desmet, Paula Martinez-Lera and Wim De Roeck, for all their support during the last four and a half years. I highly appreciate your guidance along the course of my PhD, your enthusiasm in my research work, and the trust you put in me. Thank you for your help bringing this research to a successful

ending. I would like to extend my gratitude towards all members of my doctoral examination committee for taking the time to go through this manuscript in detail and the much-valued feedback given at the occasion of the preliminary defense, allowing to considerably improve the present dissertation.

I am also very thankful to all of those with whom I have had the pleasure to work and interact during the course of my doctoral adventure. To start with, I would like to thank all the members of the aeroacoustic research group: Hervé, Vyacheslav, Antonio, Maria, Luigi, and Simon. I really appreciated our daily discussions and the friendly atmosphere in the office. Hervé, in particular, I really value your enlightening answers to all kind of technical questions that crossed my mind and your pragmatic way to solve problems. Thank you very much for your priceless assistance. I am also grateful to my friends and former colleagues at Siemens: Karim, Alessandra, Alice, Ali, Emin, Michel, Hadrien, Simone, Michael, and Verena.

The TANGO project has also been the breeding-ground for multiple scientific, cultural and social interactions, which contributed to my personal enrichment. In this regard, I am especially indebted to Professor Wolfgang Polifke for giving me the chance to spend a secondment period at the Professur für Thermofluiddynamik at the Technical University of Munich (TUM). The time there has been marked by a fruitful collaboration and the start of a good friendship with one of his students, Kilian Förner. Also a very big thanks to Muttalip Aşkın Temiz, Mico Hirschberg, and Ines Lopez Arteaga from the Technical University of Eindhoven (TUe) with whom I had the chance to collaborate at several occasions. Our exchanges and discussions have been great sources of inspiration. Many thanks also go to all the fellows and senior researchers with whom I have shared strong moments throughout the project.

I would also like to express my sincere appreciation to Lotte, to the ladies from the PMA secretariat, Lieve, Valérie and Marina, and to Marijke from the financial antenna for always helping me out with all kinds of organizational things.

Living the last years in Leuven has also been the occasion to meet several incredible persons with whom I shared great memories and who very much deserve to be listed here. To these persons belong by all means my best coffee break partners at PMA, namely Hendrik, Laurens and Vyacheslav. Thanks for the innumerable topics of discussion, facts and riddles on which I thrived. I would also like to extend my appreciation to Sepide, Anna, Marco V., Matias, Alireza, and Matteo that always keep me entertained and motivated throughout the weeks. A very special thanks on that matter also goes to my dear Simona, Valène, Marco G., Fabien, Adrien, and Vincent.

Last but not least, I would like to express my sincere gratitude to my parents, whose love and guidance are with me in whatever I pursue. Merci pour votre amour. Vous êtes sans cesse avec moi, peu importe le nombre de kilomètres qui

nous séparent. Un grand merci aussi à vous, Rémi et Benoit, mes acolytes et amis de toujours, qui êtes comme des frères pour moi. Zu guter Letzt möchte ich noch bei meiner lieben Christina von ganzem Herzen bedanken. Ich weiss, dass es nicht jeden Tag einfach für dich war, so weit voneindander entfernt zu sein, aber du hast mich immer unterstützt und motiviert. Worte können kaum ausdrücken, wie dankbar ich dir bin.

If *not everything that counts can be counted*, most likely not everyone that counts for me has been highlighted in this short note of thanks to rightly demonstrate my level of recognition. However, the past years have shown that I can count on all of you. So, thank you all for cheering me up in the hard moments, for sharing your enthusiasm and passions, for making me laugh and supporting me in all circumstances. A heartily *thank you* to be simply always there for me, each of you in your own very special way. It means the world to me.

Jonathan
January 2018

# Abstract

Passive acoustic dampers in the form of Helmholtz resonators, perforated plates and liners, are commonly used to suppress noise propagation or to control the acoustic feedback that can lead to thermo-acoustic instabilities in combustion engines. Their robustness, acoustic properties and easy integration into existing systems make them an appealing solution for noise control in many applications, from air conditioning systems in buildings to automotive mufflers or aircraft engine liners.

When designed properly, such silencers dissipate the energy contained in the passing acoustic waves within a specific frequency range. The damping mechanisms involved can differ significantly depending on the geometry of the perforations, the amplitude of the acoustic excitation, the local flow conditions and the structural response of the system. The large variety of operating conditions encountered by these silencers can be difficult to reproduce and to monitor in an experimental setup. Moreover, the applicability of many of the semi-empirical models developed to describe the acoustic behavior of perforates is severely limited by their restrictive assumptions or because important design parameters that could be used to enhance the acoustic damping are neglected. In order to better understand the physical phenomena influencing the flow-acoustic interaction at perforates and to improve the design of future passive sound absorbers, a clear need for efficient numerical prediction schemes and characterization methods comes to the fore.

For these reasons, the first part of this dissertation investigates linear acoustic operators combined with efficient high-order numerical methods to model the wave propagation through non-homogeneous medium and non-uniform flow regions, accounting for the various convective and dissipative phenomena. These linear methods are further applied to characterize the influence of local sheared flows, temperature profiles, and flow turbulence on the acoustic behavior of perforates.

In the second part, a methodology based on the computational fluid dynamics solution of the incompressible flow equations is presented and assessed for the determination of the impedance of Helmholtz resonators. This approach is used

to analyze the nonlinearities occurring at the resonator opening due to flow separation under high amplitude excitations.

The vibro-acoustic behavior of perforated plates is the focus of the last part of this work. A numerical design and optimization tool for passive noise control devices based on flexible micro-perforated panels is proposed. This technique, which couples a potential acoustic solver and structural shell elements, is validated and applied to a cylindrical resonator containing a micro-perforated plate with circular square-edged orifices.

The developed numerical methods provide novel modeling capabilities for the flow-acoustic interactions, nonlinearities, and the vibro-acoustic coupling affecting the acoustic behavior of perforates in passive acoustic dampers. As such, these techniques can provide valuable insights in the physical behavior, paving the path for the development of novel noise control solutions.

# Beknopte samenvatting

Passieve akoestische dempers in de vorm van Helmholtz resonatoren, geperforeerde platen en liners worden courant gebruikt om geluidspropagatie tegen te gaan of om de akoestische terugkoppeling, die kan leiden tot thermo-akoestische instabiliteiten in verbrandingsmotoren, te onderdrukken. Hun robuustheid, akoestische eigenschappen en integreerbaarheid in bestaande systemen maken hen een aantrekkelijke oplossing voor lawaaibeheersing in vele applicaties, van airconditioning systemen in gebouwen tot geluidsdempers in wagens of liners in vliegtuigmotoren.

Wanneer ze correct ontworpen zijn, dissiperen deze geluidsdempers de energie bevat in de propagerende akoestische golven over een specifieke bandbreedte. Hierbij kunnen verschillende dempingsmechanismes optreden, afhankelijk van de geometrie van de perforaties, de amplitude van de akoestische excitatie, de lokale stromingstoestand en de structurele respons van het systeem. De grote variatie aan bedrijfsomstandigheden waarin deze geluidsdempers opereren, zijn dikwijls moeilijk na te bootsen en op te volgen in een experimentele opstelling. Vele semi-empirische modellen, die ontwikkeld zijn om het akoestische gedrag van perforaties te beschrijven, kennen bovendien een beperkt toepassingsgebied of negeren bepaalde ontwerpparameters, die gebruikt kunnen worden om de akoestische demping te verbeteren. Om de fysische verschijnselen die voorkomen bij stromingsakoestische interacties aan perforaties beter te begrijpen en om het ontwerp van nieuwe passieve geluidsdempers te verbeteren, is er daarom een nood aan efficiënte numerieke voorspellings- en karakterisatiemethodes.

Het eerste deel van dit proefschrift onderzoekt het gebruik van lineaire akoestische operatoren in combinatie met efficiënte hoge-orde numerieke methodes voor het modelleren van de golfvoortplanting doorheen niet-homogene media en niet-uniforme stromingsgebieden, rekening houdend met verscheidene convectieve en dissipatieve fenomenen. Deze lineaire methodes worden verder toegepast om de invloed van lokale scherende stromingen, temperatuursprofielen en turbulente stroming op het akoestisch gedrag van de perforaties te karakteriseren.

In het tweede deel wordt een methodologie voor de bepaling van de

impedantie van Helmholtz-resonatoren, gebaseerd op technieken uit de numerieke stromingsleer (Computational Fluid Dynamics) en de oplossing van de onsamendrukbare stromingsvergelijkingen, voorgesteld en geëvalueerd. Deze methode wordt vervolgens toegepast om de niet-lineaire fenomenen, die plaatvinden aan de resonatoropening door de loshechting van de stroming onder hoge amplitude excitaties, te analyseren.

Het vibro-akoestische gedrag van geperforeerde platen is het onderwerp van het laatste deel van dit werk. Een numerieke ontwerp- en optimalisatietoepassing, die een model voor de akoestische potentiaal koppelt met structurele schaalelementen, wordt toegepast op passieve akoestische dempers, gebaseerd op flexibele micro-geperforeerde panelen. De validatie en een diepgaande studie worden uitgevoerd op een cilindrische resonator, die gebruik maakt van een micro-geperforeerde plaat met circulaire openingen met een rechte rand.

De ontwikkelde numerieke methodes laten toe om de stromingsakoestische interacties, de niet-lineariteiten en de vibro-akoestische koppeling die plaatvinden bij perforaties in passieve akoestische dempers, in meer detail te onderzoeken. Daardoor kunnen deze technieken een dieper inzicht verschaffen in het fysisch gedrag, wat op termijn kan leiden tot de ontwikkeling van meer performante geluidsdempers.

# List of Abbreviations

| | |
|---|---|
| ***p*-FEM** | High-order continuous Finite Element Method |
| **ABL** | Acoustic Boundary Layer |
| **APE** | Acoustic Perturbations Equations |
| **BC** | Boundary Condition |
| **CAA** | Computational AeroAcoustics |
| **CFD** | Computational Fluid Dynamics |
| **DGM** | Discontinuous Galerkin Method |
| **DNS** | Direct Numerical Simulation |
| **DoF** | Degree of Freedom |
| **f-MPP** | Flexible Micro-Perforated Plate |
| **FEM** | Finite Element Method |
| **FVM** | Finite Volume Method |
| **GLS** | Galerkin/Least-Squares |
| **HIE** | Hole Interaction Effect |
| **LBM** | Lattice Boltzmann Method |
| **LEE** | Linearized Euler Equations |
| **LES** | Large Eddy Simulation |
| **LHS** | Left-Hand Side |
| **LNS(E)** | Linearized Navier-Stokes (Equations) |
| **LPE** | Linearized Potential Equation |

| | |
|---|---|
| **MP** | Monitoring point |
| **MPI** | Message Passing Interface |
| **MPP** | Micro-Perforated Plate |
| **ODE** | Ordinary Differential Equation |
| **OHO** | "Odd-Harmonics-Only" pattern |
| **PML** | Perfectly Matched Layer |
| **RANS** | Reynolds-averaged Navier-Stokes |
| **RHS** | Right-Hand Side |
| **RKDG** | Runge-Kutta Discontinuous Galerkin |
| **RMS** | Root Mean Square |
| **SGS** | SubGrid-Scale |
| **SI** | System Identification |
| **SISO** | Single-Input, Single Output |
| **SPL** | Sound Pressure Level |
| **SST** | Shear Stress Transport |
| **SUPG** | Streamline-Upwind Petrov-Galerkin |
| **UIR** | Unit-Impulse-Response |
| **URANS** | Unsteady Reynolds Averaged Navier-Stokes |

# List of Symbols

**Roman Symbols**

| | |
|---|---|
| $A_\bullet$ | Inlet excitation amplitude (e.g. $A_f$, $A_u$, and $A_{f,o}$) |
| $b$ | Distance between orifices |
| $c_0$ | Speed of sound |
| $C_d$ | Discharge coefficient or *vena contracta* factor |
| $C_p$ | Specific heat capacity at constant pressure |
| $C_v$ | Specific heat capacity at constant volume |
| $d$ or $D$ | Diameter |
| $D_P$ | Plate flexural rigidity |
| $\mathcal{D}'_\bullet$ ($\mathbb{D}'_\bullet$) | Source/sink terms for the first-order energy (and integral values) |
| $\mathcal{D}_\mathrm{s}$ | Scheme's stabilization operator |
| $e$ | Specific energy |
| $E_P$ | Young's modulus of the material |
| $\widehat{\mathbf{f}}^{\mathbf{\Gamma}_i}$ | Riemann approximated boundary flux on boundary $\Gamma_i$ |
| $f$ | Frequency |
| $f_c$ | Cut-off frequency |
| $f_n$ | Natural structural frequency |
| $R_r$ and $G_r$ | Riemann invariants |
| $H$ or $h$ | Height |
| $h$ | Grid element size |
| He | Dimensionless Helmholtz number |
| $H_\mathrm{MF}$ | Shape factor of flow profile |
| $\mathcal{H}_n$ | Relative content of the $n^{\mathrm{th}}$ harmonic |
| $\mathbf{I}$ | Unit tensor or identity matrix |

| | |
|---|---|
| j | Imaginary unit ($\mathrm{j} = \sqrt{-1}$) |
| $J_m$ | Bessel function of the first kind of order $m$ |
| $K$ | Turbulent kinetic energy |
| $k$ | Stiffness |
| $k_0$ | Acoustic wavenumber |
| $k_{mn}^{\perp}$ | Transversal wavenumber of the mode $(m, n)$ |
| $k^{\pm}$ | Axial wavenumber of the downstream/upstream propagating plane wave |
| $k_{mn}^{\pm}$ | Axial propagation constant of the downstream/upstream mode $(m, n)$ |
| $l$ or $L$ | Length |
| $l_c$ | Convection length |
| $\mathcal{L}_{\bullet}$ | Differential acoustic wave operator (e.g. $\mathcal{L}_{\mathrm{LNSE}}$ or $\mathcal{L}_{\mathrm{LEE}}$) |
| $m$ | Mass |
| $M_0$ | Mach number of the mean flow ($M_0 = u_0/c_0$) |
| $\mathbf{n}$ | Normal unit vector |
| $N_{\bullet}$ | Number of something (e.g. $N_s$, $N_p$, $N_m$, and $N_{\mathrm{elt}}$) |
| $p$ | Order of the polynomial shape functions |
| $p$ | Pressure |
| $\mathbf{p}^{\pm}$ | Modal amplitude vector |
| Pe | Dimensionless Péclet number |
| Pr | Dimensionless Prandtl number |
| $\mathcal{Q}$ | Internal heat release rate per unit volume ($Q_v$ and $Q_t$) |
| $\mathbf{q_t}$ | Heat flux |
| $r$ | Normalized acoustic resistance ($r = Re(z)$) |
| $R$ | Ideal gas constant ($R = C_p - C_v$) |
| $r$ or $R$ | Radius |
| $R^{\pm}$ | Reflection coefficient |
| Re | Dimensionless Reynolds number |
| $R_f$ | Rounded edge radius |
| $s$ | Entropy |
| $S$ | Surface |
| $\mathbf{S}$ | Acoustic scattering matrix |
| $\mathbf{S}$ | Shear strain rate tensor |
| Sh | Dimensionless Shear number |

| | |
|---|---|
| Sr | Dimensionless Strouhal number |
| $T$ | Temperature |
| $t$ | Time |
| $t$ | Thickness |
| $T^{\pm}$ | Transmission coefficient |
| $\mathbf{u}$ or $\mathbf{v}$ | Velocity vector |
| $u_c$ | Effective convection speed of vortex |
| $V$ | Volume |
| $\mathbf{w}$ | Plate displacement vector |
| $W_{\text{diss}}$ | Dissipated acoustic power |
| $\mathcal{W}'$ ($\mathbb{W}'$) | First-order energy flux vector (and integral value) |
| $w$ or $W$ | Width |
| $\mathbf{x}$ | Position in Cartesian coordinates ($\mathbf{x} = (x, y, z)$ or $(x_1, x_2, x_3)$) |
| $Z$ | Impedance |
| $z$ | Normalized impedance |
| $Z_0$ | Characteristic impedance of the medium ($Z_0 = \rho_0 c_0$) |
| $Z_t$ | Transfer impedance |
| $z_{\text{plate}}$ | Plate structural impedance |
| $z_p^{\star}$ or $z_p^{\star\star}$ | Modified perforation impedance |

**Greek Symbols**

| | |
|---|---|
| $\alpha$ | Acoustic absorption coefficient |
| $\alpha_{\bullet}$ | Dimensionless resistive end-correction coefficient (e.g. $\alpha_s$) |
| $\gamma$ | Ration of specific heat constants ($\gamma = C_p/C_v$) |
| $\Gamma_m$ | Directivity of the RMS pressure |
| $\delta(\mathbf{x})$ | Dirac function |
| $\delta_{\bullet}$ | Dimensionless reactive end-correction coefficient (e.g. $\delta_s$) |
| $\delta_h$ | Dimensionless correction to compensate for excess reactance |
| $\delta_{ij}$ | Kronecker delta function |
| $\delta_{\text{MF}}$ | Flow boundary layer thickness |
| $\delta_{v/t}$ | Viscous or thermal boundary layer thickness |
| $\Delta l_m$ | Distance between microphone locations (or monitoring sections) |
| $\Delta t$ | Time step |
| $\epsilon$ | Turbulent dissipation |

| | |
|---|---|
| $\epsilon_\bullet$ | Relative change in parameter $\bullet$ |
| $\eta_P$ | Structural loss factor |
| $\theta_K$ | Axial attenuation coefficient |
| $\theta_{\mathrm{MF}}$ | Momentum thickness |
| $\lambda_a$ | Acoustic wavelength |
| $\Lambda_d$ | Dimensionless number for vortex disruption ($\Lambda_d = l_c/l_o$) |
| $\lambda_h$ | Hydrodynamic wavelength |
| $\lambda_t$ | Thermal conductivity |
| $\mu$ | Dynamic viscosity |
| $\mu_t$ | Turbulent dynamic viscosity or eddy-viscosity |
| $\nu$ | Kinematic viscosity |
| $\nu_P$ | Poisson ratio of the material |
| $\xi$ | Dissipation potential ($\xi_{\min}$ and $\xi_{\max}$) |
| $\xi$ | Normalized acoustic resistance ($\xi = Im(z)$) |
| $\rho$ | Mass density |
| $\sigma$ | Porosity or open area ratio |
| $\boldsymbol{\tau}$ | Viscous stress tensor |
| $\tilde{\tau}_{ij}^R$ | Perturbation Reynolds stress |
| $\tau_s$ | Numerical stabilization parameter |
| $\chi_o$ | Normalized mass reactance |
| $\Psi$ | Complex displacement amplitude |
| $\omega$ | Angular frequency ($\omega = 2\pi f$) |
| $\omega$ | Specific turbulence dissipation rate |
| $\omega_{PC}$ | Panel-cavity resonance frequency |
| $\mathbf{\Omega}$ | Vorticity ($\mathbf{\Omega} = \nabla \times \mathbf{u}$) |

**Miscellaneous symbols**

| | |
|---|---|
| $\hat{\bullet}$ | Frequency domain variable |
| $\tilde{\bullet}$ | Periodic fluctuation |
| $\phi(\bullet)$ | Phase of the variable |
| $\langle\bullet\rangle$ | Phase average |
| $\overline{\bullet}$ | Time average |
| $\bullet^T$ | Transpose of a vector/matrix |
| $\bullet^*$ | Complex conjugate or complex transpose of a vector/matrix |

| | |
|---|---|
| $\bullet^{-1}$ | Inverse matrix |
| $\bullet^{\dagger}$ | Moore Penrose pseudo-inverse |
| $\nabla$ | Nabla operator |
| $\nabla^2 \bullet$ | Laplacian operator |
| $\bullet \cdot \bullet$ | Scalar product of two vectors |
| $\bullet : \bullet$ | Scalar product of two tensors |
| $\bullet \times \bullet$ | Tensor product of two vectors |
| $\partial \bullet / \partial t$ | Time partial derivative |
| $\mathrm{D} \bullet / \mathrm{D}t$ | Material derivative ($\mathrm{D} \bullet / \mathrm{D}t = \partial \bullet / \partial t + \mathbf{u} \cdot \nabla \bullet$) |

**Sub- and Superscripts**

| | |
|---|---|
| $\bullet_0$ | Time-averaged component of a variable |
| $\bullet'$ | Perturbation around the time-averaged value |
| $\bullet''$ | Turbulent quantity |
| $\bullet^+$ | Variable associated to the downstream propagating wave |
| $\bullet^-$ | Variable associated to the upstream propagating wave |
| $\bullet_{in}$ | Variable referring to the inlet |
| $\bullet_{o/p/s}$ | Variable referring to the orifice/perforation/slit, respectively |
| $\bullet_{\mathrm{cav}}$ | Variable referring to the resonator cavity |
| $\bullet_{\mathrm{res}}$ | Variable referring to the resonance |

# Contents

# Part I

# Introduction

# Chapter 1

# Introduction

Noise is defined as "undesired sound waves", and even if it is commonly considered as a problem of comfort, it has a large impact on daily life. Noise can have dramatic effects on the human health and well-being. According to different studies [264, 316], the exposure to noise can be responsible for hearing loss, tinnitus, sleep disturbances, cardiac diseases and even cognitive impairment of children. With all these effects considered, the World Health Organization categorizes noise as being the second-worst environmental cause of ill health, behind ultra-fine particulate matter air pollution [99]. Aware of this nuisance, the legal administrations have counteracted by continuously strengthening the regulations on the allowed noise emission by systems over the last years. This trend appears to continue over the coming decades [264] and puts a lot of pressure on the development of many engineering solutions to meet the legislation targets. Engineering companies are therefore forced to consider the acoustic properties of their systems in the early stages of the design process.

## 1.1 Noise control by means of passive acoustic dampers

Noise emission reduction from a given system can be achieved by limiting the sound source itself by means of design modifications. An example of such strategy is the improvement of airframe components of an aircraft to decrease aerodynamically generated sound [197]. However, for many industrial applications, the noise source cannot be diminished and one has to add noise control devices to damp the propagation of the produced acoustic waves before they reach the actual receiver. Passive acoustic dampers with perforations in the shape of Helmholtz resonators, perforated plates, and liners, are one of the

most commonly used solutions to suppress noise propagation, together with absorbing materials. Perforate structures, as illustrated in Figs. 1.1a and 1.1b, can be used inside mufflers for automotive exhausts [10] or ventilation and air conditioning systems in buildings or vehicles [3, 5]. Both perforated and micro-perforated panels are used in room acoustics [170, 171] to improve the sound quality or in engineering applications, like to control the compressor noise in IC-engines [168]. Other examples of these passive sound absorbers are aircraft liners, which can be considered as an array of Helmholtz resonators (see Fig. 1.1c). They are commonly placed in the inlet and exhaust ducts of turbofan engines to meet the ever more restrictive noise regulations. Besides the audible nuisance provoked by noise emission, undesired sound waves are also known to threaten the efficiency and integrity of combustion-driven devices, such as gas turbine engines and domestic burners. In this case, Helmholtz resonators [30, 93, 123, 317] and perforated structures [186, 205] are used to suppress thermo-acoustic instabilities by avoiding acoustic feedback from the acoustic waves produced by the combustion process toward the flame zone (see Fig. 1.1b). If occurring, thermo-acoustic instabilities can cause large intensity pressure oscillations in the combustion chamber, yielding to possible mechanical failure.

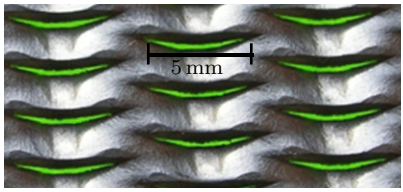


(a) Commercial MPP absorber based on slit-shaped holes (Acustimet™) [10]

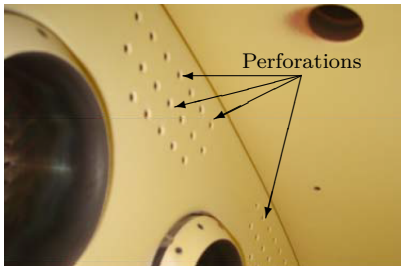


(b) Perforations included in a SGT-800 combustor for cooling and passive acoustic damping purposes [205]

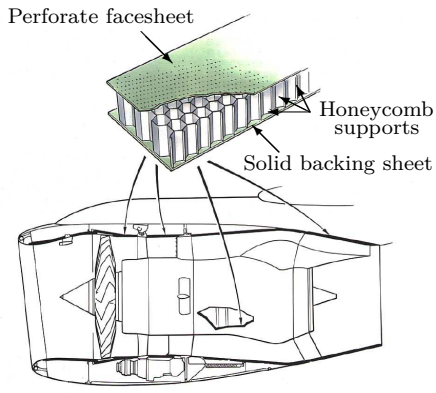


(c) Perforated liners in an aero-engine [250]

Figure 1.1. Passive acoustic dampers with perforations for noise control in industrial applications.

The suitability of Helmholtz resonators and perforated plates as passive noise control solution for engineering applications is motivated by several reasons:

- Their acoustic performance is robust compared to classical acoustic absorbers having fibrous structure (e.g. bulk absorbers with poroelastic materials and foams) since their geometrical properties are more persistent in time [210].
- Unlike classical bulk sound absorbers, resonators with perforates are not susceptible to contaminate the system, in which they are placed, with particles of dust breaking off from the absorber [226] and can withstand harsher working conditions [187].
- They can be made from a large variety of materials such as titanium, aluminum, composite or polyvinyl chloride, so that they can be more compact, lightweight and durable [210].
- They are relatively inexpensive to produce and convenient to manufacture compared to more advanced noise control solutions like metamaterials [252] and active noise devices [34].

As a result, passive silencers with perforations are an appealing solution both with respect to their damping potential and their integrability into existing systems. For this reason, different concepts with alternative arrangements of perforates and cavities have emerged [10, 48, 257].

Even though these passive acoustic dampers are rather simple devices and have been studied for many decades [157, 174, 208, 240], there are still aspects requiring further analysis in order to utilize their full potential. Their absorption properties can significantly differ depending on the geometry of the perforations [210], the amplitude of the incoming acoustic excitation [69,133,159], and the presence of both grazing [96, 166] or bias [186] flow. The large variety of the operating conditions, encountered by these silencers, can be difficult to monitor and measure in experimental setups. Additionally, many of the semi-empirical models, developed to describe their acoustic behavior, suffer from limitations in their applicability range and often neglect parameters that could be used to enhance their attenuation performance. In order to better understand the physical phenomena linked to sound-flow interaction at perforates and to improve the design of future passive sound absorbers, the need for efficient numerical prediction schemes and characterization methods comes to the fore.

## 1.2 Challenges and research methodology

This dissertation addresses three numerical methods to investigate the acoustic behavior of orifices and resonators with perforations. Each of these approaches focuses on a particular aspect of the physics of passive dampers. In this thesis, the methods are presented in conjunction with each other to deliver a global

understanding of the acoustic properties of such devices and to develop a set of numerical tools to deepen the knowledge of damping mechanisms involved. This allows to identify the driving design parameters and, finally, to optimize passive noise control devices.

Helmholtz resonators and similar perforated silencers are known [157] to behave in a linear manner at low and moderate sound pressure levels (i.e. $< 130\,\mathrm{dB}$). In this regime, it is expected that linearized governing equations and hybrid Computational AeroAcoustic (CAA) methodologies can be used to model their acoustic behavior. Due to the inherent dissipative nature of the damping mechanisms, along with the non-uniform flow effects taking place inside sound absorbers in presence of flow, the linearized Navier-Stokes equations are chosen to model the acoustic propagation. This approach has been applied before to different flow-duct geometries using both frequency-domain [114, 115, 175–177] and time-domain [295] simulations. This strategy allows to capture the linear interactions between the fluctuating acoustic, hydrodynamic, and entropy fields. Acoustic dampers constitute a challenging configuration for the numerical methods because of the large disparity of length scales of such problem and the possible importance of flow-acoustic interactions. The characteristic length scales, ranging from the acoustic wavelength to the very thin acoustic boundary layer thickness at the perforations, require the development of highly efficient numerical methods to accurately predict the acoustic wave propagation through a non-isentropic and non-homogeneous flow region.

By increasing the excitation amplitudes, nonlinear effects appear and become progressively dominant [159, 160, 268]. Such nonlinearities originate from the separation of the acoustic boundary layer at the edges of the perforations constituting the neck of the resonator. As a consequence, a substantial amount of the acoustic energy is transfered to the hydrodynamic field [69]. The creation of these vortices at the orifice significantly increases the dissipation of the acoustic energy. This feature is of large importance for the design of acoustic dampers subjected to large excitation levels, as it can substantially impact the sound wave attenuation. However, these nonlinear attenuation principles are more complex to predict accurately due to the intrinsic nature of the physical phenomena at stake. Linear numerical methods can therefore not be used at medium and high excitation amplitudes and nonlinear time-domain solvers are needed [279]. In this context, a methodology based on unsteady incompressible flow simulations is established to investigate the nonlinear damping mechanisms present in passive silencers with perforations.

As mentioned before, passive acoustic dampers can be made out of a wide variety of materials. Depending on this material, structural vibrations can become an influential parameter of the acoustic response of a silencer [190, 193, 298]. This is predominantly the case for devices with a low porosity facing sheet of low structural stiffness and perforations of small dimensions [190, 276]. This situation is typical for absorbers based on Micro-Perforated Plates (MPPs). For

such cases, the elasticity of the facing sheet should therefore be included in the design process of passive noise control systems based on MPPs to improve their absorption properties. A fully coupled vibro-acoustic Finite Element Model (FEM) is proposed to investigate the effect of structural vibrations for silencers with flexible MPPs.

The followed methodology for this dissertation is, therefore, to investigate one dedicated numerical approach for each particular aspect listed above,viz.: the linear flow-acoustic, nonlinear aeroacoustic, and vibro-acoustic phenomena.

## 1.3 Research goals and achievements

Considering the number of applications, stated in Section 1.1, that can benefit from improved design tools and an overall better understanding of the complex physics involved in sound wave absorption by perforated silencers, this dissertation pursues a dual goal:

- The research work aims to develop novel and efficient numerical techniques to characterize the aero- and vibro-acoustic behavior of perforated silencers in complex working conditions.
- These numerical methods are applied to a selected set of acoustic resonators and orifices under various conditions to characterize the damping mechanisms involved and identify potential parameters that can be included in the modeling and design of future passive silencers.

The envisaged numerical simulation and characterization approaches enable an original investigation of linear and nonlinear aeroacoustic interaction phenomena, as well as vibro-acoustic coupling mechanisms, which typically occur at perforates in passive acoustic dampers.

To achieve these objectives, the following research tasks have been completed:

**High-order solvers for the linearized Navier-Stokes equations**
In order to investigate the linear regime of perforated acoustic dampers, advanced acoustic solvers based on the linearized Navier-Stokes equations (LNSE) are implemented. Such hybrid methods, assuming the acoustic perturbation quantities to be much smaller than the mean flow variables, allow to compute the propagation of acoustic waves through nonuniform and non-isentropic flow regions, accounting for all dissipative and convective effects. Here, the contributions are:

- Development in Matlab of a frequency-domain high-order continuous Finite Element Method ($p$-FEM) solver for quasi-laminar and turbulent LNS equations for 2-D and 3-D problems.

- Extension of an existing time-domain Runge Kutta discontinuous Galerkin (RKDG) solver [242, 293] for non-isentropic conditions.
- Implementation of a set of characterization techniques for impedance determination and study of the damping mechanisms in the framework of linearized solvers.
- Validation of the $p$-FEM code regarding both flow and visco-thermal effects on acoustic waves. The reference cases cover a monopole source radiating in a plate boundary layer [273, 274], waveguides of small dimensions [42] and micro-perforated plates [289].
- Application to perforated structures with a particular focus on:
  - the influence of a grazing flow at low Mach numbers on the behavior of a slit Helmholtz resonator, compared to measurement data by Denayer [81],
  - the impact of flow turbulence on the linear acoustic predictions for an orifice configuration with bias flow (with $p$-FEM) and resonators with grazing flow (with RKDG),
  - the temperature effects in resonators by means of $p$-FEM simulations.

This work delivers efficient tools to predict and analyze the linear regime of acoustic dampers.

**Unsteady incompressible flow simulations for the characterization of nonlinearities**

A methodology based on the Computational Fluid Dynamics (CFD) solution of incompressible flow equations is considered for the acoustic characterization of Helmholtz resonators under high amplitude excitations. It constitutes a powerful tool to study aspects of the nonlinear aeroacoustic interactions at orifices and resonator necks. In this context, the following achievements are made:

- Unsteady flow simulations, using the commercial software ANSYS® Fluent, are performed on different circular orifices. A decomposed Helmholtz resonator model is adopted to predict the acoustic impedance of the complete resonators.
- The incompressible flow simulations are validated against high-fidelity compressible CFD simulations done by Förner et al. [109] and measurement data by Temiz et al. [108] and Hersh et al. [133].
- A methodology is developed at this occasion, in collaboration with Förner et al., to assure the same excitation amplitude at the resonator mouths between simulations and experiments.
- Three-dimensional effects and micro-rounding of the orifice edges are quantified.

- The nonlinear damping mechanisms are detailed in the light of the observed local flow fields. The transfer of acoustic energy towards higher harmonics is thoroughly analyzed and explained via the quasi-steady theory [72] and the novel concept of vortex disruption.

**Coupled vibro-acoustic FEM model with a patch-impedance approach**
A numerical design and optimization tool, which couples a potential acoustic solver and structural shell elements, is proposed for passive noise control devices based on flexible micro-perforated panels. Thanks to a patch-impedance approach to represent the perforations, the numerical tool enables to include the spatial effects of the perforation distribution. The contributions include:

- The development of the methodology is done jointly with Temiz et al. [288]. All simulations are performed with the commercial software LMS Virtual.Lab® [1].
- Results are validated, for the case of a micro-perforated plate clamped inside an impedance tube, by comparison to the experimental data published by Toyoda et al. [298].
- The numerical model is then refined to allow the investigation of the impact of vibrations on the orifice impedance itself.

## 1.4 Outline of the dissertation

This thesis is structured into five main parts.

**Part I** consists of this introductory and Chapter 2.

**Chapter 2** presents the physical phenomena involved in the damping of acoustic waves by means of resonators with perforations and perforated structures. This leads to the separation between linear acoustic regime, nonlinearities related to flow separation, and vibro-acoustic coupling. The state-of-the-art numerical approaches for each particular problem are reviewed and the current research work is positioned.

**Part II** discusses the numerical techniques and dedicated post-processing characterization tools for the flow-acoustic behavior of passive acoustic dampers in their linear regime.

**Chapter 3** describes the linearized models for the acoustic propagation in the presence of a non-uniform flow and non-homogeneous medium. The numerical methods, developed in this work, to solve such complex

linear acoustic problems in time and frequency domains are presented and implementation specificities are given. This chapter ends with several validation cases.

**Chapter 4** applies both frequency- and time-domain linearized propagation solvers to cases of orifices and resonators under complex environmental conditions. The impact of grazing and biased flows, mean flow turbulence and non-isentropic conditions with temperature effects are also investigated.

**Part III** presents the numerical work performed on the nonlinearities happening at Helmholtz resonator necks and orifices when the acoustic boundary layer separates for large enough excitation amplitudes.

In **Chapter 5**, a methodology using unsteady incompressible Reynolds-Averaged Navier-Stokes simulations for the acoustic characterization of Helmholtz resonator is presented. The approach is validated against both compressible flow simulations and experimental data for two resonator geometries over a broad range of frequencies and amplitudes.

**Chapter 6** focuses on the description of the scattering of the acoustic energy towards higher harmonics for orifices. A theoretical model, based on the vortex convection length inside the orifice, is derived to predict deviations from the standard pattern in the higher harmonics. This work draws the link between the local flow field, the measured impedance, and the spectrum of the acoustic response.

**Part IV** presents the research results on the vibro-acoustic behavior of perforated plates.

**Chapter 7** introduces a fully coupled vibro-acoustic Finite Element Method model using impedance patches to study the impact of structural vibrations on the acoustic absorption properties of perforated plates. The FEM approach is validated against experiment data found in the literature. The coupling of panel-controlled and hole-controlled resonance phenomena are discussed in the light of the numerical results. The effect of vibrations on the local perforation impedance is finally examined via a modified analytic impedance model accounting for the plate impedance.

**Part V**, consisting of **Chapter 8**, summarizes the main conclusions and achievements of this research work and presents suggestions for further research.

# Chapter 2

# Acoustic characterization of passive sound absorbers with perforates

This research work aims at developing numerical models to investigate different aspects of the acoustic behavior of orifices and resonators. In this chapter, the working concept of passive sound absorbers and the physics involved in the damping of acoustic waves at perforates are presented. This section introduces the essential terminology and major parameters which need to be considered for the design of passive silencers. Furthermore, this section highlights the remaining challenges and open questions relevant for an accurate aeroacoustic design of acoustic dampers, which will be tackled in the next parts of this dissertation. The second part of this chapter presents the commonly used techniques to characterize the acoustic response of perforates and to determine the related impedance value. These are required concepts and post-processing steps of the proposed numerical framework. Finally, this chapter ends with a review of the state-of-the art CAA techniques for the study of passive silencers with perforations, in order to better position the numerical methods developed throughout this thesis.

## 2.1 The physics of passive silencers with orifices

### 2.1.1 Working principle of noise control via passive acoustic dampers

Passive silencers with perforations exploit the resonance of a cavity being connected via one or several openings to its environment, as illustrated in Fig. 2.1a (bottom). When the dimensions of the opening are rather large, the silencer is qualified as purely reactive, as it uses acoustic wave interferences to cancel sound propagation [269]. Quarter-wave resonators, which are simple tubes with a closed end, are an example of purely reactive resonators. When a perforated sheet is placed on top of the cavity, the resonance leads to high particle velocities at the orifices, which causes acoustic losses through friction. Helmholtz resonators, consisting of a hole (neck) and a reacting backing volume, work according to this concept. Acoustic liners [96, 187], made of a honeycomb structure with a rigid backing plate covered by a perforated panel (resistive surface), can be considered as an array of Helmholtz resonators.

These reactive types of silencers can be used in combination with dissipative parts such as porous materials [196, 266]. Various hybrid noise control strategies are proposed to enhance the performance of reactive silencers, e.g. by using an arbitrary combination of porous and air layers backed by a hard wall [275]. The reverse concept, by embedding Helmholtz resonators inside a porous matrix [44] or porous plate [121], has also been investigated recently. They fall, however, out of the scope of the present thesis.

In general, two main types of passive acoustic treatment can be distinguished: locally reacting (also point-reacting type) and non-locally reacting (bulk-reacting) resonators. Locally reacting liners do not allow sound propagation inside the cavity, except in the normal direction to the backing wall. This is the typical situation for honeycomb liners. The locally reacting condition is usually achieved by having the perforations on top of acoustically separated and compact cavities. Acoustic compactness is determined by small values of the Helmholtz number $\mathrm{He} = k_0 L_\perp$, where $k_0 = \omega/c_0$ is the acoustic wavenumber, $\omega = 2\pi f$ is the angular frequency of the sound excitation, $c_0$ is the speed of sound, and $L_\perp$ represents the transversal dimensions of the cavity. In this case, the behavior is independent of the angle of the incident acoustic wave [229] and can be defined point-wise. Otherwise, the resonator is referred to as non-locally reacting and its behavior cannot be described by a single degree-of-freedom (SDOF) model. Examples of the latter are conical [325] or spiraling [267] geometries of large cavities or standard liners with partially communicating cells [51]. In many technical applications, resonators can be considered to be locally reacting. Hence, this thesis is restricted to this kind of silencers for the theoretical modeling part. The numerical methods developed, in particular the aeroacoustic linear solvers of Chapters 3 and 4, can nevertheless also be applied

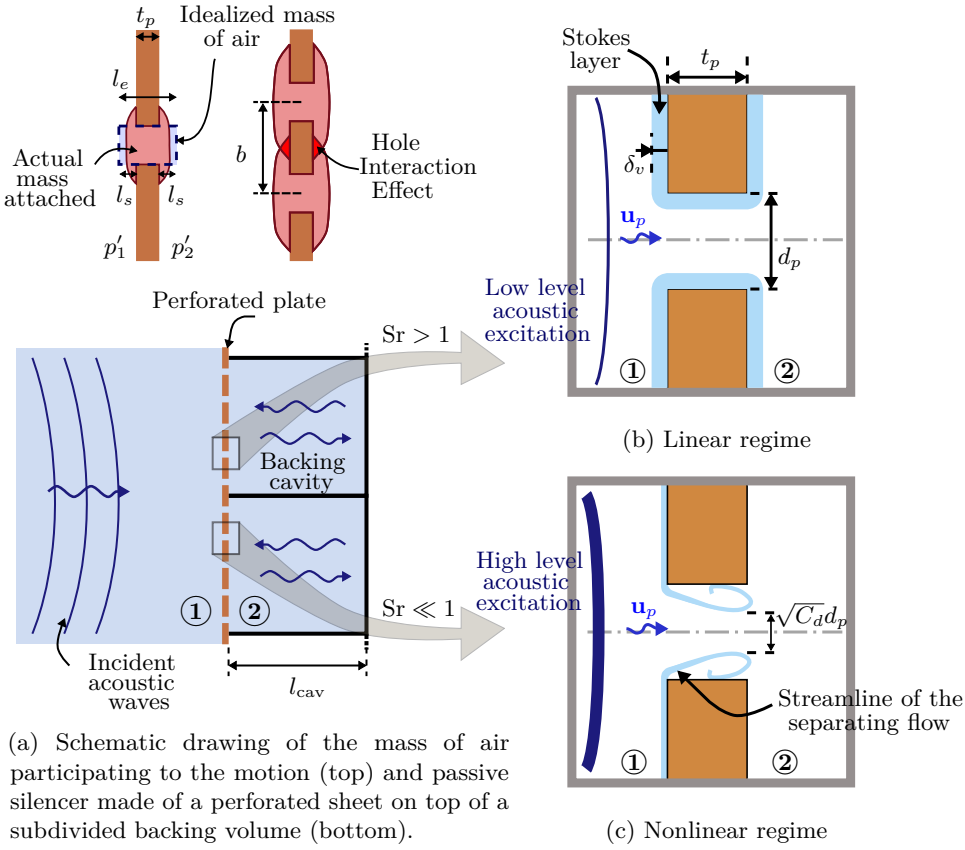


(a) Schematic drawing of the mass of air participating to the motion (top) and passive silencer made of a perforated sheet on top of a subdivided backing volume (bottom).

(b) Linear regime

(c) Nonlinear regime

Figure 2.1. Passive reactive silencer with resistive surface: (a) general geometry and differences in the acoustic energy dissipation mechanisms depending on the excitation level for the (b) linear and (c) nonlinear regimes.

to non-locally reacting cases.

The working principle of locally reacting resonators can be explained by analogy to a mechanical system [240], as illustrated in Fig. 2.2 for both a rigid and an elastic facing sheet. For the rigid wall case, the external acoustic pressure drives the effective fluid mass $m_h$ in the resonator neck or perforations to move and oscillate due to the compressibility of the backing volume, similar to the stiffness $k_{\text{cav}}$ of a spring in the mechanical analogy. The viscous losses due to friction in the holes can be related to a mechanical damper $r_h$. The energy losses by propagation inside the cavity are usually neglected, leading to the commonly accepted assumption: $r_{\text{cav}} \approx 0$. Such a mechanical analogy is justified since the fluctuating velocity $u'_p$ in the resonator neck can be expressed, according to the

semi-analytical model of Keller and Zauner [174], as:

$$\underbrace{(1+s)l_e\rho_0\ddot{u}'_p}_{\text{Air mass inertia}} + \underbrace{\left(s\rho_0(t_p+l_s)\omega + \zeta\rho_0\left|u'_p\right|\right)\dot{u}'_p}_{\text{Losses at neck}} + \underbrace{\frac{S_p\rho_0c_0^2}{V_{\text{cav}}}u'_p}_{\text{Compressibility}} = -\dot{p}'\,, \qquad (2.1)$$

where the parameters $t_p$, $d_p$ and $S_p$ denote respectively the length, diameter, and surface area of the neck. The volume of the cavity is given by $V_{\text{cav}}$ and $\sigma$ stands for the open area ratio or porosity. The term $\rho_0$ is the fluid density. The effective length $l_e$ corresponds to the corrected length of the neck to take into account the attached mass of air in the vicinity of the orifice, as illustrated in Fig. 2.1a (top). In this model, $l_s$ is a friction correction length, $\zeta = 1-(d_p/d_{\text{cav}})^4$, and the so-called boundary layer parameter $s$ accounts for the thermo-viscous dissipation. The correction lengths can be estimated [157] as $l_s \approx d_p$, and for small porosity values, $l_e \approx t_p + 8/(3\pi)d_p$. Equation (2.1) clearly indicates the mass-spring-damper character of the SDOF resonator, excited by an external fluctuating pressure $p'$. From the previous model, the angular resonance frequency $\omega_{\text{res}} = 2\pi f_{\text{res}}$ of the system, assuming the visco-thermal effects to be negligible ($s \ll 1$), can be formulated as:

$$\omega_{\text{res}} = \sqrt{\frac{k_{\text{cav}}}{m_h}} \approx c_0\sqrt{\frac{\sigma}{l_{\text{cav}}\,l_e}}. \qquad (2.2)$$

The parameter $l_{\text{cav}}$ denotes the depth of the backing cavity. The nature of the underlying mechanisms responsible for the acoustic damping is discussed in further detail in Section 2.1.2. When accounting for the elasticity of the perforated sheet, the structural parameters of the plate (mass $m_{\text{plate}}$, stiffness $k_{\text{plate}}$, and mechanical damping $r_{\text{plate}}$) have to be incorporated to properly describe the governing physics of the system. Such a coupled vibro-acoustic model of a passive silencer with a flexible perforated plate is discussed in Chapter 7.

The reactive nature of the discussed passive silencers leads to a clear stop-band behavior for the sound absorption: a typical Helmholtz resonator is only a very effective sound absorber at its resonance frequency $f_{\text{res}}$. Strategies to get sound absorbers with wide-band absorption characteristics have been proposed, for example by partitioning the adjoining cavity [203, 257], combining different air-cavity depths in one system [102] or associating perforations with distinct diameters on the facing sheet [258]. The usage of small scale perforations leads also to a more broadband acoustic absorption, yet with a decrease of the maximum value of absorption that can be achieved [210]. Micro-perforated plates (MPPs) are plates with orifices whose diameter $d_p$ is in the order of 1 mm and the open area to the plate surface ratio, defined as plate porosity $\sigma$, is in the order of 1%. Moreover, the thickness $t_p$ of a MPP is typically chosen as comparable to its perforation diameter to achieve best efficiency [210], i.e. $t_p/d_p = \mathcal{O}(1)$.

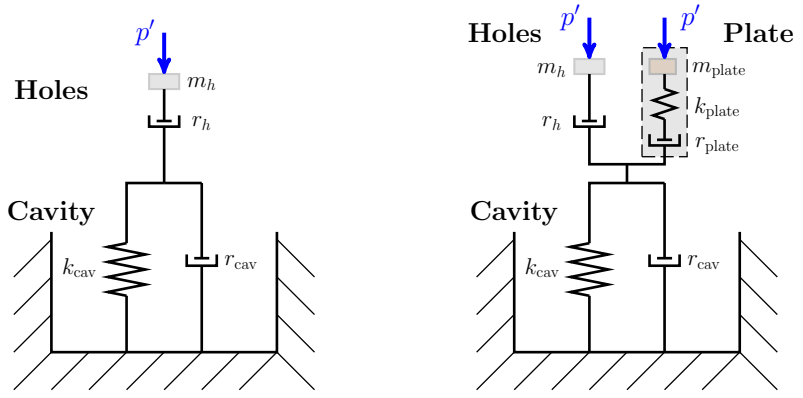


(a) Rigid Helmholtz resonator (b) Resonator with flexible plate

Figure 2.2. Mechanical equivalent model of a rigid (left) and an elastic (right) perforated panel combined with a cavity.

The distinction between the relative sizes of perforations can be made through the definition of a dimensionless number, the Shear number Sh. It is given [199] by the ratio of the perforation radius to the oscillating viscous boundary layer thickness $\delta_v = \sqrt{\nu/\omega}$, where $\nu$ is the kinematic viscosity of the acoustic medium. When $\text{Sh} = d_p\sqrt{\omega/(4\nu)} = \mathcal{O}(1)$, the oscillating viscous boundary layers tend to occupy the entire cross-section of the perforation, which results in increased acoustic energy dissipation due to viscous forces. For larger orifices, i.e. $\text{Sh} \gg 1$, the viscous losses at the resistive surface significantly decrease. In the case of MPPs, small porosity values are commonly chosen to amplify the viscous losses by ensuring high particle velocity amplitudes inside the perforations [210].

The acoustic behavior of sound treated surfaces and perforated sheets is commonly characterized using a surface impedance $Z$ or a transfer impedance $Z_t$. These quantities are defined in the frequency domain as the ratio of the pressure fluctuations $\hat{p}'$ (or pressure drop $\Delta\hat{p}'$) to the wall-normal acoustic velocity fluctuation $\hat{u}_i' n_i$. It yields:

$$Z(\omega) = \frac{\hat{p}'(\omega)}{\hat{u}_i'(\omega) n_i} = \frac{\hat{p}'(\omega)}{\sigma \hat{u}_{p,i}'(\omega) n_i}\,, \tag{2.3}$$

and

$$Z_t(\omega) = \frac{\Delta\hat{p}'(\omega)}{\hat{u}_i'(\omega) n_i} = \frac{\hat{p}_1'(\omega) - \hat{p}_2'(\omega)}{\sigma \hat{u}_{p,i}'(\omega) n_i}\,, \tag{2.4}$$

where $\Delta\hat{p}' = \hat{p}_1' - \hat{p}_2'$ is the sound pressure difference between the two ends of the orifice tube, $\hat{u}_p'$ is the averaged acoustic particle velocity in the perforation, and $\sigma$ is the open area ratio of the facing sheet. The acoustic impedance

describes the frequency response function for the pressure when the boundary is excited by a velocity fluctuation. This representation of perforates in terms of impedance is very convenient in the context of larger systems, as they can be incorporated as Robin type boundary conditions for numerical simulations or analytical models [261]. This is commonly done using the Ingard-Myers boundary condition [221], which assumes the acoustic normal displacement and pressure to be continuous across the boundary layer. More elaborate alternatives [20, 45] also exist[1], which consider the viscous and turbulent effects near the treated wall via a mixed condition between continuity of normal acoustic displacement and normal mass velocity over the lined wall [241]. The impedance value should therefore be regarded as an effective averaged boundary condition experienced by an incoming sound wave. In this work, the impedance will be mostly considered in its normalized form $z = Z/(\rho_0 c_0)$, where the product $Z_0 = \rho_0 c_0$ defines the characteristic impedance perceived by an acoustic wave propagating through the fluid. The real and imaginary parts of the complex valued normalized impedance $z = r + \mathrm{j}\,\xi$ are denoted as the resistance $r \equiv Re(z)$ and the reactance $\xi \equiv Im(z)$, respectively. Passive silencers are characterized by $Re(z) \geq 0$, corresponding to an actual sound absorption [245]. The two special situations of an ideal opening and a hard wall correspond respectively to the impedance values $z_{\text{open}} = 0$ and $|z_{\text{wall}}| = \infty$, .

Since Sivian experimentally investigated the impedance of small orifices [268] and Rayleigh laid the theoretical foundations for the acoustic modeling of small cavity-backed resonators [240], a large number of research studies have taken place during the past 60 years with the aim of understanding the physics of sound energy dissipation and improving impedance prediction models. These works, predominantly based on theoretical analyses [72, 135, 146, 149, 215], experiments [85, 160, 164] or semi-empirical approaches [96, 132], have lead to a host of impedance models for orifices and resonators under various conditions, with different validity ranges and target applications. Nevertheless, traditional experiments face difficulties to monitor and to analyze the sound-flow interaction mechanisms in complex working environments. High temperature conditions or strongly turbulent flows are examples of such situations. Consequently, numerical simulations, enabling the direct visualization and measurement of the small-scale flow features without risk of near-field contamination due to intrusive measurement setups, have recently started to contribute to the acoustic characterization and modeling of perforates (see Section 2.3).

The following sections present some of the major works that allow the description of the acoustic impedance for orifices and resonators. Specific models focusing

[1] The Ingard-Myers boundary condition was shown to be mathematically ill-posed in time-domain [45] and inaccurate in some lined wall cases due to boundary layer effects [241]. It was demonstrated that the continuity of normal displacement only holds when the ABL is much thiner than the stationary flow boundary layer.

on a particular application will be detailed in the relevant chapters when needed.

### 2.1.2 Aeroacoustic behavior of perforates and modeling

#### In quiescent medium

In the absence of flow and for low excitation amplitudes, the linear transfer impedance of a perforated plate is purely driven by the visco-thermal losses at the orifice walls [180, 208], in the so-called Stokes layer (see Fig. 2.1b). In the linear regime, the impedance is shown to be independent of the acoustic excitation level and can be expressed as function of solely the perforation geometrical parameters and frequency [286]. Common impedance models [210, 286] originate from the Kirchhoff's theory on the viscous and thermal dissipation of acoustic waves in stagnant fluid due to propagation in a capillary [180] or tube [240], or its simplified expression for short tubes by Crandall [68], combined with the end-correction theory proposed by Ingard [157] to deal with relatively thin plates. The previous classical modeling approach concentrates on the calculation of the acoustic impedance of one hole and its averaging using the fraction of perforated open area $\sigma$. Plates with perforation of small dimensions can, however, be also modeled as an equivalent fluid following the Johnson-Champoux-Allard [11,56,167] approach for rigid porous media with an equivalent tortuosity [17]. Both approaches have shown to be able to deliver similar results. In view of the broad range of orifice diameters considered in this work, and their well-defined geometric properties, impedance models based on geometrical parameters will be used throughout this dissertation.

The acoustic linearity of a perforation is defined by the ratio of its diameter $d_p$ to the acoustic particle displacement amplitude $\left|\hat{u}'_p/\omega\right|$, where $\hat{u}'_p$ is the averaged acoustic velocity amplitude in the perforation. This ratio is commonly referred to as the Strouhal number [87], noted here Sr. The acoustic response of a perforation is thus linear when $\mathrm{Sr} = (d_p\omega)/\left|\hat{u}'_p\right| \gg 1$ and strongly nonlinear when $\mathrm{Sr} \ll 1$. For decreasing Sr values, the acoustic energy damping mechanism strongly shifts from viscous dissipation within the orifice ($\mathrm{Sr} \gg 1$) to acoustic-induced vortex shedding at the edges of the orifice or perforate opening ($\mathrm{Sr} \ll 1$). Indeed, when the particle velocity at the orifice edges reaches a particular threshold, the fluid particle cannot follow the orifices contour anymore and the flow separates and a jet is formed [159, 160]. The flow separation is also characterized by a contraction of the flow through the orifice [326], as illustrated in Fig. 2.1c. The ratio of the flow core area to the geometrical cross-sectional area is defined as the *vena contracta* factor $C_d$, also referred to as the discharge coefficient [133, 319]. In the linear regime, where $\mathrm{Sr} \gg 1$, the discharge coefficient verifies $C_d \approx 1$, whereas $C_d < 1$ holds in the nonlinear regime [109].

The kinetic energy of the formed jet does not recuperate into acoustic energy but is transformed into vortices instead [69, 72]. This unsteady vortex shedding is further dissipated by the turbulent energy cascade process and viscosity. Flow separation leads to an improved acoustic dissipation at high acoustic excitation levels [69, 159]. As a result, the acoustic resistance of perforation rises with increasing particle velocity. Moreover, for $\mathrm{Sr} \ll 1$, the sound pressure in the opening is found proportional to the squared velocity $\hat{u}_p'$ and the orifice resistance at high sound pressure level is then proportional to the acoustic velocity, as stated by Ingård and Ising [159]. Even if less pronounced than for the resistance, flow separation also impacts the orifice reactance. With the increase of sound pressure levels, the orifice reactance decreases [215], linked to a reduction of the effective mass of air taking part in the oscillating motion. This corresponds to a reduction of the effective length and a shift of the resonator eigenfrequency toward higher values, as shown from Eq. (2.2). Besides the effects captured by the Strouhal number, also the edge shape has been shown to strongly influence the separation process. With sharp edges, the separation is more pronounced than with chamfers [108]. The impact of micro-rounded edges, as present on real test objects due to manufacturing, on the non-linear response of a Helmholtz resonator is discussed in Chapter 6.

The effect of flow separation can be described by the formation of a quasi-stationary jet, as given by Cummings and Eversman [72] with a quasi-steady model based on Bernoulli equations for perforations at high Shear numbers and low Strouhal numbers. Such model will be used in Chapter 6 to interpret the obtained numerical results. Similar models [37, 133, 134, 215], using a fluid mechanical approach and the discharge coefficient, were derived to determine the nonlinear behavior of orifices. Alternative nonlinear models are based on discrete vortex dynamics [165] or perturbation theories by retaining the second-order terms [324], for a single orifice or for a complete Helmholtz resonator. Although the increased generation of vorticity causes additional dissipation of acoustic energy, the latter model shows that the damping efficiency of the Helmholtz resonator actually decreases at higher amplitudes. This has been confirmed by scale-resolving direct simulation [249]. The efficiency drop is linked to the decrease of the quality factor of the oscillator, which reaches its overdamped state. Consequently, the frequency range of resonance is broadened and the relative response to excitation is weaker [324].

The case for which $\mathrm{Sr} = \mathcal{O}(1)$ is denoted as the *transition regime*. This region in-between the linear and non-linear regimes is investigated for small perforations in [287] within the range $\mathrm{Sh} \in [0.75, 8]$ and $\mathrm{Sr} \in [0.05, 10]$. It was shown that under these operating conditions, the nonlinear effects on both resistance and reactance depend predominantly on Sr and Sh. The dependence on Sh is significant for $\mathrm{Sh} = \mathcal{O}(1)$, but becomes negligible for higher values of Sh, i.e. $\mathrm{Sh} > 3$.

Another feature of the nonlinear regime is the distortion of the frequency

spectrum of the transmitted sound. Part of the acoustic energy is scattered towards higher harmonics. This effect has been demonstrated experimentally by Ingård and Ising [159] and Ingård [158] for a pure tone incident on an orifice plate in a duct terminated by an absorber, and by Cummings [69] using a tone-burst signal. This nonlinear phenomenon is the focus of Chapter 6.

The previous considerations regard the behavior of an orifice as isolated and neglect the influence of other neighboring perforations. This assumption is valid if the distance $b$ between the hole centers satisfies $d_p/b < 0.2$. In the contrary situation, the hole interaction effect (HIE) has to be accounted for, as represented in Fig. 2.1a (top). This was done by Fok [254] for low sound excitations. He derived, based on Rayleigh's work [240] and by assuming a potential flow, a polynomial approximation function $\Psi_{\mathrm{FOK}}(d_p/b)$ to modify the end-correction lengths. Hole interaction effects are further discussed by Melling [215] and Tayong et al. [284] for medium and high sound levels. The nonlinear regime resistance slope tends to be inversely proportional to the porosity, as the total shear region is reduced for interacting holes and causes a reduction in the radiation resistance [284].

### In presence of flow

The presence of a mean flow – grazing (tangential to the facing sheet), bias (flow through the orifice, also named purging), or a combination of both – can significantly influence the acoustic properties of orifices and resonators. In such situations, the complexity of the fluid mechanics significantly increases and less is known about the details of sound-flow interactions and how to accurately model them.

Quite a large number of experimental works [27,70,85,116,178,181,182,191,304] have been published on the influence of grazing flow on perforated SDOF resonators, typically liners of aero-engines. Most of the early investigations concentrate on the operating conditions of these liners, i.e. at low Strouhal numbers and mean flow boundary layers with large thickness compared to the streamwise width of the perforations, e.g. in [70,116,178,181] for circular orifices. Impedance models are predominantly summarized in empirical or semi-empirical laws. The experimental results and derived impedance models can vary in a large extent, mainly due to the different orifice geometries and flow conditions addressed [182]. Therefore, the resulting empirical models of orifice impedance lack generality [85,227], particularly in the earlier works that do not take into account the boundary layer characteristics [182]. One common trend noticed by the previous studies is that – at low Strouhal numbers – the orifice resistance increases[2] with the grazing flow velocity, while the reactance

[2] above a certain grazing flow velocity

decreases, compared to the no-flow case.

Theoretical models have been proposed to describe the underlying physics of sound absorption in presence of grazing flow at both low [244] and high [122] acoustic amplitudes. A popular one has been derived by Howe [144, 148, 149] and Howe et al. [151]. The model is based on the linear perturbation of an infinitely thin vortex sheet spanning the aperture, which models the interaction between the acoustic fluctuation and the unstable shear layer that conveys the vortices shed at the upstream edge. This model has been modified in [119] to handle different orifice geometries, and has been further adapted in [166, 227] to take into account the finite thickness of the shear layer. These theories agree, at least qualitatively, with experimental data [85] and can predict the alternating frequency ranges of sound absorption and sound generation for a number of cases.

Whereas for grazing flows, the main sound-flow coupling originates from the interaction between the acoustic perturbation and the oscillating sheared boundary layer through the orifice, the effect of bias flow on the impedance is rather similar to the effect of high level acoustic excitation, especially for the resistance [67,164]. Howe [146] derived a theoretical model based on the Rayleigh conductivity for circular orifices with high bias flow speeds, which has been widely used in numerical simulations [95]. It introduces an analytical approach to estimate the discharge coefficient and the virtual length extension of a thin orifice by providing a complex valued expression of the Rayleigh conductivity, which mainly depends on Sr. The discharge coefficient can be greatly influenced by the geometry and local flow field [272]. The particular combination of bias flow and high amplitude sound excitations has been investigated analytically by Luong et al. [207], extending Howe's model [146] based on the Cummings equation [72] describing unsteady flow through a small aperture. Some experimental works have also been performed recently for these conditions [253, 322]. The acoustic energy loss increases significantly in presence of flow since the flow sweeps away the formed vortices. Combined high-level acoustic excitations and bias flow can, however, result in flow reversal which affects discharge coefficient and therefore the acoustic wave damping [319, 322]. A combined bias-grazing flow case was also investigated in experiments by Sun et al. [272] and analytically by Tonon et al. [292] for the low Sr range with a quasi-steady flow model. The latter model relies, however, on a semi-empirical correction to obtain the correct limit behavior for pure bias flow.

An example of a semi-empirical model for perforate impedance was proposed by Elnady and Bodén [96]. It accounts for grazing and bias flow effects, as well as for high excitation levels. This model defines the normalized impedance model for a perforated plate, based on Crandall's theory [68], Bauer's model [27] and some empirical studies [96]. It illustrates the kind of semi-empirical models that are currently used in practical applications and properly summarizes the effects of the different parameters discussed in this section on the acoustic impedance

value. According to this model for circular orifices, the normalized impedance is given by:

$$\begin{aligned} Re(z) = & \underbrace{Re\left(\frac{\mathrm{j}k}{\sigma C_d}\left[\frac{t_p}{F(\mu')}+\frac{\delta_{\mathrm{re}}}{F(\mu)}f_{\mathrm{HIE}}\right]\right)+\frac{1}{\sigma}\left(1-\frac{2J_1(kd_p)}{kd_p}\right)}_{\text{Visco-thermal dissipation}} \\ & + \underbrace{\frac{1-\sigma^2}{\sigma^2 C_d^2}\frac{1}{2c_0}\left|\hat{u}_p\right|}_{\text{High excitation}} + \underbrace{\frac{0.5}{\sigma}M_{0g}}_{\text{Grazing flow}} + \underbrace{\frac{1.15}{\sigma C_d}M_{0b}}_{\text{Bias flow}}, \end{aligned} \tag{2.5}$$

$$\begin{aligned} Im(z) = & Im\left(\frac{\mathrm{j}k}{\sigma C_d}\left[\frac{t_p}{F(\mu')}+\frac{\delta_{\mathrm{im}}}{F(\mu)}f_{\mathrm{HIE}}\right]\right) - \frac{1-\sigma^2}{\sigma^2 C_d^2}\frac{1}{0c_0}\frac{|\hat{u}_p|}{3} \\ & - \frac{0.3}{\sigma}M_{0g}, \end{aligned} \tag{2.6}$$

with

$$\mu' = \mu\left[1+\frac{\gamma-1}{\sqrt{\mathrm{Pr}}}\right]^2 \approx 2.179\mu, \qquad F(\mu) = 1-\frac{4}{Kd_p}\frac{J_1(Kd_p/2)}{J_0(Kd_p/2)},$$

$$\delta_{\mathrm{re}} = 0.2\,d_p + 300\,d_p^2 + 16000\,d_p^3, \qquad \delta_{\mathrm{im}} = 0.5\,d_p, \qquad K = \sqrt{-\frac{\mathrm{j}\omega}{\nu}}, \tag{2.7}$$

$$\left|\hat{u}_p'\right| = \frac{|\Delta\hat{p}'|}{\rho_0 c_0\,\|z\|}, \qquad \text{and} \qquad f_{\mathrm{HIE}}(\sigma) = 1-1.47\sqrt{\sigma}+0.47\sqrt{\sigma^3}.$$

In these expressions, $f_{\mathrm{HIE}}$ is a correction for interaction between orifices [254,284], $k_0$ is the wavenumber, $\mathrm{Pr} = \mu C_p/\lambda_t$ denotes the Prandtl number given by specific heat coefficient $C_p$ and the thermal conductivity $\lambda_t$ of the fluid. The notation $|\bullet|$ means the absolute amplitude value. Additionally, $\Delta\hat{p}'$ is the pressure difference over the orifice, $\delta_{\mathrm{re}}$ and $\delta_{\mathrm{im}}$ are empirical end-corrections, and $\hat{u}_p'$ is the acoustic velocity inside the orifice. The parameters $\mu'$ and $\nu'$ stand for the dynamic and kinematic effective viscosities with heat conductivity at the walls and $J_{n\in\{0,1\}}$ denotes the Bessel functions of the first kind of order $n$. The terms $M_{0g}$ and $M_{0b}$ are the Mach numbers for the grazing flow and the bias flow, respectively.

### Sound-turbulence interaction

When acoustic waves propagate within a sheared flow, turbulent mixing can result in extra acoustic attenuation, as detailed by Reynolds and Hussain [243]. They showed that sound-turbulence interaction is related to oscillations in the

turbulence Reynolds stress, due to the acoustic field. These oscillations induce an additional dissipation mechanism for the acoustic wave. Following [243], the case of a turbulent grazing flow in a T-joint (at low Mach number, $M_0 \approx 0.1$) was investigated by means of a triple-decomposed LNSE model by Gikadi et al. [114], and similarly by Holmberg et al. [142]. By comparison to the measurements of Karlsson and Åbom [172], it was shown that accounting for the turbulence dissipation is required to correctly predict the acoustic response. Concerning perforates, the influence of background turbulence on their acoustic properties is not yet clearly identified and most of the actual impedance models disregard its effect. In Section 4.3, the impact of turbulence modeling on the acoustic characterization of orifices is discussed in the linear acoustic framework of the research activities.

### Temperature and non-isentropic effects

The previously reported works and the derived impedance models have been predominantly done at ambient temperature, e.g. in [96, 135, 210, 287]. A rather limited number of studies have been performed under high temperature conditions. This is a consequence of the difficulties to perform and accurately monitor pressure measurements under hot conditions, especially when flow is present. For applications at higher temperatures, the semi-empirical models developed at ambient temperature are then scaled with the fluid properties ($\rho_0$, $\mu$ and $c_0$) according to the temperature. Experimental works have been done on perforates under non-isothermal conditions, both in the absence of mean flow [97] and in the presence of a hot grazing flow [39, 67, 187, 238]. The elaboration of the required experimental setups and the related challenges to perform accurate acoustic measurements under complex conditions is well illustrated in [67, 187]. The presence of a purging flow, usually for cooling purposes, is also accounted for in the experiments of Ćosić et al. [67]. For perforated reactive silencers, a variation in the cavity temperature can be caused by the ingestion of flow through the resonator orifices and overall heat conduction, as shown by Wong et al. [315] in the context of aircraft liners. An additional exchange between the duct airflow and the resonator cavity can also occur due to a noise-pumping phenomenon at high sound pressure level. The same situation can happen to passive acoustic dampers applied in modern gas turbine combustors [187]. The influence of non-isopycnic conditions on the length corrections at the resonator neck has also been investigated with cold-flow experiments with the mixing of different gases [43]. In Section 4.2, the high temperature and temperature gradient effects on the acoustic behavior of a Helmholtz resonator is investigated numerically by means of the non-isentropic linearized Navier-Stokes (LNS) equations.

### 2.1.3 Vibro-acoustic response of perforated silencers

For a rigid perforated plate, the relative velocity of air particles is the same for each perforation when excited by a planar acoustic wave. However, when the elasticity of the plate is considered, the plate can vibrate with a particular mode shape depending on its geometry, excitation frequency, boundary conditions and material properties. A sketch of the mechanical model of a reactive cavity covered by a flexible perforate plate is depicted in Fig. 2.2b. Due to the plate motion, even under acoustic plane wave excitation, the air-frame relative velocity[3], can significantly vary from the one predicted by rigid wall theory [208, 210]. Accounting for the vibrations, the air-frame relative velocity also depends on the position of the perforation within the plate. Therefore, the perforation positions are potentially a design parameter in flexible micro-perforated plates (f-MPPs). The role of vibrations on the acoustic characterization of MPPs has been first noticed by Lee and Swenson [190]. In their experiments, they reported an additional absorption peak which cannot be explained by the rigid wall theory. This effect was found to be most relevant for perforated sheets with low porosity values and small orifice diameters [276], corresponding to silencer concepts based on MPPs.

One of the first analytical models to include vibrational effects for acoustic absorption by means of MPPs is given by Lee et al. [193] for a rectangular cavity. It is followed by Toyoda et al. [298] for a circular geometry. Both mentioned works are based on a modal representation of the coupled problem, in which both structural motion of the perforated panel and the acoustic field are described in terms of their constituting modes. The formulation further accounts for continuity of the normal particle velocity at the movable plate surface. Such a theoretical model requires the a priori knowledge of the modal decomposition of the plate structural response. It is therefore limited to cases with simple geometrical configurations. On the other hand, it delivers a set of equations which is fast to solve and provides an efficient tool for optimization. Such a modal approach has been applied, through the years, to the study of both Helmholtz-type and panel-type resonances, from the case of an infinite plate backed by a cavity [259] to cases of finite perforated plates and membranes [46, 47, 193], and multi-layer micro-perforated absorbers [48].

Besides the analytical and empirical approaches described so far, some numerical models based on the finite element method have been proposed. Hou and Bolton [143] modeled the plate as a porous material and they included the vibration effects through the elastic frame model. Their study focuses on the impact of the plate profile (V-shaped or curved) on both Helmholtz resonance and vibrational peaks in the acoustic absorption properties. Wang and

[3]defined as the relative air particle velocity with respect to the plate

Huang [305] investigated the behavior of a f-MPP backed by three partitioned cavities of distinct depths. It is done with a complete vibro-acoustic FEM model, which couples the structural vibrations of the plate with the acoustic fields in and out of the back cavity. In their model, the air particle velocity in the perforations is averaged over the flexible plate. Okuzono and Sakagami [225] proposed an efficient FEM model to analyze the sound field in room acoustics through perforated panels. The formulation of the transfer impedance is done such that it includes directly the plate motion, only by considering the structural behavior of the plate via the surface density of the MPP. The plate motion is described in a very simplistic way, which allows this "one parameter only" treatment. Therefore, it does not account for the effects of bending stiffness and for the support conditions encountered for perforated silencer applications. Moreover, as previous studies, they average the acoustic transfer impedance of the perforations over the plate.

The FEM model proposed in Chapter 7 of this dissertation allows to model as well the vibro-acoustic coupling in f-MPPs; the viscous losses in the small perforations; and the effect of perforation distribution. This is achieved by solving, in a direct manner, the set of equation resulting from the Helmholtz equation and 2-D elastic shell elements, while each perforation is represented by transfer impedance boundary patches on the flexible plate separately. The proposed finite element methodology is an alternative to other FEM approaches [225, 305] to investigate the impact of the plate vibration on the acoustic behavior of MPP, which is generic and can handle perforated panel systems of arbitrary geometries (curved or complex shape panels) and support conditions. It can also be applied to look at perforation distributions as a mean to improve the design of perforated silencers.

In all the previously mentioned works, the acoustic impedance of the orifices is assumed homogeneous through the entire plate and determined from the standard Maa model under rigid-wall assumption [208]. The effect of the vibrations on the orifice impedance itself is therefore entirely neglected. Recently, Li et al. [195] proposed a modification of the classical acoustic transfer impedance expression by Maa [210] to account for the non-zero velocity boundary condition at the inner walls of the perforations. The model was applied and verified in the case of perforated membranes. In order to analyze this effect in case of MPPs, the alternative boundary condition is included into the vibro-acoustic FEM model with impedance patch approach.

## 2.2 Impedance determination for perforates

In this section, the methods used in the following chapters to characterize the global acoustic behavior of resonators and orifices from pressure data, including the acoustic impedance, are presented. These methods were originally developed

for experiments but can also be applied to numerically computed acoustic fields as shown in Chapters 3, 4 and 7.

### 2.2.1 Multi-port network approach and scattering matrix determination

Multi-port representations are widely used in the acoustic characterization of flow duct systems [2, 4, 76]. This global "black-box" approach of a system represents a complete test section by a linear network model. It makes the comparison between simulations and experiments easier, as it inherently does not depend on the measurement positions like in-situ methods [77] and local characterization approaches [70, 181] do. They can also be used in combination of impedance eduction methods to derive the acoustic impedance of a test object [261, 309, 310]. The theory of the multi-port approach is explained briefly for the specific case of a two-port system in the plane wave regime, as it will be predominantly used in this work, along with the impedance tube configuration. Its extension to more complex network elements, like in the case of three-port for a duct with one side branch is detailed in [141]. The latest enhancements of the multi-port method consist of accounting for the high-order duct modes [82, 256] allowing an acoustic characterization beyond the first cut-off frequency. In case the acoustic network element exhibits a non-linear noise generating or dissipating behavior caused by structural vibrations, flow-acoustic instabilities or aerodynamic noise generation, an active two-port formulation [80, 189, 270] can be adopted. As this approach will be applied to the linear regime of perforates with rigid walls, the active part is not considered. The multi-port approach can also be reduced to a one-port model, typically referred as impedance tube characterization or two-microphone method in the experimental field [229].

An acoustic two-port element is defined by the relation between the complex modal amplitudes of the upstream ($\bullet^-$) and downstream ($\bullet^+$) propagating pressure waves $p^\pm$ on both of its sides, here noted ① and ②. The link between these incoming ($p_1^+$, $p_2^-$) and outgoing ($p_1^-$, $p_2^+$) acoustic wave amplitudes can be described by a matrix relation, the so-called scattering matrix $\mathbf{S}$, consisting of frequency dependent coefficients:

$$\begin{Bmatrix} p_2^+(\omega) \\ p_1^-(\omega) \end{Bmatrix} = \underbrace{\begin{bmatrix} T^+(\omega) & R^-(\omega) \\ R^+(\omega) & T^-(\omega) \end{bmatrix}}_{\mathbf{S}} \begin{Bmatrix} p_1^+(\omega) \\ p_2^-(\omega) \end{Bmatrix} \tag{2.8}$$

Although other matrix relations exist (the transfer matrix formulation relates for example the acoustic pressure $p'$ and velocity $u'$ between inlet and outlet [74]), the scattering matrix representation is adopted, as its coefficients enable a direct physical interpretation (see Fig. 2.3).

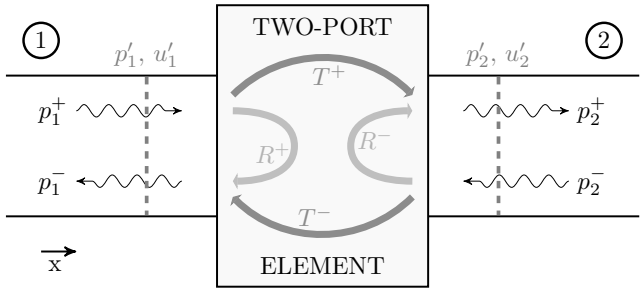


Figure 2.3. Linear two-port element description of an acoustic component. $p'$ and $u'$ are the acoustic pressure and velocity in a section, respectively.

In order to obtain the matrix representation of an element from Eq. (2.8), a minimum of two independent system states (i.e. sound fields) must be known. In an experimental context, more measurements ($N_m > 2$) can be conducted to reduce the influence of measurement errors. The obtained overdetermined system is then solved with the Moore-Penrose pseudo-inverse ($\otimes$)

$$\begin{bmatrix} T^+(\omega) & R^-(\omega) \\ R^+(\omega) & T^-(\omega) \end{bmatrix} = \begin{bmatrix} p^+_{2,I}(\omega) & \dots & p^+_{2,N_m}(\omega) \\ p^-_{1,I}(\omega) & \dots & p^-_{1,N_m}(\omega) \end{bmatrix} \begin{bmatrix} p^+_{1,I}(\omega) & \dots & p^+_{1,N_m}(\omega) \\ p^-_{2,I}(\omega) & \dots & p^-_{2,N_m}(\omega) \end{bmatrix}^{\otimes} \tag{2.9}$$

The subscripts $I \dots N_m$ indicate the independent states of the system, which are obtained by variation of the source location (multiple source method [2]) or by changing the acoustic impedance at the downstream end (multiple load method [206]).

The wave amplitudes ($p^+$ and $p^-$) in Eq. (2.8) are determined by the plane wave decomposition of the pressure values at both sides of the test section. This decomposition holds below the cut-off frequency of the first transversal duct modes, i.e. for $f < \{f_c^{0,1},\, f_c^{1,0}\}$ with

$$f_c^{mn} = \frac{k_{mn}^{\perp} c_0}{2\pi} \sqrt{1 - M_0^2}\,. \tag{2.10}$$

The transversal wavenumber $k_{mn}^{\perp}$ of the mode $(m, n)$ depends on the cross section of the duct and is given by

$$k_{mn}^{\perp} = \sqrt{\left(\frac{m\pi}{W}\right)^2 + \left(\frac{n\pi}{H}\right)^2} \quad \text{and} \quad k_{mn}^{\perp} = \frac{\alpha_{mn}}{R}\,, \tag{2.11}$$

for respectively a rectangular cross section of dimension $(H \times W)$ and a circular cross section of radius $R$. The parameter $\alpha_{mn}$ is the $(n+1)$-th zero of the derivative of $J_m$, the Bessel function of the first kind of order $m$.

The plane wave decomposition yields

$$\begin{aligned}\hat{p}'_j(\omega, x_i) &= p_j^+(\omega, x_i) + p_j^-(\omega, x_i) \\ &= p_j^+(\omega, 0)e^{-\mathrm{j}k^+ x_i} + p_j^-(\omega, 0)e^{+\mathrm{j}k^- x_i}\,,\end{aligned} \tag{2.12}$$

where $x_i$ denotes the axial position relative to an arbitrary fixed reference (here taken as $x_i = 0$) on side $j$ and $k^\pm$ are the down- and upstream wavenumbers. Different formulations for these wavenumbers can be found in literature [291]. Following the asymptotic formulation of Dokumaci [88], an expression for the axial wavenumbers $k^\pm$ is given by:

$$k^\pm = k_0 \frac{\theta_K(\omega)}{1 \pm \theta_K(\omega) M}\,, \tag{2.13}$$

based on the wavenumber in a quiescent medium $k_0 = \omega/c_0$. The expression in Eq. (2.13) takes into account both convective effects, by means of the Mach number $M$, and visco-thermal dissipation in the acoustic boundary layer, by means of the frequency dependent damping coefficient $\theta_K(\omega)$. This complex damping coefficient $\theta_K(\omega)$ is given by the Kirchhoff model, for a circular duct, and is expressed in the first order approximation as:

$$\theta_K(\omega) = 1 + \frac{1+\mathrm{j}}{\sqrt{2}\mathrm{Sh}} \left(1 + \frac{\gamma - 1}{\sqrt{\mathrm{Pr}}}\right)\,, \tag{2.14}$$

where $\gamma$ is the specific heat ratio, Pr is the Prandtl number, and $\mathrm{Sh} = \sqrt{\omega R^2/\nu}$ is the shear wave number for a duct of radius $R$. For non-circular ducts, the hydraulic radius $R_h = \mathcal{P}_d/(2S_d)$ is used instead, where $\mathcal{P}_d$ is the perimeter of the duct cross section and $S_d$ is the duct cross sectional area. In the above equation, the mean flow is assumed uniform and independent of the axial position. The visco-thermal losses are considered solely at the duct walls and not within the fluid. Finally, no damping due to the mean flow turbulence is accounted for [311].

When the axial wavenumbers are known (from Eq. (2.13)), the complex wave amplitudes $p^+$ and $p^-$ can be obtained from the pressure values measured at two distinct axial positions $x_i$, as shown in Eq. (2.12). More microphone positions $N_s$ can be used to improve the conditioning of the system of linear equations to be solved:

$$\begin{Bmatrix} \hat{p}'(\omega, x_1) \\ \hat{p}'(\omega, x_2) \\ \vdots \\ \hat{p}'(\omega, x_{N_s}) \end{Bmatrix} = \begin{bmatrix} e^{-\mathrm{j}k^+ x_1} & e^{+\mathrm{j}k^- x_1} \\ e^{-\mathrm{j}k^+ x_2} & e^{+\mathrm{j}k^- x_2} \\ \vdots & \vdots \\ e^{-\mathrm{j}k^+ x_{N_s}} & e^{+\mathrm{j}k^- x_{N_s}} \end{bmatrix} \begin{Bmatrix} p^+(\omega) \\ p^-(\omega) \end{Bmatrix} \tag{2.15}$$

The microphones are commonly positioned sufficiently far from the test object placed in the duct to limit the hydrodynamic contributions to the pressure signals.

It ensures that only acoustic pressure fluctuations are recorded. The spacing between microphones $\Delta l_m$ can also be chosen to improve the conditioning of the system in Eq. (2.15) depending on the frequency range of interest. A general guideline [4] for $\Delta l_m$ is

$$0.1\pi(1 - M_0^2) < k_0 \Delta l_m < 0.8\pi(1 - M_0^2)\,. \tag{2.16}$$

The previous considerations require, in some numerical cases, a computational domain much larger than the actual test object in order to obtain an accurate determination of the pressure wave amplitudes. This is mainly an issue at low frequencies. Therefore, high-order numerical methods, as discussed in Sections 3.2.1 and 3.2.2, are of interest to have larger elements in the duct portions for acoustic characterization. In an experimental context, parametric representations of the wavenumbers and environmental parameters can be added as unknowns to the over-determined system in Eq. (2.15), which becomes nonlinear and can be solved iteratively, to reduce the uncertainties on the experimental parameters [78].

## 2.2.2 Impedance characterization techniques

The acoustic characterization of a silencer is generally done by determining a single quantity: its acoustic impedance $Z$ or its normalized counterpart $z = Z/Z_0$. when normalized by the characteristic impedance of air $Z_0 = \rho_0 c_0$. Researchers have developed through the last decades different techniques to measure the impedance of a resonator in the presence of a flow [7, 18, 307]. The most common techniques are the in-situ measurement and impedance eduction techniques. The following paragraphs describe the impedance measurement techniques considered in this work, specifically for the configuration described in Section 4.1.1. Even if these techniques have been originally developed for experiments, they can very well be applied on pressure fields obtained from the high-order numerical methods of this work, as a post-processing step.

### The in-situ impedance measurement technique

The in-situ technique, originally proposed by Dean [77] and specifically designed for acoustic liners, is a local method which consists in computing the acoustic impedance of a resonator by directly measuring the acoustic pressure at the bottom of the resonator cavity (location B) and at the facing sheet, near the perforation (location A), as illustrated in Fig. 2.4a. This methodology assumes that for a resonant cavity a unique relationship exists between the internal acoustic pressure and the acoustic particle velocity along the facing sheet. From the measured pressure signals, the surface impedance of the resonator is given

by:

$$z = -\mathrm{j}\frac{\hat{p}_\mathrm{A}}{\hat{p}_\mathrm{B}}\frac{e^{\mathrm{j}(\phi_A-\phi_B)}}{\sin\left(k_0 l_\mathrm{cav}\right)}\,, \tag{2.17}$$

where $\hat{p}_\bullet$ and $\phi_\bullet$ represent the amplitude and phase of the pressure fluctuations at the monitoring points $\bullet$ = A, B, respectively. The parameter $k_0 = \omega/c_0$ denotes the acoustic wavenumber in the cavity and $l_\mathrm{cav}$ is the depth (or length) of the resonator backing cavity.

The in-situ technique provides a local value of the impedance, which is valid for the full extent of the object section. The technique relies on a few assumptions. First, the facing sheet of the resonator is assumed thin compared to the acoustic wavelength $\lambda_a$ and the depth of the backing cavity. Secondly, this approach is valid under the hypothesis of long wavelengths compared to the cavity cross dimensions and plane wave propagation is considered inside the resonator cavity. Regarding the difficulties linked to this technique, the location of the microphones (or monitoring points) is an important issue. Close to the orifice (location A), acoustic waves are transformed into vortical fluctuations. The hydrodynamic pressure fluctuations $p'_h$ associated with this effect can influence the pressure signal recorded at his location $p'_\mathrm{meas}$, as $p'_\mathrm{meas} = p' + p'_h$ locally [77, 263]. This hydrodynamic component of the pressure is said to pollute

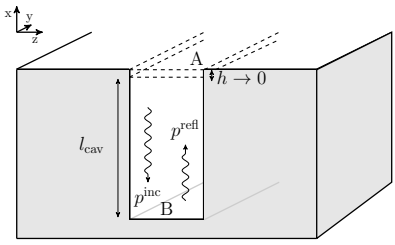


(a) Dean's in-situ impedance measurement method

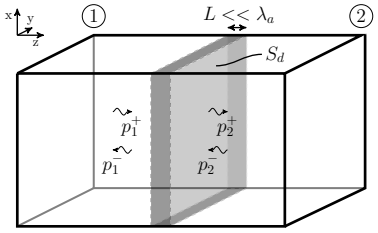


(b) Impedance eduction - Lumped model

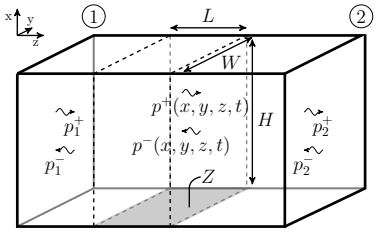


(c) Impedance eduction - One-sided impedance wall model

Figure 2.4. Setup description for the different impedance measurement techniques applied to the case of the slit resonator with grazing flow.

the acoustic pressure measurements, and influences also the results of numerical simulations [81, 320].

### Impedance eduction techniques

Impedance eduction techniques compute the impedance indirectly by comparing a particular set of measured variables to a model for the complete test section. Therefore the accuracy of such measurement techniques is largely dependent on the correctness of the model used. Various impedance eduction techniques are found in the literature, based on different measured acoustic quantities and models. Among the several existing indirect methods, the Finite Element Method techniques [265, 307–310], which consists of solving an eigenvalue problem where the material impedance is treated as an unknown and the measured acoustic field corresponds to the boundary conditions, have been extensively studied. Mode-Matching techniques [18, 98, 111], based on the modal decomposition of the acoustic pressure and velocity fields, represent an interesting alternative. The impedance can also be educed straightforwardly from the sound pressure information measured on the duct wall opposing the tested lined wall [163, 241]. In this case, the axial wavenumbers related to the least attenuated modes are extracted from the pressure values by means of a Prony-like algorithm. These wavenumbers are then further used to calculate the unknown impedance from the eigenvalue and dispersion relations based on the classical mode-decomposition analysis. The two techniques applied in this dissertation are based on a two-port representation of the test section [52, 76], as described in Section 2.2.1. Eduction techniques come with a number of advantages in comparison to direct local techniques. Among them, the acoustic variables (here the pressure fluctuations) are not measured in the close vicinity of the orifice but further up- and downstream of the resonator, avoiding the negative influence of the hydrodynamic component of the pressure.

After obtaining the scattering matrix, following Section 2.2.1, the surface impedance of the resonator can be determined by matching this scattering matrix to a model describing the test section. In a first model, the resonator is considered as a lumped element and the impedance is computed directly from the scattering matrix coefficients [7, 220]. The impedance can be determined independently for a downstream propagating wave ($z^+$) or an upstream propagating wave ($z^-$) [7]:

$$z^{\pm} = \frac{S_p}{S_d}\left(\frac{1 \mp M_0}{1 \pm M_0}\right)\frac{(1 \pm M_0)^2 + R^{\pm}}{(1 \pm M_0)(1 - T^{\pm}) - (1 \mp M_0)R^{\pm}}\,, \tag{2.18}$$

where $T^{\pm}$ and $R^{\pm}$ are the measured scattering matrix coefficients. $S_p$ is the surface area of the opening and $S_d$ is the cross-sectional area of the duct. The mean flow Mach number $M_0$ is computed assuming uniform flow inside the duct sections. This lumped model is only valid at low frequencies, to insure that the

test object is acoustically compact (see Fig. 2.4b). For the configuration treated in Section 4.1.1, the difference between the impedance for the downstream $z^+$ and upstream $z^-$ propagating waves is found small.

At higher frequencies, the previous lumped impedance model is no longer a good assumption and it is better to consider the impedance as distributed over the test section wall. In that case, an alternative model for the scattering matrix, using the model for a rectangular duct with one lined wall [261], can be used, as illustrated in see Fig. 2.4c. Note that the lined wall is considered here normal to the Cartesian plane $(\mathbf{x}, \mathbf{z})$, as shown in the schematic representation. It was shown [79] that the method from reference [261] is equivalent to solving the following system of 5 nonlinear equations with 5 unknowns $\{z,\, k_z^{\pm},\, k_x^{\pm}\}$:

$$\begin{cases} \dfrac{T^+T^- - R^+R^- + 1}{T^-} = e^{-\mathrm{j}k_z^+ L} + e^{+\mathrm{j}k_z^- L}\,, & \text{(2.19a)} \\[2ex] k_z^{\pm} = \dfrac{1}{1-M_0^2}\left[\mp M_0 k_0 + \sqrt{k_0^2 - (1-M_0^2)(k_x^{\pm})^2}\right]\,, & \text{(2.19b)} \\[2ex] z = \mathrm{j}\dfrac{k_0}{k_x^{\pm}}\left(1 \mp M_0 \dfrac{k_z^{\pm}}{k_0}\right)^2 \cot\left(k_x^{\pm} H\right)\,, & \text{(2.19c)} \end{cases}$$

once the scattering matrix $\mathbf{S}$ has been determined. The parameters $k_z^{\pm}$ and $k_x^{\pm}$ are the axial and transversal acoustic wavenumbers of the least attenuated mode in the duct of the test section. The mean flow Mach number is denoted by $M_0$, with flow also assumed uniform in the duct sections. The parameters $L$ and $H$ are respectively the length and height of the test section. Equation (2.19b) corresponds to the compatibility relation, which links the axial wavenumbers to the transversal ones. Equation (2.19c) gives the dispersion relation between the unknown surface impedance $z$ and the acoustic wavenumbers in the lined section based on the Ingard-Myers boundary condition [221].

## 2.3 CAA techniques applied to perforates - review of developments

Computational AeroAcoustics embraces the numerical methods to predict aerodynamic noise generation and its propagation through a flow. Concerning the acoustic characterization of passive silencers and orifices, the main challenges for the CAA methods are: (i) The multiple-scales character of the problem, with $\lambda_a \gg d_p$ or $\delta_v$, makes it hard to find proper compromise between high spatial resolution and a sufficiently large computational domain for impedance eduction (described in Section 2.2). It leads to excessive computational costs for high

accuracy requirements. (ii) Sound propagation near solid-wall geometries leads to boundary layer effects that play an important role in sound wave damping. They have to be accurately accounted for in the physical model and a fine spatial domain discretization is required for these small scales. (iii) Due to the various working conditions experienced by silencers investigated in this work (e.g. flow-sound interaction, temperature and turbulence effects, boundary layer separation), the numerical models should be able to describe the coupling between the different physical phenomena which combine vorticity, entropy, and acoustic modes.

In the following, the different CAA methods that can be applied to the study of orifices and acoustic resonators are listed, as well as the related reference works. Figure 2.5 summarizes the content of this section[4].

### 2.3.1 Direct simulations

#### Compressible flow simulations

With the increase of available computational power, high-fidelity simulation techniques, such as direct numerical simulations (DNS) and large-eddy simulations (LES), are becoming prospective candidates for acoustic characterization of perforates and acoustic resonators. The main difficulties for the direct methods, as addressed by Tam [280], originate from the multiple length scales involved and the disparity in the order of magnitude between the acoustic perturbation $p'$ and the hydrodynamic quantities $p'_h$, with $p' \ll p'_h$. It requires numerical schemes with minimum dispersion and dissipation. As direct numerical simulations are not based on any particular assumption or modeling, they provide a great insight into physical mechanisms. They come, however, with a high computational cost.

Tam and Kurbatskii [279] investigated via DNS the vortex shedding occurring at a two-dimensional slit under normal incidence acoustic excitation and results were experimentally validated [282]. They showed, depending on the excitation frequency and amplitude, the transition from linear to nonlinear regime with the appearance of vortex shedding. Following [69,160], the vortex bound energy was numerically quantified and successfully related to the dissipated acoustic energy. More recently, Tam et al. [281] performed DNS on a three-dimensional slit orifice. Shed vortices remain the dominant source for acoustical dissipation at high sound excitations, but the formed eddies are observed to evolve into ring vortices even for a slit orifice aspect ratio of 2.5. Finally, the effect of a grazing flow on a 2-D slit resonator under acoustic forcing was studied in [278].

[4]CFD simulations combined with acoustic analogies to reconstruct equivalent sources for linear acoustic solvers are not considered in the context of this work.

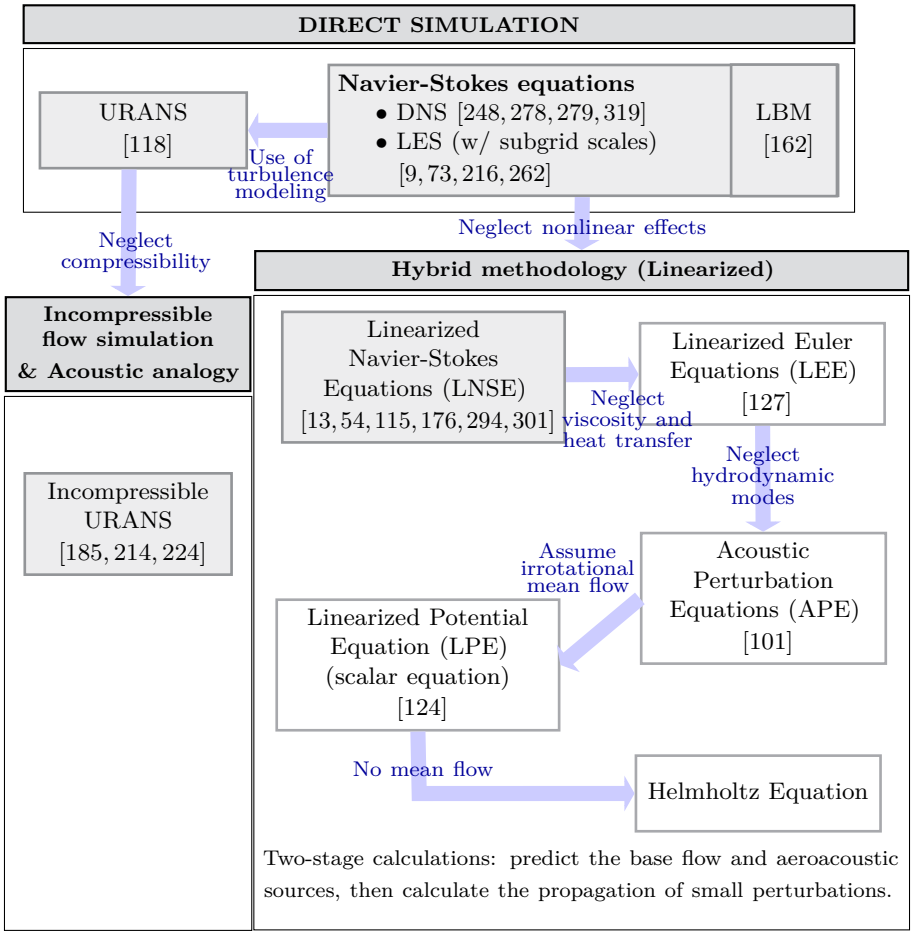


Figure 2.5. Overview of the CAA approaches and references to related works: methods applicable to the study of silencers are marked in gray blocks.

It shows the influence of the flow boundary layer on the ejected eddies. Due to the grazing flow, vortices are shed from the corners of the resonator opening and can either merge together, get absorbed by the wall boundary layer, or be dissipated by viscosity. Zhang and Bodony [318, 319, 321] also followed the DNS approach to study a circular orifice backed by a hexagonal cavity and derive time-domain impedance models. They observed that the vortices form turbulent structures under high amplitude acoustic excitations (at 150 dB and 160 dB) even for moderate Reynolds numbers based on the particle velocity [319]. They revisited in [318] the slit liner simulations of Tam and co-workers [278] and demonstrated that direct numerical simulation of an acoustic liner can be used to predict the acoustic impedance of slit liner when coupled with

Dean's method [77]. Furthermore, they analyzed the impact of laminar and turbulent grazing flow on the damping behavior [321] to assess the dynamics of the sound-turbulence-orifice interaction with a backing-cavity. Roche et al. [248] also performed 3-D DNS with the Onera CEDRE code to study the response of a cylindrical Helmholtz resonator between 100 dB and 150 dB. They found higher resistance and lower reactance for the resonator with addition of the grazing flow [249].

The effect of bias flow through an orifice was studied by means of DNS by Leung et al. [194] and of LES by Dassé [73] and others [9, 216, 262]. The numerical results showed for example the relevance of semi-empirical models like the one from Jing and Sun [164] concerning the shape of the jet separation at the aperture inlet [73]. The possibility of reverse flow is also noticed [262] for high amplitude waves, when the fluctuating velocities $u'$ exceed the mean bias flow velocity within the orifice. This phenomenon, proper to bias flow situations, can lead to major changes in the acoustic reflection and transmission properties.

The Lattice Boltzmann Method (LBM), which is based on particle collision models, can be used for aeroacoustic problems to access both aerodynamic and acoustic information using a single simulation [213]. The LBM was applied by Ji and Zhao [162] to the three-dimensional numerical simulation of an acoustically excited flow through a millimeter-size circular orifice, with good agreement with both experimental and LES results.

Despite the reported successes, the previous direct simulations are far from being applicable to extended parametric studies or to industrial usage on large-scale problems within a near future due to their long wall-clock time and computer resources requirements.

### Incompressible flow simulations

Incompressible flow simulations can also be employed to acoustically characterize perforates due to their acoustic compactness, i.e. $d_p$ or $t_p \ll \lambda_a$. In general, the incompressible framework allows for a simpler, more robust, and less computationally demanding simulation setup in comparison to compressible flow simulations. Incompressible flow computations have been successfully used in the past to characterize the acoustic behavior of confined flow systems. In the work of Martínez-Lera et al. [214], an approach combining incompressible CFD and vortex sound theory [150] was applied to a two-dimensional laminar flow through a T-joint. This methodology was further improved and applied to corrugated pipes by Nakiboğlu et al. [224] and to a large orifice configuration with through-flow by Lacombe et al. [185] for whistling prediction. The methodology presented in Chapters 5 and 6 of this dissertation makes use of this incompressible flow approach. In contrast to the previous works, the study focuses on both linear and nonlinear regimes of Helmholtz resonators in absence of mean flow. The

extension to the case with grazing flow can be done easily due to the present general formulation and arguments presented by Nakiboğlu et al. [224] and Golliard et al. [118].

### 2.3.2 Hybrid methodology and linearized acoustic solvers

In linear acoustic problems, the fluid density, pressure, and velocity fluctuations $\{\rho', p', \mathbf{u}'\}$ are very small with respect to the respective mean flow quantities $\{\rho_0, p_0, \mathbf{u_0}\}$. This observation justifies the fluid motion to be described by linear approximation of the governing Navier-Stokes equations, thus neglecting the nonlinear interactions [58]. This yields to the so called perturbed or linearized Navier-Stokes equations (LNSE). Note that the LNSE still support Kelvin-Helmholtz instabilities which may appear in time-domain problems with sheared mean flows. In absence of non-linearities, these instabilities are only attenuated by viscous or numerical damping. The LNSE can be solved in both time and frequency domains. Different spatial discretization techniques can also be used. Due to their flexibility to deal with unstructured grids and non-homogeneous media, continuous Finite Element Methods for the frequency-domain and Discontinuous Galerkin Methods (DGM) associated with explicit time integration schemes for the time-domain have become the methods of choice. Both FEM and DGM are based on local polynomial approximation of the field variables but differ in the coupling between elements. In classical FEM, two neighboring elements share the DOFs at their common boundary, whereas DGM realize the coupling between elements through a numerical flux formulation, in the manner of Finite Volume Methods (FVM).

In the frequency domain, the LNSE approach with low-order FEM has already been applied to the study of orifices [176] and area expansions [115, 177] in ducts at low Mach number flow and ambient temperature, but also for the investigation of indirect combustion noise due to entropy waves in a Laval nozzle [301, 302]. In [115, 301, 302], the LNSE are solved by a Galerkin/least-squares stabilized FEM approach as developed by Hughes et al. [154]. Carbajo et al. [54], following the work of Kampinga et al. [169], also performed standard FEM computations based on LNSE modeling to capture the visco-thermal effects appearing at perforations in absence of mean flow and examine the interaction between perforations.

As the phenomena of interest in this work have to be correctly represented from a very small scale (down to the acoustic boundary layer thickness $\delta_v$) up to the order of one meter (when performing low-frequency two-port characterization of a duct section), using standard FEM can lead to constraints in terms of memory through the discretization of the physical domain and the approximation of the field variables. The high-order finite element method ($p$-FEM) is used to limit this drawback. Details on the LNSE $p$-FEM solver and its implementation in Matlab are given in Section 3.2.1. A possibility to reduce the overall

computational cost of the LNSE approach is to spatially separate the numerical domain between a complex sheared-flow region and dissipative effects (modeled with LNSE) and an inviscid, irrotational flow region modeled with the linearized Potential Equation (LPE). This is done for example in [223] by coupling LNSE with the Helmholtz equation using an equivalent fluid model to represent a layer of porous material or in [124] by coupling LEE with LPE for the far field radiation of aircraft engine noise. The approach of using distinct physical models on different parts of the computational domain will, however, not be applied in this work due to the non-straightforward identification of these regions for the investigated applications in Chapters 3 and 4.

In time domain, the Runge-Kutta Discontinuous Galerkin method (RKDG), first introduced and analyzed by Cockburn and Shu [62, 64], was employed with an LNSE acoustic operator to study a set of different orifice geometries under grazing flow conditions [294]. Arina [13] recently developed a similar LNSE RKDG solver and applied it to a sudden area expansion in a circular duct in the presence of a mean flow. The work, reported in Section 3.2.2, on the time-domain RKDG approach for linear acoustic problems is set in the continuation of [242, 293], with a focus on visco-thermal effects at resonators.

# Part II

# Linearized numerical methods for orifices and resonators

# Chapter 3

# High-order numerical methods for solving the Linearized Navier-Stokes equations

In this chapter, the numerical methods applied for solving the problem of wave propagation in non-uniform media are presented. The physical models are based on variations of the perturbed Navier-Stokes equations in order to capture the relevant physics involved in orifice and resonator applications. Due to the linear nature of the set of equations solved, this chapter is restricted to linear acoustic operators and disregards any complex nonlinear phenomena. The latter will be treated in Chapters 5 and 6. The problem is solved both in the frequency domain, by means of a high-order continuous Finite Element Method, and in the time domain by using a Runge-Kutta Discontinuous Galerkin approach. The first section introduces the physical models. The specificities of the two numerical methods used in this work are described in Section 3.2, which covers the weighted residual formulation of the problem, the treatment of boundary conditions and sources, as well as details on the implementation. The third section, Section 3.3, explains a local analysis to quantify the different dissipation mechanisms from the solution of the linear problems solved. The final section, Section 3.4, presents some validation cases.

## 3.1 Physical models for the acoustic propagation

As mentioned in Chapter 2, the physics that determines the acoustic behavior of perforated structures in presence of a flow is rather complex, even if restrained to the linear regime. It requires to account for flow non-uniformities like sheared flow and boundary layers, as well as visco-thermal effects which can become dominant for small orifices or under non-isentropic conditions. Additionally, considering the broad range of operating conditions experienced by perforations in the relevant industrial applications, one wants to keep the physical model as general as possible. For theses reasons, the choice fell on the set of the linearized Navier-Stokes equations (LNSE).

### 3.1.1 The standard linearized Navier-Stokes equations

The compressible Navier-Stokes equations are the governing equations of fluid dynamics, and by extension of aeroacoustics. This set of partial differential equations is obtained from the equations of conservation of mass, momentum and energy for a fluid particle [26]. A Newton-Fourier ideal gas model is chosen to represent the fluid. This assumption has been shown to be accurate to model acoustic problems including effects of viscosity and other dissipative processes, see for example [219] and Chapter 10 in [230]. The Navier-Stokes equations are defined in a Cartesian coordinate system by:

**Continuity:**

$$\frac{\mathrm{D}\rho}{\mathrm{D}t} + \rho\frac{\partial u_k}{\partial x_k} = 0\,, \tag{3.1a}$$

**Momentum:**

$$\rho\frac{\mathrm{D}u_i}{\mathrm{D}t} = -\frac{\partial p}{\partial x_i} + \frac{\partial \tau_{ij}}{\partial x_j} + \rho F_i\,, \tag{3.1b}$$

**Energy:**

$$\frac{\mathrm{D}e}{\mathrm{D}t} = -p\frac{\partial u_k}{\partial x_k} + \Phi + \mathcal{Q}\,, \tag{3.1c}$$

given in function of the fluid density $\rho$, pressure $p$, internal energy $e$, and the $i^{\text{th}}$ component of the velocity in the Cartesian coordinates. $F_i$ represents any additional volume force in the $i^{\text{th}}$ direction that could be considered, similar to gravity forces. In the present work, such volume forces are disregarded, i.e. $\mathbf{F} = \mathbf{0}$. The operator $\mathrm{D}\bullet/\mathrm{D}t = \partial\bullet/\partial t + \mathbf{u}\cdot\boldsymbol{\nabla}\bullet$ denotes the material derivative of the variable $\bullet$. The Einstein summation convention is used here. In Eq. (3.1b), $\boldsymbol{\tau}$ is the shear-stress tensor, also known as Reynolds viscous tensor. It gives the molecular diffusion of momentum and is defined as

$$\tau_{ij} = \mu\left(\frac{\partial u_i}{\partial x_j} + \frac{\partial u_j}{\partial x_i} - \frac{2}{3}\frac{\partial u_k}{\partial x_k}\delta_{ij}\right)\,, \tag{3.2}$$

where $\delta_{ij}$ stands for the Kronecker delta function and $\mu$ is the dynamic viscosity of the fluid. The presented equations, Eqs. (3.1a) to (3.1c), are derived assuming the fluid to be in a local thermodynamic equilibrium or near-equilibrium state. The effect of the bulk viscosity, which takes into account the small departure of the rotational and translational modes of the molecular motion from mutual thermodynamic equilibrium, is therefore neglected in this dissertation. Such relaxation processes should however be included in the modeling, as detailed by Pierce [230], when high frequencies or large propagation distances are considered. Disregarding the fluid relaxation losses, the term $\Phi$ found in Eq. (3.1c) represents exclusively the dissipation of mechanical energy due to the viscous shear stresses and can be expressed as

$$\begin{aligned}\Phi &= \mu \left( \frac{\partial u_i}{\partial x_j} \frac{\partial u_i}{\partial x_j} + \frac{\partial u_j}{\partial x_i} \frac{\partial u_i}{\partial x_j} - \frac{2}{3} \frac{\partial u_i}{\partial x_i}^2 \right) , \\ &= \tau_{ij} \frac{\partial u_i}{\partial x_j} .\end{aligned} \tag{3.3}$$

The last term of Eq. (3.1c) is related to thermal effects. $\mathcal{Q}$ regroups internal heat sources via the heat release rate per unit volume $Q_V$ and thermal diffusion effects $Q_t$. The latter can be expressed as $Q_t = -\nabla \cdot \mathbf{q_t}$, where the local heat flux $\mathbf{q_t}$ is a function of the temperature gradient as stated by the Fourier's law of heat conduction:

$$\mathbf{q_t} = -\lambda_t \boldsymbol{\nabla} T . \tag{3.4}$$

The parameter $\lambda_t$ stands for the thermal conductivity and $T$ is the fluid temperature. As the fluid is assumed to behave like a perfect gas, the equation of state

$$p = \rho R T \tag{3.5}$$

and the entropy expression

$$s - s_{\text{ref}} = C_v \ln \left( \frac{p}{p_{\text{ref}}} \right) - C_p \ln \left( \frac{\rho}{\rho_{\text{ref}}} \right) \tag{3.6}$$

are used to complete the initial set of transport equations in order to describe the evolution in time and space of all the relevant quantities to this work. The specific gas constant $R$ is given by $R = C_p - C_v$, where $C_p$ and $C_v$ are the heat capacities at constant pressure and constant volume, respectively. The index "ref" in Eq. (3.6) denotes an arbitrary reference state to define the entropy value.

The energy equation stated in Eq. (3.1c) can be equivalently reformulated in terms of specific enthalpy $h$, entropy $s$, or pressure $p$. It is common for aeroacoustic applications to consider the energy equation expressed in function of the pressure $p$:

$$\frac{\mathrm{D}p}{\mathrm{D}t} + \gamma p \frac{\partial u_i}{\partial x_i} = (\gamma - 1) \left( \mathcal{Q} + \tau_{ij} \frac{\partial u_i}{\partial x_j} \right) , \tag{3.7}$$

where $\gamma = C_p/C_v$ is the ratio of heat capacities.

Acoustic governing equations can be obtained by linearizing the described set of compressible Navier-Stokes equations, Eqs. (3.1a), (3.1b) and (3.7), around an arbitrary mean flow state. In this analysis, any arbitrary flow quantity $q(\mathbf{x}, t)$ is described as the sum of the time-averaged quantity $q_0(\mathbf{x}) = \overline{q}(\mathbf{x})$ and a relatively smaller perturbation $q'(\mathbf{x}, t)$, i.e.

$$q(\mathbf{x}, t) = q_0(\mathbf{x}) + q'(\mathbf{x}, t) \text{ and } q'(\mathbf{x}, t) \ll q_0(\mathbf{x}), \tag{3.8}$$

with $\mathbf{x}$ being the position vector and $t$ the time. The linearized Navier-Stokes equations are then obtained by substitution of the decomposition assumption (3.8) in the Navier-Stokes equations while neglecting the higher order terms, i.e. the product of perturbed variables. The fluctuations of viscosity due to temperature perturbations, and other nonlinear phenomena, are therefore neglected. The terms related only to the mean flow state are then subtracted from the linearized equations. They are indeed assumed to respect the initial flow equations. This leads to a linear problem with only the fluctuating quantities as unknowns. The choice of variables for solving the perturbed equations is arbitrary and depends more on the application and field of research. As the focus is set here on the flow-acoustic behavior of perforated structures, the perturbed equations are expressed in terms of $\{\rho', \mathbf{u}', p'\}$. The linearized Navier-Stokes equations under general non-isentropic conditions can be written as:

**Continuity:**

$$\frac{\partial \rho'}{\partial t} + \frac{\partial (\rho_0 u'_j + \rho' u_{0j})}{\partial x_j} = 0\,, \tag{3.9a}$$

**Momentum:**

$$\frac{\partial \rho_0 u'_i}{\partial t} + \frac{\partial \rho_0 u'_i u_{0j}}{\partial x_j} + \frac{\partial p'}{\partial x_i} + (\rho_0 u'_j + \rho' u_{0j}) \frac{\partial u_{0i}}{\partial x_j} - \frac{\partial \tau'_{ij}}{\partial x_j} = 0\,, \tag{3.9b}$$

**Energy:**

$$\frac{\partial p'}{\partial t} + u_{0j} \frac{\partial p'}{\partial x_j} + u'_j \frac{\partial p_0}{\partial x_j} + \gamma p_0 \frac{\partial u'_j}{\partial x_j} + \gamma p' \frac{\partial u_{0j}}{\partial x_j} =$$

$$(\gamma - 1) \left[ \frac{\partial}{\partial x_j} (\lambda_t \frac{\partial T'}{\partial x_j}) + \tau_{0ij} \frac{\partial u'_j}{\partial x_i} + \tau'_{ij} \frac{\partial u_{0j}}{\partial x_i} + Q'_V \right], \tag{3.9c}$$

with $\tau'_{ij}$ the perturbed viscous stress tensor given by:

$$\tau'_{ij} = \mu \left( \frac{\partial u'_i}{\partial x_j} + \frac{\partial u'_j}{\partial x_i} - \frac{2}{3} \frac{\partial u'_k}{\partial x_k} \delta_{ij} \right). \tag{3.10}$$

The variables $\rho'$, $\mathbf{u}'$, and $p'$ are the density, velocity vector, and pressure perturbation fields. The temperature $T'$ and entropy $s'$ fluctuations can be retrieved through the expressions

$$s' = C_p \frac{T'}{T_0} - R \frac{p'}{p_0} \tag{3.11}$$

and

$$T' = T_0 \left( \frac{p'}{p_0} - \frac{\rho'}{\rho_0} \right) , \tag{3.12}$$

which are the linearized versions of the entropy and state equations. The term $Q'_V$ represents internal heat sources. In this work, $Q'_V = 0$ is typically assumed as no flame or unsteady heat source will be modeled.

Equation (3.9) describes the most general linear acoustic operator that can be used to represent the propagation of acoustic waves inside a non-uniform flow and a non-homogeneous medium. In case the mean flow can be considered as isentropic, a simplified expression for the energy equation can be derived, reducing the evaluation of complex terms. A flow is called isentropic when the entropy of a fluid particle is constant along its stream path. This corresponds to the condition $\mathrm{D}s/\mathrm{D}t = 0$. The flow is further called homentropic if it is isentropic and its entropy is constant in space, i.e. $\boldsymbol{\nabla} s = 0$. Under isentropic assumption, the set of linearized equations can be directly obtained from Eq. (3.9) by taking the right-hand side of the energy equation (3.9c) equal to zero, i.e. replacing Eq. (3.9c) by:

$$\frac{\partial p'}{\partial t} + u_{0j} \frac{\partial p'}{\partial x_j} + u'_j \frac{\partial p_0}{\partial x_j} + \gamma p_0 \frac{\partial u'_j}{\partial x_j} + \gamma p' \frac{\partial u_{0j}}{\partial x_j} = 0 \, . \tag{3.13}$$

The two sets of equations, Eqs. (3.9a) to (3.9c) and Eqs. (3.9a), (3.9b) and (3.13) respectively, can be written in a more compact way using a matrix formulation to define the general LNSE operator $\mathcal{L}_{\mathrm{LNSE}}$:

$$\mathcal{L}_{\mathrm{LNSE}}(\mathbf{q}) = \mathbf{S} \Leftrightarrow \frac{\partial \mathbf{q}}{\partial t} + \frac{\partial \mathbf{A}_i \mathbf{q}}{\partial x_i} + \mathbf{C}\mathbf{q} + \frac{\partial}{\partial x_i} \left( \frac{\partial \mathbf{C}_{ij} \mathbf{q}}{\partial x_j} \right) = \mathbf{S} \, , \tag{3.14}$$

with $\mathbf{q} = \{\rho', \rho_0 \mathbf{u}', p\}^T$ the vector of unknown perturbations in density, conservative velocity components, and pressure. The matrices $\mathbf{A}_i$ are the flux Jacobians. The matrices $\mathbf{C}$ and $\mathbf{C}_{ij}$ account for the non-uniform flow effects and the visco-thermal dissipation, respectively. The detailed expressions of these matrices are given in Appendix A for both the isentropic (Appendix A.1) and non-isentropic (Appendix A.2) versions of the perturbed Navier-Stokes equations. By further assuming $\lambda_t = 0$ and $\mu = 0$, the previous equations reduce to linearized Euler equations (LEE) used for dissipation-free acoustic problems [41, 127, 153, 161].

In Eq. (3.14), a source vector $\mathbf{S}$ is added to the right-hand side

$$\mathbf{S} = \begin{bmatrix} S_{\text{dens}} \\ S_{\text{mom}\,i} \\ S_{\text{press}} \end{bmatrix}, \tag{3.15}$$

to allow the modeling of excitations inside the domain for the perturbation fields. Many approaches exist in the literature to define this source vector. It can be derived from equivalent aeroacoustic source formulations determined from a simulation of the compressible or incompressible flow problem, like in the work of Bailly et al. [21] and Bogey et al. [41]. Similar to the concept developed by Lighthill [200, 201] to derive an equivalent source term for the acoustic wave equation, the source vector $\mathbf{S}$ can be obtained for the linearized Euler equations by analogy with Lilley's equation [202]. This can be further extended to the LNS operator $\mathcal{L}_{\text{LNSE}}$. Assuming the flow to be isentropic in the source region, this approach leads to

$$\mathbf{S} = \begin{bmatrix} 0 \\ -\frac{\partial\left(\rho_0 u_i' u_j'\right)}{\partial x_j} + \overline{\frac{\partial\left(\rho_0 u_i' u_j'\right)}{\partial x_j}} \\ 0 \end{bmatrix}, \tag{3.16}$$

where $\overline{\bullet}$ represents the time average. The standard acoustic analogies, like the one developed by Ffowcs-Williams and Hawkings [314] or the one from the theory of vortex sound [145, 218, 236], can be recast as well to be used as forcing terms for the LEE and LNSE operators. As an example, the theory of the vortex sound leads to the expression

$$\mathbf{S} = \begin{bmatrix} 0 \\ -\rho_0 \left(\boldsymbol{\Omega} \times \mathbf{u}\right)' \\ 0 \end{bmatrix} \tag{3.17}$$

for the source vector, where $\boldsymbol{\Omega} = \nabla \times \mathbf{u}$ is the flow vorticity. Such expression was used for example by Ewert et al., computing the source from compressible flow simulations [101] or from synthetic fluctuations obtained by means of stochastic source reconstruction methods [100].

As the focus of this dissertation is set primarily on flow-acoustics, meaning on the study of acoustic waves propagation through non-uniform flow rather than the reconstruction of flow induced sources, the modeling of $\mathbf{S}$ is kept basic. The source vector can be taken as zero inside the domain and the acoustic excitation is obtained by injection through the boundaries, e.g. by means of characteristic boundary conditions. Another possibility is to consider simple expressions of $\mathbf{S}$ to represent for example analytical monopole/dipole types of point sources, broadband pulses or harmonic excitations. This will be explained in more detail in section 3.2 for the two solvers.

In the remainder of this work, the terms perturbations, disturbances, and fluctuating quantities are used indistinctly and refer to the first order unsteady

quantities solution of Eq. (3.9). Kovasznay [183] and Chu [60] have demonstrated that the linearized Navier-Stokes equations support three distinct modes of fluctuations with the respective acoustic, vortical and entropy perturbation modes. Unlike acoustic waves, which propagate at speed of sound $c_0$ in the relative frame of the mean flow, entropy and vorticity waves are convected with mean flow. It has been shown [198] that the small-amplitude canonical disturbance modes supported by the LNS equations propagate independently within the fluid domain in a homogeneous, inviscid flow. The acoustic, vortical, and entropy modes are known, however, to interact with each other at particular boundaries because the boundary conditions apply to the total value of the fluctuation itself, and not to its components [198]. The coupling of the disturbance modes can also happen due the presence of mean flow inhomogeneities [230], such as mean temperature and velocity gradients. Such linear transfer of energy from one fluctuation mode to others will be detailed and further analyzed in Section 3.3. The nonlinear sound, vorticity, and entropy sources coming from higher order disturbance interactions are out of the scope of the present linear analysis. The interested reader can refer to [60, 198] for more information on the topic.

### 3.1.2 The triple-decomposition for linearized Navier-Stokes equations

The perturbed LNS equations, as presented in section 3.1.1, assume that the acoustic field is not directly interacting with the turbulent mixing. They represent the turbulence contribution on the propagation of the acoustic waves solely through the turbulent mean flow quantities. It corresponds to the quasi-laminar model for the perturbation Reynolds stress [243], where this quantity is set to zero. Previous studies [114, 311] have shown that this model is accurate enough at sufficiently high frequency but underestimates the effective acoustic damping at lower frequencies. In order to investigate the impact of flow turbulence on the acoustic characterization of perforates, an alternative to the previously presented linearized Navier-Stokes equations is discussed in this section.

#### Triple decomposition of the Navier-Stokes equations

In case of acoustic propagation in a turbulent flow, an alternative to the perturbation approach detailed in Section 3.1.1 is to use a triple decomposition of the variables for the Navier-Stokes linearization procedure, following the ideas of Reynolds and Hussain [243]. They derived the dynamical equations governing small amplitude wave disturbances in turbulent shear flows. In their

approach, an instantaneous variable, instead of Eq. (3.8), is defined as

$$q(\mathbf{x},t) = q_0(\mathbf{x}) + \tilde{q}(\mathbf{x},t) + q''(\mathbf{x},t)\,, \tag{3.18}$$

where $q_0 = \overline{q}$ is the time-averaged contribution, $\tilde{q}$ is the periodic fluctuation and $q''$ corresponds to the turbulent motion. The respective contributions described in Eq. (3.18) can be separated, by using time averaging $\overline{\bullet}$ to determine $q_0$ and phase averaging $\langle\bullet\rangle$ to reject the background turbulence and extract the organized motions from the total signal, i.e. $\langle q\rangle = q_0 + \tilde{q}$. For an arbitrary fluctuating quantity $q(\mathbf{x},t)$, the phase averaging is defined as

$$\langle q(\mathbf{x},t)\rangle = \lim_{N\to\infty}\sum_{n=0}^{N} q(\mathbf{x}, t+\frac{n}{f})\,, \tag{3.19}$$

where $f$ is the frequency of the coherent perturbation. In order to derive the differential equations for the organized fluctuations $\tilde{q}$, some basic properties of the time and phase average processes are useful [243]:

$$\begin{aligned}
&\langle q''\rangle = 0\,, && \overline{\tilde{q}} = 0\,, && \overline{q''} = 0\,,\\
&\overline{\tilde{q}g} = \overline{qg}\,, && \langle\tilde{q}g\rangle = \tilde{q}\langle g\rangle\,, && \langle\overline{q}g\rangle = \overline{q}\langle g\rangle\,,\\
&\overline{\langle q\rangle} = \overline{q}\,, && \langle\overline{q}\rangle = \overline{q}\,, && \overline{\tilde{q}g''} = \langle\overline{\tilde{q}g''}\rangle = 0\,,
\end{aligned} \tag{3.20}$$

indicated for two arbitrary flow quantities $q(\mathbf{x},t)$ and $g(\mathbf{x},t)$. The last of these expressions emphasizes the fact that background turbulence and organized periodic motions are uncorrelated. Finally, similarly to Section 3.1.1, the amplitudes of the organized terms are assumed small enough to satisfy the criteria for linear approximation, i.e. $\tilde{q} \ll q_0$.

Introducing the triple decomposed quantities into the Navier-Stokes equations, and sorting out the periodic fluctuations by filtering through phase- and time-averaging, leads to the following set of equations:

$$\frac{\partial\tilde{\rho}}{\partial t} + \frac{\partial(\rho_0\tilde{u}_j + \tilde{\rho}u_{0j})}{\partial x_j} = 0\,, \tag{3.21a}$$

$$\begin{aligned}
\rho_0\frac{\partial\tilde{u}_i}{\partial t} + \frac{\partial u_{0j}\rho_0\tilde{u}_i}{\partial x_j} + (\rho_0\tilde{u}_j + \tilde{\rho}u_{0j})\frac{\partial u_{0i}}{\partial x_j} + c_0^2\frac{\partial\tilde{\rho}}{\partial x_i}\\
- \frac{\partial\tilde{\tau}_{ij}}{\partial x_j} = -\frac{\partial\rho_0\left(\langle u_i''u_j''\rangle - \overline{u_i''u_j''}\right)}{\partial x_j}\,.
\end{aligned} \tag{3.21b}$$

The quantity $\tilde{\tau}_{ij}^R = \langle u_i''u_j''\rangle - \overline{u_i''u_j''} = \overset{\sim}{u_i''u_j''}$, commonly called the perturbation Reynolds stress [243,311], is the difference between the phase and time averages

of the Reynolds stress of the background turbulence $\tau_{ij}^{''R} = u_i'' u_j''$. This quantity can physically be interpreted as the oscillation components of the background Reynolds stress introduced by the passing coherent wave. As the perturbation Reynolds stress contains phase and time averages of combination of non-coherent turbulent fluctuations, it constitutes therefore a new unknown for the problem. This is a well-known closure problem, similar to the one for turbulence modeling with CFD simulations, which necessitates the representation of this quantity in terms of the harmonic perturbations to get a closed set of equations. In the past years, many researchers have developed different models for the sound-turbulence interaction at low Mach number, mostly focusing on the modeling of the perturbation Reynolds stress [89, 129, 147, 212].

### Turbulence modeling

Based on previous works [114, 142], the simple quasi-static turbulent model or Newtonian eddy model [235, 311] is adopted in this doctoral thesis. This model stems from the assumption that the time period of turbulent straining induced by the sound wave is much longer than the turbulent relaxation time. Non-equilibrium effects introduced by the wave oscillations on the turbulent flows are therefore neglected. Due to this equilibrium assumption, the Boussinesq turbulent viscosity hypothesis can be applied to the perturbation Reynolds stress by relating it to the wave shear strain rate $\tilde{S}_{ij}$ through an equilibrium eddy-viscosity. This assumes that the transfer of momentum caused by turbulent eddies is modeled with an effective eddy-viscosity, in a similar way as the momentum transfer caused by molecular diffusion (i.e. friction) is modeled with a molecular viscosity. The eddy-viscosity, also referred to as turbulent viscosity, is noted in this work as $\mu_t$ and $\nu_t$ for the dynamic and kinematic quantities, respectively. In this context, the following relation is used:

$$\tilde{\tau}_{ij}^{R} = -2\nu_t \tilde{S}_{ij} = -\frac{\mu_t}{\rho_0}\left(\frac{\partial \tilde{u}_i}{\partial x_j} + \frac{\partial \tilde{u}_j}{\partial x_i} - \frac{2}{3}\frac{\partial \tilde{u}_k}{\partial x_k}\delta_{ij}\right) \tag{3.22}$$

Such model assumes that the phase averaging process does not affect the turbulent energy [243]. Based on the Boussinesq hypothesis, which relates the unknown turbulence stresses to the mean velocity gradients, the way turbulence-sound interaction is accounted for in the LNS equations is by adding an extra damping via the eddy-viscosity diffusive terms, as can be seen from Eqs. (3.21) and (3.22). The latter assumption implies that the phase averaging process does not significantly affect the kinetic energy [114]. With the previous expression for the perturbation Reynolds stress, Eq. (3.21) can be written in the same matrix formulation as Eq. (3.14), where only the Jacobian flux matrices $\mathbf{A}_i$ and the matrices related to the diffusive terms $\mathbf{C}_{ij}$ are modified to account for the local eddy-viscosity. These matrices are detailed in Appendix A.3, expressed for two-dimensional problems.

It can be noticed that the energy equation has been dropped from the original Navier-Stokes equations in order to derive Eq. (3.21), assuming the flow to be homentropic. Consequently, the unknown coherent pressure fluctuation $\tilde{p}$ has been removed from the momentum equation by using the homentropic relation between pressure and density perturbation $\tilde{p} = c_0^2 \tilde{\rho}$. The same triple decomposition procedure can be applied to the complete set of non-isentropic linearized Navier-Stokes equations. Nevertheless, it leads to additional closure problems [243] for the energy equation expressed in function of $\tilde{p}$. These extra terms containing non-coherent quantities are very complex to physically interpret and to model.

As final remark, the same notation as in Section 3.1.1 will be used in the following for the coherent perturbed variable, i.e. $\tilde{q} \equiv q'$, to ease readability and to have one common notation for both LNSE models.

## 3.2 Numerical Methods

The numerical methods used for solving the set of the perturbed equations described in Section 3.1 are presented in this section, for both frequency and time domains.

### 3.2.1 High-order FEM LNS solver in frequency domain

The approach taken here is to solve the LNSE operator $\mathcal{L}_{\text{LNSE}}$ in the frequency domain which suppresses the growth of spurious instability waves appearing in the time space. It is also less computationally expensive compared to time domain when only a limited set of frequencies is considered. The perturbation quantities $q'$ are assumed to be harmonic time dependent variables that can be written as $q'(\mathbf{x}, t) = q'(\mathbf{x}) e^{+\mathrm{j}\omega t}$, where j is the imaginary unit, $q'$ is a complex quantity and $\omega$ is the angular frequency.

#### Weighted residual formulation

The high-order continuous Finite Element Method — noted $p$-FEM — is based, similarly to the standard FEM, on the transformation of the physical problem into an equivalent integral formulation [323] and the minimization of the weighted residual, integrated over the given computational domain $\Omega$, in order to find the best approximate solution of the vector of unknown variables $\mathbf{q}$. Multiplying Eq. (3.14) by a vector of test functions $\mathbf{w}$ and integrating over the two- or three-dimensional finite domain $\Omega$, the variational formulation of

the original problem can be written as

$$\int_{\Omega} \left( \mathbf{w}^T \mathcal{L}_{\mathrm{LNSE}}(\mathbf{q}) - \mathbf{w}^T \mathbf{S} \right) \, \mathrm{d}\Omega = \mathbf{0} \, . \tag{3.23}$$

After using the Gauss' theorem, the weak variational formulation of the linearized Navier-Stokes equations in frequency domain is given by:

$$\begin{aligned} &\mathrm{j}\omega \int_{\Omega} \mathbf{w}^T \mathbf{q} \, \mathrm{d}\Omega + \int_{\Omega} \mathbf{w}^T \mathbf{C} \mathbf{q} \, \mathrm{d}\Omega - \int_{\Omega} \frac{\partial \mathbf{w}^T}{\partial x_i} \mathbf{A}_i \mathbf{q} \, \mathrm{d}\Omega \\ &- \int_{\Omega} \frac{\partial \mathbf{w}^T}{\partial x_i} \mathbf{C}_{ij} \frac{\partial \mathbf{q}}{\partial x_j} \, \mathrm{d}\Omega = - \int_{\Gamma} \mathbf{w}^T \left[ n_i \mathbf{A}_i \right] \mathbf{q} \, \mathrm{d}\Gamma - \int_{\Gamma} \mathbf{w}^T \left[ n_i \mathbf{C}_{ij} \right] \frac{\partial \mathbf{q}}{\partial x_j} \, \mathrm{d}\Gamma \\ &+ \int_{\Omega} \mathbf{w}^T \mathbf{S} \, \mathrm{d}\Omega \, , \quad \forall \mathbf{w} \in L^2(\Omega) \end{aligned} \tag{3.24}$$

where $\mathbf{n}$ is the unit normal vector to the boundary surface $\Gamma$ in the Cartesian coordinate system $\mathbf{x} = (x_1, x_2, x_3)$. The vector $\mathbf{n}$ is chosen pointing toward the domain exterior. The superscript $\bullet^T$ denotes the Hermitian transpose. The terms on the right-hand side in Eq. (3.24) correspond to the boundary integrals and are used to define the boundary conditions of the problem, by means of the flux matrices $\mathbf{F} = n_i \mathbf{A}_i$ and $\mathbf{F}^{\mathbf{v}} = n_i \mathbf{C}_{ij}$.

### Field variable approximation and Finite Element Method model

The physical domain is discretized into triangular (in 2-D) and tetrahedral (in 3-D) mesh elements $\Omega_i$. The open-source mesh generator Gmsh [113] is used to create the geometric representation of the domain and to generate the node and element connectivities. The discretization process allows to approximate the integrals element by element, since $\int_{\Omega} = \sum_{i=1}^{N_e} \int_{\Omega_i}$, with $N_e$ the number of elements over the computational domain. The solution vector $\mathbf{q}_i$ on each element is expanded in terms of polynomial shape functions $N_i^{(j)}$ and of degrees of freedom $\mathbf{q}_i^{(j)}$ such that

$$\mathbf{q}_i(\mathbf{x}) = \sum_{j=1}^{n_{\mathrm{dof}}} \mathbf{q}_i^{(j)} N_i^{(j)}(\mathbf{x}) \, , \qquad \forall \mathbf{x} \in \Omega_i \text{ and } \forall i \in \{1, \ldots, n_e\} \, , \tag{3.25}$$

where $n_{\mathrm{dof}}$ is the number of degrees of freedom per element. The standard Finite Element Method uses only linear shape functions. That method is known to suffer from dispersion error and high memory requirements limiting its applicability to low frequencies for practical cases [31,130]. For these reasons the polynomial basis in this work consists of high-order polynomial shape functions. This leads to lower resolution requirements and a smaller number of degrees of freedom compared to standard FEM [32]. In this work, a set of the Lobatto

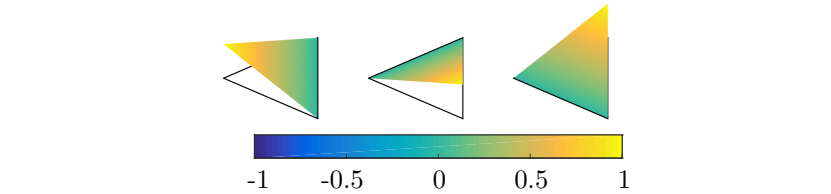


(a) Polynomial order $p = 1$

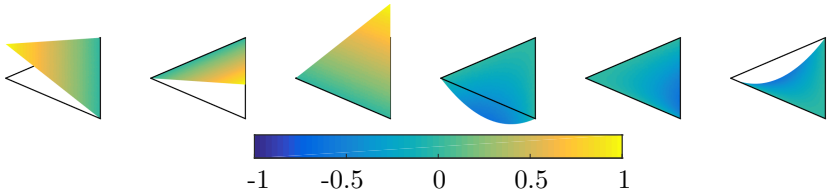


(b) Polynomial order $p = 2$

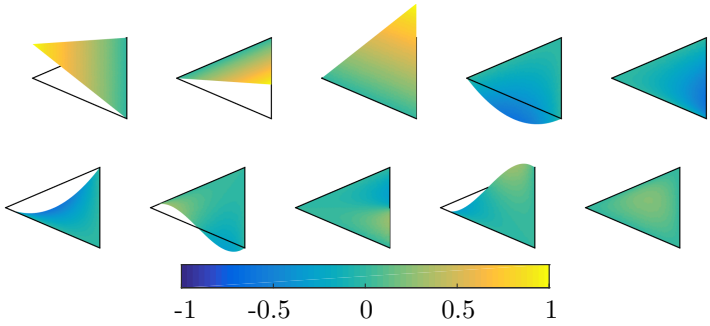


(c) Polynomial order $p = 3$

Figure 3.1. Hierarchic Lobatto shape functions on the triangular reference element, for $p$ from 1 to 3.

hierarchic shape functions, belonging to the family of modal shape functions, are used because of their good conditioning properties [303] and hierarchic attributes [32, 112]. Such function basis has already proven to be efficient for aeroacoustic problems, both based on the Helmholtz wave operator [32] and linearized Euler equations [126, 127]. The approximation basis contains high-order edge, face and bubble types of shape functions in addition to the linear vertex functions, as illustrated in Fig. 3.1. The hierarchic property of the chosen shape functions can be appreciated in this figure. For the types of geometric linear elements used in this work, the number of shape functions is given in Table 3.1. The same shape functions are adopted for each unknown variable of the vector $\mathbf{q} = \{\rho', \rho_0\mathbf{u}', p'\}^T$, as well as for each component of the weighting functions $\mathbf{w}$. In a matrix formulation, these assumptions yield:

$$\begin{cases} \mathbf{q} = \mathbf{N}\mathbf{d}_\mathbf{q} \\ \mathbf{w} = \mathbf{N}\mathbf{d}_\mathbf{w} \end{cases}, \tag{3.26}$$

**Linear triangular element**

| Type | Polynomial order | Number of shape functions on $\Omega_i$ |
|---|---|---|
| Vertex | always | 3 |
| Edge | $2 \leq p$ | $3\,(p-1)$ |
| Bubble | $3 \leq p$ | $(p-1)\,(p-2)\,/2$ |

**Linear tetrahedral element**

| Type | Polynomial order | Number of shape functions on $\Omega_i$ |
|---|---|---|
| Vertex | always | 4 |
| Linear face | $1 \leq p$ | 8 |
| Edge-based face | $2 \leq p$ | $12\,(p-1)$ |
| Genuine face | $3 \leq p$ | $4\,(p-1)\,(p-1)\,/2$ |
| Edge-based bubble | $2 \leq p$ | $6\,(p-1)$ |
| Face-based bubble | $3 \leq p$ | $4\,(p-2)\,(p-1)$ |
| Genuine bubble | $4 \leq p$ | $d\,(p-3)\,(p-2)\,(p-1)\,/6$ |

Table 3.1: Hierarchic shape functions on reference triangular and tetrahedral elements[1], as expressed in [303].

where $\mathbf{N}$ is the shape functions matrix, $\mathbf{d_q}$ is the vector of degrees of freedom, and $\mathbf{d_w}$ is an arbitrary $n_{\text{dof}}$-length vector.

For a single frequency $\omega$, the elementary integrals are computed within each element by means of a numerical quadrature and assembled to form the discrete global linear system

$$\mathbf{K}\mathbf{d_q} = \mathbf{F}\,, \tag{3.27}$$

with $\mathbf{K}$ a square, sparse, and complex matrix of size $n_{\text{dof}}^2$ and $\mathbf{F}$ the complex right-hand side vector. To facilitate the use of quadratures, reference elements are used. Coordinate mapping is therefore required to move from the physical space, e.g. $\mathbf{x} = (x_1, x_2)$, to the reference one, $\mathbf{x}^{\text{ref}} = (x_1^{\text{ref}}, x_2^{\text{ref}})$. Any variable $q$ in the formulation is then given by $q(\mathbf{x}) = q^{\text{ref}}(\mathbf{x}^{\text{ref}})$ and its gradient by $\boldsymbol{\nabla} q(\mathbf{x}) = \mathbf{J}^{-1}\boldsymbol{\nabla}^{\text{ref}} q^{\text{ref}}(\mathbf{x}^{\text{ref}})$, where $\boldsymbol{\nabla}^{\text{ref}}$ is the gradient in the reference space. The Jacobian $\mathbf{J}$, which describes the space transformation, is defined by

$$\mathbf{J} = \begin{bmatrix} \dfrac{\partial x_1}{\partial x_1^{\text{ref}}} & \dfrac{\partial x_1}{\partial x_2^{\text{ref}}} \\ \dfrac{\partial x_2}{\partial x_1^{\text{ref}}} & \dfrac{\partial x_2}{\partial x_2^{\text{ref}}} \end{bmatrix} \tag{3.28}$$

for a two-dimensional problem. On each physical element $\Omega_i$, the Gaussian quadrature evaluates the integral of an arbitrary function $f$ over the reference

[1] The same polynomial order $p$ is chosen for both element interior and the faces.

element $\Omega_i^{\text{ref}}$ such that

$$\int_{\Omega_i} f(\mathbf{x})\,\mathrm{d}\Omega = \int_{\Omega_i^{\text{ref}}} f(\mathbf{x}^{\text{ref}})\det(\mathbf{J})\,\mathrm{d}\Omega^{\text{ref}} = \sum_{k=1}^{n_q} w_k \det(\mathbf{J}) f(\mathbf{x}_k^{\text{ref}}) \tag{3.29}$$

where the weighted finite sum approximates the integral and $\det(\mathbf{J})$ is the determinant of the Jacobian. The number $n_q$ of weighting coefficients $w_k$ and the quadrature points location $\mathbf{x}_k^{\text{ref}}$ depend on the choice of the quadrature and its order. In this work, only linear representations of the element geometry are considered and the Jacobian is thus constant over an element. The standard Gauss-Legendre quadrature [303] is used for the different linear elements in this work: one-dimensional (lines), two-dimensional elements (triangular and quadrilateral elements), and three-dimensional (tetrahedrons).

Finally, a secondary linear system is added to Eq. (3.27) to impose constraints on particular degrees of freedom of the vector $\mathbf{d_q}$ if needed:

$$\mathbf{R}\mathbf{d_q} = \mathbf{V}\,, \tag{3.30}$$

where $\mathbf{R}$ is a square matrix of size $n_{\text{dof}}^2$ and $\mathbf{V}$ is a column vector of length $n_{\text{dof}}$. The secondary linear system in Eq. (3.30) is first reformulated as a change of variable applied to Eq. (3.27). The modified linear matrix system in Eq. (3.27) is then solved by means of the direct LU factorization method to obtain the unknown degrees of freedom $\mathbf{d_q}$, after applying the inverse change of variables. Note that the vector $\mathbf{d_q}$ contains the values of the unknown variables at the mesh nodes, as well as the solution of additional degrees of freedom linked to the high-order method used. The high-order interpolation of variable values at locations different from the mesh nodes can be done in a post-processing step, but requires saving all the DOFs contained in $\mathbf{d_q}$.

### Boundary conditions

In order to complete the definition of the problem, boundary conditions have to be added over the boundary surface $\Gamma$ to characterize the surface integral terms in Eq. (3.24). All walls of the physical domain are assumed impermeable and acoustically rigid. One can apply wall slip boundary conditions $\mathbf{u}' \,.\, \mathbf{n} = 0$ where the acoustic boundary layer is expected to play no significant role and a no-slip wall boundary condition otherwise. In this last case, the acoustic perturbation satisfies at the wall

$$\mathbf{u}' \cdot \mathbf{n} = 0 \qquad \text{and} \qquad \mathbf{u}' \cdot \mathbf{t} = 0, \tag{3.31}$$

where $\mathbf{u}'$ is the acoustic perturbation velocity and $\mathbf{n}$ and $\mathbf{t}$ are the normal and tangential vectors to the wall, respectively.

In cases where the energy equation Eq. (3.9c) without isentropic assumption is employed, additional boundary conditions on the temperature perturbation $T'$

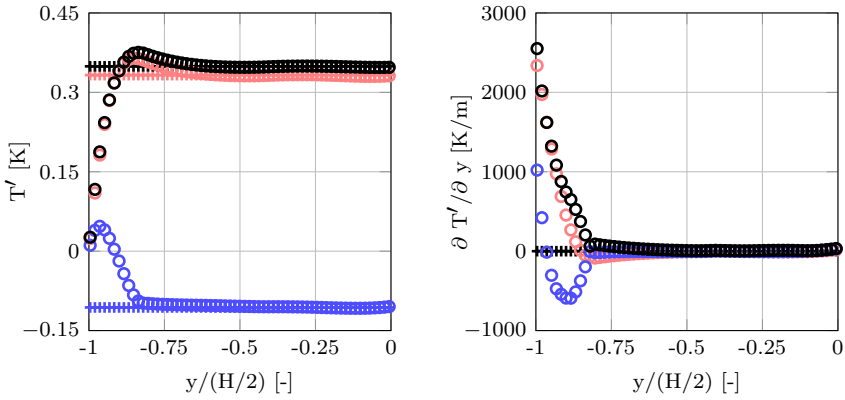


(a) Temperature $T'(y)$ (b) Temperature gradient $\partial T'(y)/\partial y$

Figure 3.2. Impact of boundary conditions on the temperature profile for a plane wave in a square waveguide of width $H = 5\,\text{mm}$: isothermal (○) and adiabatic (+) boundary conditions, real part ■, imaginary part ■, and absolute value ■. Profiles are obtained at $f = 10\,\text{Hz}$, with $p = 5$, using the grid detailed in Section 3.4.2.

have to be considered. If one assumes that the walls have a constant temperature, $T = \text{const}_{\text{.}}$ and that the temperature fluctuations vanish, i.e. $T' = 0$, Eq. (3.12) leads to the following relationship:

$$p' - \frac{p_0}{\rho_0}\rho' = 0 \tag{3.32}$$

from the linearized state equation for a perfect gas. A suitable alternative to the previous isothermal boundary condition is the adiabatic one, imposing the gradients of the mean temperature and temperature perturbation to zero, $\partial T'/\partial n = 0$. Due to the present LNSE formulation in terms of $\mathbf{q} = \{\rho', \rho_0\mathbf{u}', p'\}^T$, this condition on $T'$ appears as a non-trivial relation between pressure fluctuation $p'$, density fluctuation $\rho'$, and their respective gradients $\boldsymbol{\nabla} p'$ and $\boldsymbol{\nabla}\rho'$. This relation reads:

$$\left(\frac{1}{p_0}\frac{\partial p'}{\partial x_i} - \frac{1}{p_0^2}\frac{\partial p_0}{\partial x_i}p' - \frac{1}{\rho_0}\frac{\partial \rho'}{\partial x_i} + \frac{1}{\rho_0^2}\frac{\partial \rho_0}{\partial x_i}\rho'\right)\cdot n_i = 0\,. \tag{3.33}$$

The general extension of the latter boundary condition, prescribing an arbitrary thermal flux through the boundary, can also be done. An approach using Lagrange multipliers to substitute the complex combination of variables $\rho'$, $p'$, $\boldsymbol{\nabla}\rho'$, and $\boldsymbol{\nabla} p'$, has been implemented in the context of the LNSE $p$-FEM solver. Lagrange multipliers are often used in FEM approach at boundaries between two domains for the coupling of these domains, e.g. in Domain Decomposition Methods [75, 103, 211]. For the present case, the additional Lagrange multipliers

are simply added on the boundary elements as extra unknowns of the problem. They are then determined during the resolution of the extended global linear system, defined by Eqs. (3.27) and (3.30).

Finally, another alternative is to prescribe a Neumann type of boundary condition on the fluctuating pressure and/or density, imposing their gradients as zero:

$$\frac{\partial p'}{\partial x_i} n_i = 0 \qquad \text{and} \qquad \frac{\partial \rho'}{\partial x_i} n_i = 0\,. \tag{3.34}$$

Figure 3.2 illustrates the difference in fluctuating temperature profiles between the isothermal and adiabatic cases, for a simple square waveguide in 3-D. The profiles are given normal to the wall, along the transversal $y$-direction, up to the waveguide's center at $y = 0$. The width of the duct for this example is $H = 5\,\text{mm}$. Results shown are obtained with a polynomial order $p = 5$ and at a low frequency $f = 200\,\text{Hz}$. By assuming a zero fluctuating temperature at the boundary, a passing acoustic wave will intrinsically excite an entropy disturbance $s'$ (see Section 3.3). This can result in damping of the acoustic mode and excitation of the entropy mode, even in cases where no direct entropy perturbation was initially present in the domain.

Table 3.2 summarizes the different possible boundary conditions implemented in the continuous $p$-FEM solver for the LNS equations.

| **Boundary type** | **Condition** | **Boundary Layer resolution** |
|---|---|---|
| Isentropic slip wall | $\mathbf{u}' \cdot \mathbf{n} = 0$ | none |
| Isentropic no-slip wall | $\mathbf{u}' = \mathbf{0}$ | viscous |
| Adiabatic no-slip wall | $\mathbf{u}' = \mathbf{0}$<br>$p' - \frac{p_0}{\rho_0}\rho' = 0$ | visco-thermal |
| Isothermal no-slip wall | $\mathbf{u}' = \mathbf{0}$<br>$T' = 0$ | visco-thermal |
| No-slip wall with Neumann on $p'$ | $\mathbf{u}' = \mathbf{0}$<br>$\frac{\partial p'}{\partial x_i} n_i = 0$ | visco-thermal |
| Prescribed velocity | $\mathbf{u}' = \mathbf{U}_{\text{inlet}}$ | none |
| Prescribed pressure | $\mathbf{p}' = \mathbf{P}_{\text{inlet}}$ | none |
| Inlet mode injection | $\hat{\mathbf{q}}^+ = \mathbf{Q}_{\text{mode}}$ | none |
| Passive outlet | $\hat{\mathbf{q}}^- = \mathbf{0}$ | none |

Table 3.2: Summary of the boundary conditions used with the $p$-FEM LNS solver.

Complementary to the previous discussion on walls treatment, some details on the "open" type of boundary conditions should be mentioned. The truncation of the physical domain for numerical purposes leads to spurious reflections at these artificial boundary surfaces, deteriorating the numerical solution. For the applications in this dissertation, this situation is typically encountered at the truncated extremities of the duct in which a test object, e.g. an orifice or an acoustic resonator, is placed. It is necessary to impose at such boundaries non-reflecting boundary conditions in order to avoid outgoing waves to be artificially reflected back inside the physical domain. These boundaries can also be used to inject an acoustic excitation which will propagate through the interior domain. Two approaches are used for this purpose:

(a) Method of characteristics:

Neglecting the viscosity and thermal effects at a boundary $\Gamma$, the boundary integral terms $\int_\Gamma (\ldots)\, \mathrm{d}\Gamma$ rely solely on the flux Jacobian matrices $\mathbf{A}_i$. The projected flux Jacobian $\mathbf{F} = n_i \mathbf{A}_i$ on the direction $\mathbf{n}$ can be expressed by eigendecomposition as $\mathbf{F} = \mathbf{W}\mathbf{\Lambda}\mathbf{W}^{-1}$ [140], where $\mathbf{\Lambda}$ and $\mathbf{W}$ are the eigenvalue diagonal matrix and the non-singular eigenvectors matrix, respectively. Left-multiplying by $\mathbf{W}^{-1}$ the original set of equation leads to a system of advection equations for the quantities $\hat{\mathbf{q}} = \mathbf{W}^{-1}\mathbf{q}$. The vector $\hat{\mathbf{q}}$ contains the amplitude of the characteristic waves traveling along the direction $\mathbf{n}$ [124, 140, 295]. In a two-dimensional Cartesian coordinate system, $\hat{\mathbf{q}}$ is expressed as

$$\hat{\mathbf{q}} = \begin{bmatrix} \hat{q}_1 \\ \hat{q}_2 \\ \hat{q}_3 \\ \hat{q}_4 \end{bmatrix} = \begin{bmatrix} \rho' - \dfrac{p'}{c_0^2} \\ \rho_0 \left( n_2 u_1' - n_1 u_2' \right) \\ \rho_0 \left( n_1 u_1' + n_2 u_2' \right) + \dfrac{p'}{c_0} \\ -\rho_0 \left( n_1 u_1' + n_2 u_2' \right) + \dfrac{p'}{c_0} \end{bmatrix} \tag{3.35}$$

and

$$\begin{aligned} \mathbf{\Lambda} &= \begin{bmatrix} \lambda_1 & 0 & 0 & 0 \\ 0 & \lambda_2 & 0 & 0 \\ 0 & 0 & \lambda_3 & 0 \\ 0 & 0 & 0 & \lambda_4 \end{bmatrix} \\ &= \begin{bmatrix} \mathbf{u_0} \cdot \mathbf{n} & 0 & 0 & 0 \\ 0 & \mathbf{u_0} \cdot \mathbf{n} & 0 & 0 \\ 0 & 0 & \mathbf{u_0} \cdot \mathbf{n} + c_0 & 0 \\ 0 & 0 & 0 & \mathbf{u_0} \cdot \mathbf{n} - c_0 \end{bmatrix}. \end{aligned} \tag{3.36}$$

The characteristic variables $\hat{q}_{i, i \in \{1,2,3,4\}}$ can be perceived as perturbation waves traveling at different phase velocities $\lambda_i$. One can identify an entropy mode $\hat{q}_1$, an hydrodynamic (or vortical) mode $\hat{q}_2$, and two acoustical modes,

$\hat{q}_3$ and $\hat{q}_4$. A coupling between these modes appears when a variation in $\hat{q}_i$ is present normal to the $\mathbf{n}$-direction and in presence of non-uniformities, as mentioned in Section 3.1.1. Based on this decomposition in terms of characteristics, standard boundary conditions can be reformulated in terms of characteristic variables. In order to define a well-posed problem, the number of imposed boundary conditions has to be equal to the number of incoming characteristics. A generic set of $N_{BC}$ boundary conditions on the primitive variables $\mathbf{q}$ is considered, defined by $\mathbf{Mq} = \mathbf{s}$, with $\mathbf{M}$ a $(N_{BC} \times N_q)$ coefficient matrix, $\mathbf{s}$ the right-hand side vector, and $N_q$ the number of variables contained in $\mathbf{q}$. Written in terms of the characteristic wave amplitudes, this yields to

$$\hat{\mathbf{M}}\hat{\mathbf{q}} = \begin{bmatrix}\hat{\mathbf{M}}^{+} & \hat{\mathbf{M}}^{-}\end{bmatrix} \begin{Bmatrix}\hat{\mathbf{q}}^{+} \\ \hat{\mathbf{q}}^{-}\end{Bmatrix} = \mathbf{s}\,, \tag{3.37}$$

where $\hat{\mathbf{M}} = \mathbf{MW}$ and the characteristics are separated between incoming characteristics $\bullet^{+}$ (corresponding to negative eigenvalues $\lambda_i$ for the definition $\mathbf{n}$ decided) and outgoing ones $\bullet^{-}$ (corresponding to positive eigenvalues). This reformulation allows to express the amplitude of the incoming characteristics with respect to the outgoing ones. Finally, following [124], the boundary integral can be written as:

$$\begin{gathered}\int_{\Gamma} \mathbf{w}^T \mathbf{Fq}\, \mathrm{d}\Gamma = \int_{\Gamma} \mathbf{w}^T \mathbf{W}\boldsymbol{\Lambda}\mathbf{R}\mathbf{W}^{-1}\mathbf{q}\, \mathrm{d}\Gamma + \int_{\Gamma} \mathbf{w}^T \hat{\mathbf{s}}\, \mathrm{d}\Gamma\,, \\ \text{with } \mathbf{R} = \begin{bmatrix} \mathbf{I} & \mathbf{0} \\ -\left(\hat{\mathbf{M}}^{-}\right)^{-1}\hat{\mathbf{M}}^{+} & \mathbf{0}\end{bmatrix} \text{ and } \hat{\mathbf{s}} = \mathbf{W}\boldsymbol{\Lambda}\begin{Bmatrix}\mathbf{0} \\ \left(\hat{\mathbf{M}}^{-}\right)^{-1}\mathbf{s}\end{Bmatrix}.\end{gathered} \tag{3.38}$$

The matrix $\mathbf{R}$ represents the reflection between incoming and outgoing characteristic waves. This generic formulation can be applied to various boundary conditions, e.g. to prescribe the pressure or the velocity, or to inject acoustic duct modes. Detailed expressions of $\mathbf{R}$ and $\hat{\mathbf{s}}$ for different boundary conditions can be found in the work of Hamiche [124] for the LEE operator in 2-D and 3-D. This technique can be directly applied to define boundary conditions for problems modeled with the LNS equations (Eqs. (3.14) and (3.21)). The characteristic decomposition can indeed be performed in a similar manner as described previously by only considering the hyperbolic part of the LNSE operator. This corresponds to an approximation, by neglecting visco-thermal effects near such boundaries, which is found to be satisfying for the cases presented in this work. This presents the advantage of having direct analytic expressions for $\mathbf{R}$ and $\hat{\mathbf{s}}$ [124]. In case where the turbulence viscosity is considered and exhibits a non-zero gradient near the domain limit, the eigenvalue decomposition of the flux Jacobian matrices and the reconstruction of $\mathbf{R}$ and $\hat{\mathbf{s}}$ can be performed numerically.

(b) Perfectly Matched Layer (PML) technique:

The main concept behind the Perfectly Matched Layer approach is the addition of an extra damping zone to the physical domain to absorb the outgoing waves and reduce reflections towards the domain by means of a time/space change of coordinates [29, 152]. In this artificial domain, the real physical coordinates are transformed into the complex plane with imaginary part of coordinates leading to acoustic wave damping. Such transformation can be expressed, considering a wave propagating along the z-direction, by the following change of variable

$$\hat{z}(z) = z + \frac{f_z(z)}{jk_0} \tag{3.39}$$

The function $f_z$ is chosen following the guidelines drawn up by other authors [29, 33, 152]: it must satisfy the continuity of space variables between the PML and physical domains, be positive and increase monotonically ($e^{+\mathrm{j}\omega t}$ convention) to guarantee the absorption of waves leaving the domain, and give sufficiently strong negative value at the outer boundary to avoid spurious reflection. A Lorentz transformation of the time coordinate $\hat{t}$ in the PML is also applied to deal with the issue originating from possible inverse upstream modes [29, 153]. It reads

$$\hat{t}(z,t) = t - \frac{\mu_z}{\omega}\left(\hat{z}(z) - z_{\text{int}}\right) , \tag{3.40}$$

where $z_{\text{int}}$ is the position of the interface between the PML and physical domains and $\mu_z$ is a constant correction coefficient. A detailed analytical study of the PML in the context of high-order FEM can be found in [124] for the 1-D and 2-D Helmholtz equation. It shows that finding a unique optimal stretching function for both evanescent and propagating modes is not realizable. A logarithmic stretching function $f_z$, as introduced by Bermúdez et al. [33], and the correction coefficient $\mu_z$ defined by Bécache et al. [29] are adopted in this work. For a PML domain of size $L_{z,\,\text{PML}}$, it yields:

$$\begin{cases} f_z(z) = -\ln\left(1 - \dfrac{z - z_{\text{int}}}{L_{z,\,\text{PML}}}\right) \\ \mu_z = \dfrac{k_0 M_{0z}}{1 - M_{0z}^2} \end{cases} , \tag{3.41}$$

with $k_0 = \omega/c_0$ and $M_{0z}$ the local Mach number in the $z$-direction.

In practice, using the introduced space-time transformation of coordinates, the LNS operator $\mathcal{L}_{\text{LNSE}}$ in Eq. (3.14) can be recast in the PML domain $\hat{\Omega}$ as:

$$\begin{aligned} &\mathrm{j}\omega\mathbf{q} + \mathrm{j}\mu_{x_i}\mathbf{A}_i\mathbf{q} + \frac{1}{\gamma_i}\frac{\partial \mathbf{A}_i\mathbf{q}}{\partial x_i} + \mathbf{C}\mathbf{q} - \mu_{x_i}\mu_{x_j}\mathbf{C}_{ij}\mathbf{q} \\ &+ \mathrm{j}\left(\frac{1}{\gamma_j}\mu_{x_i}\frac{\partial \mathbf{C}_{ij}\mathbf{q}}{\partial x_j} + \frac{1}{\gamma_i}\mu_{x_j}\frac{\partial \mathbf{C}_{ij}\mathbf{q}}{\partial x_i}\right) + \frac{1}{\gamma_i\gamma_j}\frac{\partial}{\partial x_i}\left(\frac{\partial \mathbf{C}_{ij}\mathbf{q}}{\partial x_j}\right) = \mathbf{0}\,, \end{aligned} \tag{3.42}$$

where the complex coordinate derivatives $\gamma_i$ are given by

$$\gamma_i = \frac{\mathrm{d}\hat{x}_i(x_i)}{\mathrm{d}x_i} = 1 + \frac{1}{\mathrm{j}k_0}\frac{\partial f_{x_i}(x_i)}{\partial x_i}. \tag{3.43}$$

The weighted residual formulation over $\hat{\Omega}$ in the 2-D coordinate system $\mathbf{x} = (x_1, x_2)$ reads:

$$\begin{aligned}
&\int_{\hat{\Omega}} \gamma_1\gamma_2 \mathbf{w}^T \left(\mathrm{j}\omega\mathbf{q} + \mathbf{C}\mathbf{q} + \mathrm{j}\mu_{x_k}\mathbf{A}_k\mathbf{q} - \mu_{x_i}\mu_{x_j}\mathbf{C}_{ij}\mathbf{q}\right) \mathrm{d}\Omega - \int_{\hat{\Omega}} \left(\gamma_2 \frac{\partial \mathbf{w}^T}{\partial x_1}\mathbf{A}_1\mathbf{q}\right. \\
&\left. + \gamma_1 \frac{\partial \mathbf{w}^T}{\partial x_2}\mathbf{A}_2\mathbf{q}\right) \mathrm{d}\Omega - \int_{\hat{\Omega}} \mathrm{j}\gamma_1\gamma_2 \left(\frac{\partial \mathbf{w}^T}{\partial x_j}\frac{\mu_{x_i}}{\gamma_j} + \frac{\partial \mathbf{w}^T}{\partial x_i}\frac{\mu_{x_j}}{\gamma_i}\right)\mathbf{C}_{ij}\mathbf{q}\,\mathrm{d}\Omega \\
&- \int_{\hat{\Omega}} \frac{\partial \mathbf{w}^T}{\partial x_i}\frac{\gamma_1\gamma_2}{\gamma_i\gamma_j}\mathbf{C}_{ij}\frac{\partial \mathbf{q}}{\partial x_j}\,\mathrm{d}\Omega = -\int_{\hat{\Gamma}} \mathbf{w}^T\left[\gamma_2 n_1\mathbf{A}_1 + \gamma_1 n_2\mathbf{A}_2\right]\mathbf{q}\,\mathrm{d}\Gamma \\
&- \int_{\hat{\Gamma}} \frac{\mathrm{j}\mu_{x_i}\gamma_1\gamma_2}{\gamma_j}\mathbf{w}^T\left[n_j\mathbf{C}_{ij}\right]\mathbf{q}\,\mathrm{d}\Gamma - \int_{\hat{\Gamma}} \frac{\mathrm{j}\mu_{x_j}\gamma_1\gamma_2}{\gamma_i}\mathbf{w}^T\left[n_i\mathbf{C}_{ij}\right]\mathbf{q}\,\mathrm{d}\Gamma \\
&- \int_{\hat{\Gamma}} \mathbf{w}^T\frac{\gamma_1\gamma_2}{\gamma_i\gamma_j}\left[n_i\mathbf{C}_{ij}\right]\frac{\partial \mathbf{q}}{\partial x_j}\,\mathrm{d}\Gamma\,, \qquad \forall \mathbf{w} \in L^2(\hat{\Omega})
\end{aligned} \tag{3.44}$$

using the property that $\mathrm{d}\hat{\Omega} = \gamma_1\gamma_2\,\mathrm{d}\Omega$ from the coordinate transformation. The main advantage of the PML technique over the method of the characteristics is that outgoing waves are absorbed regardless of their angle of incidence. The PML approach can also be applied to inject incident modes into the computational domain, by applying the PML transformation solely to the reflected field [125, 161].

### Numerical stabilization method

The classical Galerkin finite element formulation is known to suffer from stability issues for convection-dominated problems [90], i.e. for which mesh Péclet numbers Pe are higher than 1. The Péclet number represents the ratio between the convective and diffusive processes. It is defined as $\mathrm{Pe} = v_c h/(2c_d)$, where $h$ is the mesh size, $v_c$ is the convection velocity and $c_d$ the diffusivity coefficient. For such problems, spurious oscillations can originate from the difference in diffusion between the Galerkin scheme and the exact solution scheme [53]. These oscillations can significantly deteriorate the accuracy of the numerical solution, as shown by Astley and Eversman [16] for the LEE operator with linear FEM. Even if it was shown that increasing the polynomial order to represent the field variables helps to limit the appearance of instabilities for convection-diffusion transport problems with FEM [53], the issue remains.

The main existing stabilization techniques rely on the addition of a stabilization term in the original variational formulation, such that:

$$\underbrace{\int_\Omega \mathbf{w}^T \mathcal{L}(\mathbf{q})\,\mathrm{d}\Omega = 0}_{\textbf{Original problem}} \Rightarrow \underbrace{\int_\Omega \mathbf{w}^T \mathcal{L}(\mathbf{q})\,\mathrm{d}\Omega + \int_\Omega \mathcal{D}_\mathrm{s}(\mathbf{w})^T \boldsymbol{\tau}_\mathbf{s} \mathcal{L}(\mathbf{q})\,\mathrm{d}\Omega = \mathbf{0}}_{\textbf{Stabilized problem}}\ , \quad (3.45)$$

expressed in the absence of interior source ($\mathbf{S} = \mathbf{0}$), where $\mathcal{D}_\mathrm{s}$ is the stabilization operator, $\boldsymbol{\tau}_\mathbf{s}$ is the matrix of the stabilization parameters, and $\mathcal{L}$ is the differential acoustic operator considered. Stabilization techniques differ in the choice of $\mathcal{D}_\mathrm{s}$. An overview of the most common stabilization techniques for convection-diffusion problems can be found in [65, 237] for standard Finite Element Methods, and in [50] for high-order ones. The main stabilization approaches are the Streamline-Upwind Petrov-Galerkin (SUPG) method [55, 155], the SubGrid-Scale (SGS) method [66], and the Galerkin/Least-Squares (GLS) [154].

Following the work of Hamiche et al. [125, 127] on the standard Petrov-Galerkin stabilization approaches applied to the LEE differential operator $\mathcal{L}_\mathrm{LEE}$ for $p$-FEM computations in the frequency domain, it has been observed that the standard Galerkin/Least-Squares (GLS) stabilization scheme allows to considerately improve the accuracy of the linearized Euler equation computations. The classical steady stabilization parameter [154] was found to be the most efficient for the high-order treatment of aeroacoustic harmonic problems [124], and will thus be used here. Furthermore, the SUPG and GLS methods have shown to behave very similarly for the LEE operator in frequency domain. Rao and Morris [239] have also used the SUPG technique for the LEE operator in the frequency domain and obtained good improvement in accuracy by considering a simple stabilization matrix $\boldsymbol{\tau}_\mathbf{s}$ depending on the coefficient matrices spectral radii. As the convective terms are similar in the linearized Navier-Stokes equations, the same stabilization approach is applied in the present work. A previous study by Gikadi et al. [115], on the application of the GLS technique for the $\mathcal{L}_\mathrm{LNSE}$ operator, supports this decision. GLS approach is based on the mathematical idea of reducing the least square error arising in the numerical solution [154]. The main effect of the stabilization operator on the numerical scheme can be interpreted as the addition of artificial diffusion. In practice, it can be seen as the modification of the test function applied to the weighted residual formulation via the operator $\mathcal{D}_\mathrm{s}$. In the GLS approach, the operator $\mathcal{D}_\mathrm{s}$, applied to obtain the modified test function $\mathbf{w}^\star$, contains the differential operator of the original problem, i.e. in our case $\mathcal{D}_\mathrm{s} = \mathcal{L}_\mathrm{LNSE}$. This leads, for the weighting function of the $i^{th}$ component of the vector of unknowns $\mathbf{q}$, to:

$$\mathbf{w}_i^\star = \mathbf{w}_i + \boldsymbol{\tau}_{\mathbf{s}i}\, \mathcal{L}_{\mathrm{LNSE},i}(\mathbf{w}_i)\,, \qquad \forall i \in \{1, \ldots, 4 \text{ or } 5\}\ . \quad (3.46)$$

The stabilization parameters $\boldsymbol{\tau}_{\mathbf{s}i}$, which correspond to each of the scalar equations of the matrix system in Eq. (3.14), can be treated independently. These stabilization parameters are nevertheless taken here all equal, as done

in [115, 239]. This unique stabilization parameter is simply noted $\tau_{\mathrm{s}}$ and is defined as [124, 126]:

$$\tau_{\mathrm{s}} = \boldsymbol{\tau_{\mathbf{s}}}_{i \in \{1,\cdots,4 \text{ or } 5\}} = \max\left(\frac{\alpha_{\mathrm{num}} h_j}{\lambda_j}\right). \tag{3.47}$$

The parameter $\lambda_j$ denotes the spectral radius of the system's flux matrix $\mathbf{A_j}$, $h_j$ the local mesh size in the $j$-direction and $\alpha_{\mathrm{num}}$ is a chosen constant for a simulation case, taken as $\alpha_{\mathrm{num}} = 1/(2p)$ with $p$ the order of the polynomial shape functions used [126].

In the physical domain $\Omega$, as the stabilization contributions are defined only inside element interiors where the shape functions are $\mathcal{C}^{\infty}$, the weighted residual formulation can be written as:

$$\int_{\Omega} \mathbf{w}^T \mathcal{L}_{\mathrm{LNSE}}(\mathbf{q}) \, \mathrm{d}\Omega + \sum_{e=1}^{N_{elt}} \int_{\Omega_e} \mathcal{L}_{\mathrm{LNSE}}(\mathbf{w})^T \tau_{\mathrm{s}} \mathcal{L}_{\mathrm{LNSE}}(\mathbf{q}) \, \mathrm{d}\Omega_e = 0\,, \tag{3.48}$$

disregarding once more the term $\mathbf{S}$. Even if not explicitly detailed here, the stabilization also has to be applied in the PML domains, which leads to additional terms appearing in the $p$-FEM formulation inside $\hat{\Omega}$ via the PML time/spatial coordinate transformation.

### Source terms inside the domain

As previously explained, the excitation of the numerical domain can be achieved by injecting a perturbation through one of the domain's boundaries or by directly prescribing a source in its interior. The latter case corresponds to volumetric source terms expressed as the right-hand side $\mathbf{S}$ of the variational formulation in Eq. (3.24). Concerning acoustic sources (monopoles, dipoles, and quadrupoles), analytical expressions are implemented in the LNSE $p$-FEM solver.

A monopole of amplitude $m$, placed at a location $\mathbf{x_s}$, can be defined as a point source with the help of the Dirac function $\delta$:

$$S_m = m\,\delta(\mathbf{x} - \mathbf{x_s})\,. \tag{3.49}$$

A dipole of amplitude $d_i$ in the direction $i$ can be seen as the result of two monopoles of amplitude $d_i/\Delta_i$ separated by an arbitrary small distance $\Delta_i = \|\mathbf{\Delta_i}\|$ (but finite) and opposite signs. It yields:

$$S_d = d_i \frac{\delta(\mathbf{x} - \mathbf{x_s} - \mathbf{\Delta_i}/2) - \delta(\mathbf{x} - \mathbf{x_s} + \mathbf{\Delta_i}/2)}{\Delta_i}. \tag{3.50}$$

Finally, a quadrupole of strength $q_{ij}$ in the directions $i$ and $j$ can be represented with four monopoles of amplitude $q_{ij}/(\Delta_i \Delta_j)$ separated by arbitrary small

distances $\Delta_i = \|\mathbf{\Delta_i}\|$ and $\Delta_j = \|\mathbf{\Delta_j}\|$ (finite here again). It reads:

$$\begin{aligned} S_q =& q_{ij} \left( \frac{\delta(\mathbf{x} - \mathbf{x_s} - \mathbf{\Delta_i}/2 - \mathbf{\Delta_j}/2) + \delta(\mathbf{x} - \mathbf{x_s} + \mathbf{\Delta_i}/2 + \mathbf{\Delta_j}/2)}{\Delta_i \Delta_j} \right. \\ & \left. - \frac{\delta(\mathbf{x} - \mathbf{x_s} - \mathbf{\Delta_i}/2 + \mathbf{\Delta_j}/2) + \delta(\mathbf{x} - \mathbf{x_s} + \mathbf{\Delta_i}/2 - \mathbf{\Delta_j}/2)}{\Delta_i \Delta_j} \right) \end{aligned} \tag{3.51}$$

After integration over the domain $\Omega$, the previous point sources appear in the right-hand side of the variational formulation. For the example of a scalar operator, the following expressions for the $p$-FEM representation of the acoustic source terms can be derived:

**Monopole:**

$$\text{RHS} = \int_\Omega m \delta(\mathbf{x} - \mathbf{x_s}) \, \mathrm{d}\Omega = m \, N(\mathbf{x_s}) \,, \tag{3.52a}$$

**Dipole:**

$$\text{RHS} = d_i \frac{N(\mathbf{x_s} + \mathbf{\Delta_i}/2) - N(\mathbf{x_s} - \mathbf{\Delta_i}/2)}{\Delta_i} \approx d_i \frac{\partial N(\mathbf{x_s})}{\partial x_i} \,, \tag{3.52b}$$

**Quadrupole:**

$$\text{RHS} \approx q_{ij} \frac{\partial^2 N(\mathbf{x_s})}{\partial x_i \partial x_j} \,, \tag{3.52c}$$

where $N(\mathbf{x})$ corresponds to the $p$-FEM approximation field function, as described in Eq. (3.25). In the case of the LNS operator, the vector source $\mathbf{S}$ is defined as

$$\mathbf{S} = \begin{bmatrix} \frac{1}{c_0^2} \epsilon_s \\ 0 \\ 0 \\ \epsilon_s \end{bmatrix} \,, \text{ where } m = -\mathrm{j} \epsilon_s \omega \tag{3.53}$$

for the example of an acoustic monopole in a 2-D domain. The quantity $\epsilon_s$ describes the amplitude of the source terms for the LNS operator in Eq. (3.14), whereas $m$ defines the actual amplitude of the modeled radiating monopole. An alternative to the point representation of the source terms given by Eq. (3.52) consists in averaging the contribution of these terms over the entire element that contains the source. This is done in practice by integrating one of the previous expressions over the element by means of the Gauss-Legendre quadrature and by normalizing the result by the element surface (volume) in 2-D (3-D). The normalization assures the correct source amplitude, independently of the size of the element containing the source. In a 2-D problem, the RHS expression for a monopole localized in a triangular element can be, for example, written as

$$\text{RHS} = \sum_{k=1}^{n_q} w_k \frac{1}{2} m \, N(\mathbf{x_s^{ref}}) \,, \tag{3.54}$$

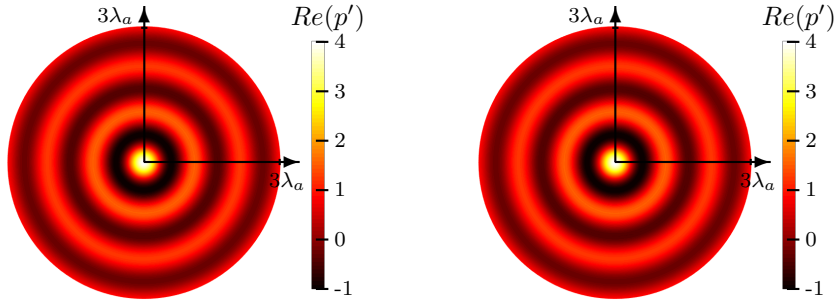


(a) Numerical solution (b) Analytical solution

Figure 3.3. Monopole source in free field in the absence of flow: numerical solution obtained with $p = 5$ and amplitude $m = \omega/(\mathrm{j}\gamma)$. Nodal error from analytical solution $\epsilon_m = 4.29\,\%$.

where $n_q$ is the number of weighting coefficients $w_k$ used for the quadrature. Such implementation was found to give a satisfying representation of a point source, but often requires a grid refinement at the source location.

In Figs. 3.3 and 3.4, the numerical results for the free-field radiating acoustic monopole and dipole, based on the expressions in Eq. (3.52), are compared to the theoretical solutions obtained from the free-field Green's function for the Helmholtz equation (see Appendix E of [246]). The source vector $\mathbf{S}$ is taken as defined in Eq. (3.53). Recasting the set of isentropic LNS equations in the absence of mean flow and visco-thermal dissipation leads to the reduced wave equation:

$$\nabla^2 p' + k_0^2 p' = m\,\delta(\mathbf{x} - \mathbf{x_s})\,, \tag{3.55}$$

where $k_0 = \omega/c_0$ is the wavenumber and $m$ represents the amplitude of the monopole source, given by Eq. (3.53). Assuming the solution to vanish at infinity and to respect causality, Eq. (3.55) solved for two-dimensional problems yields to the pressure fluctuation of a radiating monopole in a quiescent medium, expressed as:

$$p'_{\text{anal}}(\mathbf{x}) = m\,\frac{\mathrm{j}}{4} H_0^{(2)}\left(k_0 R\right), \text{ with } R = \sqrt{(x_1^2 + x_2^2)} \tag{3.56}$$

in terms of Cartesian coordinates $(x_1, x_2)$ with the adopted convention $\exp(+\mathrm{j}\omega t)$. The function $H_n^{(2)}(x) = J_n(x) - \mathrm{j}Y_n(x)$ is the Hankel function of order $n$, defined from the $n$-th order ordinary Bessel function of the 1$^{\text{st}}$ kind, $J_n$, and of the 2$^{\text{nd}}$ kind, $Y_n$. This solution is plotted in Fig. 3.3b. Similarly, the solution for a dipole source can be derived as

$$p'_{\text{anal}}(\mathbf{x}) = -\frac{k_0^2}{4Rc_0}\left(H_1^{(2)}\left(k_0 R\right) d_i x_i\right). \tag{3.57}$$

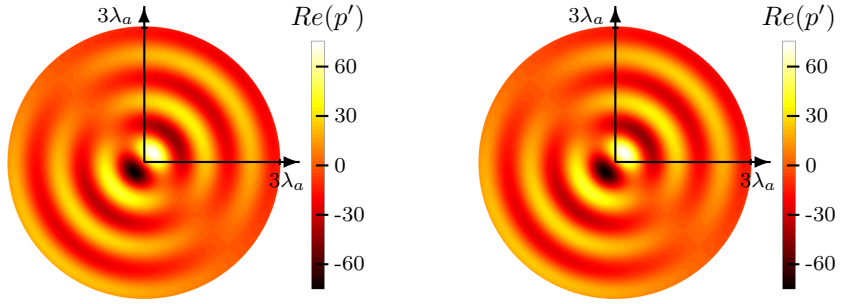


(a) Numerical solution (b) Analytical solution

Figure 3.4. Dipole source in free field in the absence of flow: numerical solution obtained with $p = 5$ and amplitude $\mathbf{d} = \omega/(\mathrm{j}\gamma)\,(1,1)$. Nodal error from analytical solution $\epsilon_d = 6.04\,\%$.

In Figs. 3.3 and 3.4, the nodal error $\epsilon_m$ for the representation of the point sources is given as

$$\epsilon_m = \frac{\|p' - p'_{\text{anal}}\|}{\|p'_{\text{anal}}\|}\,, \tag{3.58}$$

where $\|\bullet\|$ represents the Euclidean norm and $p'_{\text{anal}}$ is the reference pressure solution. The numerical resolution of the presented cases is characterized by a number of DOFs per wavelength $d_\lambda \equiv \lambda_a p/h \approx 17$, obtained for the chosen mesh size $h = 0.33\lambda_a$.

The previous formulations of an acoustic interior source will be further applied in the validation case discussed in Section 3.4.1. However, for perforate applications and two-port characterization methods, exciting the system via the domain's boundaries was found more convenient and will prevail over inner source definition.

To conclude this section on the implementation of interior source terms for the frequency domain LNSE solver, note that it is also possible to model interior entropy sources by introducing a volumetric source term $Q'_V(\mathbf{x},\omega)$ in the linearized energy equation. The source term $\mathbf{S}$ in this case takes the form

$$\mathbf{S} = (\gamma - 1)\begin{bmatrix} 0 \\ 0 \\ 0 \\ Q'_V(\mathbf{x},\omega) \end{bmatrix}. \tag{3.59}$$

The difficulty lies in obtaining accurate transfer functions to describe correctly the spatial variation and the frequency dependence of the source $Q'_V(\mathbf{x},\omega)$ for particular applications. An example can be found in [301] for the representation of a "hot-spot" in a so-called Entropy Wave Generator [22]. An approximation

of the heat source $Q'_V(\mathbf{x}, \omega)$ is then given, valid in a quasi-one dimensional mean flow in the absence of gradients.

### 3.2.2 Runge-Kutta Discontinuous Galerkin LNS solver in time domain

In time domain, the numerical approach followed to solve acoustic problems with the LNSE operator $\mathcal{L}_{\mathrm{LNSE}}$ is based on a Runge-Kutta Discontinuous Galerkin scheme.

#### Existing code and own contributions

The solver was originally developed by Reymen [242] for the linearized Euler equations, based on the work of Hesthaven and Warburton [138, 139]. A quadrature-free DG formulation is used, resulting in a computationally efficient numerical scheme. This initial work also includes the development of a time-domain impedance formulation based on recursive convolution. Later, the solver was improved by Toulorge [293]. Optimized Runge-Kutta schemes, delivering the minimal computational cost for a given error tolerance, were investigated. A curved boundary treatment, with local quadratic elements, was also added to the solver. This mixed approach offers an optimal compromise between the computational efficiency of the quadrature-free formulation for the linear elements and the geometrical accuracy of the second-order elements near curved walls. Concerning the physics, the LEE were extended to the homentropic and isentropic versions of the LNS equations by adding the viscous term in the momentum equation. A latest major improvement in the numerical efficiency of the acoustic DG solver was reached by its parallelization [83] via Message Passing Interface (MPI). Using the discontinuous character of the spatial discretization, the linear matrix system can be solved simultaneously for different partitions of the domain. The inter-element coupling between elements of different partitions is achieved via the Riemann fluxes received from MPI processes.

Considering the maturity of the RKDG solver and the numerous existing references [242, 293] about the implementation details, this section will focus solely on the specificities of the RKDG scheme applied to the complete LNS equations. In the present work, the existing solver has been only extended to include visco-thermal effects inside the energy equation (see Eq. (3.9c)). Additional boundary conditions, as summarized in Table 3.2, have been further implemented. The presence of the visco-thermal terms in the energy equation also requires the computation of extra mean flow quantities, namely the second spatial derivatives of the mean flow velocity field. These terms have been added to the numerical scheme.

Throughout this dissertation, the time integration is done using an 8 stage 4th-order Runge-Kutta scheme, optimized for the spatial discontinuous Galerkin operator [295]. For the spatial discretization, the Discontinuous Galerkin scheme is applied on an unstructured triangular mesh in 2-D, and tetrahedral mesh in 3-D. No contribution from the author was done on this core of the code.

### Runge-Kutta Discontinuous Galerkin for the LNS equations

Similarly to the continuous FEM method discussed in Section 3.2.1, a high-order polynomial approximation of the field variables $\mathbf{q}$ is used on each element. The physics of wave propagation, and hereby the continuity of the field variables through the numerical domain, is accounted for by solving the (approximate) Riemann problems that arise from the discontinuous representation of the solution at element interface. For each element $\Omega$ of the partitioning of the computational domain, a basis $\mathcal{B}_p^\Omega = \left\{\phi_j^\Omega, j = 1 \dots N_p\right\}$ of $\mathcal{P}_p(\Omega)$, the space of polynomial functions of degree at most $p$ on $\Omega$, is defined. An approximation of the variable $q$ on $\Omega$ is then obtained by a projection on this basis:

$$q^\Omega(\mathbf{x}, t) = \sum_{j=1}^{N_p} q_j^\Omega(t)\phi_j^\Omega(\mathbf{x})\,. \tag{3.60}$$

The basis functions $\phi_j^\Omega$ defining $\mathcal{B}_p^\Omega$ are chosen here as Lagrange polynomials of order $p$ [138]. In practice, the element matrices are computed in a polynomial basis that is orthogonal and analytically integrable on a chosen reference element $\Omega_{\text{ref}}$, and transformed back to the nodal basis $\mathcal{B}_p^\Omega$ through Vandermonde matrices based on the interpolation properties of Lagrange polynomials. The choice of nodal sets is critical to assure the quality of the interpolation, which affects the conditioning of the mass matrix $\mathbf{M}^\mathbf{\Omega}$ of the problem. Therefore, specially optimized nodal sets are used for the triangular [136] and tetrahedral elements [137]. For simplex elements, the number of nodes $N_p$ constituting these nodal sets is given by

$$N_p = \frac{\prod_{r=1}^{\dim}(p+r)}{d!}\,, \tag{3.61}$$

where dim is the dimension of the problem.

The presence of the visco-thermal terms in the LNSE leads to second-order spatial derivatives of the unknown perturbation $\mathbf{q}$, as expressed in Eq. (3.14). This elliptic characteristic of the partial differential equations requires a special formulation to ensure the stability of the DG method. Indeed, the DG operator cannot be directly applied twice in a weak variational formulation using a discontinuous function space without leading to spurious instabilities (see Chapter 7 in [139]). The spatial discretization of the visco-thermal terms is constructed here by resorting to a mixed Finite Element formulation.

Both unknown variables and their gradients are approximated in the same discontinuous function space. This formulation, commonly named "BR-1", was originally developed by Bassi and Rebay [24]. This formulation appends the spatial derivatives of the vector of unknowns $\mathbf{q} = \{\rho', \rho_0 \mathbf{u}', p'\}^T$ as separate auxiliary variables to the system of equations. Equation (3.14) is therefore reformulated as the following coupled system for the unknowns $\mathbf{q}$ and $\mathbf{q_d}$:

$$\frac{\partial \mathbf{q}}{\partial t} + \frac{\partial \mathbf{A}_i \mathbf{q}}{\partial x_i} + \frac{\partial \mathbf{F^v}_i}{\partial x_i} + \mathbf{C}\mathbf{q} = \mathbf{S} \tag{3.62a}$$

$$\mathbf{q}_\mathbf{d}^i - \frac{\partial \mathbf{q}}{\partial x_i} = \mathbf{0} \tag{3.62b}$$

where $\mathbf{F^v} = \mathbf{F^v}\left(\mathbf{q}_\mathbf{d}^1, \mathbf{q}_\mathbf{d}^2, \mathbf{q}_\mathbf{d}^3\right)$ is the visco-thermal flux vector, function of the additional unknowns $\mathbf{q}_\mathbf{d}^i$, with $i = 1 \dots 3$. The auxiliary system Eq. (3.62b) gives the derivatives $\mathbf{q}_\mathbf{d}^i$ of the variables $\mathbf{q}$ in the direction $x_i$. Note that compared to the isentropic and homentropic versions of the LNS, for which the auxiliary system can be restrained to the velocity components only, Eq. (3.62b) is solved for the entire vector of unknowns $\mathbf{q}$. Both Eqs. (3.62a) and (3.62b) are discretized with the DG method, using the same polynomial space $\mathcal{P}_p$ for the sake of simplicity, although $\mathbf{q}_\mathbf{d}^i$ is of lower order. The use of an explicit time-stepping scheme allows a decoupled solution of Eq. (3.62). Primary and auxiliary systems are solved sequentially at each time step. First, Eq. (3.62b) is solved. The latter can be reformulated, in a semi-discrete form, for an element $\Omega$ consisting of $N_\Gamma$ faces as:

$$\mathbf{M}^{\mathbf{\Omega}}\, \mathbf{q}_\mathbf{d}^{\mathbf{\Omega}} + \sum_{r=1}^{d} \mathbf{K}_r^{\mathbf{\Omega}}\, \mathbf{f_s}^{\mathbf{\Omega}}{}_r - \sum_{i=1}^{N_\Gamma} \mathbf{M}^{\mathbf{\Gamma}_i} \widehat{\mathbf{f}}_\mathbf{s}^{\,\mathbf{\Gamma}_i} = \mathbf{0}\,, \tag{3.63}$$

in a Cartesian coordinate of dimension $d$, where $\mathbf{q}_\mathbf{d}^{\mathbf{\Omega}}$, $\mathbf{f_s}^{\mathbf{\Omega}}{}_r$, and $\widehat{\mathbf{f}}_\mathbf{s}^{\,\mathbf{\Gamma}_i}$ are vectors collecting the first spatial derivatives of the unknown variables on $\Omega$, the secondary flux Jacobian $\mathbf{f_s}^{\mathbf{\Omega}} = \mathbf{q}^{\mathbf{\Omega}}$, and Riemann approximated boundary flux. This latter is computed by using a central numerical flux, which reads:

$$\widehat{\mathbf{f}}_\mathbf{s}^{\,\mathbf{\Gamma}_i} = \frac{1}{2}\left(\mathbf{f_s}^{\mathbf{\Omega}^-} + \mathbf{f_s}^{\mathbf{\Omega}^+}\right) \cdot \mathbf{n}\,, \tag{3.64}$$

depending on the flux $\mathbf{f_s}$, computed on elements $\Omega^-$ and $\Omega^+$ that locally share $\Gamma_i$. The element mass matrix $\mathbf{M}^{\mathbf{\Omega}}$, the element stiffness matrices $\mathbf{K}_r^{\mathbf{\Omega}}$ and the face matrices $\mathbf{M}^{\mathbf{\Gamma}}$ are given by:

$$(\mathbf{M}^{\mathbf{\Omega}})_{lm} = \int_\Omega \phi_l^\Omega \phi_m^\Omega \,\mathrm{d}\mathbf{x}\,, \qquad (\mathbf{K}_r^{\mathbf{\Omega}})_{lm} = \int_\Omega \frac{\partial \phi_l^\Omega}{\partial x_r} \phi_m^\Omega \,\mathrm{d}\mathbf{x}\,,$$
$$\text{and } (\mathbf{M}^{\mathbf{\Gamma}_i})_{lm} = \int_{\Gamma_i} \phi_l^\Omega \phi_m^\Omega \,\mathrm{d}\mathbf{x}\,. \tag{3.65}$$

Once the variables $\mathbf{q}_{\mathbf{d}}^{i}$ are known, they are used to compute the viscous flux $\mathbf{F}^{\mathbf{v}}$, which is integrated by parts like its convective (inviscid) counterpart $\mathbf{F}_r = \mathbf{A}_r\mathbf{q}$. Equation (3.62a) results to the semi-discrete formulation:

$$\mathbf{M}^{\mathbf{\Omega}}\frac{\partial \mathbf{q}^{\mathbf{\Omega}}}{\partial t} - \sum_{r=1}^{d}\mathbf{K}_r^{\mathbf{\Omega}}\left(\mathbf{A}_r^{\mathbf{\Omega}}\mathbf{q}^{\mathbf{\Omega}} + \mathbf{F}^{\mathbf{v}\mathbf{\Omega}}{}_r\right) + \sum_{i=1}^{N_\Gamma}\mathbf{M}^{\mathbf{\Gamma}_i}\left(\widehat{\mathbf{f}}^{\mathbf{\Gamma}_i} + \widehat{\mathbf{f}}^{\mathbf{v}\mathbf{\Gamma}_i}\right) + \mathbf{M}^{\mathbf{\Omega}}\mathbf{C}^{\mathbf{\Omega}}\mathbf{q}^{\mathbf{\Omega}} = \mathbf{M}^{\mathbf{\Omega}}\mathbf{S}^{\mathbf{\Omega}}\,, \tag{3.66}$$

where $\mathbf{q}^{\mathbf{\Omega}}$ and $\mathbf{S}^{\mathbf{\Omega}}$ are the unknown quantities and source matrices on the element $\Omega$, respectively. The matrix $\widehat{\mathbf{f}}^{\mathbf{\Gamma}_i}$ denotes the primary inviscid flux computed on the element face $\Gamma_i$, whereas $\widehat{\mathbf{f}}^{\mathbf{v}\mathbf{\Gamma}_i}$ represents the visco-thermal fluxes. As they are the most widely used to solve linear PDEs, the Lax-Friedrichs and upwind fluxes are applied to determine the inviscid flux contribution $\widehat{\mathbf{f}}^{\mathbf{\Gamma}_i}$. The approximation of this numerical flux on the face $\Gamma_i$, common to the element $\Omega^-$ and its neighbor $\Omega^+$, is expressed for the Lax-Friedrichs flux as:

$$\widehat{\mathbf{f}}_{\mathrm{LF}}^{\mathbf{\Gamma}_i} = \frac{1}{2}\left[\left(\mathbf{A}^{\mathbf{\Omega}}\cdot\mathbf{n}^{\mathbf{\Gamma}_i}\right)\left(\mathbf{q}^{\mathbf{\Omega}^-} + \mathbf{q}^{\mathbf{\Omega}^+}\right) - ||\mathbf{A}^{\mathbf{\Omega}}||\left(\mathbf{q}^{\mathbf{\Omega}^+} - \mathbf{q}^{\mathbf{\Omega}^-}\right)\right], \tag{3.67}$$

where $\mathbf{A}^{\mathbf{\Omega}} = \mathbf{A}_r^{\mathbf{\Omega}}\mathbf{r}$ and $\mathbf{n}^{\Gamma_i}$ is the outgoing unit normal to the element face $\Gamma_i$ of $\Omega^-$. The term $||\mathbf{A}^{\mathbf{\Omega}}||$ stands for the largest characteristic velocity found in the eigen-decomposition of the Jacobian flux matrix $n_i\mathbf{A}_{\mathbf{i}}^{\mathbf{\Omega}}$. The Lax-Friedrichs flux corresponds, thus, to the average flux corrected by a upwind term function of the jump of the quantities over the interface. In the case of the upwind flux formulation, the inviscid flux is given by:

$$\widehat{\mathbf{f}}_{\mathrm{Upwind}}^{\mathbf{\Gamma}_i} = \begin{cases} \left(\mathbf{A}^{\mathbf{\Omega}}\cdot\mathbf{n}^{\mathbf{\Gamma}_i}\right)\mathbf{q}^{\mathbf{\Omega}^-}\,, & \mathbf{A}^{\mathbf{\Omega}}\cdot\mathbf{n}^{\mathbf{\Gamma}_i} \geq 0\,, \\ \left(\mathbf{A}^{\mathbf{\Omega}}\cdot\mathbf{n}^{\mathbf{\Gamma}_i}\right)\mathbf{q}^{\mathbf{\Omega}^+}\,, & \mathbf{A}^{\mathbf{\Omega}}\cdot\mathbf{n}^{\mathbf{\Gamma}_i} < 0\,. \end{cases} \tag{3.68}$$

The central flux is chosen over the Lax-Friedrichs or upwind fluxes to calculate the visco-thermal contribution $\widehat{\mathbf{f}}^{\mathbf{v}\mathbf{\Gamma}_i}$ on the element boundary, as the diffusive nature of this term does not exhibit any preferred direction, unlike the convective contribution $\widehat{\mathbf{f}}^{\mathbf{\Gamma}_i}$.

### Discussion on the stability of the applied scheme

The scheme used in this work, resulting from the formulation in Eq. (3.62), is conservative and consistent [24]. It has nevertheless some limitations. First, it has been shown to potentially be unstable when applied to purely elliptic problems or when the convective term is negligible with respect to the diffusive term. The "BR-1" method is indeed only weakly stable, due to the absence of any penalty term for both primary and secondary fluxes. This formulation can also lead to unsatisfactory convergence rates for the polynomial approximations of odd order (shown on purely elliptic problems), with a sub-optimal order of

accuracy equal to $\mathcal{O}(h^p)$. Another important issue is that the scheme is not compact. The enlarged stencil of the scheme implies substantial additional cost, both in terms of storage and computational time. This non-compactness is introduced through the jump contribution of the auxiliary variables $\mathbf{d}_{\mathbf{q}}^{\mathbf{\Omega}}$. In this case, the primal unknowns $\mathbf{q}^{\mathbf{\Omega}}$ are coupled not only with the unknowns of the neighboring elements but also with the unknowns associated to the neighbors of the neighbors. Several alternative formulations, which overcome the above mentioned limitations, exist in the literature. Douglas et al. [15] have derived a unified framework of the different approaches which allows the direct comparison of the existing schemes via their primal formulation. Most of these methods are based on the relaxation of the primary and/or auxiliary flux by means of a kind of penalty term. Among the methods that are shown to be simultaneously consistent and stable, one can list the extension of the "BR-1" scheme by Brezzi et al. [49], the so-called "BR-2" method of Bassi et al. [23, 25] and its generalizations called the local discontinuous Galerkin (LDG) methods introduced in [63] and further studied in [61], and numbers of variants classified as Interior Penalty (IP) methods [14, 91, 247, 312]. From these methods, the "BR-2" scheme is the only one that achieves optimal order of accuracy at any order $p \geq 1$ with a compact stencil. The LDG form [63] is not generally compact on unstructured meshes. The stabilization parameter required for the optimal accuracy in the Brezzi et al. [49] scheme can grow very large at higher order $p$. However, the "BR-2" formulation uses complex lift operators, which become very costly in an explicit RKDG framework. The auxiliary system in Eq. (3.63) is replaced in the case of the "BR-2"scheme by a system for the lift operator vector on each face/edge $\Gamma_i$ of each element $\Omega$. Another issue with this more sophisticated formulation is the significant adverse effect of the diffusion on the conditional stability of the method. The viscous CFL condition can severely restrict the maximum time step. Taking this into account, the "BR-1" formulation is considered sufficient for the purpose of this work and the application cases investigated. It was used previously for the study of different neck designs of a Helmholtz resonator with grazing flow, by means of the homentropic version of the RKDG LNS solver [294].

### Mean flow mapping

The RKDG solver disposes of an advanced mapping scheme to transfer the information from a cloud of points in the CFD to the actual acoustic mesh [120, 293]. Following the nodal DG procedure [138], the mean flow variables $\mathbf{q_0} = \{p_0, \rho_0, \mathbf{u_0}, T_0, \mu, \lambda_t\}^T$ are approximated in an element $\Omega$ with a function $\mathbf{q}_{\mathbf{0}}^{\mathbf{\Omega}} \in \mathcal{P}_p(\Omega)$. The direct computation of the components $\mathbf{q}_{\mathbf{0}}^{\mathbf{\Omega}}{}_j$ of this polynomial function is to be avoided if mean flow features are under-resolved, as it is likely to cause spurious oscillations of $\mathbf{q}_{\mathbf{0}}^{\mathbf{\Omega}}$ at high order $p$, due to the Runge's phenomenon. In order to alleviate this issue, a least-square approach is used that fits the approximation to the ideal solution. The mean flow data are first

sampled on a dense cloud of points on each element $\Omega$, using the same basis $\mathcal{B}_p^\Omega$ but at a higher order $p'$ (here $p' = p + 4$). A least-square technique is then used to find the polynomial $\mathbf{q_0^\Omega} \in \mathcal{P}_p(\Omega)$ which best approximates the sampled values. The least-square approximation can be solved for each element $\Omega$ individually or in a global manner for all elements simultaneously.

Another technical difficulty arises from the DG representation of the flux terms (in $\mathbf{A}_r^\Omega \mathbf{q}^\Omega$ and $\mathbf{F}^{\mathbf{v}\Omega}$) and mean flow terms (in $\mathbf{C}^\Omega \mathbf{q}^\Omega$). Both the solution $\mathbf{q}^\Omega$ and the mean flow variables $\mathbf{q_0^\Omega}$ are given in $\mathcal{P}_p(\Omega)$. Therefore, the corresponding flux terms are of order $2p$. This implies an interpolation of a polynomial of degree $2p$ by a polynomial of degree $p$, which is prone to cause aliasing errors: the modes of order higher than $p$ are transformed into spurious contributions to modes of order lower than $p$ by the interpolation. For this reason, an additional anti-aliasing modal filter [120, 138] is applied to the DG discretization, to damp the higher-order modes and avoid aliasing instabilities.

Concerning the particular case of the LNS operator $\mathcal{L}_{\text{LNSE}}$, the presence of the viscous terms in the energy equations requires to compute the second spatial derivatives of the mean flow velocity field, due to the terms $\partial \tau_{0\,ij}/\partial x_i$ and $\partial \tau_{0\,ij}/\partial x_j$ included in the matrix $\mathbf{C}$ shown in Eq. (3.62a). The second derivatives of the shape functions $\phi^\Omega_{j\in\{1\dots N_p\}}$ have thus been added. The expressions of these basis functions, as well as their first and second derivatives, are given in Appendix C for the case of triangular elements.

### Boundary conditions and sources in DG

The characteristic boundary conditions are applied to treat the truncation of the numerical domain. Similarly to the use of the method of the characteristics for the frequency solver, detailed within "Boundary conditions" of Section 3.2.1, the numerical Riemann flux on the boundary $\Gamma_i$ of the element $\Omega$ can be expressed, by reformulating the upwind flux on each characteristic variable, as

$$\widehat{\mathbf{f}}^{\mathbf{\Gamma}_i} = \mathbf{W}\left(\mathbf{\Lambda}^+ \mathbf{W}^{-1} \mathbf{q}^{\mathbf{\Omega}} + \mathbf{\Lambda}^- \mathbf{W}^{-1} \mathbf{q}^{\mathbf{\Omega}'}\right), \tag{3.69}$$

where $\Omega'$ is the element sharing the face $\Gamma_i$ with $\Omega$, and $\mathbf{\Lambda}^+$ and $\mathbf{\Lambda}^-$ are the positive and negative parts of $\mathbf{\Lambda}$, respectively. At a boundary of the computation domain, substituting $\mathbf{q}^{\mathbf{\Omega}'} = \mathbf{q}^{\mathbf{\Omega}}_{\mathbf{BC}}$ can be used to introduce an excitation in the domain through the boundary. If the boundary is meant to be passively absorbing, then $\mathbf{q}^{\mathbf{\Omega}}_{\mathbf{BC}} = 0$ is chosen, and only the outgoing characteristics contribute to the numerical flux. Additionally, the same formalism as described in Eq. (3.38), with usage of the reflection matrix, is also used to enforce general boundary conditions, such as prescribed velocity or pressure type of boundaries.

To take advantage of the time-domain simulations, it is interesting to consider a broadband excitation of the numerical domain, contrary to the frequency domain

that was restrained to mono-frequency computations. Such an excitation can be achieved via a specific definition of the initial condition for the perturbation fields. For the case of aeroacoustic applications in confined environment, like for duct and channel acoustic, a plane Gaussian pulse is defined as:

$$\mathbf{q}(\mathbf{x}, t=0) = \exp\left[-\frac{\log(2)}{w_p^2}\left(x_i - x_{si}\right)^2\right]\begin{bmatrix}\rho_{\text{init}}\\ \mathbf{x}_{\text{init}}\\ p_{\text{init}}\end{bmatrix} \tag{3.70}$$

for a pulse in the direction $x_i$, at the location $x_{si}$ on this axis and of width $w_p$. The values $\{\rho_{\text{init}}, \mathbf{x}_{\text{init}}, p_{\text{init}}\}$ refer to the amplitude chosen for the pulse. A low-pass filtered Gaussian pulse can also be used for cases where a broadband excitation is only needed at low frequencies, for example below a defined frequency, like the cut-off frequency of a duct.

### 3.2.3 Overall comparison of the two solvers

Both frequency- and time-domain approaches used in this work to solve aeroacoustic problems by means of the linearized Navier-Stokes equations have been detailed in the previous sections, Section 3.2.1 and Section 3.2.2. For the purpose of characterizing perforated silencers and orifices, both high-order $p$-FEM and RKDG approaches exhibit advantages and drawbacks [12]. Those are listed here and will be further specified in Section 3.3 and Chapter 4 for perforate applications.

By concept, the frequency-domain approach is particularly suitable for tonal noise aeroacoustic problems since only a single frequency or a few frequencies have to be solved for. Frequency-based computations are often considered a way to avoid linear instability waves, which are supported by the set of LNS equations. These convective instabilities can completely overwhelm the acoustic solution by unbounded growth in time-domain problems. Examples are shear layer instabilities, the well-known Kelvin–Helmholtz instabilities, which can be suppressed by assuming time-harmonic responses in the frequency domain [6]. The major downside of the frequency-domain solutions comes with the necessity of solving global system matrices which involves large memory requirement. This issue increases rapidly with the problem size, the frequency and the number of variables to solve. This drawback is particularly present for problems requiring to resolve small scale physics with use of the LNS operator (five variables in a 3-D problem), as the spatial discretization involves very small FEM elements. The high-order FEM approach, using large elements everywhere, cannot be used to its full extent due to the spatial refinement required.

The time-domain approach allows to compute broadband sound in a single simulation. One main advantage over frequency-domain computation is the relative low memory requirements resulting from an explicit time-stepping

scheme. For large problems (e.g. three-dimensional, high frequencies) time-domain simulations were found to be more efficient than their frequency-domain counterparts [57, 128]. In the case of the RKDG method, the coupling between elements is realized through a numerical flux formulation. This weak coupling ensures efficient parallel computation capabilities, although the discontinuity at element boundaries implies additional degrees of freedom. Working in the time domain further permits to treat transient acoustic problems [63], to account for unsteady aerodynamic source terms [21, 28], and can even be extended to deal with non-linear acoustics [139]. A particular drawback for the use of the LNSE RKDG solver appears when trying to capture the physics at the wall boundaries. The presence of locally refined mesh elements, to resolve the visco-thermal boundary layers, forces the effective time step to be drastically smaller to respect the CFL conditions. It results in vastly increasing the computational effort over the whole domain. One method to cope with this problem would be to use locally varying time steps over the domain [138, 204, 217, 299].

## 3.3 Analysis of the dissipation mechanisms from LNS simulations

A particular advantage of using numerical methods to investigate the acoustic behavior of perforates, here by means of linearized Navier-Stokes equations solvers, is the ability to gain information on the continuous variable fields over the complete domain. It allows a thorough investigation of the different physical mechanisms participating in the dissipation of acoustic waves, which would not be possible from a global characterization based on pressure measurements performed at a limited number of monitoring points, as described in Section 2.2.1. This is done here on the basis of:

- a global integral energy balance performed on the complete computational domain or a subset of it. This corresponds to a generalization of the concept of acoustic energy for any perturbation in a steady flow based on the expansion of the flow energy conservation equation derived by Myers [222].
- the perturbed transport equations for vorticity and entropy in order to visualize the spatial contribution of the different mechanisms involved in the transfer of energy between the disturbance modes.

The theory of these two approaches to better understand and quantify the interaction of acoustic, vorticity and entropy modes is presented in this section. They have been implemented for the continuous high-order FEM solver of the non-isentropic LNS equations. Applications and results for the case of perforated structures in their linear regime will be presented in Chapter 4.

### 3.3.1 Integral energy balance

Myers [222] derived an exact equation for the transport of energy associated with disturbance in an arbitrary steady flow. The generalized formulation of this corollary is obtained by perturbation expansion of the energy conservation equation of the fluid. The latter is valid for an unsteady disturbance at any order of magnitude. Considering only first order perturbations, it yields to the following expression for the energy of the perturbed field:

$$\frac{\partial \mathcal{E}'}{\partial t} + \frac{\partial \mathcal{W}'_i}{\partial x_i} = \mathcal{D}' \,, \tag{3.71}$$

where $\mathcal{E}'$ defines the first-order disturbance energy density, $\mathcal{W}'$ is the first-order energy flux vector, and $\mathcal{D}'$ represents the source/sink term for the first-order energy. $\mathcal{D}'$ describes the volumetric rate at which the first-order disturbance energy is being dissipated. This equation, which contains only first-order perturbation quantities, is a complete and consistent representation of the principle of total fluid energy conservation at order $\delta^2$. The disturbance energy density $\mathcal{E}'$ is further given by:

$$\mathcal{E}' = \frac{p'^2}{2\rho_0 c_0^2} + \frac{1}{2}\rho_0 \mathbf{u}'^2 + \rho' \mathbf{u_0} \cdot \mathbf{u}' + \frac{\rho_0 T_0 s'^2}{2C_p} \,. \tag{3.72}$$

The disturbance energy density of Eq. (3.72) includes the usual potential energy per unit volume resulting from reversible elastic compression, i.e. $p'^2/(2\rho_0 c_0^2)$. The second term of $\mathcal{E}'$ can be related to the disturbance kinetic energy per unit volume, whereas the last contribution, proportional to the square of the first-order entropy fluctuation, is mostly important for perturbations primarily related to heat conduction, like the one originating from so-called hot spots. This is discussed in Pierce [230]. The source terms $\mathcal{D}'$ can be expressed as the sum of the contributions of each of the physical mechanisms involved in the growth/decrease of the perturbed energy inside the control volume. One distinguishes here between mechanisms related to the vorticity $\mathcal{D}'_v$, entropy $\mathcal{D}'_s$, viscous diffusion $\mathcal{D}'_\mu$, internal heat source $\mathcal{D}'_q$, and thermal diffusion $\mathcal{D}'_t$. These terms can be expressed as:

$$\begin{cases} \mathcal{D}'_v = \rho_0 \mathbf{u_0} \cdot (\mathbf{\Omega}' \times \mathbf{u}') + \rho' \mathbf{u}' \cdot (\mathbf{\Omega_0} \times \mathbf{u_0}) \,, \\ \mathcal{D}'_s = -s' \mathbf{m}' \cdot \boldsymbol{\nabla} T_0 + s' \rho_0 \mathbf{u_0} \cdot \boldsymbol{\nabla} T' \,, \\ \mathcal{D}'_\mu = -\left(\dfrac{\tau_{ij}}{\rho}\right)' \dfrac{\partial m'_j}{\partial x_i} + m'_j \left(\dfrac{\tau_{ij}}{\rho^2} \dfrac{\partial \rho}{\partial x_i}\right)' \,, \\ \mathcal{D}'_q = \dfrac{T'}{T_0} \left(Q'_V - T' Q_{V0}\right) , \\ \mathcal{D}'_t = \left(\dfrac{-\lambda_t \boldsymbol{\nabla} T}{T}\right)' \cdot \boldsymbol{\nabla} T' - T' \left(\dfrac{-\lambda_t \boldsymbol{\nabla} T \cdot \boldsymbol{\nabla} T}{T^2}\right)' \,, \end{cases} \tag{3.73}$$

where $m' = (\rho_0 \mathbf{u}' + \rho' \mathbf{u_o})$ is the mass flux vector perturbation and $\mathbf{\Omega}$ the vorticity $\nabla \times \mathbf{u}$. The component in the $i$-direction of the first-order disturbance energy flux vector $\mathcal{W}'$ is defined as:

$$\begin{aligned} \mathcal{W}'_i = \; & m'_i \left(\frac{p'}{p_0} + \mathbf{u_0} \cdot \mathbf{u}'\right) - m'_j \left(\frac{\tau_{ij}}{\rho}\right)' + \rho_0 u_{0i} T' s' + \\ & \frac{T'}{T_0} \left(-\lambda_t \frac{\partial T'}{\partial x_i} + \frac{\lambda_t}{T_0} \frac{\partial T_0}{\partial x_i} T'\right) . \end{aligned} \tag{3.74}$$

The first term of the right-hand side in Eq. (3.74) corresponds to the perturbed acoustic energy flux, whereas the second gives the viscous stress power and the two last ones represent entropy and thermal effects. The complexity of the expression of some terms in Eq. (3.73) and Eq. (3.74) tends to preclude a stricter physical interpretation of each separate term.

Similarly to [302], but accounting here for the visco-thermal losses, the time-average of the perturbed energy equation defined in Eq. (3.71) is integrated over the volume $V$ with surface $S$ and unity normal vector $\mathbf{n}$ to describe the overall energy balance. It gives:

$$\begin{gathered} \int_V \overline{\frac{\partial \mathcal{E}'}{\partial t}} \, \mathrm{d}V + \int_S \overline{\mathcal{W}'} \cdot \mathbf{n} \, \mathrm{d}S = \int_V \overline{\mathcal{D}'} \, \mathrm{d}V \\ \Leftrightarrow \\ \mathbb{E}' + \mathbb{W}' = \mathbb{D}' \,. \end{gathered} \tag{3.75}$$

The first term on the left is the time rate of change of disturbance energy in the control volume. The second term represents the net rate at which the energy is flowing through the control volume's surface. The term on the right hand side of Eq. (3.75) is the dissipation rate of the energy caused by hydrodynamic and entropy interactions, as well as visco-thermal diffusion. The

integral terms in the energy balance are here referred to as $\mathbb{E}'$, $\mathbb{W}'$, and $\mathbb{D}'$. In Section 4.2, the integration volume $V$ will represent either the complete numerical domain or an arbitrary subset of it. The integrals defined in Eq. (3.75) are computed numerically in a post-processing step after solving the initial problem described in Eq. (3.9) and Eq. (3.13). The same order of polynomial basis as the initial problem is taken to compute the energy balance. The same subscript conventions are kept for the source/sink integral terms $\mathbb{D}'_\bullet$ to distinguish between the different types of dissipation mechanisms.

### 3.3.2 Perturbed transport equation for vorticity and entropy

The perturbed transport equations for vorticity and entropy can be used to interpret, localize, and visualize the contribution of the distinct mechanisms involved in the transfer of energy between the disturbance modes.

By taking the curl of the momentum equation of the complete Navier-Stokes equations (see Eq. (3.1b)), a vector equation for the flow vorticity can be written [198], using the fact that $\boldsymbol{\nabla}\cdot\boldsymbol{\Omega}=0$ and $\nabla\times(\boldsymbol{\Omega}\times\mathbf{u})=(\boldsymbol{\nabla}\cdot\mathbf{u}+\mathbf{u}\cdot\nabla)\boldsymbol{\Omega}-(\boldsymbol{\Omega}\cdot\nabla)\mathbf{u}$. Applying again an expansion of the variables and limiting the contribution to the first order, one can derive the following expression for the vorticity perturbation $\boldsymbol{\Omega}'$:

$$\begin{aligned}\frac{\mathrm{D}_0\boldsymbol{\Omega}'}{\mathrm{D}t} = &-\underbrace{\mathbf{u}'\cdot\boldsymbol{\nabla}\boldsymbol{\Omega}_\mathbf{0}}_{I}+\underbrace{\boldsymbol{\Omega}_\mathbf{0}\cdot\boldsymbol{\nabla}\mathbf{u}'}_{II}+\underbrace{\boldsymbol{\Omega}'\cdot\boldsymbol{\nabla}\mathbf{u}_\mathbf{0}}_{III}-\underbrace{\boldsymbol{\Omega}_\mathbf{0}\boldsymbol{\nabla}\cdot\mathbf{u}'}_{IV}-\underbrace{\boldsymbol{\Omega}'\boldsymbol{\nabla}\cdot\mathbf{u}_\mathbf{0}}_{V}\\ &+\underbrace{\frac{\boldsymbol{\nabla}\rho'\times\boldsymbol{\nabla}p_0}{\rho_0^2}}_{VI}+\underbrace{\frac{\boldsymbol{\nabla}\rho_0\times\boldsymbol{\nabla}p'}{\rho_0^2}}_{VII}-\underbrace{2\frac{\rho'}{\rho_0^3}\left(\boldsymbol{\nabla}\rho_0\times\boldsymbol{\nabla}p_0\right)}_{VIII}+\underbrace{\nu\nabla^2\boldsymbol{\Omega}'}_{IX}\,.\end{aligned} \tag{3.76}$$

The left-hand side of Eq. (3.76) describes the time rate of change in vorticity of a fixed fluid element, with the material derivative operator $\mathrm{D}_0\bullet/\mathrm{D}t=\partial\bullet/\partial t+\mathbf{u_0}\cdot\boldsymbol{\nabla}\bullet$. The terms $\boldsymbol{I}$ to $\boldsymbol{IX}$ on the right-hand side of this equation represent therefore vorticity source or sink terms. The vorticity disturbance can be triggered or influenced by diverse physical phenomena:

- Terms $\boldsymbol{I}$, $\boldsymbol{II}$, and $\boldsymbol{IV}$: Vorticity waves can arise from acoustic or vortical perturbation modes propagating in a rotational mean flow, i.e. for which $\boldsymbol{\Omega_0}\neq\mathbf{0}$. This is the case for example for sheared flows and boundary layers at wall vicinity.
- Term $\boldsymbol{III}$: The presence of velocity gradients in the mean flow, $\boldsymbol{\nabla}\mathbf{u_0}\neq\mathbf{0}$ can lead to both stretching and bending of the vortex perturbation tubes.
- Term $\boldsymbol{V}$: Mean flow dilatation or compressibility effects can impact the vorticity perturbations. Term $\boldsymbol{V}$ is therefore only non-zero for compressible

flows. An expansion of the cross-sectional area of a vortex structure, corresponding to an effective positive dilatation, results in a reduction of the vorticity perturbation. This occurs for example when vorticity disturbances get damped as they propagate through a so called "hot spot" or a flame in the context of thermo-acoustic problems.

- Term ***VI***, ***VII***, and ***VIII***: Vorticity can be produced via baroclinic mechanisms due to acoustic (term ***VII***) and entropy waves (terms ***VI*** and ***VIII***). This appears when the density and pressure gradients are misaligned, between the mean flow and the perturbation (terms ***VI*** and ***VII***) or in the mean flow itself (term ***VIII***), and results in torque induction.
- Term ***IX***: This elliptical term, containing the Laplacian of the vorticity perturbation $\nabla^2\boldsymbol{\Omega}'$, represents the loss of energy of the vortical mode towards heat through viscous dissipation.

It is important to note that the right-hand side of Eq. (3.76) covers the actual sources of vorticity perturbation inside a domain (through flow shear, no-slip boundaries or by baroclinic torque) but also the others terms that describe the amplification, stretching, bending, or diffusion of vorticity that already exists in the flow or that has been injected at the boundaries of the domain. Expression (3.76) only disregards the effects of external rotational body forces.

Similarly, a transport equation for the entropy disturbance $s'$ can be obtained from the linearized energy equation Eq. (3.9c):

$$\begin{aligned}\rho_0 T_0 \frac{\mathrm{D}_0 s'}{\mathrm{D}t} = &- \underbrace{\mathbf{u}'\rho_0 T_0 \boldsymbol{\nabla} s_0}_{1} - \underbrace{\mathbf{u_0}\rho' T_0 \boldsymbol{\nabla} s_0}_{2} - \underbrace{\mathbf{u_0}\rho_0 T' \boldsymbol{\nabla} s_0}_{3} \\ &+ \underbrace{2\mu\left[\boldsymbol{\nabla}\mathbf{u_0} : \boldsymbol{\nabla}\mathbf{u}' + \boldsymbol{\nabla}\mathbf{u_0} : \boldsymbol{\nabla}\mathbf{u}'^{T} - \frac{2}{3}(\boldsymbol{\nabla}\cdot\mathbf{u_0})(\boldsymbol{\nabla}\cdot\mathbf{u}')\right]}_{4} \\ &+ \underbrace{\lambda_t \nabla^2 T'}_{5} + \underbrace{Q'_V}_{6} \,.\end{aligned} \tag{3.77}$$

The terms on the right-hand side of Eq. (3.77) represent the different mechanisms involved in the alteration of an entropy wave along its stream path. A physical interpretation of these terms leads to the following interpretation.

- Terms ***1***, ***2***, and ***3***: An entropy disturbance $s'$ propagating through a non-isentropic mean flow, i.e. $\boldsymbol{\nabla} s_0 \neq \mathbf{0}$, is altered due to the interactions of the acoustic and vorticity fluctuations (terms ***1*** and ***2***), as well as the entropy fluctuations (term ***3***), with the mean flow.
- Term ***4***: The viscous dissipation of both acoustic and vortical perturbations leads to an increase in entropy $s'$.

- Term ***5***: Entropy disturbances are subject to diffusion due to heat convection.
- Term ***6***: Finally, entropy waves can arise from the presence of an unsteady volumetric heat source, like in the case of a flame.

Note that the dissipation mechanisms of vorticity and entropy waves are of drastically distinct nature. The diffusion and dissipation of vorticity waves caused by viscous effects act as sources for the entropy waves, whereas the diffusion of entropy waves originates from heat conduction. The latter is, however, of lower importance compared to the dispersion caused by shear flow effects [302]. In the frame of the present linearized Navier-Stokes solvers, it is possible to compute locally these different source/sink terms for the respective vorticity and entropy fluctuations.

## 3.4 Validation cases

A selection of reference cases is presented here, in order to verify the correct implementation of the previously discussed acoustic solvers—predominantly the $p$-FEM one.

### 3.4.1 Monopole source radiating in a plate boundary layer

An example for the acoustic propagation in a strongly non-uniform mean flow situation is considered here with the 2-D sound radiation of a monopole located in the boundary layer of a laminar mean flow. The setup of this case is illustrated in Fig. 3.5. An analytical solution of this problem, using Green's functions, has already been compared to Direct Numerical Simulations of the full Navier-Stokes equations with good agreement [273, 274]. Other numerical works, like the APE-DG solver by Bauer et al. [28] and a wave operator based on Möhring's acoustic analogy, discretized using a discontinuous Galerkin method [94], have also used this test case as verification.

The conditions for the mean flow and acoustic excitation correspond to *Case D* of Ref. [274]. A free-stream Mach Number $\mathrm{M}_\infty = 0.3$ and an acoustic wavelength to mean flow boundary layer thickness ratio equal to $\lambda_a/\delta_{\mathrm{MF}} \approx 1$ are chosen. The mean flow density and pressure are taken as $\rho_0 = 1$ and $p_0 = 1/\gamma$ in order to have a speed of sound $c_0 = 1$. The computational domain is made of a semi-circular mesh of radius $R_0 = 23$, centered at $(x, y) = (0, 0)$. The laminar mean flow profile over the plate $\mathbf{U}_\infty = (u_0, 0)$ is given by a Polhausen velocity profile [273, 274]:

$$u_0(y) = \begin{cases} c_0\mathrm{M}_\infty \left(2y - 2y^3 + y^4\right) & \text{for } 0 \leq y \leq 1 \\ c_0\mathrm{M}_\infty & \text{for } y > 1 \end{cases} , \tag{3.78}$$

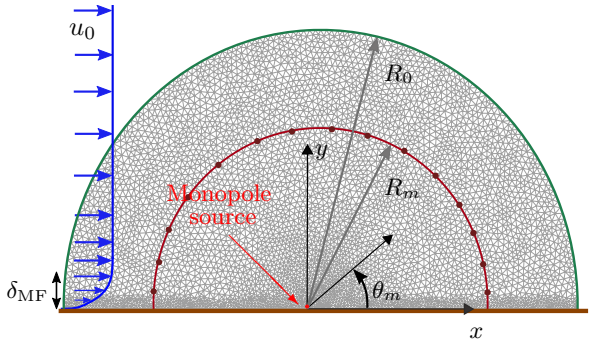


Figure 3.5. Case configuration of a monopole in the boundary layer of a plate.

which gives a boundary layer thickness $\delta_{\mathrm{MF}}$ equal to 1. A slip rigid wall boundary condition is imposed on the lower limit of the domain (i.e. the plate), and the remaining boundary is treated with passive non-reflecting characteristic BC. The monopole source is added inside the flow boundary layer at the location $(x_{\mathrm{s}} = 0, y_{\mathrm{s}} = 0)$. For the frequency domain, the monopole source is expressed as in Eq. (3.52a).

As shown in Fig. 3.6, the presence of the flow has a significant impact on the directivity of the radiated sound from the monopole. Convective effects can be observed through the change in acoustic wavelength $\lambda_a$ between upstream and downstream direction (with $\lambda_{a,\,\mathrm{upstream}} < \lambda_{a,\,\mathrm{downstream}}$). Strong refraction effects are apparent for angles $\theta_m \leq 8°$ with the channeled waves within the downstream boundary layer (sound waves "trapped" near the wall) and the shadow zone upstream $\theta_m \in [155°, 180°]$, clearly visible on Fig. 3.6b.

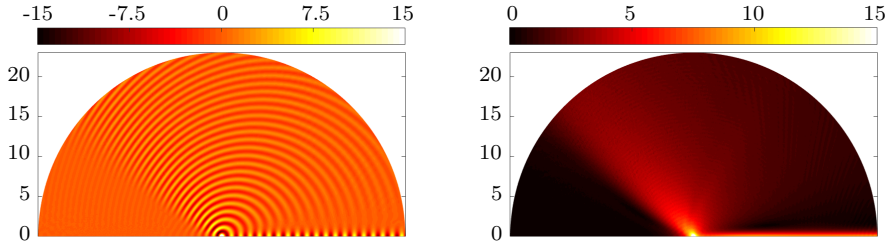


(a) Real part of pressure fluctuation $Re(p')$ [-]

(b) Absolute value of pressure fluctuation $|p'|$ [-]

Figure 3.6. Pressure perturbation field $p'$ obtained with the isentropic LNSE $p$-FEM solver for $p = 7$, $M_\infty = 0.3$, and $f = 1$.

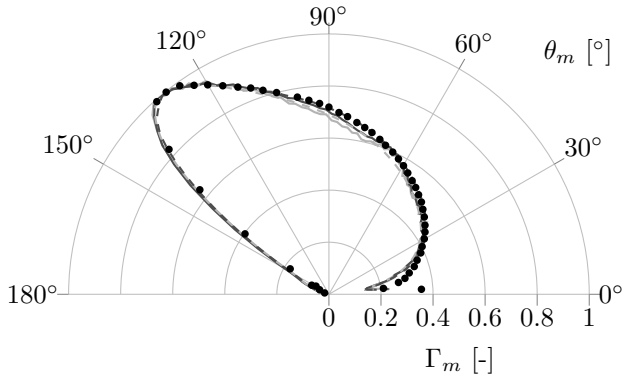


Figure 3.7. Directivities $\Gamma_m(\theta_m)$ of the monopole in boundary layer obtained from the LNSE operator solved with $p$-FEM ( $\mu = 0$ and $\mu = 8 \times 10^{-5}\,\mathrm{Pa \cdot s}$) and RKDG ( $\mu = 0$ and $\mu = 8 \times 10^{-5}\,\mathrm{Pa \cdot s}$) compared to DNS data [274] (●): $p = 7$, $M_\infty = 0.3$, and $f = 1$.

The pressure fluctuation root mean square (RMS) is monitored at 100 points placed on a circle of radius $R_m = 15$, centered on the monopole source. Because the monopole source is modeled differently in the reference DNS and in the present linear acoustic simulations [28, 293], the directivity values $\Gamma_m(\theta_m)$ are normalized with respect to the maximum RMS pressure in the direct radiation zone happening at the angle $\theta_{\max} \approx 129°$, i.e. $\Gamma_m(\theta_m) = p'_{\mathrm{RMS}}(\theta_m)/p'_{\mathrm{RMS}}(\theta_{\max})$.

Figure 3.7 compares directivities calculated by means of the frequency linearized solver to both time-domain LNSE/LEE DG results from [293] and the DNS reference performed by Suzuki and Lele [274]. The grid used is depicted in Fig. 3.5. This mesh is composed of nearly 9600 triangular linear elements, with the smallest dimension $h_{\min} \approx \delta_{\mathrm{MF}}/5$ for the elements located near the wall. The order of the polynomial approximation is set to $p = 7$, similar to [293]. A good agreement of the numerical results can be stated. Figure 3.7 shows that both numerical tools give a good prediction of the pressure field in presence of the non-uniform mean flow profile, both in terms of the peak angle $\theta_{\max} \approx 129°$ and critical angle $\theta_{\mathrm{c}} \approx 155°$ (beyond which there is no direct radiation). Accounting for the viscous effects in the acoustic operator yields results that correlate slightly better with the DNS results for both $p$-FEM and RKDG simulations. Overall the viscosity is found to have a larger impact on the relative weight between channeled waves and direct radiation rather than on the shape of the direct radiation itself. The main observed discrepancies between the LNS results and the DNS reference data concerns the channeled waves and the small angle radiation ($\theta_m \leq 10°$). The modeling differences from the DNS case, with regards to the boundary layer profile and the source representation (DNS source is more localized), are plausible causes of these discrepancies, as

commented in [28, 293].

Overall, given the modeling differences between the present simulations and the DNS, the agreement can be considered as satisfactory and the linear acoustic solvers presented in Section 3.2 are shown capable of correctly predicting sound wave propagation in complex non-uniform flows.

### 3.4.2 Case of a closed-end waveguide of small dimensions

In Section 3.3, it was shown that the perturbation fields in a viscous medium consist of a superposition of three parts: the acoustic mode, the vorticity mode and the entropy mode. When an acoustic wave propagates through a duct or waveguide, the vorticity and entropy mode are present close to the duct walls, i.e. within the boundary layers, and lead to a loss of energy of the acoustic mode. To validate the high-order $p$-FEM and RKDG implementations of the linearized Navier-Stokes equations, as defined in Eq. (3.9), the problem of a small fluid-filled rectangular duct with a closed-end is investigated here.

#### Description of the closed-end waveguide case

This work focuses only on the thermo-viscous terms in the LNS equations and therefore no mean flow will be considered in this section. The dimensions of the considered rigid walled waveguide are chosen according to the work of Bossart [42] for comparison. The waveguide has a length $L_{z,WG}$ of 170 mm and has a squared cross-section of dimensions $L_{x,WG} = L_{y,WG} = 5$ mm. As the emphasis is put on the dissipation process taking place in both viscous and thermal boundary layers, the frequency range for this study has been chosen around the first axial resonance frequency of the waveguide, i.e. [900 Hz - 1050 Hz]. In this frequency range, the transverse dimensions assure that the acoustic field in the waveguide has a plane wave character. Concerning the boundary conditions, the waveguide is defined at one end by a plane piston source, corresponding to a prescribed inlet velocity $\mathbf{V_{in}} = \{0, 0, V_{in}\sin(\omega t)\}^T$, and by a rigid wall at the other end and on the sides (see Fig. 3.8). The inlet velocity condition is obtained by means of the characteristic method and the reflection matrix (see Eq. (3.38)) for both frequency- and time-domain solvers.

The acoustic boundary layer, already defined in Section 2.1.1, has a thickness of characteristic length $\delta_v = \sqrt{2\nu/\omega}$. The characteristic length scale for the thermal boundary layer is $\delta_t = \delta_v/\sqrt{\mathrm{Pr}}$, where Pr is the Prandtl number. The thickness of the thermal boundary layer can be seen [246] as the width of the near-wall region in which the rate of increase of internal energy is just balancing the net rate of heat conduction. In the present case, the waveguide transverse dimensions are significantly greater than the thickness of both these boundary layers, i.e. $\delta_{v/t} \ll L_{x/y,WG}$. Nevertheless, as it will be shown afterwards,

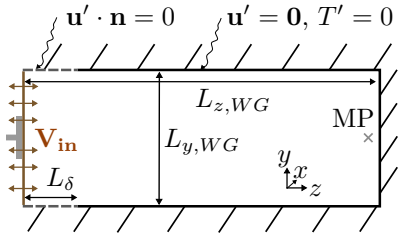


Figure 3.8. Setup of a waveguide excited by a plane piston source for the investigation of visco-thermal effect by means of $\mathcal{L}_{\text{LNSE}}$ in frequency domain.

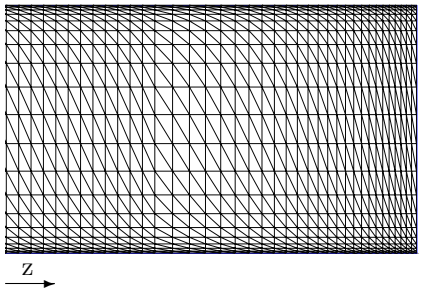


Figure 3.9. Partial view of the numerical mesh, on the side of the closed extremity, constituted in total of 13000 triangular linear elements, used for the two-dimensional linearized Navier-Stokes RKDG simulations on the waveguide case.

the accurate representation of the visco-thermal losses, which requires grid refinement near the walls as illustrated in Fig. 3.9, plays an important role for the estimation of the pressure field inside the waveguide and its resonance frequency.

The amplitude of the pressure fluctuation at the closed end of the duct $p'_{\text{wall}}$ (at the location "MP" in Fig. 3.8) is computed for an inlet velocity $V_{in} = 1\,\text{m/s}$. The numerical results obtained from the linearized Navier-Stokes equations are compared to the analytic solution, expressed as:

$$p'_{\text{wall}}(L_{z,WG}) = \rho_0 c_0 V_{in} \frac{k_0}{k_{00}} \frac{1}{j \sin\left(k_{00} L_{z,WG}\right)}\,, \tag{3.79}$$

where

$$k_{00}^2 = k_0^2 \left[1 + \frac{(1-j)}{\sqrt{k_0}} \frac{2\sqrt{2}}{L_{x,WG}} \left(\sqrt{l'_v} + (\gamma - 1)\sqrt{l'_h}\right)\right]\,, \tag{3.80}$$

in the particular case of a squared cross-section (i.e. $L_{x,WG} = L_{y,WG}$). Equation (3.80) gives the complex wavenumber accounting for the viscous and thermal losses near the wall in a 1-D approximation. The lengths $l'_v$ and $l'_h$ are the characteristic lengths for the viscous and thermal dissipation processes, defined as $l'_v = \mu/(c_0\rho_0)$ and $l'_h = \lambda_t/(c_0\rho_0 C_p)$, respectively [42]. In this example, air at ambient temperature is considered, for which density $\rho_0 = 1.2\,\text{kg} \cdot \text{m}^{-3}$ and speed of sound $c_0 = 343.8\,\text{m/s}$ are chosen.

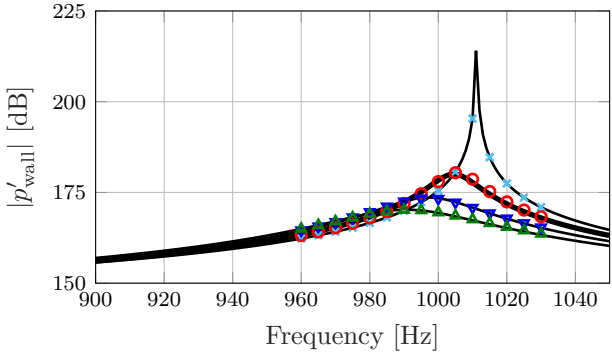


Figure 3.10. Amplitude (dB) of the pressure fluctuation at the backing wall of the 3-D waveguide predicted with the LNS $p$-FEM compared to analytic solution (—): no losses (×), thermal losses only (○), viscous losses only (▽), visco-thermal losses (△).

### Results in frequency domain

Figure 3.10 shows a very good agreement of the numerical results for the pressure fluctuation $p'_{\text{wall}}$ inside the three-dimensional waveguide with the theoretical solution (see Eq. (3.79)). The resonance phenomenon, taking the different losses into account, is captured correctly in terms of both resonance frequency and damping attenuation of the acoustic field, i.e. peak amplitudes. Thermal dissipation effects at the boundary layer appear to be of lesser importance than viscous dissipation under the chosen conditions.

The strategy for the accurate resolution of the boundary layers, in the frame of the frequency domain $p$-FEM LNS solver, is further investigated with the present test case. It is found that only increasing the order $p$ of the interpolation function for the field variables is not enough to achieve a good resolution of the boundary layers if the first element near the wall has a dimension $h \gg \delta_{v/t}$. This element should have about the size of the smallest boundary layer, which is the viscous one in air, i.e. $h \approx \delta_v$. The use of much larger element sizes leads to an over-prediction of the boundary layers thickness and, therefore, to an overshoot of the acoustic dissipation. Figure 3.11 shows the improvement in the representation of the viscous boundary layer with increasing interpolation order $p$, once the aforementioned criterion is met. The velocity $u'_z$ is shown normalized by the axial velocity at the duct centerline $u'_{z,\text{c}}$ obtained with $p = 6$.

The same test case was also used for validation of the 2-D implementation of the frequency domain $p$-FEM LNS solver. Similarly good agreements of the 2-D numerical results with the theoretical pressure values were obtained. Nevertheless, this comparison with the analytic expression in Eq. (3.79) requires

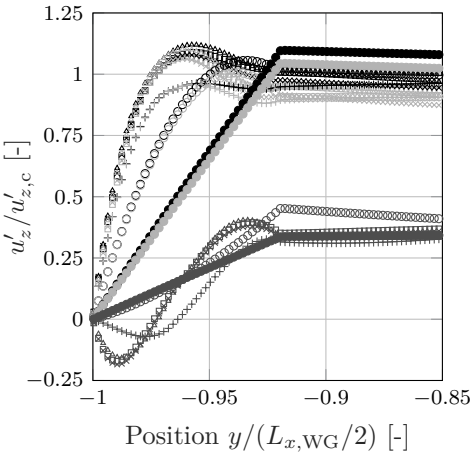


Figure 3.11. Resolution of the boundary layers with $p$-FEM approach. Real part (■), imaginary part (▭), and absolute value (■) of the axial velocity $u'_z$ profile along a cross-sectional line in the wall vicinity: $p = 1$ (●), $p = 2$ (○), $p = 3$ (✚), $p = 4$ (△), $p = 5$ (✕), and $p = 6$ (□).

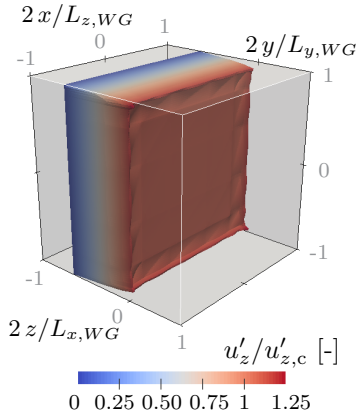


Figure 3.12. Axial velocity $u'_z$ profile inside the waveguide when both viscous and thermal losses are taken into account, at the frequency $f = 960\,\mathrm{Hz}$.

a particular scaling to accurately represent the different dissipative mechanisms. The height of the 2-D duct $H_{2-D}$ has to be adapted to ensure that the ratio of surface area occupied by the boundary layers to the cross-sectional area of the waveguide is the same for 2-D and 3-D cases. For the particular case of a waveguide with a squared cross-section, the following scaling is thus needed:

$$\frac{2\,\delta_{v/t}}{H_{2-D}} \approx \frac{4\,\delta_{v/t}}{H_{3-D}} \Rightarrow H_{2-D} \approx \frac{H_{3-D}}{2}\,, \tag{3.81}$$

where $H_{2-D}$ and $H_{3-D}$ are the duct heights for the two- and three-dimensional configurations. This result implies that the 3-D effects, directly linked to the corners of a rectangular duct, as visualized in 3.12 and sketched in 3.13, do not have a significant impact on the overall acoustic behavior of the investigated waveguide. For decreasing waveguide cross-sectional areas, as the corners relative impact increases, three-dimensional effects become non-negligible and the scaled 2-D results start to deviate from the 3-D ones.

It is not suitable to have directly at the inlet boundary, defined through the method of characteristics, boundary conditions of the no-slip and isothermal type. The local perturbation field violates the assumptions on which the method of characteristics is based, leading to numerical instabilities. Therefore, the slip

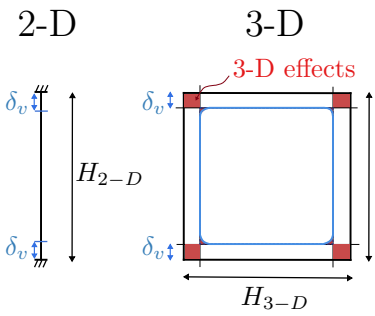


Figure 3.13. Description of the scaling required to compare 2-D numerical results with analytic solution in Eq. (3.79).

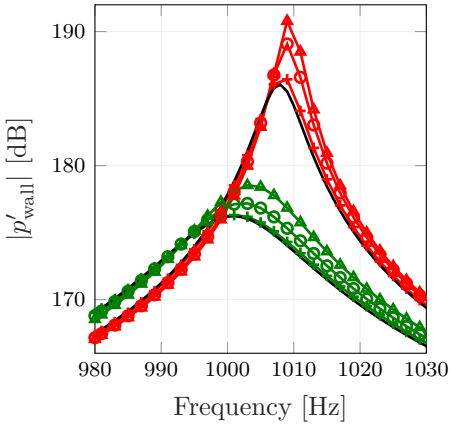


Figure 3.14. Amplitude of the pressure fluctuation $p'_{\text{wall}}$ predicted with the LNS $p$-FEM compared to analytic solutions (—): $L_\delta = 11/16 L_{z,WG}$ (—△—), $L_\delta = 13/16 L_{z,WG}$ (—○—), $L_\delta = 15/16 L_{z,WG}$ (—+—) accounting for thermal losses only (■) and visco-thermal losses (■).

boundary condition is used in the vicinity of the waveguide inlet, along a length $L_\delta$ in the axial direction. Figure 3.14 illustrates the influence of this length $L_\delta$ on the pressure perturbation computed with the LNS $p$-FEM solver in the 2-D case. As expected, the smaller $L_\delta$ is, the more damping is obtained inside the waveguide. This is clearly observed by the pressure curves at the monitoring points going down as $L_\delta$ decreases, converging towards the analytic solutions.

### Results in time domain

The previous waveguide configuration (see Fig. 3.8) is now used with the LNS RKDG solver in the time domain. Some specificities of time-domain RKDG simulations for this configuration are further discussed in Appendix B. It was found more challenging to get accurate pressure amplitude by means of fast Fourier transforms compared to the direct frequency-domain computations. The accuracy of the computed pressure values $p'_{wall}$ strongly depends on the type of inlet excitation applied. Based on the observations of Appendix B, the choice of a mono-frequency inlet excitation, with a limited set of considered frequencies, is made for the validation of the visco-thermal dissipation mechanisms.

The simulations are performed with the order of polynomial approximation

$p = 7$ and a non-dimensional time step $\Delta t^\star = c_0 \Delta t / l_{\text{ref}} = 1 \times 10^{-6}$, with $l_{\text{ref}}$ an arbitrary reference length taken as 1 m. The simulations are run until non-dimensional time $t^\star = 20$. The fluctuating pressures are recorded at a frequency corresponding to the sampling time step $\Delta t_s^\star = 1 \times 10^{-3}$.

The pressure values at the backing wall $p'_{wall}$, computed with the LNS RKDG solver accounting for visco-thermal dissipation, are presented in Fig. 3.15. The results demonstrate the expected trends with the shift toward lower values of the resonance frequency and the decrease in pressure peak amplitude when the different dissipative mechanisms are added to the problem. As already observed for the inviscid case in time domain (Appendix B), the spreads between the numerical and analytical solutions are larger than in the frequency domain away from the resonance. The pressure values are slightly overestimated at the extremities of the frequency range. This is thought to originate from the rather short time series ($t^\star = 0 \ldots 20$) used for the Fourier transform of the pressure signals. The monitored pressure signal, obtained at $f = 985$ Hz, is further displayed in Fig. 3.16 for $t^\star = 0.7 \ldots 1.2$. The impact on the sound wave of the dissipative mechanisms, taking place predominantly in the acoustic boundary layer, are clearly visible. In the light of these results, the implementation of the non-isentropic linearized Navier-Stokes equations appears to give satisfying results.

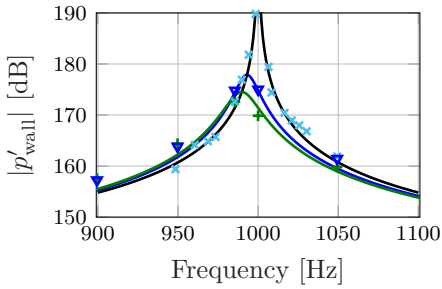


Figure 3.15. Amplitude of the pressure fluctuation at the backing wall of the 2-D waveguide predicted with LNS RKDG compared to analytic solution (—): no losses (×), viscous losses only (▽), visco-thermal losses (+).

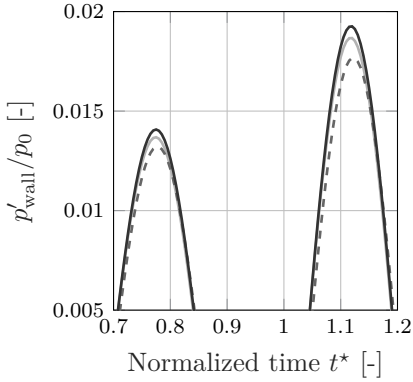


Figure 3.16. Time evolution of the pressure fluctuation at the backing wall obtained with LNS RKDG at $f = 985$ Hz accounting for different damping mechanisms: visco-thermal losses (- - -), only viscous losses (— —), only thermal losses (—).

### 3.4.3 Micro-Perforated Plate (MPP) with a slit in absence of mean flow

In this part, the high-order FEM numerical method for the linearized Navier-Stokes equations is applied to compute the linear response of a slit orifice to an acoustic excitation, in a 2-D geometry.

#### Case of a MPP with slit perforation

The configuration consists of a plate with one single slit orifice placed inside a duct, as described in Fig. 3.17. This configuration allows to use the two-port model detailed in Section 2.2.1 to determine the scattering matrix of the micro-perforated plate. The acoustic transfer impedance of the MPP, $z_{\mathrm{t,\,MPP}}$, is further derived from the computed scattering matrix. The system is excited by injecting an acoustic plane wave at one of the extremities of the duct (▬ ▬ in Fig. 3.17), whereas the other extremity is defined as a non-reflecting characteristic boundary condition (▪▪▪▪). The duct walls (▬) are represented by a rigid slip wall boundary condition and the acoustic boundary layer is disregarded at these boundaries. Such assumption is justified, the focus being here on the viscous losses at the perforation itself. It also limits the mesh refinement in the duct and the related computational costs. The walls of the plate are taken as rigid no-slip wall boundaries (▬) as the accurate resolution of the acoustic boundary layer inside and in the vicinity of the slit orifice is expected to have a large effect on $z_{\mathrm{t,\,MPP}}$. The isentropic set of the LNS equations, see Eqs. (3.9a), (3.9b) and (3.13), is considered here, disregarding the visco-thermal dissipative processes in the energy equation. The latter are expected to be negligible for homogeneous ambient conditions [230, 246].

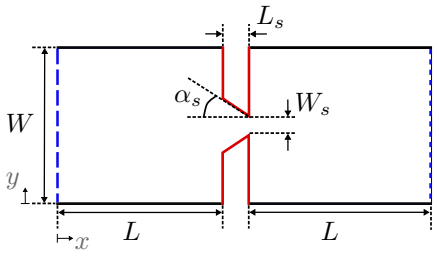


Figure 3.17. Geometry of the MPP with 2-D slit with slit angle $\alpha_s \approx 30\,°$.

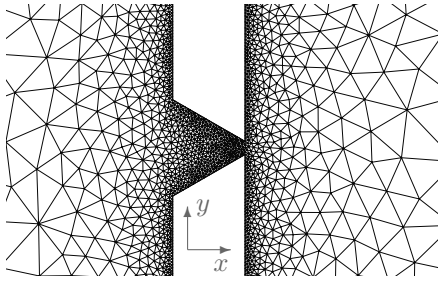


Figure 3.18. Unstructured triangular mesh used for the LNS $p$-FEM simulations, with element refinement near the plate walls and inside the slit orifice, $h_{\min} \approx \delta_a$.

The computed impedance values are compared to experimental results performed by Temiz [289]. The geometric parameters of the problem are therefore chosen corresponding to the MPP with slit, referred as "Sample S1", in the reference work [289] and are listed in Table 3.3. The duct length has been taken long enough on each side of the plate to allow the two-port characterization of the test sample.

| **Symbol** | **Geometric parameter** | **Value** | **Unit** |
|---|---|---|---|
| $W_s$ | Slit width | 0.36 | [mm] |
| $L_s$ | Plate thickness | 2.0 | [mm] |
| $\sigma_{\mathrm{MPP}}$ | Plate porosity | 0.86 | [%] |
| $W$ | Duct width | $W_s/\sigma_{\mathrm{MPP}} = 41.9$ | [mm] |
| $L$ | Duct length | 300 | [mm] |
| $\alpha_s$ | Slit angle | 29.9 | [°] |

Table 3.3: Geometric specifications of the investigated 2-D micro-perforated plate with slit orifice.

The air properties chosen for the simulations are summarized in Table 3.4 and are selected to match the experimental conditions.

| **Symbol** | **Medium property** | **Value** | **Unit** |
|---|---|---|---|
| $\gamma$ | Ratio of specific heats | 1.4 | $[-]$ |
| $\rho_0$ | Density | 1.205 | $[\mathrm{kg} \cdot \mathrm{m}^{-3}]$ |
| $c_0$ | Speed of sound | 340 | $[\mathrm{m} \cdot \mathrm{s}^{-1}]$ |
| $M_0$ | Mach number | 0 | $[-]$ |
| $\mu$ | Dynamic viscosity | $1.821 \times 10^{-5}$ | $[\mathrm{kg} \cdot \mathrm{m}^{-1} \cdot \mathrm{s}^{-1}]$ |
| $\nu$ | Kinematic viscosity | $1.511 \times 10^{-5}$ | $[\mathrm{m}^2 \cdot \mathrm{s}^{-1}]$ |

Table 3.4: Conditions used for the simulations.

Apart from being a validation case for the proposed numerical methods, this present case has been further used to cross-validate an impedance model for MPPs that allows to estimate the acoustic behavior of micro-perforated plates in their transition regime from computation in the linear regime. Such extension of the linear impedance model implies to characterize the entire operating range of MPPs by solely linear acoustic simulation, like with the LNS operator. More information on this impedance model can be found in [287, 289].

| **Run number** [−] | **Slit angle** $\alpha_s$ [°] | **Element min. size** $h_{\min}$ [m] | **Order** $p$ [−] | **Edge radius of curvature** $R_f$ [m] |
|---|---|---|---|---|
| 1 | 29.9 | $\delta_a = 8.29 \times 10^{-5}$ | $2 \dots 5$ | / |
| 2 | 29 | $\delta_a$ | 3 | / |
| 3 | 31 | $\delta_a$ | 3 | / |
| 4 | 29.9 | $\delta_a/80$ | 3 | $0.01W_s = 3.6 \times 10^{-6}$ |
| 5 | 0 | $\delta_a$ | 3 | / |

Table 3.5: List of the simulations performed.

### Results in the frequency domain

Simulations with the $p$-FEM solver are performed in the frequency range [100 Hz − 700 Hz], which assures that only plane wave modes are present at the monitoring sections along the duct branches. These control sections are placed on both sides of the test object at a minimal distance of 0.1 m, with at least two monitoring sections separated by the distance $\Delta l_m$ which follows the rule stated in Eq. (2.16) [4]. A frequency step of 20 Hz is adopted, which gives a total of 31 simulations to be carried out for each independent state of the two-port system. The results presented here are obtained with a fully unstructured mesh constituted of 20000 triangular elements. The mesh is very refined at the plate wall and inside the orifice, with a minimum size $h_{\min} = 8.29 \times 10^{-5}$ m, which corresponds to the boundary layer thickness at the upper limit of the frequency range. The present results are shown to be unaffected by further mesh refinement and higher order $p$ of the used shape functions, tested with $p \in \{2 \dots 5\}$. Additionally to the independence study, some geometric parameters are checked: the angle of the slit orifice $\alpha_s$ and the rounding of the slit edges (with radius $R_f$). The values of these parameters can indeed vary between the experimental setup and the numerical model. For that reason, it is interesting to quantify how much these uncertainties can affect the generated results. Table 3.5 indicates the parameters of the simulations performed for this case. The local mesh refinement required for the geometric representation of the rounded edges increases the number of triangular elements to 25000.

The scattering matrix of the two-port system representing the MPP with slit orifice is shown in Fig. 3.19. For this figure, the length of the two-port system has been taken equal to the actual thickness of the perforated plate $L_s = 2$ mm. Only the upstream coefficients $T^+$ and $R^+$ are given as the computed scattering matrix was found symmetric for all five cases due to the absence of mean flow and the compactness of the orifice ($W_s$ and $L_s \ll \lambda_a$). Figure 3.19a shows

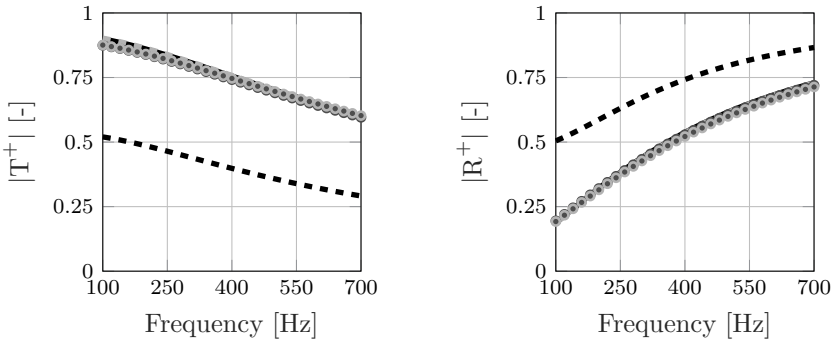


(a) Amplitude $|\bullet|$ of the coefficients

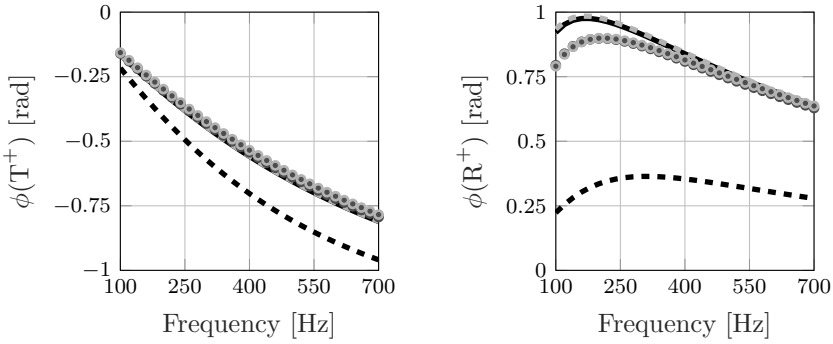


(b) Phase $\phi(\bullet)$ of the coefficients

Figure 3.19. Scattering matrix of the MPP with slit orifice: $\alpha_s = 30\,^\circ$ with sharp edges (—), $\alpha_s = 29\,^\circ$ with sharp edges (●), $\alpha_s = 31\,^\circ$ with sharp edges (○), $\alpha_s = 0\,^\circ$ with sharp edges (- - -), and $\alpha_s = 30\,^\circ$ with rounded edges of radius $R_f = 0.01W_s$ (- - -).

that the presence of the slit angle $\alpha_s$ results in an amplitude increase of the transmission coefficients $T^\pm$ and a decrease of the reflection coefficient $R^\pm$ compared to the case $\alpha_s = 0\,^\circ$. The latter is also characterized by larger phase jump through the plate, due to the increase in inertial effects linked to the smaller aperture. From "Runs 2 and 3", the geometric deviation of $\pm 1\,^\circ$ in $\alpha_s$ appears to have no significant impact on the amplitude of the scattering matrix, only on the phase of $R+$. From "Run 4", the micro-rounding of the edges does not at all influence the obtained scattering properties of the slit, as expected in the linear regime of the slit.

From the scattering matrices presented in Fig. 3.19, the lumped model [7] discussed in Section 2.2.2 can be used to retrieve the transfer impedance of the test object. For the quiescent case, the normalized transfer impedance of the

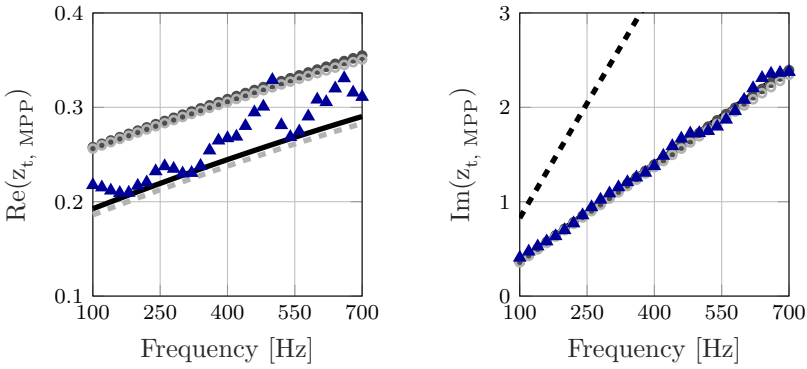


(a) Resistance (b) Reactance

Figure 3.20. Normalized impedance $z_{\mathrm{t,\,MPP}}$ of the MPP with slit orifice: $\alpha_s = 30\,^\circ$ with sharp edges (—), $\alpha_s = 29\,^\circ$ with sharp edges (●), $\alpha_s = 31\,^\circ$ with sharp edges (◎), $\alpha_s = 0\,^\circ$ with sharp edges (- - -), $\alpha_s = 30\,^\circ$ with rounded edges of radius $R_f = 0.01 W_s$ (- - -), and experimental data (▲).

MPP with slit $z_{\mathrm{t,\,MPP}}$ is thus given by:

$$z_{\mathrm{t,\,MPP}} = \frac{Z_{\mathrm{t,\,MPP}}}{\rho_0 c_0} = 2\left(\frac{1}{T^{\pm}} - 1\right). \tag{3.82}$$

The impedance results for Runs 1 to 4, displayed in Fig. 3.20, are in good agreement with the experimental data obtained by Temiz [289]. Even if some little oscillations can be observed for the experimental values, the trends and linear slopes for both resistance and reactance are correctly predicted by the numerical method. By considering the possible deviation in $\alpha_s$ that can exist for the actual test sample, due to manufacturing processes, the experimental resistance curve lies between the numerically obtained ones. Furthermore, even if the reactance curve is not much affected by a deviation of $\pm 1\,^\circ$ in $\alpha_s$, this change leads to a tangible increase in $Re(z_{\mathrm{t,\,MPP}})$ of 0.06. The resistance values obtained numerically for $\alpha_s = 0\,^\circ$ are much larger (not represented in Fig. 3.20a) than in the case $\alpha_s = 30\,^\circ$, going from 1.76 at $f = 100\,\mathrm{Hz}$ to 1.95 at $f = 700\,\mathrm{Hz}$. This increase in resistance is explained by the increase in friction forces due to reduced cross-sectional area of the slit along the plate thickness compared to the inclined opening. This is paired with a significant increase in reactance, shown in Fig. 3.20b.

## 3.5 Conclusion

In this chapter, the theory and implementation of the proposed high-order numerical models for the linearized Navier-Stokes equations have been presented. Approaches in both frequency domain, with a continuous Finite Element Method approach, and time domain, with a Runge-Kutta Discontinuous Galerkin method, are developed to investigate the acoustic behavior of perforates and silencers in their linear regime. The numerical strategies, regarding for example the treatment at boundaries, the source terms, and the scheme's stabilization, are detailed for each solver. A general framework for the analysis of the interactions between acoustic, vorticity and entropy perturbations is described in Section 3.3. The different coupling mechanisms between the perturbation modes are quantified based on specific transport equations and integral energy balances. The latter approach is particularly effective coupled with the proposed high-order methods and allows a thorough evaluation of the physics of perforates.

The propagation of coupled acoustic, vorticity and entropy waves have been checked through a set of chosen reference cases. The mean flow effects have been assessed for the case of a monopole radiating in the sheared flow of a plate. The correct implementation of the dissipative terms in the LNS equations has been verified by means of two dedicated cases. First, the results obtained for a closed-end waveguide with the high-order methods are compared to an analytic solution. Secondly, experimental data of a rigid micro-perforated plate are used to further validate the numerical methods. From these reference cases, the ability of both proposed high-order numerical methods to investigate the linear regime of acoustic dampers is confirmed. Practical guidelines for the application of the high-order methods to scale-resolved problems have also been drawn from these first examples.

# Chapter 4

# Study of perforates in their linear regime

In this chapter, the high-order numerical methods presented in Chapter 3 are used to study the linear behavior of perforations and acoustic dampers under complex conditions. An slit resonator is first investigated in the presence of grazing flow. The solutions from time and frequency domains are compared to experimental data from a dedicated measurement campaign. The different strategies available for the impedance determination of such resonators are examined at this occasion. The physics of a similar acoustic resonator, this time in a hot environment, is then studied. The effect of high temperature and temperature gradients are thoroughly explored. The observations support and supplement previous experimental works from the literature on the subject. In the last section, the topic of the sound attenuation originating from the interaction of acoustic waves with turbulent flows is tackled for two cases: an orifice geometry with through-flow and a parametric study on a Helmholtz resonator with grazing flow, varying the orifice width.

## 4.1 Slit resonator at ambient temperature with grazing flow

As discussed in Chapter 2, it is shown that a Helmholtz resonator behaves linearly at low and moderate sound pressure levels [279], typically below 130 dB.

**Section 4.1 is largely based on:** Denayer et al. (2014) Combined Numerical and Experimental Study of a Slit Resonator Under Grazing Flow [84].

For this regime, it is expected that linearized governing equations, like the ones presented in Section 3.1, can be used to model the acoustic behavior of such silencers. This section can be seen as the continuation of a previous study [81] and focuses on the study of a slit resonator geometry subjected to grazing flow with the presented hybrid approach. Due to the chosen cold flow conditions, the isentropic set of the linearized Navier-Stokes equations are used here to capture the linear interactions between the acoustic and hydrodynamic fields [230, 246].

A few experimental studies on slit resonators can be found in the literature, but to the author's knowledge, they consider relatively large perforations [283] or assume acoustic waves under normal incidence [277,318]. In order to provide the necessary validation data for the numerical simulations, a dedicated experimental campaign on this particular configuration has been carried out by Denayer for different grazing flow speeds, using the aeroacoustic test rig of the department of Mechanical Engineering at KU Leuven [81].

### 4.1.1 Specification of the problem

#### Slit resonator configuration

The configuration investigated in this work consists of a slit resonator attached to one sidewall of a long rectangular duct of cross-section $H_{\text{duct}} = 40\,\text{mm} \times W_{\text{duct}} = 90\,\text{mm}$. The resonator itself is composed of a rectangular cavity ($H_{\text{cav}} = 50\,\text{mm} \times L_{\text{cav}} = 25\,\text{mm}$), which is connected to the main duct by a rectangular slit of width $l_s = 1\,\text{mm}$ and thickness $h_s = 1\,\text{mm}$. In the span-wise direction, the cavity extends to the full width of the duct, i.e. $W_{\text{cav}} = W_{\text{duct}} = 90\,\text{mm}$. For manufacturing reasons, the slit ends at 2 mm from both walls of the duct, i.e. $W_s = 86\,\text{mm}$. Figure 4.1 shows the actual test object, mounted on the measurement rig by means of flanges.

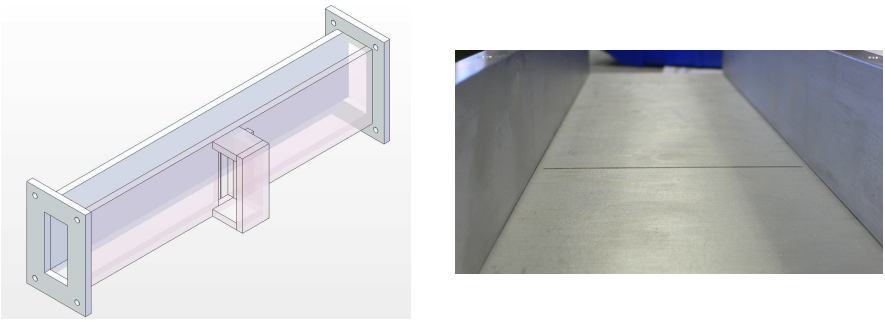

Figure 4.1. Schematic overview of the test section (left) and picture of the opened test object with close-up on the resonator slit (right) [84].

The hybrid approach based on the LNS equations is applied to the slit resonator geometry. To limit the size of the numerical problem, and therefore keep reasonable execution time and cost for the simulations, only two-dimensional computations (both for the aerodynamic and acoustic fields) are carried out. This approach is supported by the "quasi 2-D" nature of the resonator, for which the slit's span-wise dimension is much greater than its width and thickness, i.e $l_s$ and $h_s \ll W_s$. Figure 4.2 shows the computational domain used in the simulations, which is the centered longitudinal cross section of the geometry of the actual test object used in the experiments.

### Determination of the mean flow field

The use of the LNS equations to solve the acoustic wave propagation through the test section requires first the mean flow to be known. The mean flow field is computed using a steady RANS simulation, carried out with the commercial CFD software ANSYS® Fluent. A uniform axial velocity, with a turbulence intensity of TI = 10%, is imposed at the duct inlet. This TI level is expected to match the experimental conditions. Four different Mach numbers, $M_0 \in \{0.025, 0.05, 0.075, 0.1\}$ are considered in this section[1], all falling into the low Mach number category ($M_0 < 0.3$). The corresponding inlet velocities and Reynolds numbers are indicated in Table 4.1. The outlet is modeled using a pressure condition and all walls are represented by a no-slip boundary condition.

The equations are solved with the SIMPLE algorithm and a standard finite volume spatial discretization with second-order accuracy. The SST $K$-$\omega$ model is chosen together with enhanced wall functions in order to resolve the viscous

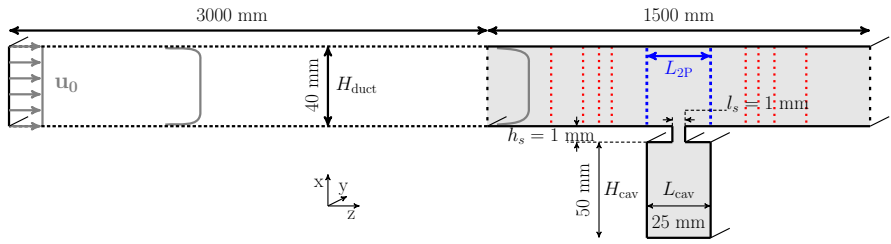


Figure 4.2. Schematic overview of the geometry under consideration (scale not respected). The gray region indicates the acoustic computational domain, whereas the dotted lines show the extended domain used for the mean flow simulations.

[1]These Mach numbers have been selected based upon the flow range of the blowers in the experimental setup.

| $M_0$ [-] | $u_{0z,\,\mathrm{inlet}}$ [m/s] | Re [-] |
|---|---|---|
| 0.025 | 8.5 | $2.33 \times 10^4$ |
| 0.05 | 17.0 | $4.66 \times 10^4$ |
| 0.075 | 25.5 | $6.99 \times 10^4$ |
| 0.1 | 34.0 | $9.32 \times 10^4$ |

Table 4.1. Summary of the mean flow conditions for the different simulations.

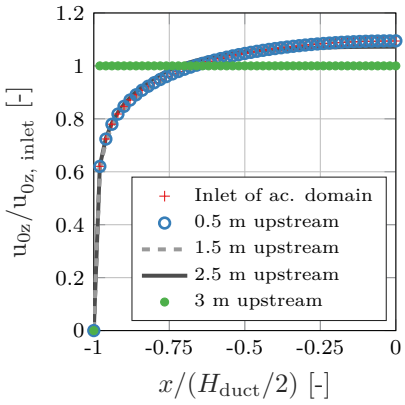


Figure 4.3. Axial velocity $u_{0z}$ profile at different locations in the duct for $M_0 = 0.075$.

sub-layer at the walls. A single structured grid is used for all flow simulations and the mesh element sizes are adapted to assure that the non-dimensional wall distance of the first grid cells is one or lower, i.e. $y^+ < 1$, at all walls based on the highest Mach number.

Considering the long portion of pipe upstream of the test section in the experimental setup, it is estimated that the mean flow in the duct is fully developed when it reaches the slit resonator. In order to obtain a fully developed flow at the inlet of the computational domain used for the LNSE simulations, the CFD domain is extended 3 m upstream, as illustrated in Fig. 4.2. Figure 4.3 shows the axial velocity profile $u_{0z}(x)$ at different locations in the duct for $M_0 = 0.075$: at the inlet of the acoustic domain and at 0.5 m, 1.5 m, 2.5 m, and 3.0 m upstream of this plane. It confirms that the mean flow is fully developed when it enters the computational domain of the acoustic simulations. In the following, the indicated Mach numbers refer to the imposed uniform inlet velocity.

The obtained mean flow profile is shown in Fig. 4.4 for an inlet Mach number $M_0 = 0.075$. As expected, the flow mainly grazes over the facing sheet. It generates a shear layer over the slit with a weak clockwise circulation inside the orifice. The air in the back cavity is nearly quiescent. Due to the small dimension of the orifice, the amplitude of the counter-rotating vortex appearing inside the cavity is very small ($< 0.5$ m/s). For the other Mach numbers considered in this work, a similar mean flow field is observed.

The mean flow field obtained from the steady RANS simulations has to be mapped from the fine CFD grid to the coarser acoustic grid. For the RKDG method, this is done using the global least-squares interpolation procedure

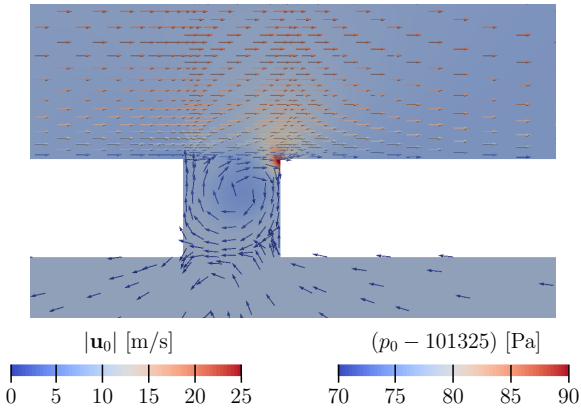


Figure 4.4. Vector representation of the mean flow velocity field $\mathbf{u_0}$ superimposed on the contour map of the static pressure in the vicinity of the orifice ($M_0 = 0.075$).

of references [120, 293]. Concerning the mapping of the CFD data on the acoustic grid in the frequency domain, a linear fitting for the field variables and their derivatives is adopted. This simple mapping approach was found to be sufficient for the present case and requires less computational effort than the more advanced mapping by least-square approximation of high-order polynomials. The same RANS mean flow fields are used for both linearized numerical methods.

### Acoustic simulations

One of the objectives of this section is to compare the two linear acoustic solvers discussed in Section 3.2 for the present slit resonator configuration. The RKDG and $p$-FEM simulations of the acoustic field are, therefore, performed on a unique unstructured grid composed of 1505 triangular elements (see Fig. 4.5a), generated with Gmsh [113]. The time-domain simulations have been conducted by Denayer [81, 84]. The frequency range of interest for this work is restricted to relatively low frequencies, with $f \in [200\,\text{Hz} - 1700\,\text{Hz}]$, centered around the expected resonance frequency $f_{\text{res}}$. In this range, only plane wave modes propagate through the duct sections, as the frequency is below the first mode cut-off frequency $f_{\text{c}} = c_0/(2H_{\text{duct}}) \approx 4250\,\text{Hz}$. The spatial discretization is done by means of $5^{\text{th}}$-order polynomial shape functions to represent the acoustic field variables in both time and frequency domains. This assures the independence of the numerical results from the choice of polynomial order, based on the scattering matrix coefficients. The maximum relative deviation in terms of $T^{\pm}$ is found, indeed, below 1 % over the frequency range of interest (determined for

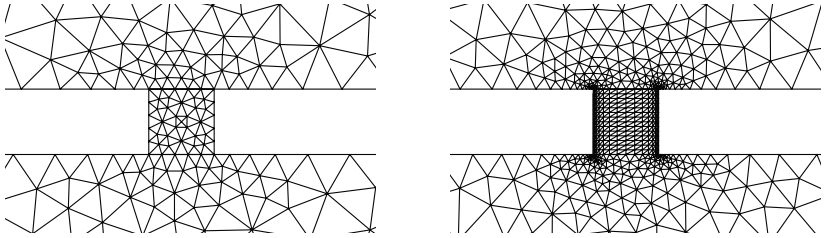

(a) Coarse unstructured acoustic mesh ($h_{\min} \approx l_s/5$)

(b) Refined mixed acoustic mesh ($h_{\min} \approx l_s/100$)

Figure 4.5. Triangular meshes used for the frequency domain $p$-FEM and time-domain RKDG acoustic simulations with LNS operator.

$M_0 = 0.05$, between $p = 5$ and $p = 7$). Even though the mesh used is not fine enough to completely resolve the acoustic boundary layer (as $h_{\min} > \delta_{\mathrm{v}}$), this grid is expected [114, 142, 175, 176] to be sufficient to capture adequately the interactions between the vorticity in the shear layer at the orifice and the passing acoustic wave. Additionally, the grid shown in Fig. 4.5b is used with the $p$-FEM solver to investigate the impact of properly resolving the acoustic boundary layer inside the orifice. This second mesh, consisting of 2311 triangular elements, is drastically refined at the orifice's inner walls, with $h_{\min} \approx \delta_{\mathrm{v,min}}$, to correctly capture the boundary layer phenomena.

In the frequency domain, the LNS simulations have been carried out over the given frequency range with a step $\Delta f = 36\,\mathrm{Hz}$. The acoustic excitation is obtained by injecting at an extremity of the duct a plane wave by means of the method of characteristics. As the two-port model will be used to characterize the test section, two independent states of the system are needed. This is realized by two simulations per frequency, with the excitation injected upstream and downstream of the slit resonator. The other end of the computational domain is represented by a non-reflecting characteristic boundary condition. In the frequency domain, a slip condition is imposed on every rigid wall for the coarse mesh, whereas a no-slip condition is prescribed on the orifice's inner walls in case of the refined grid. The later wall conditions have been also used with the coarse mesh in the time domain simulations.

The pressure fluctuations are stored at the points required for the different impedance measurement techniques described in Section 2.2.2. For the in-situ impedance measurement method, the pressure fluctuations at the facing sheet and at the bottom of the cavity are required. In order to average out the influence of the hydrodynamic component of the pressure, the facing sheet pressure is recorded at 9 points on a half circle with radius $l_s/2$ around the orifice and the signals are averaged before further processing. Doubling and tripling the number of monitoring points used for the pressure averaging has shown to have a very limited impact on the obtained impedance values, with a

maximum relative deviation of 2.4 % over the frequency range of interest and for the different flow speeds. At the bottom of the cavity, due to the quasi-quiescent condition, the pressure is simply averaged over 3 points located against the bottom wall. The impedance eduction methods are based on the determination of the scattering matrix representing a particular segment of the duct containing the slit. This black-box segment is taken as the part of the duct above the cavity, corresponding to a length $L_{2P} = 25\,\text{mm}$, for the distributed model. In case of the lumped model, $L_{2P} = 0\,\text{mm}$ is considered. The scattering matrix, computed as described in Section 2.2.1, requires the pressure fluctuations at two monitoring points on each side of the test object. In practice, four measurement sections (shown with dotted lines in Fig. 4.2), leading to an overdetermined systems, are used to solve the plane wave decomposition problem on each side. The monitoring planes are located at a distance $z_i = \pm 0.08\,\text{m}$, $\pm 0.15\,\text{m}$, $\pm 0.27\,\text{m}$ and $\pm 0.50\,\text{m}$ from the center of the orifice. These monitoring sections allow to properly cover the full frequency range of interest as recommended in [4]. For each of these sections, the averaged pressure fluctuations over 8 equally spaced monitoring points are used in equation Eq. (2.15) in order to suppress the influence of the decaying cut-off modes.

### 4.1.2 Results for the acoustic field and observations

#### Comparison of the numerical results with experimental data

Scattering matrix

The numerical results are first compared with the experimental data in terms of scattering matrices, to assess how well the proposed numerical methodologies can predict the overall acoustic behavior of the slit resonator in presence of a grazing flow. Only the coarse grid is used here. Figure 4.6 shows the absolute value of the scattering matrix components obtained for the particular Mach number of $M_0 = 0.05$. The general band-stop filter behavior of the slit resonator is clearly visible in the dip of the transmission and peak of the reflection coefficients. Due to the presence of a flow, the scattering matrix no longer exhibits a symmetric behavior. The downstream coefficients ($R^+$ and $T^+$) are found slightly higher than their counterparts in the upstream direction ($R^-$ and $T^-$). This observation holds for the other grazing flow velocities considered in this section.

Considering the numerical results, some discrepancies can be observed between the RKDG and the $p$-FEM results in Fig. 4.6. The RKDG results have a lower resonance frequency and show a more damped behavior than the $p$-FEM results. This is verified especially at low grazing flow velocities. Since the mesh, the mean flow field, and the post-processing used are identical for both methods, this discrepancy is mainly caused by the difference in the treatment of the

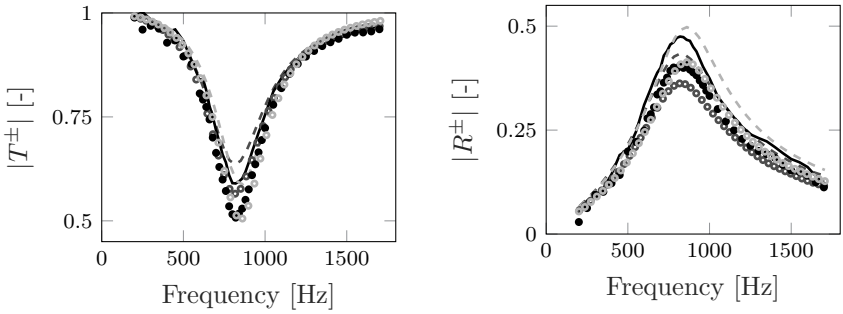


(a) Transmission $T^{\pm}$

(b) Reflection $R^{\pm}$

Figure 4.6. Amplitude of the scattering matrix coefficients for a grazing flow at $M_0 = 0.05$: computed with the $p$-FEM (- - - down- and ○ upstream) and RKDG (- - · down- and ○ upstream) LNSE solvers, and obtained experimentally (— down- and ● upstream).

orifice's inner wall. The $p$-FEM results presented in Fig. 4.6 assume a slip wall boundary condition, whereas a no-slip condition is prescribed inside the orifice for the RKDG simulations. Considering the viscous boundary layer, even if not completely resolved due to the relatively large element size inside the orifice, leads to more acoustic dissipation. This difference between the two numerical methods is seen to decrease for higher grazing flow velocities. Indeed, at higher flow velocities, the losses related to the interaction of the acoustic field with the shear layer over the orifice will dominate the viscous scrubbing losses in and around the orifice.

The experimental results appear to be somehow in-between the numerically predicted scattering matrix. The ratios between the amplitudes of upstream and downstream coefficients are very similar across all results. This observation supports the fact that the interactions between the vorticity in the shear layer and the acoustic field is captured adequately with the rather coarse mesh chosen. The agreement is overall satisfying considering the multiple reasons for discrepancies between the numerical models and the experimental setup. Firstly, the ratio of the mass of air in the slit to the volume of the cavity is slightly higher in the 2-D numerical case than in the experimental setup. This results in a slightly lower resonance frequency in 2-D than the actual one in the experiments. The estimated difference is $\Delta f_{\text{res}} \approx 2.5\%$. Secondly, the dimension of the grid elements inside the orifice do not assure to correctly estimate the boundary layer effects. The acoustic damping via viscous frictions at the wall can therefore be under- or over-estimated.

Figure 4.7 presents the amplitude of the downstream transmission and reflection coefficients for different grazing flow velocities. In term of $T^{+}$, the dip around the resonance frequency broadens and become less deep for increasing flow

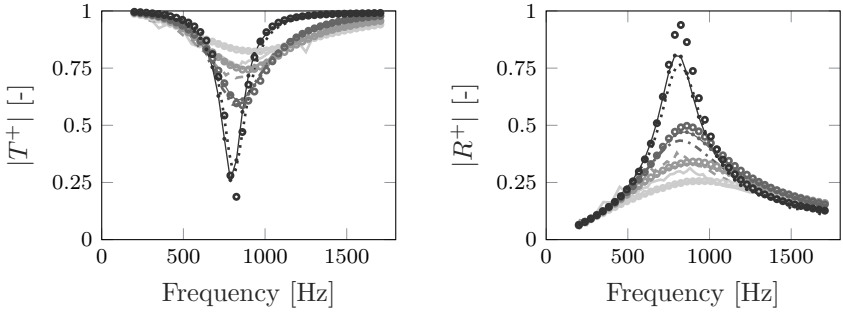


(a) Transmission coefficient $T^+$ (b) Reflection coefficient $R^+$

Figure 4.7. Amplitude of the downstream coefficients of the scattering matrix for different grazing flow velocities: computed with the frequency-domain LNSE solver with slip BC ($M_0 = 0.025$, $M_0 = 0.05$, $M_0 = 0.075$, $M_0 = 0.1$) and with no-slip BC inside the orifice ($M_0 = 0.025$, $M_0 = 0.05$, $M_0 = 0.075$, $M_0 = 0.1$), compared to experiment data ($M_0 = 0.025$, $M_0 = 0.05$, $M_0 = 0.075$, $M_0 = 0.1$).

rate. An increased Mach number in the duct leads indeed to stronger velocity gradients at the neck opening, which strengthen the sheared flow effects at the resonator mouth. This extra "blockage" effect smooths out the peak in the transmission coefficients around $f_{\text{res}}$, leading to a lower quality factor[2] for the resonator. At the same time, the resonance frequency is slightly shifted towards higher values. Both trends are correctly predicted by the simulations, illustrating that the LNSE solvers are capable of representing the flow-acoustic interaction mechanisms that take place in the sheared flow of the resonator neck. As expected from the previous arguments, the experimental results show a more damped behavior than the numerical results with prescribed slip boundary conditions, predominantly at low flow rates. Considering a no-slip boundary condition at the orifice's inner walls with the $p$-FEM solver, in combination with the refined grid, reduces this discrepancy in the viscous damping. This is shown in Fig. 4.7 for all mean flow speeds. Similar observations hold for the reflection coefficient. The grazing flow results in a lower, but broader peak around $f_{\text{res}}$. The resonator therefore becomes less effective in blocking the incoming sound waves in presence of flow, but acts on a broader frequency range.

Resonator impedance

At low frequency, the resonator can be considered as a lumped impedance connected to the duct [220, 230]. Based on the model described in Section 2.2.2

[2]The quality factor for the resonator is defined as $\text{Q}_{\text{HR}} = f_{\text{res}}/\Delta f_{\text{res}}$, where $\Delta f_{\text{res}}$ is the resonance width.

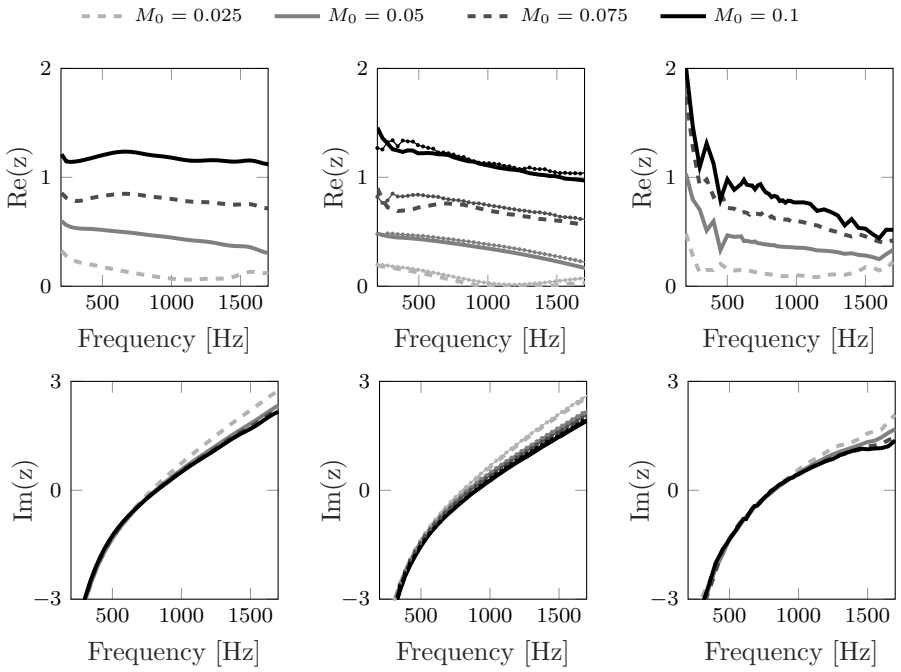


(a) RKDG (b) $p$-FEM (c) Experiment

Figure 4.8. Influence of the grazing flow velocity on the normalized resistance (top) and reactance (bottom), obtained with the lumped impedance eduction approach from both numerical and experimental results. Additional $p$-FEM results obtained with refined grid and resolved ABL (—•—).

and the expressions given in Eq. (2.18), the impedance of the resonator can be computed independently for a downstream or upstream propagating wave. For the present configuration, the difference between $z^+$ and $z^-$ is very small. The average of these expressions is presented in Fig. 4.8 for the set of Mach number considered.

A generally good agreement of the impedance values computed from the simulated and measured scattering matrices can be appreciated. The resistance, relatively small at a very low Mach number, increases significantly for higher flow velocities. The experimental resistance values appear to slightly decrease towards high frequencies. This trend appears better captured by the $p$-FEM solver with properly chosen wall BCs than by the RKDG simulations with coarse grid and no-slip BC. The quantitative agreement is found better, mostly for $M_0 = 0.025$ and $M_0 = 0.05$, when the no-slip boundary condition is accounted for. The general quantitative agreement is less good at higher flow velocities. As shown in Fig. 4.8b, resolving properly the ABL leads to a systematic increase in

the resistance, even if relatively limited. Concerning the imaginary part of the impedance, the resonator reactance is dominated by the stiffness of the cavity at low frequencies and increases as $1/\omega$. This contribution is mainly determined by the resonator geometry and is not affected at all by the presence of flow. At higher frequencies, the inertial effects at the resonator neck dominate and the reactance increases linearly with frequency. This contribution is related to the mass of air attached to the orifice. From Fig. 4.8, it appears that the reactance decreases with increasing grazing flow rates. This phenomenon can be interpreted as the attached mass of air in the orifice being "blown away" by the flow [251]. Although the quantitative agreement is not excellent, the simulations predict correctly the inertial characteristics of the flow effect on the resonator. Due to the 2-D/3-D geometrical difference mentioned earlier, a lower reactance in the experimental results is nevertheless expected. The previous conclusions about the flow effects on the resonator impedance are in agreement with earlier experimental [7, 131, 166, 181] and numerical [81, 318] observations on Helmholtz resonators with various geometries.

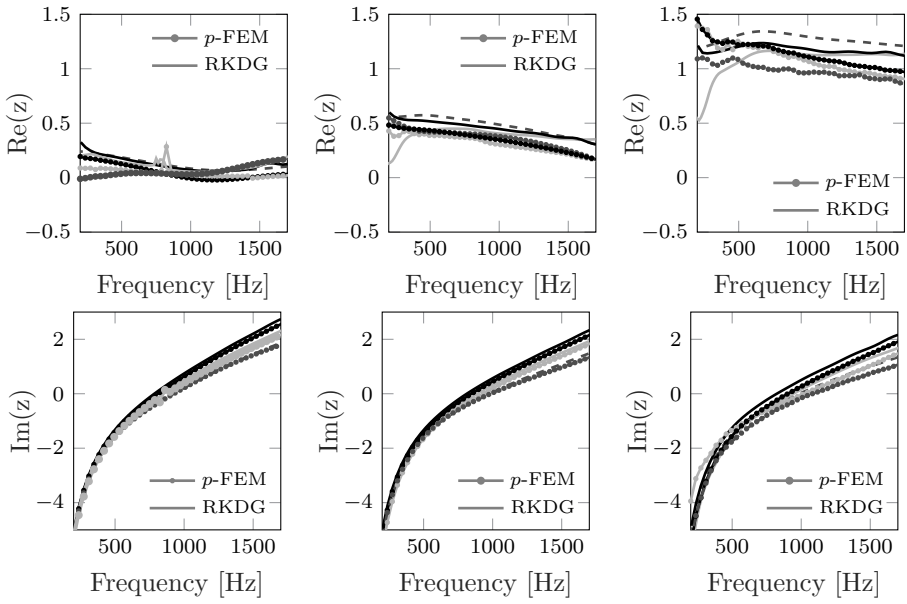


(a) At $M_0 = 0.025$ (b) At $M_0 = 0.05$ (c) At $M_0 = 0.1$

Figure 4.9. Normalized resistance (top) and reactance (bottom), obtained with the in-situ method (- - -), the lumped impedance eduction (—) and the distributed impedance eduction (—) approaches from the LNSE results.

### Comparison of the impedance measurement techniques

Figure 4.9 shows the impedance of the resonator, computed from the simulation results by means of the three methods described in section Section 2.2.2: the Dean's in-situ method [77] and both lumped [7] and distributed [79, 261] models for the eduction technique. Even if some differences appear in the determined impedance values, the three characterization techniques lead to a similar interpretation of the flow effects on the resonator impedance. The lumped model was expected to only provide valuable impedance estimations at low frequencies. Figure 4.9 reveals that this model performs rather well on the complete instigated frequency ranges. Due to the difference in the treatment of the orifice walls, the $p$-FEM results with slip boundary condition deliver systematic lower values for both resistance and reactance than the RKDG simulations with no-slip boundary. This observation is verified for all flow rate and for the three characterization methods.

Comparing the different characterization techniques, no clear trends can be identified regarding the resistance. Concerning the reactance curves, the distributed eduction method is found to lie in-between the two other curves for all $M_0$ cases. The reactance given by the in-situ technique is systematically lower than the educed ones. The distributed eduction approach appears to have some limitations in the low frequency range. A peculiar behavior can also be observed very locally around 800 Hz for the $M_0 = 0.025$ case.

Additionally, it was noticed that obtaining the resistance with the in-situ method is a challenging task. A small variation of the measurement positions at the facing sheet can result in changes for the resistance curve. This dependency is illustrated in Fig. 4.10 with fluctuating pressure values obtained with the LNSE $p$-FEM solver. The location of the monitoring points is changed between

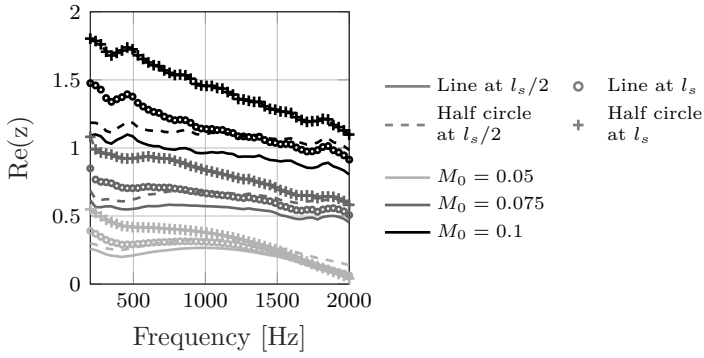


Figure 4.10. Influence of the monitoring point location on the predicted normalized resistance $Re(z)$ computed with the in-situ method.

a straight line and a half-circle placed at a distance $l_s$ and $l_s/2$ from the orifice center. The scattering of the resistance curves is found to increase with increasing mean flow velocities. This is due to the larger local hydrodynamic pressure fluctuations for rising flow rates. The results further show that a distance $\approx l_s/2$ is best suitable to determine correct resistance values. The reactance curves obtained with the in-situ technique are much less sensitive with respect to the facing sheet measurement position.

### 4.1.3 Conclusions

The LNSE simulation results were compared to experimental data, obtained from a dedicated measurement campaign on a slit resonator. It was shown that the simulations predict the correct trends in terms of scattering matrix and acoustic impedance with respect to the grazing flow velocity and the frequency. Simulations appear to slightly overestimate the flow effect at the highest flow rates considered. The adequate modeling and resolution of the viscous boundary layers were found important at very low Mach numbers for the investigated slit geometry of 1 mm width. The small discrepancies between simulations and experiments can have multiple causes. The simulations are carried out in 2-D while the experiments consider a 3-D object. There are no certainties that the RANS mean flow representation matches exactly the experimental conditions (e.g. in terms of TI and boundary layer characteristics) as no detailed aerodynamic measurements were done to validate the mean flow profile used. The performed acoustic simulations are based on quasi-laminar isentropic assumption in the LNSE, therefore neglecting dissipative effects in the energy equation and the turbulence damping. These phenomena could, however, play a role in the acoustic behavior of the resonator, especially at higher velocities. Taking these factors into account, the agreement between numerical and experimental results is deemed satisfactory. The LNSE model is proven capable of capturing the complex interactions between acoustic wave and shear layer over an orifice.

Three impedance characterization techniques were applied to the simulation results. They all predict the same trends with respect to the grazing flow velocity. Some small discrepancies between the approaches could nevertheless be observed. Especially for the in-situ technique, significant variations in terms of resistance were observed depending on the location of the monitoring points at the facing sheet. The different impedance measurement techniques show overall a reasonable agreement for both resistance and reactance. Some systematic differences can, however, be observed for the reactance.

## 4.2 Temperature effects on the acoustic behavior of passive silencers

In this section, the thermal effects that can affect the acoustic behavior of acoustic dampers in particular applications are numerically investigated with the help of the linearized Navier-Stokes equations. Perforates of small dimensions, coupled with a backing volume, can indeed be subjected to a wide range of temperatures and to significant temperature gradients in practical situations [67]. This is for example the case inside the combustion chamber of a turbine [93,187] or for hot stream acoustic liners in an engine exhaust duct [315]. The problem of a slit resonator placed in a high temperature environment and subjected to thermal gradients is chosen to reproduce these conditions. Unlike in Section 4.1, no flow is accounted for here.

As already stated in Section 2.1.2, most of the existing impedance models for orifices and acoustic dampers have been derived at ambient temperature [96,135, 215]. This is a consequence of the difficulties to perform pressure measurements under controlled hot conditions, especially when flow is present [67, 187]. Numerical methods appear, therefore, as an appealing alternative to investigate temperature effects. In this work, the complete set of the non-isentropic linearized Navier-Stokes equations is solved in the frequency domain. By accounting for the coupling of acoustic, vorticity and entropy modes, as described in the works of Chu [58,59], the simulations allow to quantify each of the physical source/sink terms responsible for the acoustic damping at the resonator neck in the linear regime.

In this section, the objectives are the following:

- An estimation of the acoustic impedance at high temperature can be obtained by scaling the impedance resulting from measurements and simulations under cold conditions with adequate fluid properties (density, viscosity, and speed of sound). This scaling is investigated here, along with the impact of temperature gradients in the resonator neck.
- Results from both isentropic and non-isentropic sets of LNS equations are compared to assess the accuracy of isothermal non-isopycnic approaches [43]. For this purpose, an extended parametric study on the resonator geometry and the temperature profile inside its neck and cavity is performed. The different dissipation mechanisms involved in the attenuation of acoustic waves in hot environment are further quantified and discussed from the numerical results.

### 4.2.1 Parametric study on Helmholtz resonators in hot environment

The configuration of a two-dimensional Helmholtz resonator with orifice diameter $d_o = 1.5\,\text{mm}$, orifice thickness $l_o \in \{1\,\text{mm},\ 2\,\text{mm},\ 4\,\text{mm}\}$, back cavity length $l_{\text{cav}} \in \{17.5\,\text{mm},\ 35\,\text{mm},\ 52.5\,\text{mm},\ 70\,\text{mm}\}$ and diameter $d_{\text{cav}} = 10\,\text{mm}$ is investigated at three different temperatures $T_0 \in \{300\,\text{K},\ 500\,\text{K},\ 700\,\text{K}\}$. The environmental parameters used are summarized in Table 4.2. The resonator (see Fig. 4.11) is placed at the end of an impedance tube of length $l_{\text{duct}} = 500\,\text{mm}$ and diameter $d_{\text{duct}} = 40\,\text{mm}$, in which a multi-microphone system identification technique, similar to the two-microphone method by Bodén and Åbom [2, 38], is performed to extract the resonator reflection coefficient $R$ and normalized acoustic impedance $z$. $R$ is given by the ratio of the reflected acoustic wave $p'_r$ to the incoming one $p'_i$, i.e. $p'_r/p'_i$. The resonator normalized impedance $z$ is defined as $Z/(\rho_0 c_0)$ and can be computed from the reflection coefficient by means of the expression:

$$z = \frac{(1+R)}{(1-R)}\,. \tag{4.1}$$

To determine the acoustic scattering matrix of the Helmholtz resonator, pressure values are interpolated at a set of monitoring points (MP), placed at different axial positions $x$ in the duct. The interpolation at these monitoring points is performed on the same polynomial basis as the one used for the unknown fields $\{\rho',\ \rho_0 u'_x,\ \rho_0 u'_y,\ p'\}$. The acoustic behavior of the resonator geometries is studied numerically by means of two versions of the linearized Navier-Stokes equations high-order FEM solver, referred to as "*isentropic*" and "*non-isentropic*", depending on the set of equations considered, Eq. (3.9c) or Eq. (3.13). The results obtained from these two sets of equations are compared to assess the accuracy of isothermal non-isopycnic approaches [43].

| $T$ [K] | $\rho_0$ [kg/m$^3$] | $c_0$ [m/s] | $\mu$ [Pa · s] | $\lambda_t$ [W/(m · K)] |
|---|---|---|---|---|
| 300 | 1.1586 | 347.3 | $1.8155 \times 10^{-5}$ | 0.0258 |
| 500 | 0.6952 | 448.3 | $2.7356 \times 10^{-5}$ | 0.0384 |
| 700 | 0.4966 | 530.5 | $3.7407 \times 10^{-5}$ | 0.0471 |

Table 4.2: Air properties at different temperatures used for the simulations, estimated with semi-empirical formulas [97].

Following the observations made for the closed-end waveguide configuration in Section 3.4.2, all the meshes used for the present case satisfy the spatial resolution of the thinnest boundary layer encountered in the chosen frequency range [300 Hz − 4000 Hz]. The Stokes layer thickness reaches its minimal dimension $\delta_{v,\min}$ at the upper limit of the investigated frequency range, i.e.

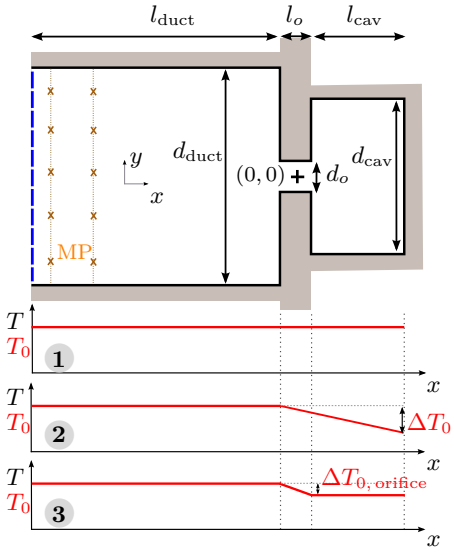


Figure 4.11. Helmholtz resonator configuration and temperature profiles: 1) homogeneous, 2) and 3) linear profiles.

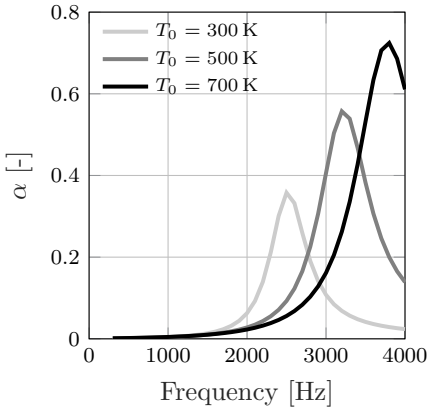


Figure 4.12. Absorption coefficient $\alpha$ in function of the frequency, for $l_o = 1 \times 10^{-3}\,\text{m}$ and $l_{\text{cav}} = 0.0175\,\text{m}$, obtained with the non-isentropic LNSE solver.

$f_{\max} = 4000\,\text{Hz}$, and at the lowest temperature considered, i.e. $T_0 = 300\,\text{K}$, as $\nu$ increases with the temperature. The grids used satisfy a minimal element size near the no-slip wall of value $h_{\min} < \delta_{v,\min} = 3.5 \times 10^{-5}\,\text{m}$. More details on the grids used are given in Appendix D. The no-slip boundary condition is prescribed at the walls of the orifice and on the two sides of the facing sheet. The remaining walls of the impedance tube and resonator cavity are set as slip boundary condition. The dashed line in Fig. 4.11 represents the inlet of the impedance duct, used to inject the incoming acoustic excitation via a characteristic BC (see Section 3.2.1). The results presented in this section have been shown to be independent of the mesh and of the polynomial order used for the representation of the unknown variables (see Appendix D).

### 4.2.2 High temperature resonator without temperature gradient

In this part, the temperature is considered uniform throughout the entire computational domain (see case ① of Fig. 4.11). As the temperature increases, the resonance frequency of the resonator shifts towards higher values. This is illustrated in Fig. 4.12 in terms of absorption coefficient $\alpha$ and corresponds to the experimental observations reported in [39, 97]. This shift originates from

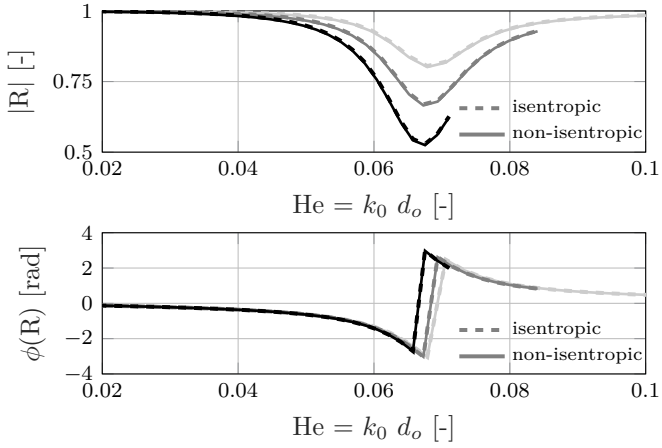


Figure 4.13. Reflection coefficient $R$ for the Helmholtz resonator with $l_{\text{cav}} = 0.0175\,\text{m}$ computed with the LNSE $p$-FEM solvers, with $T_0 = 300\,\text{K}$ (▭), $T_0 = 500\,\text{K}$ (▭), and $T_0 = 700\,\text{K}$ (▭).

the increase in the speed of sound inside the backing volume, whereas the cavity dimensions stay the same. By expressing the frequency in terms of the dimensionless Helmholtz number He, defined here as $\text{He} = k_0\, d_o$, the change in speed of sound is filtered out. As a consequence, the frequency shift due only to the temperature effects on the visco-thermal losses is apparent.

Figure 4.13 shows the impact of the temperature on the amplitude (top) and phase (bottom) of the reflection coefficient $R$ in function of He. From these curves, it can be seen that the visco-thermal losses rise with increasing temperature. A slight shift towards lower Helmholtz numbers can be observed for the resonance peak as well. This shift is found to be larger between $T_0 = 500\,\text{K}$ and $700\,\text{K}$ than between $T_0 = 300\,\text{K}$ and $500\,\text{K}$. By comparing the results from the isentropic LNSE $p$-FEM solver and the ones coming from the complete set of non-isentropic LNS equations, it appears that only very little additional thermal dissipation is added by resolving the thermal boundary layer inside the resonator neck. This observation holds for the three investigated temperatures and all tested resonator geometries under homogeneous conditions. In these cases, accounting for the thermal dissipation delivers an increase only up to $1.5\,\%$ in predicted absorption coefficient $\alpha$.

### Scaling of impedance models with temperature

Figure 4.14 shows the computed impedance values for the studied Helmholtz resonator compared to the impedance values predicted with a semi-empirical model scaled with the fluid properties ($\rho_0$, $\mu$ and $c_0$) according to the

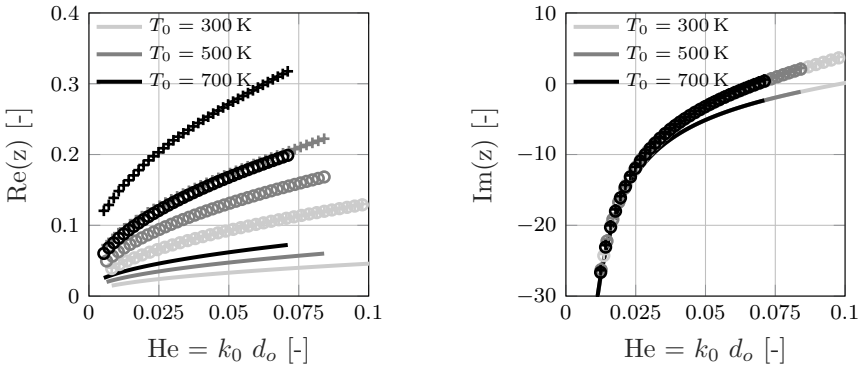


(a) Normalized resistance

(b) Normalized reactance

Figure 4.14. Normalized resistance (left) and reactance (right) of the Helmholtz resonator ($l_{\mathrm{cav}} = 0.0175\,\mathrm{m}$, $l_o = 1\,\mathrm{mm}$) at three temperature levels, obtained from Maa/Allam [10,209] model discarding end-corrections (—), from complete Maa/Allam model scaled with fluid properties (○) and computed from $p$-FEM LNS solver (+).

temperature. As the present simulations are carried out for a 2-D geometry and end-corrections for 2-D models are not easily available in the literature, the semi-empirical impedance model used here is the one given by Maa [209] and Allam [10] for a slit-shaped orifice. This model defines the normalized resistance and reactance in the linear regime as

$$\mathrm{Re}(z) = \mathrm{Re}\left(\frac{j\omega l_o}{\sigma c_0}\left[1 - \frac{\tanh\left(\mathrm{Sh}\sqrt{j}\right)}{\mathrm{Sh}\sqrt{j}}\right]^{-1}\right) + \frac{\alpha_s R_s}{\sigma\rho_0 c_0} + \frac{\sigma_{\mathrm{BC}}\alpha_s R_s}{\sigma\rho_0 c_0}\,, \tag{4.2}$$

$$\mathrm{Im}(z) = \mathrm{Im}\left(\frac{j\omega l_o}{\sigma c_0}\left[1 - \frac{\tanh\left(\mathrm{Sh}\sqrt{j}\right)}{\mathrm{Sh}\sqrt{j}}\right]^{-1}\right) + 0.5\,\frac{\delta_s\omega}{\sigma c_0} + 0.5\,\frac{\sigma_{\mathrm{BC}}\delta_s\omega}{\sigma c_0}\,. \tag{4.3}$$

Here, the dimensionless shear number Sh relates the orifice radius to the viscous boundary layer thickness and is defined as $\mathrm{Sh} = d_o\sqrt{\omega\rho_0/(4\mu)}$. Note that the model is expressed here for the case where the back cavity diameter differs from the duct diameter in which the resonator is placed, as it is the case in the present work. $\sigma$ represents the open area ratio on the side of the impedance duct, whereas $\sigma_{\mathrm{BC}}$ is the one on the backing volume side. The porosities $\sigma$ and $\sigma_{\mathrm{BC}}$ are therefore given by $\sigma = S_o/S_{\mathrm{duct}} = d_o^2/d_{\mathrm{duct}}^2$ and $\sigma_{\mathrm{BC}} = S_o/S_{\mathrm{cav}} = d_o^2/d_{\mathrm{cav}}^2$, respectively. $R_s$ is the surface resistance on one side of the plate which is given by $R_s = 0.5\sqrt{2\mu\rho_0\omega}$, according to Rayleigh [240]. The end-correction parameter $\alpha_s$ for the resistance and the one for the reactive part $\delta_s$, which depends on the fictitious third dimension of the orifice $l_s$ through an equivalent diameter $d_{\mathrm{eq}} = 2\sqrt{d_o l_s/\pi}$, have been fitted to match the numerical results for the case at

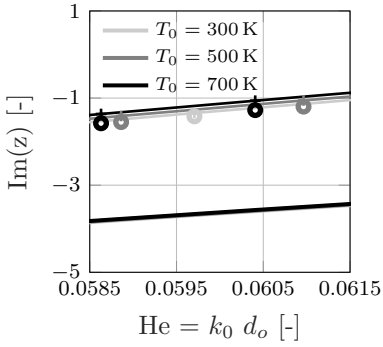


Figure 4.15. Close-up on the reactance for the investigated resonator ($l_{\mathrm{cav}} = 0.0175\,\mathrm{m}$, $l_o = 1\,\mathrm{mm}$) at three temperature levels, obtained from Maa/Allam [10, 209] model discarding end-corrections (—), from complete Maa/Allam model scaled with fluid properties (O) and computed from $p$-FEM LNS solver (+).

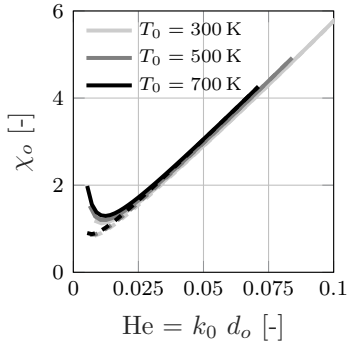


Figure 4.16. Normalized mass reactance $\chi_o$ of the resonator neck (for $l_{\mathrm{cav}} = 0.0175\,\mathrm{m}$) in different homogeneous temperature environments, computed with the isentropic LNS solver (- - -) and with the non-isentropic one (—).

$T_0 = 300\,\mathrm{K}$. This case is taken here as reference, as such model has been first developed for ambient conditions. The values found for these parameters are: $\alpha_s = 2.25$ [−], $\delta_s = 0.85\,d_{\mathrm{eq}}$ with $l_s = 0.01\,\mathrm{m}$ for $l_o = 1\,\mathrm{mm}$.

The basic scaling of the model with respect to the fluid properties appears to deliver good results for the reactance (see Fig. 4.14b). A close-up view of the reactance curves, given in Fig. 4.15, however, reveals a slight increase in the inertia in the numerical results, which is not captured at all by the semi-empirical model. The normalized mass reactance $\chi_o$, representing the end-correction effects at the resonator neck, is shown in Fig. 4.16. This quantity is found to increase with temperature and can be related to both increase in reactance and shift towards lower He values for the reflection peak. The slope of the curves in Fig. 4.16 is nearly the same for the majority of the investigated He range. The results given by the two solvers are here also very close, with discrepancies in the predicted normalized mass reactance appearing only for the very low He limit (for $\mathrm{He} < 0.025$). This deviation is thought to originate from the increased thermal losses for very small He and the difficulty to invert Eq. (4.1) when the reflection coefficient is very close to 1. Concerning the resistive part, the applied scaling is found to be less suitable. Even if the dependence of resistance on temperature is found similar for the model and the numerical predictions, the scaled semi-empirical model is unable to capture correctly the amount of additional visco-thermal losses due to temperature increase. The higher the temperature, the more inaccurate the model is. The experimental work done

| T [K] | $l_{\text{cav}}$ [m] | $\alpha_s$ [-] ($\epsilon_{\alpha_s}$ [%]) | | |
|---|---|---|---|---|
| | | $l_o = 1\,\text{mm}$ | $l_o = 2\,\text{mm}$ | $l_o = 4\,\text{mm}$ |
| 300 | 0.0175 | 2.25 (0.7 %) | 2.15 (0.9 %) | 2.0 (2.8 %) |
| | 0.0350 | 2.3 (1.7 %) | 2.20 (2.4 %) | 2.10 (4.8 %) |
| | 0.0525 | 2.3 (1.6 %) | 2.20 (2.1 %) | 2.05 (3.8 %) |
| 500 | 0.0175 | 3.4 (2.0 %) | 3.65 (1.5 %) | 4.2 (1.3 %) |
| | 0.0350 | 3.45 (1.4 %) | 3.75 (1.3 %) | 4.4 (1.8 %) |
| | 0.0525 | 3.5 (3.4 %) | 3.8 (3.3 %) | 4.55 (4.8 %) |
| 700 | 0.0175 | 4.5 (4.1 %) | 5.1 (3.6 %) | 6.35 (2.6 %) |
| | 0.0350 | 4.5 (3.1 %) | 5.2 (2.7 %) | 6.65 (2.9 %) |
| | 0.0525 | 4.6 (2.8 %) | 5.3 (2.6 %) | 6.85 (2.7 %) |

Table 4.3: Values of the end-correction parameter $\alpha_s$ in Eq. (4.2) giving the best fit with the $p$-FEM LNS impedance results and relative error $\epsilon_{\alpha_s}$.

by Elnady et al. [97] leads to similar conclusions, even if in their case some nonlinear effects and the impact of a small temperature gradient through the orifice might be present as well. The impedance model by Elnady nonetheless tends to overestimate the visco-thermal losses.

The analytical part of the impedance model given by Eq. (4.2) and Eq. (4.3) is based on an approximated solution of the Kirchhoff theory [180] derived first by Rayleigh [240] and Crandall [68] assuming the thermal conductivity negligible. This expression does not account for non-isentropic effects, as opposed to more elaborated solutions by Stinson [271] and Tijdeman [291] for 3-D orifice geometries. Nevertheless, as both isentropic and non-isentropic versions of the LNS solver deliver very similar values for the orifice resistance when $\Delta T_0 = 0$, the aforementioned under-prediction in resistance is thought to originate predominantly from the end-correction parts of Eq. (4.2). The parameter $\alpha_s$ of this expression is therefore modified to fit the numerical values as well as possible. The fitting of $\alpha_s$ is obtained by modifying $\alpha_s$ by steps of 0.05 and retaining the value leading to the smallest overall error on the complete frequency ranges. Table 4.3 regroups the adjusted $\alpha_s$ parameters for the different geometries and temperatures of this study. The averaged relative errors over the frequency range of the fitted model with the resistance from the LNS solver are indicated in the table (referred to as $\epsilon_{\alpha_s}$, in gray) as well. The temperature appears to be the factor with the largest impact on the $\alpha_s$ values, whereas the cavity length has overall a very small influence on them. The length of the orifice seems to gain in importance with increasing temperature. However, no clear trend is found. For the case with $T_0 = 300\,\text{K}$, an increase in $l_o$ leads to slightly smaller $\alpha_s$ values, whereas this is reversed for the two other temperature levels ($T_0 = 500\,\text{K}$ and $T_0 = 700\,\text{K}$). The accuracy of the fitting is found to become poorer (i.e. larger $\epsilon_{\alpha_s}$) at higher temperature levels. This

implies that it is not sufficient to simply adapt the $\alpha_s$ parameter as a single value at higher temperature. A proper expression for $\alpha_s$ should include frequency and fluid properties dependency. This observation is in agreement with the work from Temiz [286], where the $\alpha_s$ parameter is an inverse function of the shear number Sh. The given expression, derived from experimental results at ambient temperature, delivers increased $\alpha_s$ values, and therefore larger resistances, at higher temperatures and frequencies, as it is observed in Fig. 4.14a.

### End-effects at the resonator neck

In order to study the impact of the orifice finite length $l_o$ on the end-effects, Fig. 4.17 represents the numerical velocity profiles at six different sections of the orifice. It can be observed that end-effects are bounded to a particular length from the orifice face-sheets, nearly independent of $l_o$ disregarding the slight shift in frequency between the cases. For this case at $T_0 = 300\,\mathrm{K}$, the impacted part of the orifice reaches $l_{\text{end-effects}} = 0.5\,\mathrm{mm}$. As it can be seen in Fig. 4.17a for

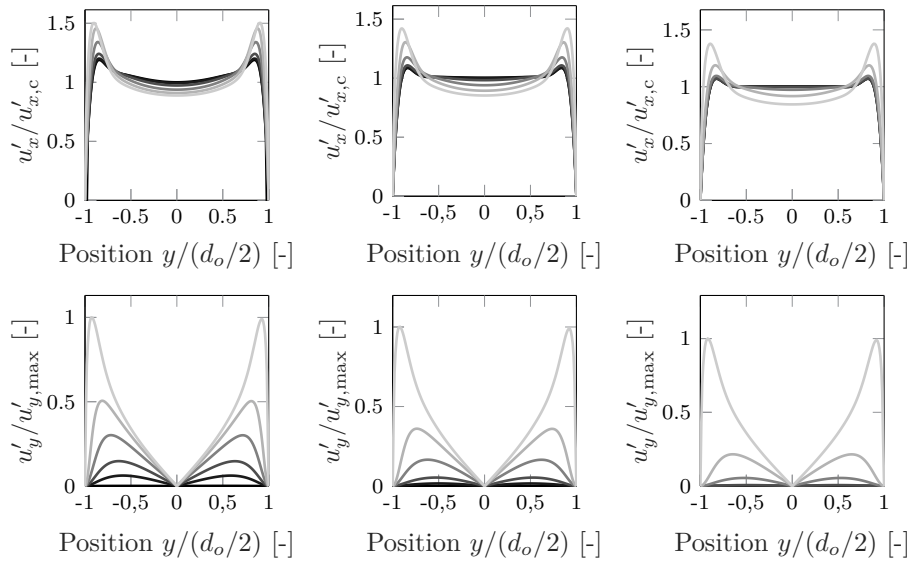


(a) For $l_o = 1\,\mathrm{mm}$, at $f = 1600\,\mathrm{Hz}$ near resonance frequency

(b) For $l_o = 2\,\mathrm{mm}$, at $f = 1500\,\mathrm{Hz}$ near resonance frequency

(c) For $l_o = 4\,\mathrm{mm}$, at $f = 1300\,\mathrm{Hz}$ near resonance frequency

Figure 4.17. Velocity profiles at different sections of the orifice for the case with $l_{\text{cav}} = 0.035\,\mathrm{m}$ at $T_0 = 300\,\mathrm{K}$, axial velocity $u'_x$ (top) and radial velocity $u'_y$ (bottom) components: sections at positions $x/(t/2) = 0$ (—), 0.25 (—), 0.5 (—), 0.75 (—), 0.9 (—), 1.0 (—).

$l_o = 1\,\text{mm}$, all profiles are different, whereas in the case of $l_o = 4\,\text{mm}$ only the most outer profiles are distinct from the orifice center profile.

### Impact of cavity length on absorption curves

Figure 4.18 illustrates the effect of changing the backing cavity length $l_{\text{cav}}$ on the absorption behavior of the Helmholtz resonator. As expected, the increase in cavity length leads to lower resonance frequencies for the Helmholtz resonator, as the cavity volume becomes larger. The absorption coefficient $\alpha$ is also found to decrease for increasing $l_{\text{cav}}$. A second resonance peak appears at high frequencies (around $\text{He} = 0.082$) for the largest value of $l_{\text{cav}}$. This second peak is not related to a Helmholtz type of resonance but to the backing cavity acting as a quarter-wave resonator. Nevertheless, the frequency $f_{\lambda/4}$ at which this resonance is observed deviates slightly from the one expected for a pure quarter-wave resonator $f_{\lambda/4} = c_0/(2l_{\text{cav}})$. The peak takes place at a higher frequency, corresponding to a shorter effective length of the cavity due to the opening (with a rather small open area ratio $\sigma$), which differs from the situation with a planar acoustic wave front. For the other values of $l_{\text{cav}}$, this phenomenon appears beyond the investigated range of frequencies.

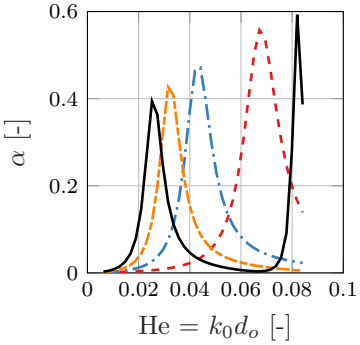


Figure 4.18. Impact of $l_{\text{cav}}$ on the absorption coefficient as a function of He, obtained for ($T_0 = 500\,\text{K}$, $l_o = 1\,\text{mm}$) with the non-isentropic LNSE solver: $l_{\text{cav}} = 0.0175\,\text{m}$ (- - -), $l_{\text{cav}} = 0.035\,\text{m}$ (—·—), $l_{\text{cav}} = 0.0525\,\text{m}$ (— —), and $l_{\text{cav}} = 0.07\,\text{m}$ (——).

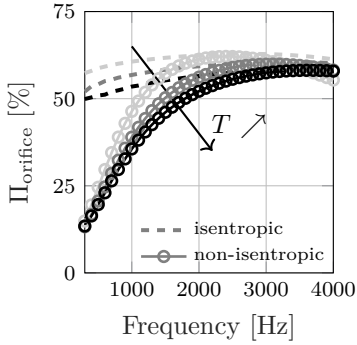


Figure 4.19. Contribution of the orifice inner part to the global acoustic energy dissipation $\Pi_{\text{orifice}}$ in function of the temperature, with $\Delta T_{0,\text{orifice}} = 0\,\text{K}$: $T_0 = 300\,\text{K}$ (□), $T_0 = 500\,\text{K}$ (■), $T_0 = 700\,\text{K}$ (■).

### Dissipation mechanisms in homogeneous conditions

Following Section 3.3, the total integral term for the acoustic energy dissipation $\mathbb{D}'$ is computed by numerical integration over different parts of the domain, as given by Eq. (3.75). By computing the integral terms for the dissipation mechanisms over the inner part of the orifice only (referred to as $\mathbb{D}'_{\text{orifice}}$) instead of the complete domain (namely $\mathbb{D}'_{\text{Total}}$), one can estimate the amount of energy that is dissipated solely inside the resonator neck. The remaining dissipation takes place as end-correction in the close vicinity of the orifice ends and at the walls of the resonator facing sheet. This is illustrated in Fig. 4.19. The contribution $\Pi_{\text{orifice}}$ of the orifice to the total dissipative integral terms is found to be rather similar at different temperatures, with $\Pi_{\text{orifice}}$ around 60 % near the resonance frequencies. A slight decrease in $\Pi_{\text{orifice}}$ can be seen in Fig. 4.19 with increasing temperature. This is explained by the relative increase in internal resistance compared to the end-correction contribution. The latter originates from the air in the close vicinity outside the orifice. This result is consistent with the expression in Eq. (4.2), and can also be visualized in Fig. 4.14a.

The integral terms related to dissipative effects $\mathbb{D}'$ are now computed on different spatial subsets of the numerical domain at an arbitrary temperature. The orifice's inner part ("orifice"), the orifice including the air in direct vicinity ("orifice + EC"), as well as a zone including the orifice and the facing sheet walls ("orifice + EC + walls") are considered, as depicted in Fig. 4.20a. Each

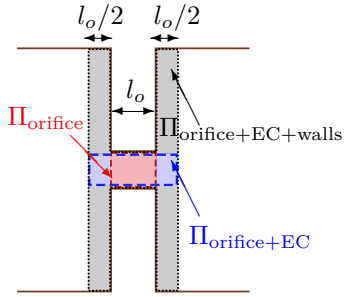


(a) Drawing of the zones considered to compute the spatial contribution to the dissipative mechanisms.

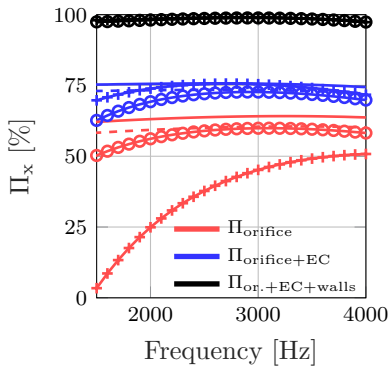


(b) Contribution $\Pi_x$ of different zones to the integral dissipative term $\mathbb{D}'$.

Figure 4.20. Contribution of different zones to the total acoustic energy dissipation for the case with $l_o = 2\,\text{mm}$, $l_{\text{cav}} = 0.0175\,\text{m}$, and $T_0 = 500\,\text{K}$: $\Delta T_{0,\,\text{orifice}} = 0\,\text{K}$ with isentropic (- - -) and non-isentropic (-o-) LNSE, $\Delta T_{0,\,\text{orifice}} = 40\,\text{K}$ with isentropic (——) and non-isentropic (-+-) LNSE.

contribution is defined as:

$$\Pi_{\mathrm{x}} = 100\,\frac{|\mathbb{D}'_{\mathrm{x}}|}{|\mathbb{D}'_{\mathrm{Total}}|}\,, \tag{4.4}$$

where $\mathbb{D}'_{\mathrm{Total}}$ and $\mathbb{D}'_{\mathrm{x}}$ are the integral terms for the dissipation over the complete computational domain and over the zone x, respectively.

The contributions $\Pi_{\mathrm{x}}$ of the different zones are plotted in Fig. 4.20b, for both isentropic and non-isentropic LNS solvers. As it can be expected, the contribution of a zone increases with its size and almost all the dissipative effects are happening in the zone "orifice + EC + walls", as $\Pi_{\mathrm{orifice+EC+walls}} \approx 100\,\%$. The majority of the acoustic energy dissipation, i.e. $\approx 75\,\%$, is taking place in the orifice and close-by mass of air. The results for the situation with a temperature gradient through the orifice, $\Delta T_{0,\,\mathrm{orifice}} = 40\,\mathrm{K}$, have been added to Fig. 4.20b. The difference between the isentropic and non-isentropic solvers for each contribution is much bigger in the presence of temperature gradients. The specific contribution of the end-corrections also appears to be larger when a temperature gradient exists through the orifice. This is related to the augmented thermal conduction in the latter case.

### 4.2.3 High temperature resonator with temperature gradient

A temperature gradient is now considered, either through the orifice and back cavity (see ② in Fig. 4.11) or through the orifice only (see ③ in Fig. 4.11). Only linear temperature profiles are reported here as other shapes have led to similar observations.

#### Dissipation mechanisms in non-homogeneous conditions

First, an arbitrary linear temperature profile is imposed, defined between the resonator face sheet at $T_0$ and the temperature at the backing wall $T_w = T_0 - \Delta T_0$, for $\Delta T_0 \in [0\,\mathrm{K} - 500\,\mathrm{K}]$, see Fig. 4.11. The temperature inside the impedance duct is taken equal to $T_0 = 700\,\mathrm{K}$ to allow such a large temperature change through the resonator cavity. This provides a maximal temperature gradient of $T_{0,\,\mathrm{orifice}} = 21.6\,\mathrm{K}$ through the orifice. Figure 4.21 shows for the three cases, i.e. $\Delta T_0 = 0\,\mathrm{K}$, $\Delta T_0 = 100\,\mathrm{K}$ and $\Delta T_0 = 500\,\mathrm{K}$, the distinct terms of the perturbed energy balance in Eq. (3.73), displayed as $10\log\left(|\mathbb{D}'_{\bullet}|^2\right)$. Due to the choice of harmonic perturbation fields, the first term in Eq. (3.75) is equal to zero, i.e. $\mathbb{E}' = 0$. In all cases, the numerical results satisfy the energy balance given in Eq. (3.71). The relation $\mathbb{W}' = \mathbb{D}'$ is indeed verified over the entire frequency range of this study.

In absence of mean flow and interior heat sources terms, $\mathbb{D}'_v$ and $\mathbb{D}'_{\dot{q}_V}$ are equal to zero. The dissipation terms are maximal at the resonance frequency

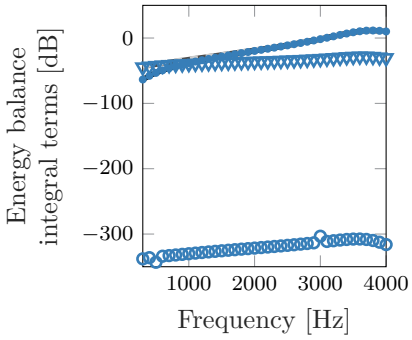


(a) $T_0 = 700\,\mathrm{K}$ and $\Delta T_0 = 0\,\mathrm{K}$

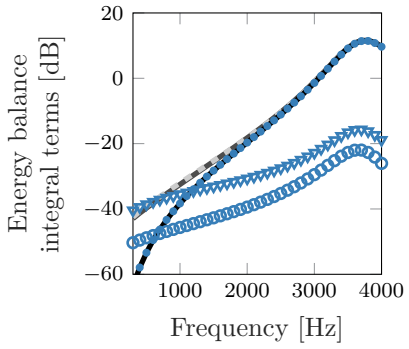


(b) $T_0 = 700\,\mathrm{K}$ and $\Delta T_0 = 100\,\mathrm{K}$

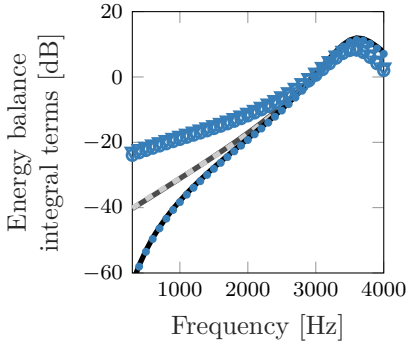


(c) $T_0 = 700\,\mathrm{K}$ and $\Delta T_0 = 500\,\mathrm{K}$

Figure 4.21. Integral terms defined in Eq. (3.73) for the energy balance over the computational domain from the non-isentropic set of LNS equations: total energy source $\mathbb{D}'$ (—), total energy flux $\mathbb{W}'$ (- - -), and the contributions of $\mathbb{D}'_v$ (□), $\mathbb{D}'_s$ (○), $\mathbb{D}'_\mu$ (●), $\mathbb{D}'_{\dot{q}V}$ (△), and $\mathbb{D}'_t$ (▽). $\mathbb{D}'$ values obtained with simulations under isentropic assumption are also indicated (—).

(around $f = 3700\,\mathrm{Hz}$), as the amplitudes of the velocity and temperature fluctuations are maximal at the resonance. For the homogeneous temperature case, i.e. Fig. 4.21a, the viscous losses are clearly the predominant ones. Thermal losses are quantitatively not varying significantly through the frequency range and are of importance only at low frequencies. The dissipation term related to entropy is, as expected, close to zero in the absence of temperature gradients. For $\Delta T_0 \neq 0$, it can be observed in Figs. 4.21b and 4.21c that the terms related to entropy $\mathbb{D}'_s$ and thermal diffusion $\mathbb{D}'_t$ increase significantly with $\Delta T_0$. The range of frequencies for which these mechanisms are determining is getting wider. It is also found that the term $\mathbb{D}'_s$ rises faster than $\mathbb{D}'_t$ for increasing temperature gradients. In Fig. 4.21c, $\mathbb{D}'_s$ and $\mathbb{D}'_t$ reach a similar order of magnitude. Overall, the peak amplitude of the total dissipation term $\mathbb{D}'$ varies

very little with increasing $\Delta T_0$, with an increase of the order of 1 dB from $\Delta T_0 = 0\,\mathrm{K}$ to $\Delta T_0 = 500\,\mathrm{K}$. This observation is actually the superposition of two opposite effects: an overall drop of the average temperature inside the orifice (which tends to decrease the dissipation) and an increasing temperature gradient (which contributes to enhance the thermal conduction). Same conclusions and similar curves are obtained for the temperature distribution ③, as most of the extra dissipation terms $\mathbb{D}'_s$ and $\mathbb{D}'_t$ originate from the orifice region.

### Deviation between isentropic and non-isentropic LNS solvers in presence of a temperature gradient

The configuration ③ makes the comparison easier between results of the parametric study on the parameters $l_o$ and $l_{\mathrm{cav}}$ and will be adopted in the following. This parametric analysis aims at understanding and quantifying the importance of the entropy and thermal effects on the dissipation of acoustic waves. It has been observed [296] for a given resonator geometry, that the discrepancy between the absorption coefficient curves predicted from the isentropic and non-isentropic solvers, referred to as $\epsilon_\alpha$, becomes larger with growing temperature gradient $\Delta T_0$. The deviation $\epsilon_\alpha$ is given by the following expression:

$$\epsilon_\alpha = \frac{|\alpha_{\mathrm{isent}}(f_{\mathrm{res}}) - \alpha_{\mathrm{non-isent}}(f_{\mathrm{res}})|}{|\alpha_{\mathrm{isent}}(f_{\mathrm{res}})|}\,, \tag{4.5}$$

where $f_{\mathrm{res}}$ is the resonance frequency of the resonator. A parametric study on $\epsilon_\alpha$ is considered here. This is achieved by computing the absorption coefficient of different resonator geometries under several thermal conditions, taking $\Delta T_{0,\,\mathrm{orifice}} \in \{5\,\mathrm{K},\ 10\,\mathrm{K},\ 20\,\mathrm{K},\ 40\,\mathrm{K},\ 80\,\mathrm{K}\}$. The orifice length varies as $l_o \in \{1\,\mathrm{mm},\ 2\,\mathrm{mm},\ 4\,\mathrm{mm}\}$, and the back cavity length takes the values $l_{\mathrm{cav}} \in \{17.5\,\mathrm{mm},\ 35\,\mathrm{mm},\ 52.5\,\mathrm{mm},\ 70\,\mathrm{mm}\}$. Figure 4.22 summarizes the results on $\epsilon_\alpha$ obtained by varying the cavity length $l_{\mathrm{cav}}$. The figure confirms, for all cases, that an increase in $\Delta T_{0,\,\mathrm{orifice}}$ leads to larger deviation $\epsilon_\alpha$ between the isentropic and non-isentropic solvers. The change in $l_{\mathrm{cav}}$ is predominantly affecting the resonance frequency of the resonator. It was expected that the left shift in resonance frequency for increasing $l_{\mathrm{cav}}$ would lead to enlarged deviation in terms of computed absorption coefficient. Nevertheless, it is shown in Fig. 4.22 that $\epsilon_\alpha$ is decreasing with increasing $l_{\mathrm{cav}}$ values. This trend can be observed systematically at each $\Delta T_{0,\,\mathrm{orifice}}$ value for the case of an orifice of length $l_o = 1\,\mathrm{mm}$, as well as for other $l_o$ values. Following the present results, the impact of $l_{\mathrm{cav}}$ on $\epsilon_\alpha$ can be characterized as secondary or minor. It appears that even if the dissipation terms related to thermal $\mathbb{D}'_t$ and entropy $\mathbb{D}'_s$ effects are more important at lower frequencies, they tend to compensate each other for the overall energy balance. The relative difference between the two solvers is found to be overall small for the investigated cases of Fig. 4.22, with $\epsilon_\alpha \leq 2.5\,\%$.

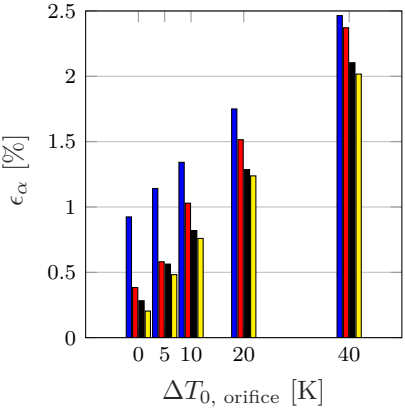


Figure 4.22. Impact of $l_{\text{cav}}$ on the deviation in estimation of the peak magnitude of the absorption coefficient between the isentropic and non-isentropic $p$-FEM solvers, in function of $\Delta T_{0,\,\text{orifice}}$: $l_{\text{cav}} = 0.0175\,\text{m}$ (■), $l_{\text{cav}} = 0.035\,\text{m}$ (■), $l_{\text{cav}} = 0.0525\,\text{m}$ (■), and $l_{\text{cav}} = 0.07\,\text{m}$ (■).

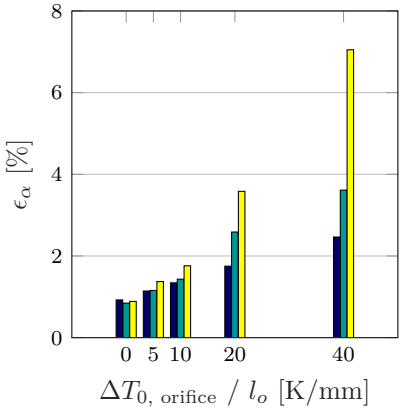


Figure 4.23. Impact of $l_o$ on the deviation in estimation of the peak magnitude of the absorption coefficient between the isentropic and non-isentropic $p$-FEM solvers, in function of $\Delta T_{0,\,\text{orifice}}/l_o$: $l_o = 1\,\text{mm}$ (■), $l_o = 2\,\text{mm}$ (■), $l_o = 4\,\text{mm}$ (■).

The influence of the orifice length on the error $\epsilon_\alpha$ in terms of absorption coefficient $\alpha$ is shown in Fig. 4.23. It is found that for a given temperature jump through the orifice $\Delta T_{0,\,\text{orifice}}$, the longer the orifice is, the more important it is to consider non-isentropic effects. This can be explained by the global increase in dissipation due to the visco-thermal terms in the energy equation, predominantly the thermal ones, linked to a longer orifice. For the investigated configurations, the difference in terms of predicted absorption coefficient reaches 7 % at maximum.

### 4.2.4 Conclusions

The LNS $p$-FEM was applied to the case of Helmholtz resonators in a hot environment, with given temperature profiles inside their neck and cavity. The results from the numerical linearized approach are in agreement with previous experimental observations. The validity of the traditional scaling of an equivalent cold flow impedance model appears to be limited with regard to the resistance. Compared to high-temperature experiments, the numerical approach allows a precise control over the temperature field inside the resonator neck and the thorough investigation of the different mechanisms involved in the acoustic

energy dissipation in presence of temperature gradients. The latter is achieved by means of the numerical integration of the energy balance for the acoustically perturbed field. A parametric study on the resonator neck length, the backing cavity depth and the temperature jump across the facing sheet was performed. For the considered set of geometries and thermal conditions, the isentropic and non-isentropic versions of the linearized Navier-Stokes equations can deliver divergent results in terms of absorption peak amplitude, with a relative deviation which can reach up to 7 %. The analysis of the different mechanisms involved in the dissipation of acoustic energy has shown that entropy and thermal effects become relevant in the low Helmholtz numbers range in the presence of temperature gradients through the resonator neck. The length of the resonator neck is found to be an important factor to consider in this regard.

## 4.3 Impact of turbulence on perforates

The main contributions to sound attenuation in laminar flow configurations come from visco-thermal effects, mean flow convection and interaction with entropy and vorticity modes. These different phenomena have been examined for the case of perforates in their linear regime in Sections 3.4, 4.1 and 4.2. When sound waves propagate within a turbulent flow, turbulent mixing can result in extra acoustic attenuation due to energy loss by turbulent absorption. This absorbing mechanism can be attributed to the turbulent stress acting on the sound wave. The purpose of this section is to investigate the mechanisms of sound-flow and sound-turbulence interactions for orifices at low Mach number by means of the hybrid numerical methodology described in Section 3.2 based on the triple (Section 3.1.2) and double (Section 3.1.1) decompositions of the compressible Navier-Stokes equations.

A comparison between triple (turbulent) and double (quasi-laminar) decomposed sets of equations has been made in [114] for the case of a T-junction in the Strouhal number Sr range from 0 to 4. It has been observed that for small Strouhal numbers, $\mathrm{Sr} < 0.5$, the behavior tends to a quasi-stationary response, with turbulent and quasi-laminar LNSE giving similar results for the scattering matrix of the T-joint geometry. Additionally, it exists a frequency range where flow turbulence affects the acoustic wave propagation. The idea of this section is to investigate if such conclusions are holding in case of an orifice under bias and grazing flow conditions.

### 4.3.1 Orifice with turbulent bias flow

A single orifice under bias flow condition with a normal acoustic excitation is considered at first. A similar configuration has already been successfully

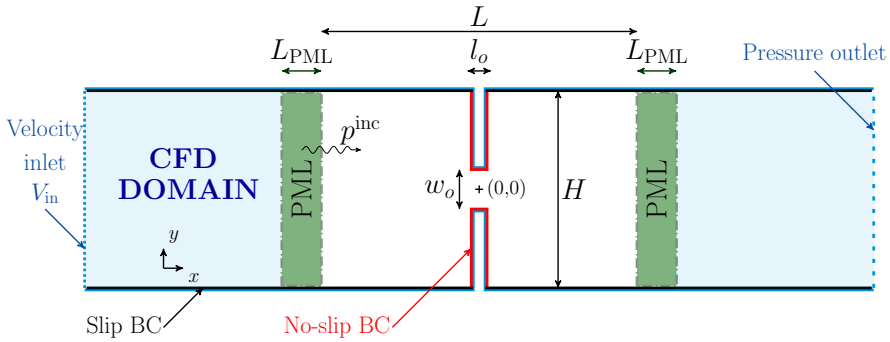


Figure 4.24. Overview of the geometry for the 2-D orifice in a duct.

studied by Kierkegaard et al. [175] by means of a frequency-domain LNSE standard FEM solver. The linearized approach has proven to correctly predict the whistling potential of such orifices. The present work aims at assessing the impact of flow and flow turbulence on the acoustic behavior of such an orifice with a frequency domain LNS high-order FEM solver. A comparison between quasi-laminar and turbulent LNS models is performed on this particular configuration to assess the impact of flow turbulence on the acoustic behavior of orifices.

### Configuration

This work focuses on the acoustic scattering of a plane wave impinging on a plate with a relatively large single hole with flow passing through. A sketch of the computational domains used for the CFD simulations and the acoustic propagation computations is depicted in Fig. 4.24. The dimensions of the setup are ($l_o = 0.004\,\mathrm{m} \times w_o = 0.02\,\mathrm{m}$) for the perforation and ($L = 33.2\,w_o \times H = 2\,w_o$) for the duct. The PML domains (see Section 3.2.1) for injection of the acoustic plane mode into the physical domain and non-reflective boundary conditions have a length $L_{\mathrm{PML}} = 0.5\,w_o$. Boundary conditions for the CFD and LNSE models are indicated as well in Fig. 4.24.

### Discussion on flow results

The mean flow field is computed using a steady RANS simulation, carried out with the commercial CFD software ANSYS® Fluent. The $K$-$\epsilon$ model combined with enhanced wall functions is solved using the SIMPLE algorithm. The spatial discretization is a standard volume method, where the momentum and pressure equations, as well as the turbulent kinetic energy and the specific dissipation rate

| Symbol | Flow property | Value | Unit |
|---|---|---|---|
| $\gamma$ | Ratio of specific heats | 1.4 | [-] |
| $p_0$ | Operating pressure | 101325 | [Pa] |
| $\rho_0$ | Fluid density | 1.205 | [kg/m$^3$] |
| $c_0$ | Speed of sound | 343.11 | [m/s] |
| $M_{0,\text{inlet}}$ | Inlet Mach number | 0.0396 | [-] |
| $\mu$ | Dynamic viscosity | $1.8208\,10^{-5}$ | [Pa · s] |
| $\nu$ | Kinematic viscosity | $1.5110\,10^{-5}$ | [m$^2$/s] |
| $T_0$ | Ambient temperature | 293.15 | [K] |

Table 4.4: Flow parameters for the 2-D orifice case under bias flow condition.

equations, are all discretized with second-order accuracy schemes. A turbulence intensity TI = 10 % is assumed. The eddy-viscosity data are exported from the $K$-$\epsilon$ model RANS computations, given by $\mu_t = \rho_0 C_\mu K^2/\epsilon$, where $K$ is the turbulence kinetic energy, $\epsilon$ is the turbulent dissipation, and $C_\mu$ is a defined constant. The solution of the RANS simulation is mapped onto the coarser acoustic grid, applying linear interpolation of the flow field variables and their derivatives. The flow parameters selected for the CFD simulations are listed in Table 4.4.

An inflow velocity $V_{\text{in}} = 13.6\,\text{m/s}$, corresponding to a Mach number $M_{0,\text{inlet}} = 0.0396$, is chosen. It ensures to have a low Mach number flow throughout the entire computational domain. The Reynolds number, based on the duct height, is

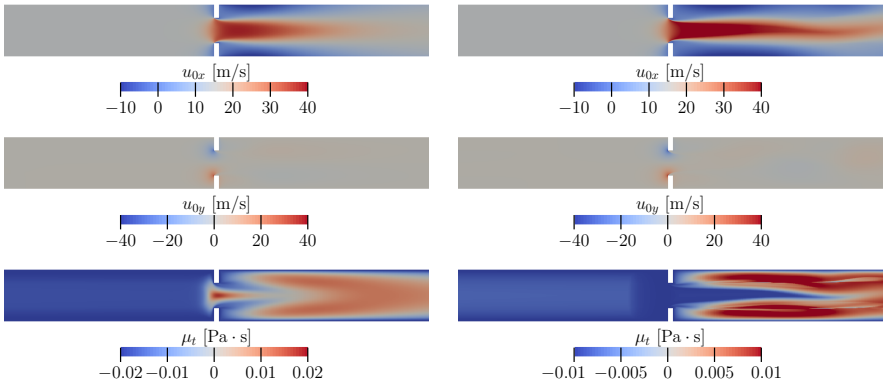


(a) $K$-$\epsilon$ model (b) SST $K$-$\omega$ model

Figure 4.25. Mean flow field obtained from steady RANS simulations (mapped on the acoustic mesh): axial velocity $u_{0x}$ (top), radial velocity $u_{0y}$ (center), and eddy-viscosity $\mu_t$ (bottom).

equal to $\mathrm{Re} = 3.6 \times 10^4$. A maximum velocity magnitude of $|\mathbf{u_0}|_{\max} = 38.4\,\mathrm{m/s}$, i.e. $M_0 = 0.11$, is obtained in the region of the orifice by the formation of a jet, which expands downstream of the perforation. Typical recirculation areas can be seen in Fig. 4.25 downstream of the orifice and in the orifice itself.

Additionally to the $K$-$\epsilon$ model, the SST $K$-$\omega$ model has been used as well to generate an alternative mean flow field (Fig. 4.25b). Both the recirculation area, with the reattachment length, and the spatial distribution of eddy-viscosity show a dependency on the choice of the RANS model used, as shown in Fig. 4.25. The SST $K$-$\omega$ is also found more prone to generate a jet flow which tends to attach itself to one of the duct walls. This phenomena is known as the Coandă effect [300] and can been seen in Fig. 4.25b, where the jet is not perfectly symmetric along the axial direction.

Considering a slip boundary condition on the duct side walls has a direct influence on the flow profile inside the duct sections. It also affects the recirculation zone downstream of the plate and the flow near the orifice. Previous works, e.g. [8], tend however to show that the scattering by the orifice plate is not sensitive to the side wall boundary condition used. Therefore, in this work, only a slip wall boundary condition is considered at the side walls.

### Sound-turbulence interaction at orifice with bias flow

The LNS $p$-FEM simulations of the perturbed field have been performed on a 2-D computational grid with approximately 37000 linear triangular elements and $3^{th}$-order interpolating Lobatto polynomial functions, yielding a system of about 487000 degrees of freedom. The isentropic set of LNS equations

(a) Complete mesh: physical domain (—) and PML (—)

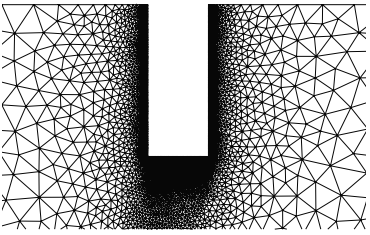

(b) Close-up view on the orifice zone

Figure 4.26. Unstructured triangular grid used for the frequency domain $p$-FEM acoustic simulations with the isentropic LNS operator.

is used here and dissipation terms in the energy equation are disregarded for this case at ambient temperature. The size of the smallest element is determined from the ABL thickness $\delta_a = \sqrt{2\nu/\omega}$. The value taken corresponds to $\delta_{a,\min} = \delta_a(f = 5000\,\text{Hz}) = 3.1015 \times 10^{-5}\,\text{m}$, higher limit of the chosen frequency range [200 - 5000] Hz. The chosen frequency step is $\Delta f = 200\,\text{Hz}$. The mesh elements $h$ inside the orifice are of the size $\delta_{a,\min}$, whereas the element size is growing outside the duct linearly along the duct axis, up to $h = 0.005\,\text{m}$ at $x = \pm 0.02\,\text{m}$ and is constant further away. The grid used for the acoustic simulations is shown in Fig. 4.26.

Perturbation fields for an orifice with bias flow:

The coherent fields of the density $\rho'$ and momentum component $\rho_0 u_x'$ are shown for three different frequencies in Figs. 4.27 and 4.28, respectively. The selected dimensionless frequencies Sr = 0.104, Sr = 0.3125 and Sr = 0.521 cover the range of frequencies in this study. Strouhal number values are here based on the orifice thickness $l_o$ and the mean flow speed in the orifice $\mathbf{u}_{\text{ori}}$ by $\text{Sr} = f l_o / |\mathbf{u}_{\text{ori}}|$. The perturbed field consists of both acoustic and hydrodynamic contributions. The propagating acoustic plane wave, injected in the computational domain through the upstream PML zone in Figs. 4.27 and 4.28, can clearly be identified with its related acoustic wavelength $\lambda_a = (1 + M_0)c_0/f$. The hydrodynamic

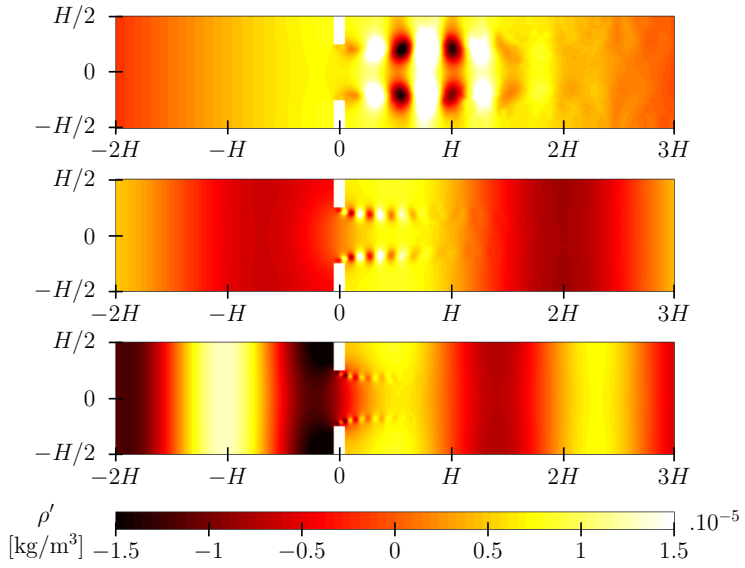


Figure 4.27. Quasi-laminar LNS results for the real part of the density perturbation $\rho'$ [kg/m$^3$] at Sr = 0.104 (top), Sr = 0.313 (center), and Sr = 0.521 (bottom).

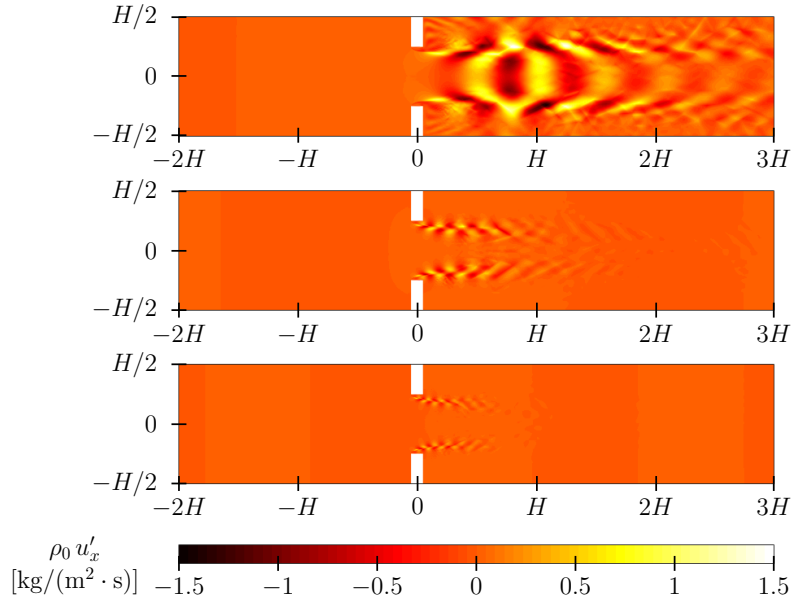


Figure 4.28. Quasi-laminar LNS results for the real part of the momentum perturbation component $\rho_0 u_x'$ [kg/(m$^2$ · s)] at Sr = 0.104 (top), Sr = 0.313 (center), and Sr = 0.521 (bottom).

modes originating from the sound-flow interaction near the orifice edges are characterized by their shorter hydrodynamic wavelength $\lambda_h = |u_0|/f$. The structures of the hydrodynamic modes observed in this study strongly depend on Sr. These modes propagate rather far from the orifice section at lower frequency, and are still significant in magnitude after a distance of several duct diameters. They can therefore pollute acoustic two-port measurements performed with microphones in this region. At low Strouhal numbers, the maximum magnitude of the hydrodynamic perturbations is larger than at higher Sr. In a low frequency range (estimated here as Sr $\in [0.06 - 0.12]$, i.e. $f \in [600 - 1200]$ Hz) these hydrodynamic modes can also propagate through the large recirculation areas downstream of the orifice. These results, obtained with the quasi-laminar LNSE $p$-FEM solver and shown in Figs. 4.27 and 4.28, are qualitatively in good agreement with observations made in a previous study [175], even if they cannot be quantitatively compared because of the differences in terms of flow conditions and dimensions.

Double impact of turbulence modeling on the perturbed fields:

Figure 4.29 shows the density perturbation $\rho'$ obtained from quasi-laminar (top) and turbulent (bottom) LNSE simulations with two different turbulence

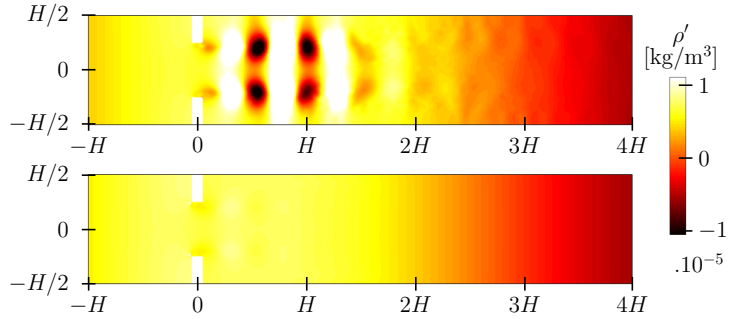


(a) $Re(\rho')$ obtained from a RANS mean flow with $K$-$\epsilon$ model: quasi-laminar LNS (top) and turbulent LNS (bottom).

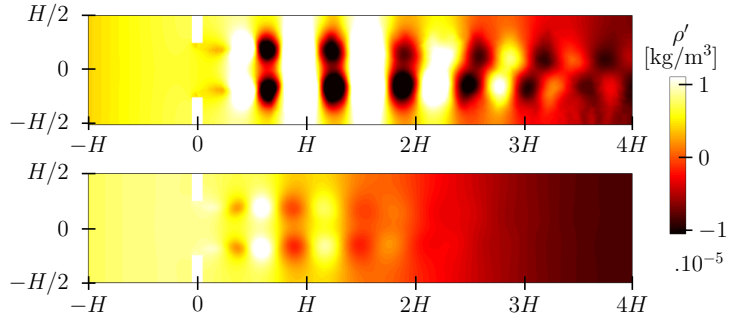


(b) $Re(\rho')$ obtained from a RANS mean flow with $K$-$\omega$ SST model: quasi-laminar LNS (top) and turbulent LNS (bottom).

Figure 4.29. Impact of turbulence modeling on the LNSE $p$-FEM results for the real part of the density perturbation $\rho'$ [kg/m$^3$] at Sr $= 0.104$ (i.e. $f = 1000$ Hz).

RANS models. The choice of the RANS model affects the predicted harmonic perturbations through the base flow properties (see quasi-laminar results) but also through the eddy-viscosity. In both turbulent cases, the extra damping from the eddy-viscosity decreases the amplitude of the vortical structures appearing at the orifice edges. The $K$-$\epsilon$ model gives higher values of eddy-viscosity inside the orifice than the SST $K$-$\omega$ model (see Fig. 4.25), which leads to an increased impact of the turbulence on the generated hydrodynamic fluctuations. The effect of turbulence on the acoustic field itself, as perceived in the far field, is further quantified in the following of this part.

Local vorticity field and choice of the physical models:

Figure 4.30 shows the real part of the vorticity perturbations, defined as $\Omega' = \partial u'_y/\partial x - \partial u'_x/\partial y$, in the vicinity of the orifice down part. Four different

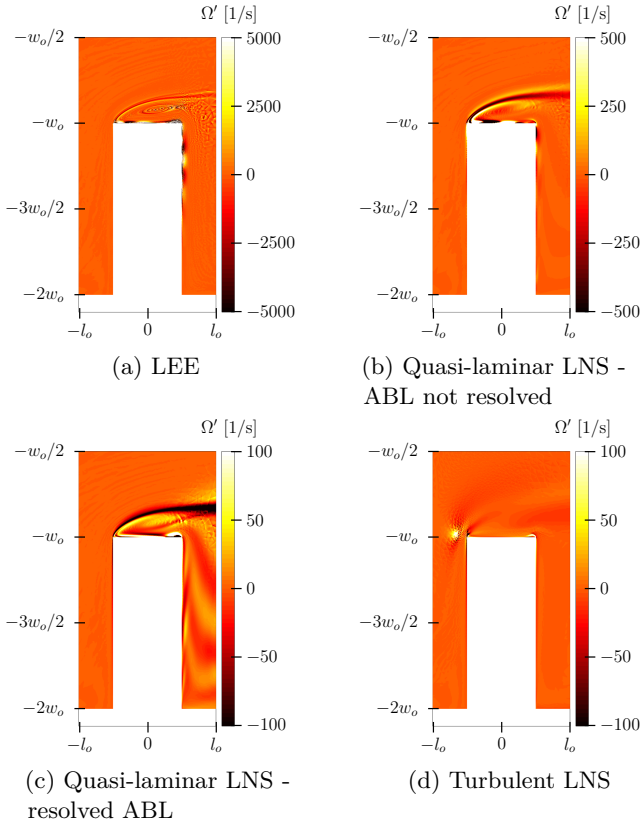


(a) LEE

(b) Quasi-laminar LNS - ABL not resolved

(c) Quasi-laminar LNS - resolved ABL

(d) Turbulent LNS

Figure 4.30. Vorticity field Re(Ω′) [1/s] at $St = 0.104$ for different physical models.

physical models have been investigated: LEE, quasi-laminar LNSE with slip boundary condition (without resolving the ABL), quasi-laminar LNSE with no-slip boundary condition and resolving the ABL, and turbulent LNS with no-slip boundary resolving the ABL (with $K$-$\epsilon$ model). The results are displayed here at frequency Sr = 0.104. The same acoustic mesh is used in all cases, with mesh size $\delta_{a,\min}$ inside the duct. This mesh refinement corresponds to approximatively three elements inside the ABL at Sr = 0.104.

Vorticity is shed at the leading edge and is convected along the base flow streamlines. The choice of the physical model plays an important role on the local representation of the interactions between acoustic and hydrodynamic modes in the orifice region. The addition of the no-slip condition prevents the appearance of spurious modes inside the ABL and an acoustic boundary layer is formed at the orifice plate wall. The inclusion of the turbulence eddy-viscosity reduces the amplitude of the vorticity but the edges still have the dominant

impact on the vorticity. The representation scale in Fig. 4.30 has been adapted for each case, as amplitudes of the vorticity real part change up to two orders the more diffusion is added to the model, with LEE showing the highest values. Note that the computation of the vorticity field is performed element by element and therefore discontinuities can be noticed between elements when their size is large. From the simulation run, it was observed that a refinement of the acoustic mesh is not only needed in the orifice region but also in the area of strong base flow gradients caused by the orifice shear. The local refinement of the mesh inside the orifice improves the accuracy of the computed perturbations since it better captures the complex sound-flow interactions localized in the acoustic and turbulent boundary layers. If this area is not refined enough, the error generated inside the orifice can propagate downstream in the shear region.

Turbulence effect on the global acoustic behavior of the orifice:

A two-port model, as detailed in Section 2.2.1, fully describes the linear acoustic behavior of a given component. It can also be used to determine the maximum and minimum acoustic power the two-port element can dissipate. This is of particular relevance for passive silencers in flow configurations as complex flow-acoustic coupling can appear under particular circumstances leading to whistling. Such whistling can drastically counteract the performance of an installed acoustic damper, and must therefore be avoided. These instabilities are non-linear phenomena, for which acoustical power is transferred into the vorticity field that can interact with the mean flow shear layers and in turn generate amplified acoustic energy[3]. Nevertheless, their onset can be predicted using linear multi-port models and their dissipation potential [19]. This approach has been discussed extensively in literature, e.g. for orifices in ducts [175,184,255,290] and T-junctions [105, 141, 173].

The acoustic power dissipated by a two-port element is given by the difference between the power entering $W_{\text{in}}$ and leaving $W_{\text{out}}$ the element. The vectors $\mathbf{w}_{\text{in}}$ and $\mathbf{w}_{\text{out}}$ regroup the contributions of the modes which enter and leave the two-port element. The acoustic power balance for the element can be written in terms of the incident sound field, characterized by $\mathbf{w}_{\text{in}}$. It stands:

$$W_{\text{diss}} = W_{\text{in}} - W_{\text{out}} = \mathbf{w}_{\text{in}}^{*} \left(\mathbf{I} - \mathbf{S}_{\mathbf{e}}^{*}\mathbf{S}_{\mathbf{e}}\right) \mathbf{w}_{\text{in}} \,, \tag{4.6}$$

where $W_{in} = \mathbf{w}_{\text{in}}^{*}\mathbf{w}_{\text{in}}$ and $\mathbf{S_e}$ is the exergy scattering matrix. The operator $\bullet^{*}$ denotes the Hermitian transpose. Below the first cut-off frequency, and by

[3]If this acoustic power amplification occurs in a frequency range corresponding to any resonance frequencies of the system, it may lead to a resonant feedback loop yielding very large perturbation amplitudes such that a transition from the linear to non-linear regime can take place.

analogy to the standard scattering matrix $\mathbf{S}$, $\mathbf{S_e}$ is given by

$$\begin{Bmatrix} \Pi_2^+(\omega) \\ \Pi_1^-(\omega) \end{Bmatrix} = \underbrace{\begin{bmatrix} T_e^+(\omega) & R_e^-(\omega) \\ R_e^+(\omega) & T_e^-(\omega) \end{bmatrix}}_{\mathbf{S_e}} \begin{Bmatrix} \Pi_1^+(\omega) \\ \Pi_2^-(\omega) \end{Bmatrix} \Leftrightarrow \mathbf{w}_{\text{out}} = \mathbf{S_e}\,\mathbf{w}_{\text{in}}\,, \tag{4.7}$$

with the upstream exergy $\Pi_1^{\pm}$ and downstream exergy $\Pi_2^{\pm}$ defined as

$$\Pi_i^{\pm} = \frac{(1 \pm M_i)}{\rho_0} p_i^{\pm} \qquad \forall i \in \{1, 2\}\,. \tag{4.8}$$

Since the vectors $\mathbf{w}_i^{\pm}$ are related to the modal amplitude vectors $p_i^{\pm}$ by Eq. (4.8), a direct relation exists between the standard scattering matrix and the exergy scattering matrix. For upstream and downstream ducts with same cross-sectional area, this relations is:

$$\mathbf{S_e} = \mathbf{M}_{\mathbf{S}\leftrightarrow\mathbf{S_e}}\,\mathbf{S}\,{\mathbf{M}_{\mathbf{S}\leftrightarrow\mathbf{S_e}}}^{-1} \text{ with } \mathbf{M}_{\mathbf{S}\leftrightarrow\mathbf{S_e}} = \begin{bmatrix} \frac{(1+M_0)}{\rho_0} & 0 \\ 0 & \frac{(1-M_0)}{\rho_0} \end{bmatrix} \tag{4.9}$$

Following the derivations of Aurégan and Starobinsky [19], the power balance of Eq. (4.6) can be reformulated as:

$$W_{\text{diss}} = \mathbf{d}^*(\mathbf{I} - \mathbf{\Lambda})\mathbf{d}\,, \tag{4.10}$$

where the diagonal matrix $\mathbf{\Lambda}$ contains the eigenvalues of the Hermitian matrix $(\mathbf{S_e^*S_e})$. The vector $\mathbf{d}$ is given by $\mathbf{d} = \mathbf{V}\mathbf{w}_{\text{in}}$ where $\mathbf{V}$ contains the eigenvectors of $(\mathbf{S_e^*S_e})$. The quadratic form of Eq. (4.10) can be reduced to a sum of squares and the dissipated power $W_{\text{diss}}$ can be expressed [19] as

$$W_{\text{diss}} = \sum_{i=1}^{2}(1 - \lambda_i)|d_i|^2 = \sum_{i=1}^{2}\xi_i|d_i|^2 \tag{4.11}$$

in the plane wave regime.

Equation (4.11) defines the dissipation potentials $\xi_i = 1 - \lambda_i$. The smallest and largest dissipation potentials $\xi_{\min} = 1 - \lambda_{\max}$ and $\xi_{\max} = 1 - \lambda_{\min}$ determine, respectively, the minimum and maximum sound power dissipation by the two-port element, [19] considering an incident acoustic wave. The matrix $(\mathbf{S_e^*S_e})$ is a positive definite Hermitian matrix. Its eigenvalues are therefore always positive. The dissipation potentials $\xi_i$ remain thus always smaller than unity, which is linked to the fact that a two-port element cannot dissipate more energy than the incoming quantity. A passive system solely dissipates the acoustic energy, and is then defined by: $\xi_i > 0\,\forall i$. In case a negative dissipation potential exists, the system is likely to amplify the acoustic power for a specific incident field and the element could start whistling [290].

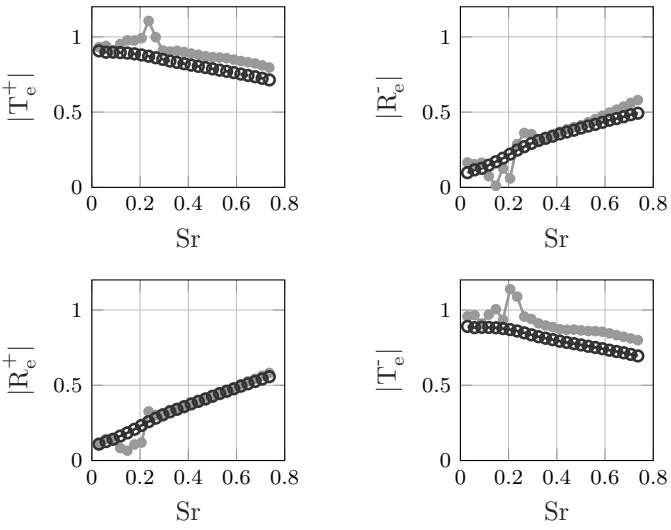


Figure 4.31. Exergy scattering matrix $\mathbf{S_e}$ for the orifice with bias flow from RANS $K$-$\epsilon$ model, $M_{0,\text{inlet}} = 0.0396$: quasi-laminar LNSE solver (—●—) and turbulent LNSE solver (—⊖—).

Figure 4.31 shows the exergy scattering matrix $\mathbf{S_e}$ for the case of the investigated orifice at $M_0 = 0.0396$ with the RANS mean flow description based on the $K$-$\epsilon$ model. The components of $\mathbf{S_e}$ obtained from both quasi-laminar and turbulent LNS $p$-FEM are indicated. The quasi-laminar case delivers transmission coefficient amplitudes $|T_e^{\pm}|$ larger than unity around a specific frequency, $\text{Sr} \approx 0.23$. These peaks in the transmission coefficients can be related to the appearance of whistling in this particular Strouhal number range. It is shown in Fig. 4.32, by means of the dissipation potentials $\xi_{\min}$ and $\xi_{\max}$, with $\xi_{\min}$ taking negative values for $\text{Sr} \in [0.18 - 0.31]$. It indicates that an overall acoustic energy amplification is likely to happen in this Sr range. Comparing the results obtained from the turbulent LNSE solver in the frequency domain, the components of the exergy scattering matrix are monotonically decreasing for $T_e^{\pm}$ (respectively increasing for $R_e^{\pm}$) and the zone of potential whistling is not observed, as confirmed by the curves obtained for $\xi_{\min/\max}$ in Fig. 4.32. The additional damping present in the turbulent LNSE solver, due to accounting for the eddy-viscosity, leads the system to behave as a passive component over the complete frequency range, i.e. $\xi_{\min/\max} > 0 \,\forall\, \text{Sr}$. The difference between $\mathbf{S_e}$ from the two LNSE solvers appears small for the reflection coefficients except in the whistling frequency range. The transmission coefficients predicted with the additional turbulence eddy-viscosity are overall slightly lower than when this latter is disregarded.

These results show that accounting or not for the turbulent character of the

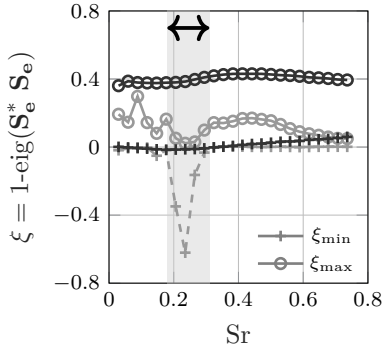


Figure 4.32. Dissipation potentials $\xi$ for the orifice configuration with bias flow obtained with RANS and $K$-$\epsilon$ model, $M_{0,\text{inlet}} = 0.0396$: quasi-laminar LNSE solver (▭) and turbulent LNSE solver (■).

mean flow inside the acoustic solver can drastically change the interpretation of the numerically predicted acoustic behavior of the orifice with bias flow for the particular case detailed in this work.

### 4.3.2 Helmholtz resonator with turbulent grazing flow

The previous results have shown that including acoustic dissipation due to flow turbulent mixing into linear acoustic solvers can lead to non negligible discrepancies compared to the quasi-laminar alternative. The case of Helmholtz resonators grazed by a turbulent flow is investigated in this section.

#### Configuration and numerical setup

The configuration is similar to the one described in Section 4.1.1 and illustrated in Fig. 4.2. Contrary to Section 4.1.1 where the geometry of the resonator neck was fixed, different slit widths are considered in the present section, namely $l_s \in \{1\,\text{mm}, 2\,\text{mm}, 3\,\text{mm}, 4\,\text{mm}, 8\,\text{mm}\}$. The other geometric parameters are kept as previously: $H_{\text{cav}} = 50\,\text{mm}$, $L_{\text{cav}} = 25\,\text{mm}$, $t_s = 1\,\text{mm}$. The work is performed with an inlet velocity corresponding to a low Mach number of $M_0 = 0.05$. The base flow fields are computed using a steady RANS simulation with SST $K$-$\omega$ model for the turbulence modeling. The flow simulations are carried out with the commercial CFD software ANSYS® Fluent. Different turbulence levels for the mean flow have been accounted for, based on the Turbulence Intensity (TI), with $\text{TI} \in \{1\,\%, 5\,\%, 10\,\%, 20\,\%\}$. Results for the two extreme values considered, TI = 1% and TI = 20%, are presented here. Table 4.5 summarizes the characteristics of the flow boundary layer grazing on

| $l_s$ [mm] | 1 | | 3 | | 8 | |
|---|---|---|---|---|---|---|
| TI [%] | 1 | 20 | 1 | 20 | 1 | 20 |
| $U_\infty$ [m/s] | 18.92 | 18.70 | 18.92 | 18.70 | 18.93 | 18.71 |
| $\delta_{\mathrm{MF}}$ [mm] | 15.9 | 14.9 | 15.9 | 14.9 | 15.9 | 14.9 |
| $\theta_{\mathrm{MF}}$ [mm] | 1.5 | 1.5 | 1.5 | 1.5 | 1.5 | 1.5 |
| $H_{\mathrm{MF}}[-]$ | 1.35 | 1.20 | 1.35 | 1.20 | 1.35 | 1.20 |

Table 4.5: Boundary layer characteristics of the computed mean flow, measured at $4L_{\mathrm{cav}}$ upstream from the slit center: free-stream velocity $U_\infty$, boundary layer thickness $\delta_{\mathrm{MF}}$, momentum thickness $\theta_{\mathrm{MF}}$, and shape factor $H_{\mathrm{MF}}$.

top of the resonator opening. The parameter values are computed upstream from the slit and are found to be identical regardless of the width of the slit, as expected.

The computed effective viscosity $\mu_{\mathrm{eff}} = \mu + \mu_t$ is shown in Fig. 4.33. It appears that for small slit widths, the value of $\mu_{\mathrm{eff}}$ inside the orifice is limited to the dynamic viscosity $\mu$. For larger $l_s$ values, the turbulence influences also the

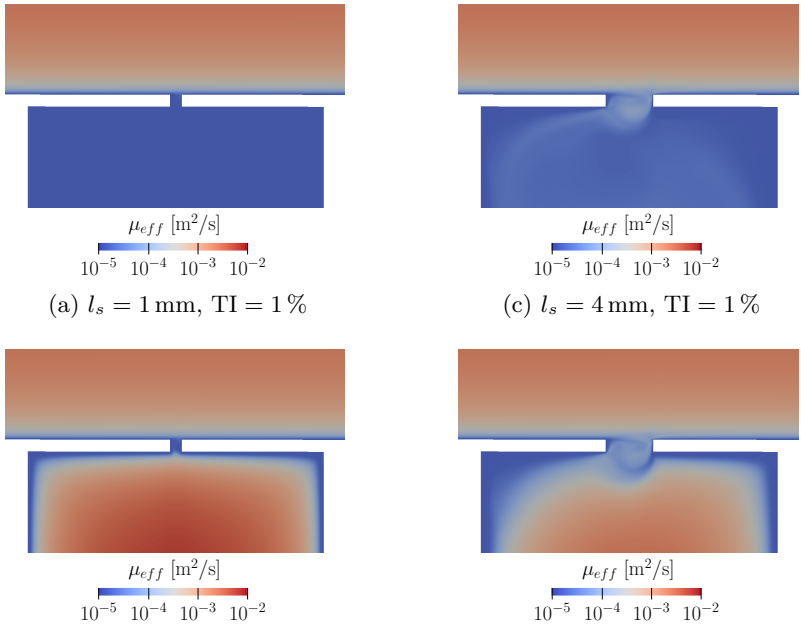


(a) $l_s = 1\,\mathrm{mm}$, TI $= 1\,\%$ (c) $l_s = 4\,\mathrm{mm}$, TI $= 1\,\%$

(b) $l_s = 1\,\mathrm{mm}$, TI $= 20\,\%$ (d) $l_s = 4\,\mathrm{mm}$, TI $= 20\,\%$

Figure 4.33. Effective dynamic viscosity $\mu_{\mathrm{eff}}$ obtained from the RANS simulations for TI $= 1\,\%$ and TI $= 20\,\%$: $l_s = 1\,\mathrm{mm}$ (a, b) and $l_s = 4\,\mathrm{mm}$ (c, d).

recirculation region inside the resonator neck. An increase in turbulence intensity leads as expected to overall higher $\mu_{\text{eff}}$ values, with a noticeable impact inside the resonator cavity.

The acoustic perturbation fields are computed by means of the time-domain RKDG method to solve both quasi-laminar and turbulent LNS equations. The 2-D computational domain is taken similar to the one in Section 4.1.1. Unstructured triangular meshes are used for each orifice geometry considered, with a maximum of 5300 elements for the case $l_s = 8\,\text{mm}$. Refinement of the mesh is done in the resonator neck region with approximately 10 elements along the slit thickness, as illustrated in Fig. 4.34. From previous results, this refinement is judged sufficient to model accurately the phenomena governing the interaction between the grazing flow and the acoustic field for the considered cases. A polynomial order $p = 7$ is chosen for all simulations, leading to a dimensionless time step $t^\star = c_0\, t = 1.0 \times 10^{-6}$ to ensure stability of the numerical scheme. The acoustic field is triggered by a pulse excitation in the duct region applied upstream (at $z = -14 L_{\text{cav}}$) and downstream (at $z = 22 L_{\text{cav}}$) of the resonator. This allows to perform the two-source approach to characterize the two-port element of width $L = L_{\text{cav}}$ containing the resonator. Simulations are run until the dimensionless time reaches $t^\star_{\text{final}} = 6$, which is long enough to assure that all energy has left the domain. The acoustic pressure values are monitored at the locations $z_{\text{up}} = [-0.3\,\text{m}, \ldots, -0.09\,\text{m}]$ and $z_{\text{down}} = [0.29\,\text{m}, \ldots, 0.50\,\text{m}]$ with a constant spacing $\Delta z = 0.03\,\text{m}$.

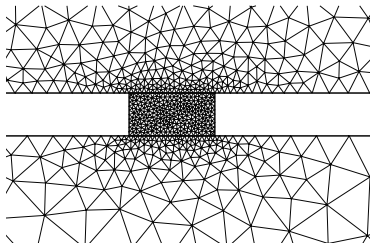

Figure 4.34. Unstructured triangular grid used for the time-domain RKDG solver with the turbulent and quasi-laminar formulation of the LNS operator – $l_s = 2\,\text{mm}$.

### Acoustic results

The scattering matrix obtained from the numerical results of the time-domain RKDG method are represented in Fig. 4.35 for the case of lowest TI. A clear change in the acoustic behavior of the system can be observed with increasing slit width. For the smaller values of $l_s$, the resonator behaves as expected from an acoustic damper with a distinct resonance frequency. An increase in the slit width leads to a shift of this resonance frequency towards higher values, as

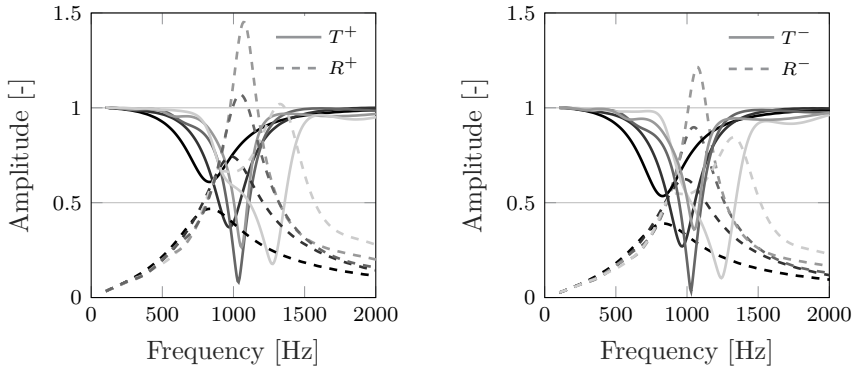


(a) Upstream coefficients: $T^+$ and $R^+$ (b) Downstream coefficients: $T^-$ and $R^-$

Figure 4.35. Scattering matrix for the resonators with grazing flow at $M_{0,\text{inlet}} = 0.05$ and TI = 1 % computed with the time-domain turbulent LNSE solver: $l_s = 1\,\text{mm}$ (■), $l_s = 2\,\text{mm}$ (■), $l_s = 3\,\text{mm}$ (■), $l_s = 4\,\text{mm}$ (■), $l_s = 8\,\text{mm}$ (□).

expected from Eq. (2.2) with $\sigma$ increasing. The convective effects of the grazing flow, leading to an asymmetry of the upstream and downstream coefficients of the scattering matrices, are visible in these results.

For larger orifice sizes, the behavior of the resonator captured by the LNSE simulations changes considerably. With increasing $l_s$ values, the peak in the reflection coefficient rises up to exceed the threshold value 1. Also a shift in frequency appears between the peak in the $|R^{\pm}|$ curves and the minimal values of the $|T^{\pm}|$ curves. Under these conditions the Helmholtz resonator is not working as a proper silencer. Sound-flow couplings leading to hydrodynamic instabilities and non-linear noise production[4] can be expected. The change in the general shape of the scattering matrix coefficients also signifies that the standard model of a resonator, as illustrated in Fig. 2.2a, is violated and cannot be used to describe the behavior of the system anymore. From the computed scattering matrices, this observation concerns predominantly the cases $l_s = 8\,\text{mm}$ and $l_s = 4\,\text{mm}$. For these geometries, an oscillating mass of air in the neck is not a valid assumption.

Concerning the modeling differences between the quasi-laminar and turbulent LNSE solvers, the conclusions are also depending on the width of the slit considered. For small orifices and low turbulence levels, no difference at all is observed between the quasi-laminar and turbulent models, as shown in Fig. 4.36a. For higher turbulence intensities, a difference due to the additional

[4]The LNSE are not able to capture the physics of such instabilities but they have been shown to correctly predict their onset.

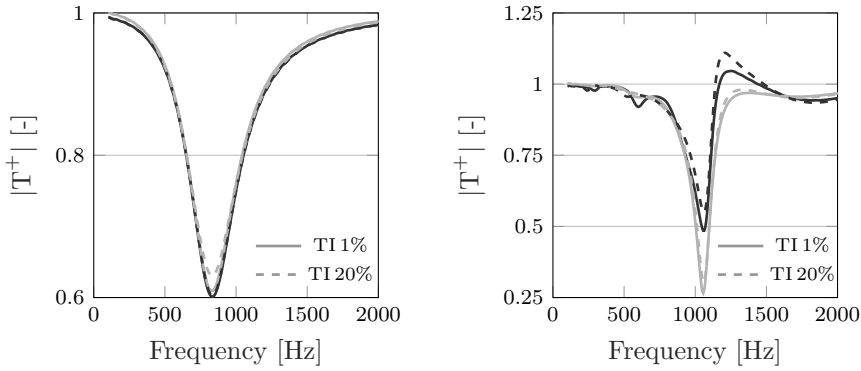


(a) $l_s = 1\,\text{mm}$ (b) $l_s = 4\,\text{mm}$

Figure 4.36. Comparison of the upstream transmission coefficient $|T^+|$ computed with the two versions of the time-domain LNSE solver: quasi-laminar (▬) and turbulent (▬) LNSE.

turbulent damping can be seen. This discrepancy between the double and triple decomposed LNSE models is, however, very limited for small orifices and can therefore be neglected. For larger orifices, as in Fig. 4.36b, the computed scattering matrices are much more sensitive to both flow turbulence and modeling approach. Accounting for the turbulent damping in the acoustic solver appears to have more influence on the results than the TI level itself. The previous conclusions hold for the computed dissipation potentials $\xi$ as illustrated in Figs. 4.37 and 4.38. Potential flow-acoustic coupling appears at

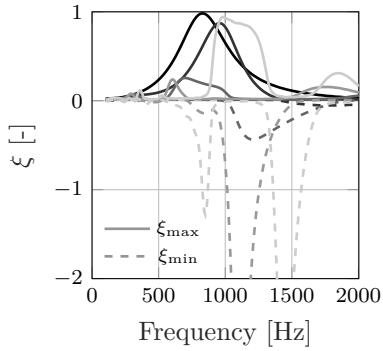


Figure 4.37. Dissipation potentials $\xi$ for the Helmholtz resonator configuration with grazing flow at $M_{0,\text{inlet}} = 0.05$ and TI = 1 % obtained with the quasi-laminar LNSE solver: $l_s = 1\,\text{mm}$ (■), $l_s = 2\,\text{mm}$ (■), $l_s = 3\,\text{mm}$ (■), $l_s = 4\,\text{mm}$ (■), $l_s = 8\,\text{mm}$ (□).

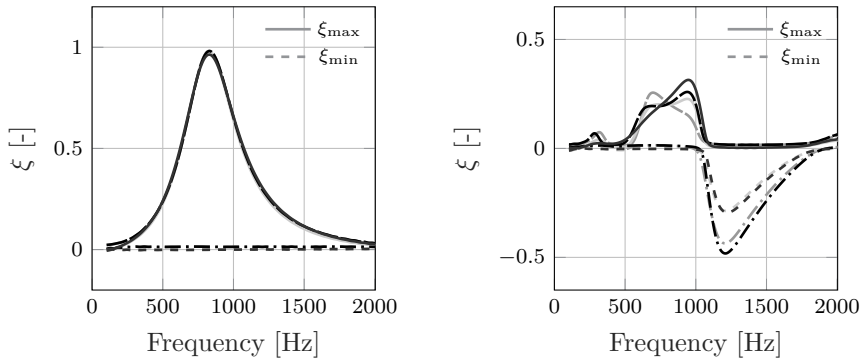


(a) $l_s = 1\,\text{mm}$ (b) $l_s = 3\,\text{mm}$

Figure 4.38. Dissipation potentials $\xi$ for the Helmholtz resonator configuration with grazing flow at $M_{0,\text{inlet}} = 0.05$ computed with the two versions of the time-domain LNSE solver: quasi-lam. LNSE with TI = 1 % (▬·▪ or ▬▬), turbulent LNSE with TI = 1 % (▪▪▪ or ▬▬), quasi-laminar LNSE with TI = 20 % (▬·▪ or ▬▬), turbulent LNSE with TI = 20 % (▪▪▪ or ▬▬).

specific frequency range for the larger orifices. Figure 4.38b shows, similar to the bias flow configuration, that the turbulent LNSE lead to smaller zones of potential instabilities. The triple decomposition approach is, therefore, best advisable for the prediction of the onset of instabilities for large perforate geometries. For smaller orifices in grazing flow configuration, turbulence effects can mostly be disregarded.

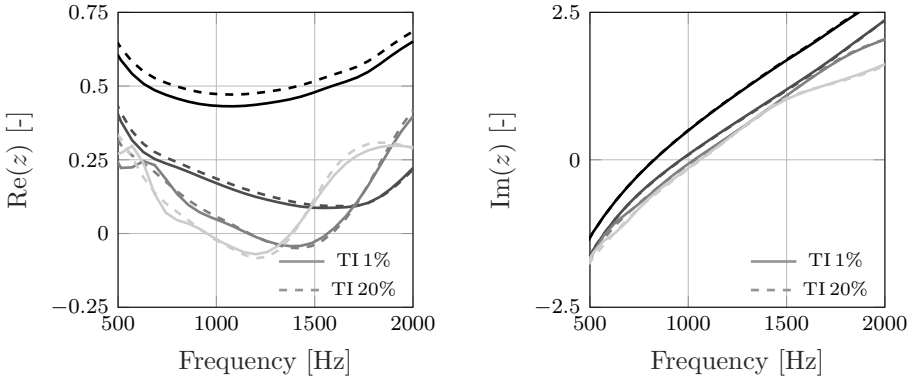


Figure 4.39. Normalized resonator resistance (left) and reactance (right) obtained with the turbulent LNSE solver and the lumped impedance model: $l_s = 1\,\text{mm}$ (■), $l_s = 2\,\text{mm}$ (■), $l_s = 3\,\text{mm}$ (■), $l_s = 4\,\text{mm}$ (■).

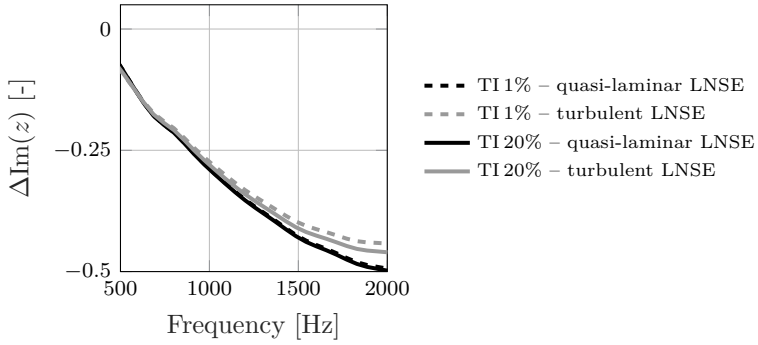


Figure 4.40. Relative change in reactance with respect to its value in a medium at rest, $\Delta Im(z) = Im\{z(M_0)\} - Im\{z(M_0 = 0)\}$, computed with the time-domain LNSE solver for $l_s = 1\,\text{mm}$.

In terms of impedance, accounting for the flow turbulence in the acoustic solver leads to slightly higher resistance and reactance, as illustrated in Figs. 4.39 and 4.40. The mean flow turbulence is, therefore, found to counteract the decrease in the mass of air attached to the orifice due to the grazing flow. These changes are, however, found to be small for the geometries and flow conditions considered.

To finish this section, the impact of the boundary layer profile on the acoustic behavior of the smallest orifice considered in this work ($l_s = 1\,\text{mm}$) is discussed. This effect was disregarded in the previous discussion since all the mean flow fields were very similar (see 4.5). The same Mach number as previously, $M_0 = 0.05$, is taken and a turbulence intensity $\text{TI} = 20\,\%$ is considered. The distance $L_{\text{dev}}$ upstream of the resonator opening on which the mean flow develops is changed in the CFD simulations in order to modify the characteristics of the flow boundary layer. The four boundary layers considered in this work are indicated in Table 4.6.

| Case | BL-A | BL-B | BL-C | BL-D |
|---|---|---|---|---|
| $L_{\text{dev}}$ [m] | 2 | 0.5 | 0.25 | 0.1 |
| $U_\infty$ [m/s] | 18.70 | 18.17 | 17.77 | 17.36 |
| $\delta_{\text{MF}}$ [mm] | 15.0 | 12.7 | 7.3 | 2 |
| $\theta_{\text{MF}}$ [mm] | 1.3 | 1.0 | 0.6 | 0.2 |
| $H_{\text{MF}}[-]$ | 1.35 | 1.36 | 1.45 | 1.79 |

Table 4.6: Boundary layer characteristics of the computed mean flow, measured at $L_{\text{cav}}$ upstream from the slit center: free-stream velocity $U_\infty$, boundary layer thickness $\delta_{\text{MF}}$, momentum thickness $\theta_{\text{MF}}$, and shape factor $H_{\text{MF}}$.

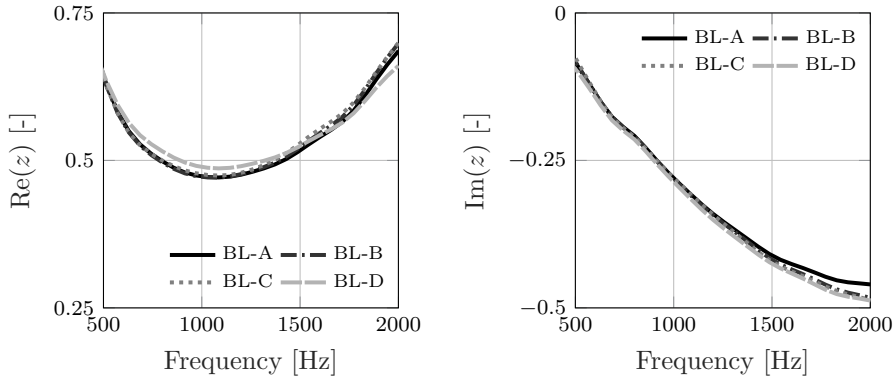


Figure 4.41. Impact of the boundary layer profile on the resonator resistance (left) and relative change in reactance with respect to its value in a medium at rest (right), obtained with the turbulent LNSE for TI = 20 % and $l_s = 1\,\text{mm}$.

The influence of the boundary layer on the acoustic impedance of the resonator is shown in Fig. 4.41. A smaller boundary layer is found to increase the resistance and to lower the reactance. These trends are in agreement with previous experimental observations made for larger orifices with grazing flow [117]. Overall, the impact of the boundary layer shape is relatively small compared to the effect of the flow itself for such a narrow slit.

### 4.3.3 Conclusions

In this section, the effect of flow turbulence on the behavior of orifices and resonators predicted by LNSE solvers has been investigated. Results have shown that the triple decomposition can lead to small differences in terms of both acoustic impedance and dissipation potentials. The bias flow configuration appears to be more sensitive than the grazing flow one. Accounting for the turbulence in the LNSE approach leads to narrower frequency ranges for which hydrodynamic instabilities can be expected. The larger the orifices considered are, the more important it is to include turbulent damping inside the acoustic propagation model. For small perforation dimension, e.g. a slit width $l_s = 1\,\text{mm}$, both damping effect and profile of the mean flow boundary layer are found to be one order smaller than the effect of the flow itself.

# Part III

# Orifices and Helmholtz resonators in their nonlinear regime

# Chapter 5

# Determination of acoustic impedance for Helmholtz resonators through incompressible unsteady flow simulations

In this chapter, a methodology based on incompressible Computational Fluid Dynamics (CFD) simulations is proposed and assessed to study the acoustic behavior of Helmholtz resonators under a large range of excitation amplitudes. It constitutes an alternative approach to the more widespread one based on compressible flow simulations to analyze the non-linear regime of Helmholtz resonators. The concept and theory of the proposed methodology are first described. The results obtained with the incompressible simulations are then compared, for validation purposes, to both numerical results of the full compressible equations and experimental data for two resonator geometries at different SPLs.

As already discussed in Chapter 2, the acoustic dissipation mechanisms involved in passive acoustic dampers differ significantly depending on the amplitude of the incoming acoustic excitation. For low excitation amplitudes, the acoustic impedance is independent of the sound amplitude and the resonator or orifice behaves like a linear system. Numerical methods based on linearized equations, as detailed in Chapters 3 and 4, allow for an efficient treatment of this linear regime with limited computational costs. By increasing the excitation amplitudes, nonlinear effects appear and become progressively dominant. Such

nonlinear effects originate from the separation of the acoustic boundary layer itself at edges, which transfers acoustic energy to the hydrodynamic field. The creation of vortices at the orifice edges increases considerably the dissipation of the acoustic energy. This feature is of importance for the design of acoustic dampers, as it impacts substantially the sound wave attenuation. The nonlinear regime is, however, more complex to predict accurately due to the intricate nature of the physical phenomena taking place. Linear numerical methods are therefore not suitable at medium and high excitation amplitudes and nonlinear time domain solvers are needed. The case of a quiescent medium is considered here, even if the proposed methodology can be extended to deal with flow.

This chapter is to a large extent based on the journal paper:

> Tournadre et al., Determination of acoustic impedance for Helmholtz resonators through incompressible unsteady flow simulations, *AIAA Journal 55*, 3 (2017), 790–798 [297]

in collaboration with Kilian Förner [109] and Wolfgang Polifke at the Technical University of Munich (TUM).

## 5.1 Description of the methodology and case study

The present work investigates the capability of an incompressible unsteady computational fluid dynamic approach to study numerically the aeroacoustic response of a Helmholtz resonator to an external acoustic excitation. Incompressible flow computations have already successfully been used in the past to characterize the acoustic behavior of confined flow systems. In the work of Martínez-Lera et al. [214], an approach combining incompressible CFD and vortex sound theory [150] was applied successfully to a two-dimensional laminar flow through a T-joint. This methodology has been further improved and applied to corrugated pipes by Nakiboğlu [224] and to a large orifice configuration with through-flow by Lacombe et al. [185] for whistling prediction. In contrast to those previous works, the present study focuses on both linear and nonlinear regimes of Helmholtz resonators in absence of mean flow. The extension to the case with flow can be done easily due to the present general formulation and arguments presented by Nakiboğlu [224] and Golliard et al. [118], which consist of subtracting the mean flow induced pressure drops upstream and downstream of the test section by considering the additional case of a straight duct.

### 5.1.1 Decomposed Helmholtz resonator

A Helmholtz resonator placed at the termination of a duct, as illustrated in Fig. 5.1a, is considered in this part. The direct study of this configuration by incompressible CFD simulations is not possible, due to the incompressible nature

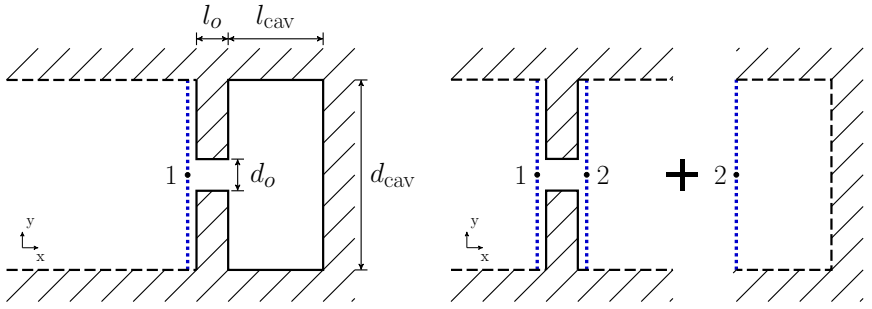


(a) Complete Helmholtz resonator

(b) Decomposition into orifice and backing volume

Figure 5.1. Sketch of the considered geometry and reference cut planes 1 and 2 for the decomposed resonator model.

of the fluid which would violate the principle of mass conservation if a non-zero inlet velocity is prescribed at the inlet of the duct. The methodology proposed here to face this issue is to decompose the complete Helmholtz resonator into its two main components: the orifice neck and the backing cavity (see Fig. 5.1b).

Such a decomposition has already been proposed by Ingard and Ising [159]. For most of the configurations of interest, the orifice can be considered acoustically compact, i. e., the Helmholtz number He, which describes the ratio of the neck length or diameter to the acoustic wavelength $\lambda_a$, is small (He $\ll 1$). Thus, the flow through the orifice can be treated as incompressible. The compressible effects occur solely in the backing volume. The orifice transfer impedance $Z_{to}$ is often used to quantify the acoustic behavior of an orifice. It is defined as the ratio of the Fourier component ($\hat{\bullet}$) of the fluctuating pressure drop $\Delta\hat{p}' = \hat{p}'_1 - \hat{p}'_2$ and velocity normal to the reference surface in the duct front of the resonator $u'$, i. e.,

$$Z_{to} = \frac{\Delta\hat{p}'}{\hat{u}'} \ . \tag{5.1}$$

Note that in the above definition, the velocity $\hat{u}'$ is the cross-sectional surface averaged velocity in the resonance tube. There are other authors using the cross-sectional surface averaged velocity in the orifice $u'_o$ instead. These two velocities are related via the porosity of the resonator plate $\sigma$, such that $u' = \sigma u'_o$. The porosity is defined as $\sigma = S_o/S_{\text{cav}}$, with $S_o$ and $S_{\text{cav}}$ denoting the cross-sectional areas of the orifice and backing cavity, respectively.

The contribution of the backing volume can be described in terms of a surface impedance $Z_{\text{cav}} = \hat{p}'_2/\hat{u}'_2$, which is done here analytically, as described later.

Therefore, the orifice transfer impedance can be expressed as:

$$Z_{to} = \frac{\hat{p}'_1 - Z_{\text{cav}}\hat{u}'_2}{\hat{u}'_1} \ . \tag{5.2}$$

Due to the acoustically compact neck and the same areas on both sides of the orifice, it is reasonable to assume $\hat{u}'_1 = \hat{u}'_2$. Thus, the surface impedance of the resonator $Z_r$ is given in this lumped model as (c. f. Ingard and Ising [159]):

$$Z_r = Z_{to} + Z_{\text{cav}} \ . \tag{5.3}$$

The present study builds on this Helmholtz resonator decomposition and aims to investigate the validity of this decomposition at different levels of sound excitation. In doing so, the advantages of an incompressible solver are exploited for the simulation of the flow through the orifice, including the vortex generation responsible for the nonlinear acoustic losses. Details on the estimation of the orifice transfer impedance and backing volume surface impedance are given in the following.

**Orifice impedance $Z_{to}$:**

The methodology to get the orifice transfer impedance from the incompressible simulations is explained in this section. In the plane wave regime, a 1-D approximation along the duct is possible and the area-averaged absolute pressure at several sections of the duct is stored at each time step of the flow simulation. This allows computing the pressure differences between two arbitrary chosen sections separated by the orifice: $\Delta p_{AB} = p_A - p_B$ is the pressure jump (or loss) between the sections $A$ on the inlet side and $B$ on the outlet side (see Fig. 5.2).

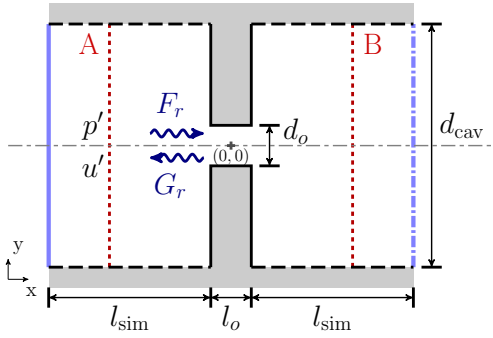


Figure 5.2. Geometrical configuration for the Helmholtz resonator study and boundary conditions: slip wall (▬ ▬), no-slip wall (▬), prescribed fluctuating velocity (▬), and fixed pressure (▬ · ▬) boundary conditions.

In a general manner, for an incompressible fluid the momentum equation yields

$$\boldsymbol{\nabla} P = -\rho \frac{\partial \mathbf{u}}{\partial t} - \rho(\boldsymbol{\Omega} \times \mathbf{u}) + \rho\nu\nabla^2\mathbf{u}\,, \tag{5.4}$$

where $P$ is the total pressure $P = p + \rho \left\|\mathbf{u}\right\|^2/2$ with $\mathbf{u}$ stands for the velocity, $\boldsymbol{\Omega} = \boldsymbol{\nabla} \times \mathbf{u}$ denotes the vorticity, and $\rho$ and $\nu$ are the medium density and kinematic viscosity, respectively. The second term on the right-hand side of Eq. (5.4) is related to the acoustic power in an inviscid and homentropic flow according to Howe's energy corollary [150]. The third term describes the viscous dissipation effects. The total pressure difference $\Delta P$ between two sections can be expressed as the sum of two distinct contributions: $\Delta P = \Delta P_{\text{pot}} + \Delta P_s$. The pressure difference $\Delta P_{\text{pot}}$ is related to a potential flow solution (first term on the right-hand side of Eq. (5.4)) which would be the solution in absence of vorticity and viscous effects, whereas $\Delta P_s$ is linked to sink/source terms for the sound with both vorticity and viscous effects taken into account (last two terms on the right-hand side of Eq. (5.4)). In the numerical models, the viscous dissipation at the walls of the main duct is neglected and slip boundary conditions are applied. As a consequence, the vorticity and viscous effects can be neglected for the wave propagation in the ducts, so that $\Delta P_{\text{duct,s}} = 0$ inside the duct segments. In the 1-D approximation, $\Delta P_{\text{pot}}$ can be expressed as

$$\Delta P_{\text{pot}} = -\rho \int_L \frac{\partial u_x}{\partial t}\,\mathrm{d}x\ , \tag{5.5}$$

with $L$ the total length between the two sections, $x$ the coordinate along the duct axis, and $u_x$ the axial component of the velocity at the $x$-location (see Fig. 5.2). Inside the duct segments, $\Delta P_{\text{duct,pot}}$ can be interpreted as a result of the propagation along the duct of the fluctuation in velocity $u_x$. The pressure losses can be divided spatially between ducts and orifice parts, leading to

$$\begin{aligned} \Delta P_{AB} &= \Delta P_o + \Delta P_{\text{duct}}\ , \\ &= \Delta P_o + \Delta P_{\text{duct,pot}} + \cancelto{0}{\Delta P_{\text{duct,s}}}\ , \end{aligned} \tag{5.6}$$

with $\Delta P_{AB}$ the total pressure losses between the measurement sections A and B, and $\Delta P_{\text{duct}}$ the total pressure losses in the two duct segments. From this, the expression to compute the orifice pressure drop $\Delta P_o$ is

$$\Delta P_o = \Delta P_{AB} - \Delta P_{\text{duct,pot}}. \tag{5.7}$$

There are two different ways to determine the orifice transfer impedance values from the measured pressure time series, depending on whether the potential flow pressure loss correction inside the duct is done directly on the pressure time data, or in the frequency domain on the impedance itself. Those two approaches to estimate the orifice impedance from the pressure and velocity time series are schematized in Fig. 5.3.

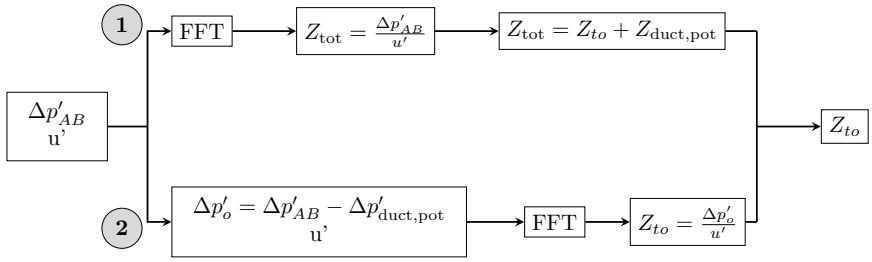


Figure 5.3. Diagram of the two approaches to get the transfer impedance of the orifice from $\Delta p'$ - approach 1 (top), approach 2 (bottom).

In approach 1, the impedance due to the duct potential pressure loss $Z_{\text{duct,pot}}$ is subtracted from the total measured impedance $Z_{\text{tot}}$ to estimate the transfer impedance from the orifice $Z_{to}$ as

$$Z_{to} = Z_{\text{tot}} - Z_{\text{duct,pot}}. \tag{5.8}$$

For an orifice of thickness $l_o$ placed between the measurement sections A and B, as illustrated in Fig. 5.2, $Z_{\text{duct,pot}}$ is computed as

$$Z_{\text{duct,pot}} = \mathrm{j}\rho\omega(L_{AB} - l_o)u' \ , \tag{5.9}$$

where $L_{AB}$ is the distance between the two measurement sections A and B, and $u'$ is the velocity perturbation inside the duct parts.

In approach 2, the duct pressure loss is directly subtracted from the time pressure data. As $u'$ does not depend on the position $x$ in the duct segments, one gets

$$\Delta P_{\text{duct}} = \rho(L_{AB} - l_o)\frac{\partial u'}{\partial t} \ . \tag{5.10}$$

$\partial u'/\partial t$ can be computed analytically for harmonic excitation inlet velocity or has to be computed numerically from the velocity time series in case of broadband excitation.

### Backing volume impedance $Z_{\text{cav}}$:

The contribution of the backing volume can also be described in terms of a surface impedance $Z_{\text{cav}} = \hat{p}'_2/\hat{u}'_2$, which can be determined through an analytical model. Two analytical expressions for the backing volume are shown here. Using the one-dimensional acoustic equations, the impedance is given as

$$Z_{\text{cav}} = -\mathrm{j}\,\cot(k\,l_{\text{cav}})\rho c \ , \tag{5.11}$$

where $k$ denotes the wave number $k = \omega/c$, $c$ the speed of sound in the medium, and $l_{\text{cav}}$ the length of the backing cavity. When the whole volume $V_{\text{cav}} = S_{\text{cav}} l_{\text{cav}}$

is compressed and expanded simultaneously, the following expression for the impedance can be derived using the isentropic compressibility $\beta \equiv 1/(\rho c^2)$:

$$Z_{\mathrm{cav}} = -\mathrm{j}\,\frac{\rho c^2 S_{\mathrm{cav}}}{V_{\mathrm{cav}}\omega}\ . \tag{5.12}$$

This is the same formulation as, e. g., in Keller and Zauner [174]. Both Eqs. (5.11) and (5.12) describe the same behavior for $l_{\mathrm{cav}} \ll \lambda_a$. This can be observed by means of the Laurent series of Eq. (5.11): $Z_{\mathrm{cav}}/(\rho c) = -\mathrm{j}\,[1/(kl_{\mathrm{cav}}) - kl_{\mathrm{cav}}/3 - k^3 l_{\mathrm{cav}}^3/45 + \mathcal{O}(k^5 l_{\mathrm{cav}}^5)]$. The first term of the expansion is identical to the expression in Eq. (5.12). Note that both expressions deliver a purely reactive contribution from the backing cavity. Equation (5.12) is used in the present study.

### 5.1.2 Case configuration and numerical set-up

The geometric configuration for the incompressible simulations as well as the definition of the boundary conditions for the unsteady CFD are illustrated in Fig. 5.2. The numerical domain consists of an orifice of diameter $d_o$ and thickness $l_o$, placed in a duct of diameter $d_{\mathrm{cav}}$. Those dimensions have been chosen according to the reference data [108], corresponding to the case with sharp edges, used for comparison (see Section 5.1.3) and listed as geometry HRA in Table 5.1. An additional validation case, taken from Hersh et al. [133] and noted HRB in Table 5.1, is also considered. The extension of the duct in the axial direction $l_{\mathrm{sim}}$ should be long enough to allow measurement sections to be put out of the area that is influenced by hydrodynamic fluctuations. For the investigated cases described through this work, $l_{\mathrm{sim}}/d_{\mathrm{cav}}$ equals 10 and has been taken long to allow different measurement sections at $x/d_{\mathrm{cav}} = [\pm\ 8, \pm\ 6, \pm\ 4, \pm\ 2]$ along the duct for assessment of the methodology. Numerically determined impedance results have been shown independent of the location of the chosen measurement sections after post-processing. This ensures that the impedance results are not polluted because of vortices crossing the measurement sections. The length $l_{\mathrm{sim}}/d_{\mathrm{cav}} = 2$ has been found to be sufficient for the investigated geometries at the selected SPLs, and it reduces considerably the computational cost and time.

| | $l_o$ [mm] | $d_o$ [mm] | $l_{\mathrm{cav}}$ [mm] | $d_{\mathrm{cav}}$ [mm] | $\sigma$ [%] | $l_{\mathrm{sim}}/d_{\mathrm{cav}}$ [−] | $f_{\mathrm{H,\ lin}}$ [Hz] |
|---|---|---|---|---|---|---|---|
| HRA | 4.0 | 4.2 | 20 | 50 | 0.71 | 10 | 373 |
| HRB | 1.59 | 6.35 | 25.4 | 50.8 | 1.56 | $\approx 10$ | 555 |

Table 5.1: Geometric properties of the Helmholtz resonators investigated in this work: HRA taken from Förner et al. [108] and HRB from Hersh et al. [133].

Figure 5.2 presents also the boundary conditions used for the unsteady incompressible CFD computations. The wall of the duct is defined as slip-wall boundary condition. This assumption implies that no boundary layer develops along the duct and that the velocity profile is constant through the section. Such hypothesis is fair, as it has been observed in various compressible studies, e.g. the LES computations performed by Alenius [8], that changing this boundary condition does not affect the local orifice behavior. This assumption is of importance for the present study, as it allows easily to discard pressure losses occurring in the duct upstream and downstream of the orifice. The wall of the orifice plate is however prescribed as no-slip boundary condition as the resolution of the boundary layers in the vicinity of the orifice is of major importance for a correct orifice impedance estimation. The velocity is prescribed at the duct inlet boundary as a time-dependent harmonic fluctuation with zero mean. Finally, a fixed pressure boundary condition is applied to the outlet side of the duct to close the problem definition.

The present approach is limited to cases where the hydrodynamic vortex structures are contained inside the numerical domain. As the boundary conditions for the incompressible simulations are defined through prescribed velocity and pressure values, vortices crossing the domain limits are not accounted for by boundary treatment. Violation of this rule has shown to deliver inaccurate results as the numerical problem formulation is inconsistent in that case. If vortices approach the in-/outflow boundaries, the computational domain has to be extended. This can be required for configurations with orifices of small diameters at high excitation amplitudes, since for these cases the vortices can travel far away from the production zone.

In this work, the incompressible finite volume solver of a commercial code (ANSYS® Fluent v14/v15) is used to characterize the flow. The chosen solver is pressure-based, time-dependent, implicit and second-order in time and space. The pressure correction scheme applied is the Semi-Implicit Method for Pressure-Linked Equations (SIMPLE). No turbulence modeling is applied for the presented simulations results as the Reynolds number based on the orifice size and velocity fluctuation amplitude at the orifice is rather low (maximum $Re \approx 3000$ at high excitation levels). Turbulence modeling has shown very limited impact on the estimated orifice transfer impedance under the present operating conditions. Comprehensive parameter studies regarding grid, time-step, and solver parameters have been performed to ensure that the presented results are independent of these numerical settings. Standard parameters for the results presented here are: minimal size of mesh cell $h_{min} = 1 \times 10^{-5}$ m, time-step $\Delta t = 1 \times 10^{-6}$ s, number of iterations per time-step $N_{iter} = 20$ iter/time-step. Both 2-D axi-symmetric and 3-D simulations have been carried out in this work to investigate 3-D effects.

### 5.1.3 References for the validation of the method

As mentioned in the introduction of this chapter, the results computed from incompressible unsteady CFD simulations are compared to two different data sets: compressible CFD results and experimental data performed on two particular Helmholtz resonator geometries. This paragraph describes only briefly these references, for which more details can be found in the papers [106, 108].

#### Numerical compressible CFD reference data

The compressible flow simulations used for comparison in this work have been performed by Kilian Förner [106, 108] at the Professur für Thermofluiddynamik at the TUM.

The compressible simulations of the Navier-Stokes equations with both laminar and turbulent models (LES with $K$-equation eddy-viscosity model) were done with the Pimple algorithm of OpenFOAM [110]. In order to distinguish between the differences originating from the numerical solvers and from the modeling part for the computed impedance values, both open-end tube (without accounting for the cavity backing wall) and closed-end tube (complete Helmholtz resonator) configurations are simulated with the compressible solver. It was also verified that the turbulence modeling leads only to very minor differences. With the turbulence model activated, the acoustic resistance increased very slightly. This shows that turbulent structures as represented by the sub-grid scale model do not have a significant impact on the separation mechanism itself in the chosen SPL range.

In the compressible flow simulations, the computational domain is excited from the boundary opposite to the resonator at a distance $l_{\mathrm{sim}}/d_{\mathrm{cav}} = 2$ by imposing a propagating characteristic wave $F_r$ of amplitude $A_f$ (see Fig. 5.2). For this purpose, the Navier-Stokes characteristics boundary condition (NSCBC), given by Poinsot and Lele [232], is applied. Particular care has been taken to match $A_f$ with the value of the amplitude $A_u$ in the incompressible flow simulations to ensure the same excitation state of the orifice in both closed or open tubes. The method to define correctly the excitation amplitude is discussed in detail in Section 5.1.4. The $F_r$ wave can be imagined as an incoming wave traveling towards the resonator whereas $G_r$ is the reflected wave traveling back to the domain inlet. Shortly after the inlet, area averaged pressure and velocity fluctuations are evaluated across a reference plane to determine $F_r$ and $G_r$ time series and then to evaluate the reflection coefficient $R_{num}$. For harmonically excited simulations, the reflection coefficient is determined through $R_{num}(\omega) = \hat{G}_r(\omega)/\hat{F}_r(\omega)$, with angular frequency $\omega$. The reflection coefficient is transformed to the resonator normalized surface impedance $z_r$, using the relation $z_r = (1 + R_{num/exp})/(1 - R_{num/exp})$.

#### Experimental reference data

In addition to the numerical results, a measurement campaign has been performed by Temiz M. A. and co-workers at the Eindhoven University of Technology [108] on a Helmholtz resonator configuration. The experiments have been carried out with an impedance tube. The resonator sample was placed at one extremity of the impedance tube. The measurement data give the surface impedance of the complete Helmholtz resonator. The tube has six BSMA MPA microphones with an average sensitivity of 50.45 mV/Pa, equally distributed along a 1-m long tube. The microphones have been calibrated to measure the reflection coefficient $R_{exp}$ in the frequency range [100 Hz - 700 Hz]. The numerical work is limited to this frequency range. The reflection behavior of the test object has been studied for various SPLs. Data for the cases 89.3 dB and 119.7 dB are presented here for assessment of the investigated methodology. These SPL values are controlled over the entire frequency range at a reference position, which is here defined by the closest microphone from the resonator front plate placed 49.7 mm away. The 89.3 dB case is in the linear regime while in the 119.7 dB case nonlinearities are present.

### 5.1.4 Setting the excitation amplitudes

For the purpose of comparing results of the incompressible simulations with existing experimental data, it is necessary to ensure that the velocities in the orifice agree with each other for the different set-ups. This fact is also relevant for comparison with the compressible solver, as the definition of the excitation between compressible and incompressible solvers is fundamentally different. The excitation is given by a time varying axial velocity fluctuation at the inlet boundary for the incompressible simulations, whereas it is defined through injection of an acoustic wave $F_r$ for the compressible ones. The reflection coefficient is therefore a key parameter to match results in the nonlinear regime. This has been found to be a challenge from a practical point of view. Drawing impedance curves for a given resonator at a particular SPL can also be achieved by the present incompressible approach. It does not necessitate the prior knowledge of intermediate variables such as the reflection coefficient. Nevertheless, this can require several simulation trials for one case, in which the input velocity is progressively modified until the SPL matches the target one.

To compare the results from the investigated methodology to the existing data sets, the following procedure has been applied, based on the relations between propagating waves $F_r$ and $G_r$ and primitive variables $p'$ and $u'$. Below the cut-on frequency of the duct, and in case of no mean-flow, the acoustics can be described as the superposition of the Riemann invariants defined by $F_r = 1/2\,(p'/(\rho c) + u')$ and $G_r = 1/2\,(p'/(\rho c) - u')$. In the resonance tube, a

standing wave is developed with a fluctuating pressure at the position $x$

$$p'(x) = \rho c \, (F_r(x) + G_r(x)) \ . \tag{5.13}$$

In the experimental set-up, the reference microphone was mounted at a distance of $l_{ref} = 0.0497\,\mathrm{m}$ away from the resonator front face. This is selected as the reference position $x_{ref}$ for the SPL. Moreover, the reflection coefficient $R = G_r/F_r$ depends on both frequency and amplitude. The reflected wave at the reference position is thus $G_r(x_{ref}) = R(\omega, \mathrm{SPL}) \exp(-\mathrm{j}\omega\, 2l_{\mathrm{ref}}/c) F_r(x_{ref})$. Accordingly, the fluctuating pressure at position $x_{ref}$ is given as $p'/(\rho c) = [1 + R(\omega, \mathrm{SPL}) \exp(-\mathrm{j}\omega\, 2l_{\mathrm{ref}}/c)]\ F_r(x_{ref})$. Considering the ratio of RMS values to harmonic amplitude being $1/\sqrt{2}$, the amplitude $A_f$ of the incoming wave $F_r = A_f \exp(\mathrm{j}\omega t)$ is given as

$$A_f = 10^{\mathrm{SPL}/20} \, \frac{\sqrt{2}\ p_a}{|1 + R(\omega, \mathrm{SPL}) \exp(-\mathrm{j}\omega\, 2l_{\mathrm{ref}}/c)|\ \rho c} \ , \tag{5.14}$$

where $p_a = 20\,\mu\mathrm{Pa}$ is the commonly used reference sound pressure in air.

The fluctuating velocity $u'$ is given as the difference of the Riemann invariants, i. e., $u' = F_r - G_r$. Thus, the amplitude of the velocity $A_u$ at the resonator mouth position (at $x_o = -l_o/2$ in this work) can be calculated as

$$A_{u(x_o)}(\omega, \mathrm{SPL}) = A_f(\omega, \mathrm{SPL})\, |1 - R(\omega, \mathrm{SPL})| \ . \tag{5.15}$$

For the incompressible simulations, the inlet amplitude prescribed at the inlet boundary is directly given by Eq. (5.15). For the compressible simulations, in the case of the full resonator configuration, the inlet boundary condition is $A_f$ given by Eq. (5.14). Finally, exchanging the backing cavity with a non-reflecting outlet ($Z_0 = \rho c$), the amplitude of the $F_r$ wave has to be corrected. The reflection coefficient of the corresponding orifice $R_o$ (i. e. open tube) can be estimated as

$$R_o = \frac{z_r - z_{\mathrm{cav}}}{z_r - z_{\mathrm{cav}} + 2} \ . \tag{5.16}$$

Thus, the amplitude of the $F_r$ wave in the open-end tube configuration $A_{f,o}$ should be set equal to

$$A_{f,o} = A_f \frac{|1 - R|}{|1 - R_o|} \ . \tag{5.17}$$

Table 5.2 lists the values of the different excitation amplitudes needed to ensure the same state at the orifice neck for five frequencies close to the resonator eigenfrequency and for the two investigated SPLs. As the primitive variables and Riemann variables are linked through the reflection coefficient, values of velocity at the orifice coming from the compressible simulations were still

| Frequency [Hz] | 340 | 360 | 380 | 400 | 420 |
|---|---|---|---|---|---|
| | | | SPL = 89.3 dB | | |
| $A_f$ [m/s] | 0.0020 | 0.0033 | 0.0019 | 0.0013 | 0.0011 |
| $A_u$ [m/s] | 0.0021 | 0.0043 | 0.0024 | 0.0014 | 0.0009 |
| $A_{f,o}$ [m/s] | 0.0076 | 0.0165 | 0.0097 | 0.0057 | 0.0041 |
| | | | SPL = 119.7 dB | | |
| $A_f$ [m/s] | 0.0552 | 0.0601 | 0.0574 | 0.0490 | 0.0401 |
| $A_u$ [m/s] | 0.0411 | 0.0474 | 0.0471 | 0.0407 | 0.0295 |
| $A_{f,o}$ [m/s] | 0.1500 | 0.1823 | 0.1891 | 0.1693 | 0.130 |

Table 5.2: Example of inlet excitation amplitudes for $F_r$ and $u'$ at two different SPLs.

slightly different, but these deviations have been judged to have only a small impact on the estimated impedance values. Note that in the linear regime (here at 89.3 dB), even if specific values are given in Table 5.2, computations give the same impedance values taking different inlet velocity amplitudes, as long as these prescribed excitation amplitudes are small enough to remain in the linear regime of the resonator. The above considerations are, however, of major relevance for the nonlinear regime.

## 5.2 Results obtained for small excitation amplitudes

For harmonic pulsating flows at the orifice, the impedance value for each excitation frequency is computed by dividing the Fourier coefficients of the fluctuating pressure loss through the orifice $\Delta\hat{p}'$ with the velocity perturbation $\hat{u}'$. Each frequency requires therefore one CFD simulation. The harmonic fluctuating inlet velocity is given for a given angular frequency $\omega$ by:

$$u'(t) = A_u \sin(\omega t), \tag{5.18}$$

where the amplitude of inlet velocity $A_u$ is defined as described in Section 5.1.4.

### 5.2.1 Resonator impedance in the linear regime

Figure 5.4 shows the obtained normalized surface impedance curves for the case SPL = 89.3 dB over the frequency range [100 Hz - 700 Hz] compared to the experimental data and the values obtained with System Identification (SI) techniques applied to the compressible solution of the complete 3-D resonator model. Impedance values are normalized by the specific impedance $Z_0$. For

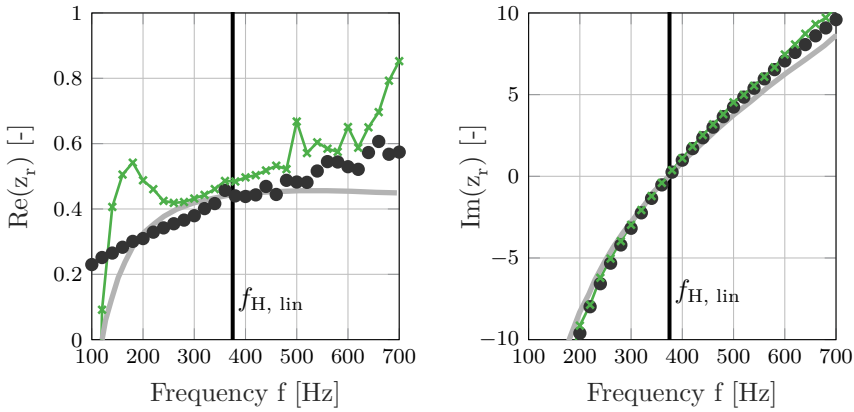


Figure 5.4. Normalized resistance $\mathrm{Re}(z_r)$ (left) and reactance $\mathrm{Im}(z_r)$ (right) of the Helmholtz resonator, obtained with the methodology based on incompressible simulations, compared to experimental data and broadband compressible numerical results (Case SPL = 89.7 dB): 2-D incompressible (●), 3-D compressible with broadband excitation (—), experimental data (—✱—).

each simulation set, it is verified that the impedance values are independent of the measurement sections selected for determining the pressure loss.

All results show a fair agreement around the Helmholtz resonance frequency $f_{\mathrm{H,lin}} = 372\,\mathrm{Hz}$ in the linear regime. The reactance $\mathrm{Im}(z_r)$ matches well with the experimental data over the entire frequency range. However, one can see that the discrepancies increase slightly with increasing frequency. The incompressible harmonic results lead to a better reactance prediction than the compressible solver far from the resonator eigenfrequency. Same observation can be made on the resistance $\mathrm{Re}(z_r)$. Notice also that both experimental and compressible values present a large error far from the resonance frequency as the impedance values are obtained using the reflection coefficient $R_{exp}$ or $R_{num}$, so that even a small error on the reflection coefficient gives a larger uncertainty on the impedance in such condition. This comes from the fact that the transformation from $R_{exp/num}$ to $\mathrm{Re}(z_r)$ is ill-conditioned away from the eigenfrequency in the case of the complete Helmholtz resonator, since the magnitude of the reflection coefficient is close to unity at these frequencies. The resistance obtained by incompressible simulations seems a bit lower than experimental data, but the trend in frequency (given by the slope) is well predicted.

### 5.2.2 Broadband excitation and system identification

The objective of the transfer function identification is to obtain a frequency-dependent impedance $Z(\omega)$ that relates the output orifice pressure differences $\Delta p_o$ to the input excitation velocities $u'$, based on a unique simulation with a broadband excitation. The reduction to a single run with broadband input signal is possible only because of the linear and time-invariant behavior of aeroacoustic flow problems for sufficiently small excitation amplitudes [233]. The method for system identification used in this work for linear systems is based on the Finite Impulse Response approach, solving the Wiener-Hopf equation for a single-input, single output (SISO) system (see Fig. 5.5). The present implementation of this method was done by Föller [104] and was used in combination to Large Eddy Simulations. It is applied here to the outputs of the incompressible flow simulations.

In order to evaluate the transfer function $F_t(\omega)$, which can be directly identified as an impedance, one wants to find for each time $t_i = i\,\Delta t$ the discrete function $\mathbf{h}$, also called Unit-Impulse-Response (UIR), that relates the discrete response $\mathbf{\Delta p'}$ to the discrete excitation velocity $\mathbf{u'}$. It yields

$$\mathbf{\Delta p'}_i \approx \sum_{k=L_s}^{L_e} \mathbf{h}_k\, \mathbf{u'}_{i-k}\,, \tag{5.19}$$

for a finite number of coefficients ranging from $k = L_s \cdots L_e$. Typically, a causal system is defined by ($L_s = 0$, $L_e = L_S$), whereas ($L_s = -L_S/2$, $L_e = L_S/2$) are chosen for a non-causal one. The parameter $L_S$ is related to the memory of the system. Some constraints on $L_S$ have been emphasized in [234]. The length of the UIR $L_S$ must be chosen such that the memory time $t_{mem} = L_S\,\Delta t$ of the filter is not smaller than any relevant time lag of the chosen system to be identified. It should also not be too large to avoid degrading the conditioning of the Wiener-Hopf system. The subscript $i$ is used as time index. The UIR vector $\mathbf{h}$ is found by solving the Wiener-Hopf equation:

$$\mathbf{h} = \mathbf{\Gamma_S^{-1} C_S}, \tag{5.20}$$

where $\mathbf{\Gamma_S}$ approximates the auto-correlation matrix of the signal $u'$ and $\mathbf{C_S}$ the cross-correlation vector of $u'$ with $\Delta p'$. The vector $\mathbf{C_S}$ and matrix $\mathbf{\Gamma_S}$ are given, for a causal system, by

$$\mathbf{C_S}_i \approx \frac{1}{K_S} \sum_{k=L_S}^{N_S} \mathbf{u'}_{k-i} \mathbf{\Delta p'}_k \tag{5.21}$$

and

$$\mathbf{\Gamma_S}_{ij} \approx \frac{1}{K_S} \sum_{k=L_S}^{N_S} \mathbf{u'}_{k-i} \mathbf{u'}_{k-j}\,, \tag{5.22}$$

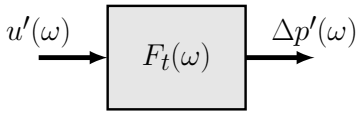


Figure 5.5. SISO system to determine the orifice impedance.

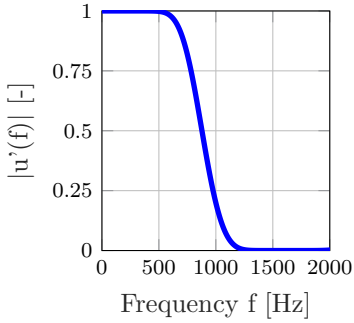


Figure 5.6. Spectrum amplitude of the input velocity signal $|u'(f)|$.

respectively. $K_S = N_S - L_S + 1$ is a normalization factor accounting for the time series sample length $N_S$ and the number of UIR coefficients considered. After the UIR vector $\mathbf{h}$ has been determined, the $z$-transformation is applied to compute the transfer impedance function $F_t(\omega) = Z(\omega)$:

$$Z(\omega) = \sum_{k=0}^{L_S} \mathbf{h}_k \, e^{-\mathrm{j}\omega\Delta t k} \, . \tag{5.23}$$

The inlet velocity time series used as excitations have been generated respecting the criteria listed by [104] for an optimal identification of acoustic scattering coefficients. The excitation is therefore uncorrelated with itself, and consists of a broadband low-pass filtered excitation spectrum with constant amplitude at frequencies lower than the cut-off frequency $f_c$. Considering the range of frequencies of interest [100 Hz − 700 Hz], $f_c$ has been chosen as 800 Hz (see Fig. 5.6). The amplitude of the input has been chosen small enough, with $A_u = 0.002\,\mathrm{m/s}$ to ensure the linear working regime of the orifice, as verified from the harmonic computations.

The CFD data have been generated with a time-step $\Delta t = 5 \times 10^{-6}\,\mathrm{s}$ and a length of 100 000 time-steps, corresponding to 0.5 s in total. Data for the first 0.05 s have been cut out to avoid any spurious numerical transient effect and the remaining data are used to solve the Wiener-Hopf equation. The time series are split into two samples: the teaching sample for the determination of the filter parameters, and the testing sample for the assessment of the quality of the obtained filter. Figure 5.7 shows the estimated Helmholtz resonator impedance obtained with the broadband system identification compared to the harmonically excited one and the experimental values. As one can see, the agreement with the impedance values obtained by mono-harmonic excitation is very good. Broadband impedance values shown in Fig. 5.7 are obtained with both causal and non-causal models with different values of the parameter

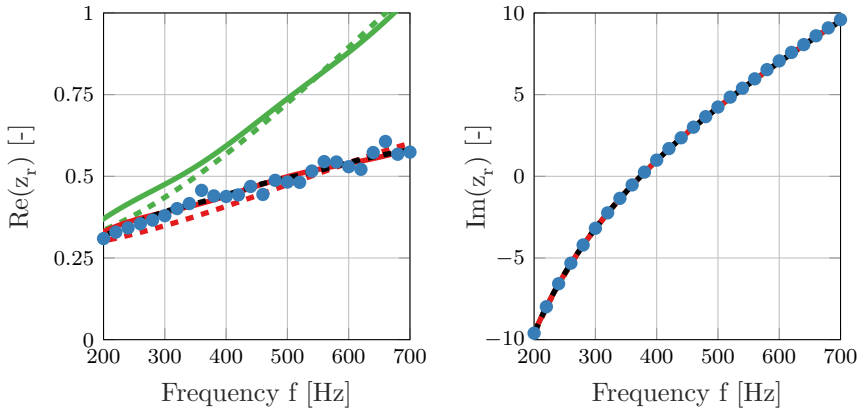


Figure 5.7. Normalized resistance $\mathrm{Re}(z_r)$ (left) and reactance $\mathrm{Im}(z_r)$ (right) of the Helmholtz resonator evaluated with broadband excitation with SI technique: causal ($L_S = 50$, $L_S = 500$, $L_S = 1000$) and non-causal models ($L_S = 50$, $L_S = 500$) compared to harmonic results (●).

$L_S$. $\Delta p'$ is computed from the pressure time series at sections 0.3 m away from the orifice. The potential flow contribution is subtracted after the system identification step in terms of impedance (reactive part) and the analytical backing cavity impedance is added to get the final impedance values plotted in Fig. 5.7, referred to as approach 1 in Fig. 5.3. The broadband approach presents the advantage that only a single CFD simulation is required to generate the time data sufficient to get the impedance value over a possibly large frequency range at once. The results obtained have shown to be rather robust to variations in the SI parameters ($L_S$ and $N_S$). Reducing the time data length $N_S$ by a factor 2 and 4 gives similar result for the impedance. The choice of $L_S$ mostly impacts the estimated resistance. A sufficient high value of $L_S$ is required to get a converged value for the resistance. Here taking $L_S \geq 500$ appears to be adequate. Regarding the choice of models (causal or non-causal), it was expected from the compressible case [234], that the use of the primitive variables $\{p', u'\}$ requires the use of non-causal filter models to give satisfying results, whereas the choice of causal models necessitates the use of the Riemann invariant variables $\{F_r, G_r\}$ instead. Nevertheless, as shown in Fig. 5.7, the causal model appears to give a better estimate of the impedance than the non-causal one. A causal filter model is thus more suitable to describe the present system, illustrated in Fig. 5.5. The difference between the type of models concerns predominantly the acoustic resistance.

### 5.2.3 Comparison of the two approaches

The two approaches to extract $Z_o$ from the incompressible results, as discussed in Section 5.1.1, are investigated here in the case of the linear regime for both mono-harmonic and broadband excitations. The difference in concept between these approaches lies in limiting the black box model to the orifice or including the duct inside this system. The correction in terms of pressure losses in the duct segments is thus performed in the frequency domain (approach 1) or in the time domain (approach 2). Approach 2 requires therefore to get the pressure directly at inlet/outlet of the orifice. In the harmonic case, this is directly done using the analytical expression of $\partial u'/\partial t$ from the known sinusoidal input signal. For the broadband excitation case, $\partial u'/\partial t$ is estimated numerically from the time series of $u'$. The broadband results presented in Fig. 5.8 are obtained with a causal filter taking $L_S = 500$.

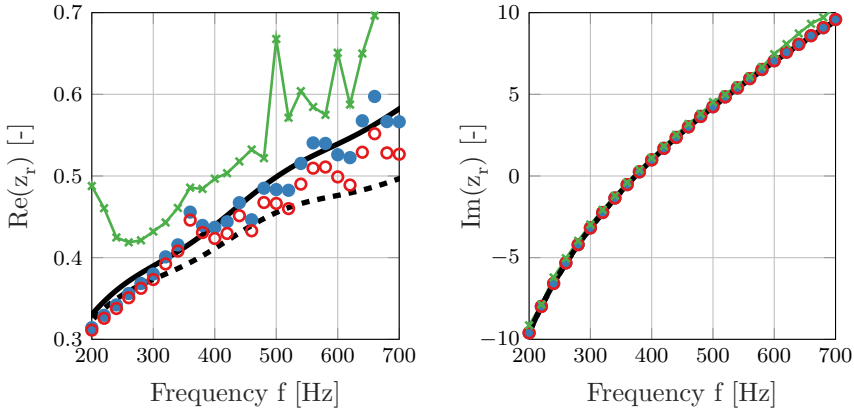


Figure 5.8. Normalized resistance $\mathrm{Re}(z_r)$ (left) and reactance $\mathrm{Im}(z_r)$ (right) of the Helmholtz resonator evaluated from incompressible simulations: approach 1 harmonic (●), approach 2 harmonic (○), approach 1 broadband (—), approach 2 broadband (- - -), experimental results (-✱-).

The impedance values resulting from both approaches are overall close, as shown in Fig. 5.8. The reactance values in particular are very similar. More discrepancies can be noticed for the resistance and these disparities grow with increasing frequency. Approach 2 delivers consistently lower resistance values than approach 1, being then further away from the experimental reference. Additionally, approach 1 gives broadband results closer from the harmonic solution. Finally, it was observed that approach 2 is more sensitive to the simulation parameters (time-step, mesh refinement, dependency of measurement section) than approach 1. For these reasons, approach 1 can be favored for its robustness. These conclusions, drawn for the linear regime with both harmonic and broadband excitations, hold as well for the nonlinear regime.

## 5.3 Results obtained for higher excitation amplitudes

This section presents the results obtained at higher excitation amplitudes, for which the ABL separates at the edges of the resonator neck, i. e. in the nonlinear regime of the resonator.

### 5.3.1 Resonator impedance in the nonlinear regime

Figure 5.9 presents the normalized impedance obtained at a SPL of 119.7 dB from the different numerical methods performed on the investigated resonator geometry compared to the experimental data. 3-D simulations have been performed with a much shorter computational domain with $l_{\mathrm{sim}} = 2\,d_{\mathrm{cav}}$. The 3-D mesh consists of nearly 1.5 million cells. Impedance results from different measurement sections have been shown to be identical. Only simulations with a mono-harmonic excitation are performed in the nonlinear regime, as the method presented in Section 5.2.2 is no longer applicable.

The main conclusion from this work is that the tested numerical models, in spite of their differences in terms of physics and methodology, are in very good agreement. Nevertheless, a systematic over-prediction of the resistance

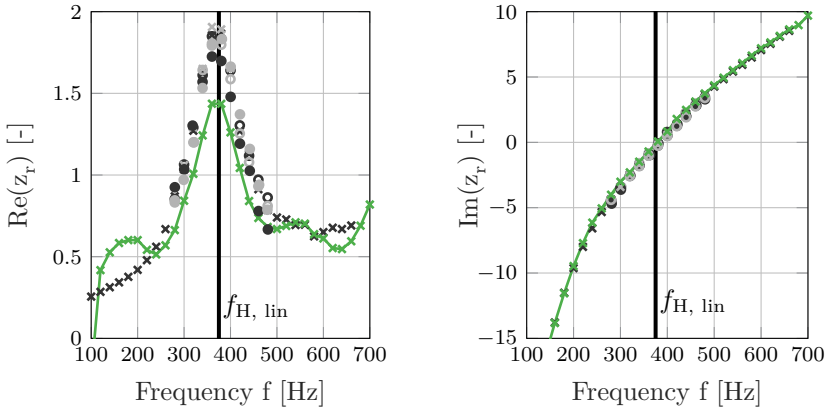


Figure 5.9. Normalized resistance $\mathrm{Re}(z_r)$ (left) and reactance $\mathrm{Im}(z_r)$ (right) of the Helmholtz resonator evaluated from incompressible simulations at 119.7 dB: experimental results [108] (–✕–), 2-D incompressible decomposed model (✕), 2-D compressible decomposed model (○), 2-D full resonator (●), 3-D incompressible decomposed model (×), 3-D compressible decomposed model (○), 3-D full resonator (●).

compared to experimental results can been seen. The discrepancy is expected to be of physical nature, as mesh/time-step influences have been discarded. The comparison of the results for the whole resonator and the results obtained by simulating separately the orifice and the back cavity shows overall that the combined model gives very satisfying results and that this model is still valid for this range of moderately high sound amplitudes. Some small differences between the 2-D and 3-D models can be observed, but the overall impact of 3-D effects is rather small, although it clearly increases with increasing velocity at the orifice. The spatial visualization of the formed eddies is represented in Fig. 5.10 using the common $Q_v$-criterion [156] for incompressible flows, fixing an arbitrary threshold value for $Q_v$. $Q_v$ is defined as the positive second invariant of the velocity gradient tensor. It is expressed as

$$Q_v \equiv \frac{1}{2}\left(u_{i,i}^2 - u_{i,j}\, u_{j,i}\right) = \frac{1}{2}\left(\|\mathbf{\Omega}\|^2 - \|\mathbf{S}\|^2\right), \tag{5.24}$$

and described the vortices as the regions where the vorticity $\mathbf{\Omega}$ magnitude prevails over the strain-rate $\mathbf{S}$ magnitude. It can be seen from Fig. 5.10 that even if the eddies dissipate in an asymmetrical manner, the separation process at the orifice edges itself is not influenced. The eddies structure in the vicinity of the orifice is characterized by an axisymmetric shape ("donuts-like" shape). Linking this observation to the good prediction from 2-D axisymmetric solver allows to conclude that, at the excitation levels considered, 3-D effects related to the propagation of the vortices in the duct and the dissipation of the eddies energy do not affect significantly the predicted acoustic behavior of the orifice.

Concerning the reactance, numerical and experimental data are very similar, with a very good match of all numerical results. In detail, it seems however that the numerical approaches under-predict to some very small extent the reactance, giving a slightly higher resonance frequency. Compared to the linear

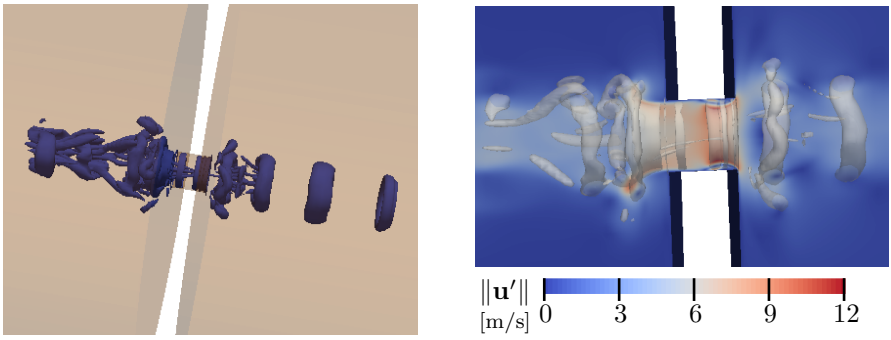


Figure 5.10. Visualization of the formed eddies for the resonator HRA at $f = 380\,\mathrm{Hz}$ and $\mathrm{SPL} = 119.7\,\mathrm{dB}$: (left) with a $Q_v$-criterion level $Q_v = 5 \times 10^5\,\mathrm{s}^{-1}$, (right) with a $Q_v$-criterion level $Q_v = 2 \times 10^6\,\mathrm{s}^{-1}$ superimposed on velocity magnitude field.

regime case, the reactance is only affected in a minor way by variation of the excitation amplitude.

Complementary computations have been run for a different Helmholtz resonator geometry, based on the case studied by Hersh et al. [133] (see Fig. 12(a) in the referred work), to see if the over-prediction in resistance is also present. For this second geometry, noted HRB, the dimensions of the acoustic resonator are $l_o = 1.59\,\text{mm}$, $d_o = 6.35\,\text{mm}$, $l_{\text{cav}} = 25.4\,\text{mm}$, and $d_{\text{cav}} = 50.8\,\text{mm}$. Figure 5.11 shows the comparison of the numerical results from both incompressible and compressible numerical approaches to the experimental data of the literature. The general trends for both resistive and reactive parts with respect to increasing excitation amplitudes are correctly captured by the numerical methods. A good quantitative agreement is also obtained. A shift in the resonance frequency can be clearly observed in Fig. 5.11, with a growing deviation from its value in the linear regime $f_{\text{H,lin}}$ towards higher frequencies for increasing SPLs. This shift occurs due to a decrease of the reactance for increasing excitation amplitudes, which is related to a reduction of the effective length by vortex shedding [287]. Since the neck geometric length is smaller in this case than for the first resonator configuration investigated, this effect is much more visible here. The present cases correspond to high Shear numbers $\text{Sh} \gg 1$, with $\text{Sh} \in [25 - 60]$, where $\text{Sh} = d_o\sqrt{\omega\rho/(4\mu)}$. The physical interpretation of the nonlinear impedance at such high Shear number values was shown [287] to be more complicated than at smaller Sh, due to complex vortex shedding effects, and requires further investigation. The resistance over-prediction from the numerical methods seems to be still present in this case, even if significantly less pronounced.

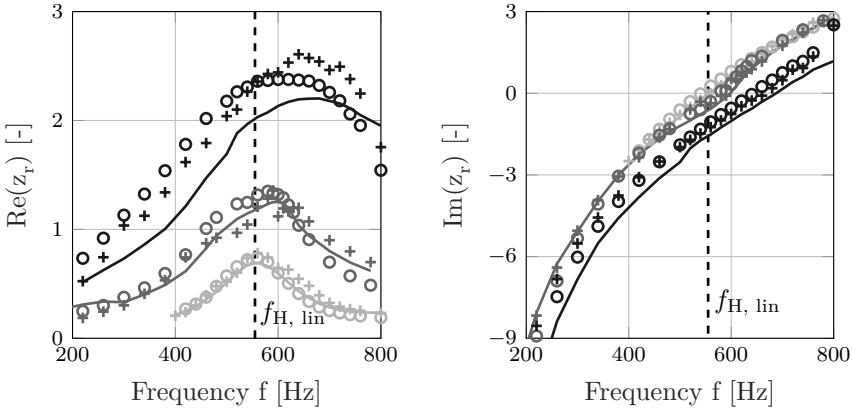


Figure 5.11. Normalized resistance $\text{Re}(z_r)$ (left) and reactance $\text{Im}(z_r)$ (right) for HRB at three SPLs — 120 dB (▭), 130 dB (▭), 140 dB (▭): obtained from incompressible method (+), compressible method (○), and experimental data from Hersh [133] (—).

### 5.3.2 Effects of rounded edges

One possible reason for the systematic difference between experimental and numerical impedance results is thought to originate from the existence of some rounding of the edges for the experimental Helmholtz resonator test sample. It was already shown in previous works [108, 188] that the presence of chamfers strongly changes the structures of the produced vortices and the resistance at moderate and high excitation amplitudes. In the present study, the size of the considered chamfers is much smaller, so that one can speak about micro-chamfers or micro-rounded edges. These micro-rounded edges are investigated as representing more realistic edges, similarly to the ones expected from manufacturing processes.

Figure 5.12 shows the impact of micro-rounded edges on the impedance for both linear and nonlinear regimes. In the linear regime, the presence of micro-rounded edges does not affect the computed resistance nor the reactance. This is expected as the volume of the orifice is not considerably modified by the micro-chamfering and therefore the reactance, related to the inertial effects,

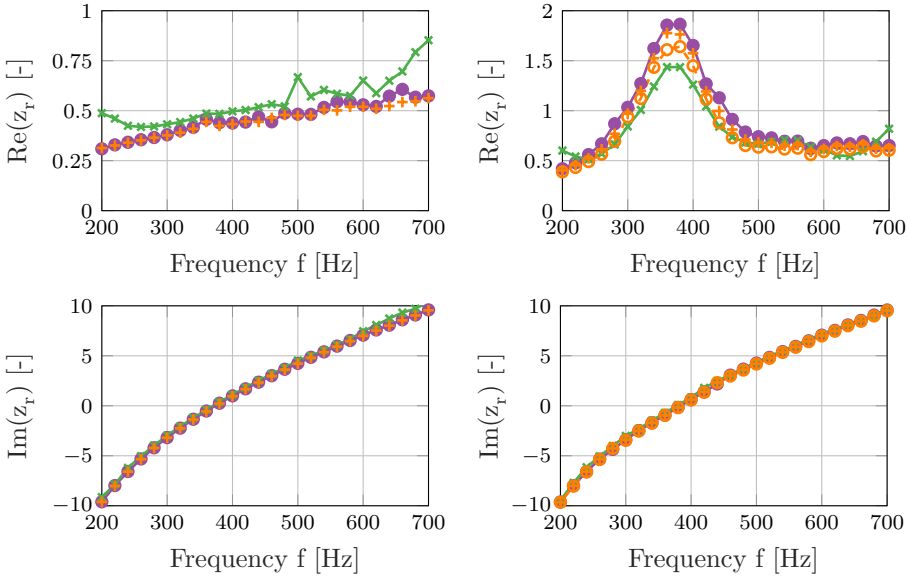


(a) Linear regime (89 dB) (b) Nonlinear regime (118 dB)

Figure 5.12. Impact of edge rounding on the computed normalized impedance for the geometry HRA: sharp edges incompressible (●), $R_f = 40\,\mu m$ rounded edges incompressible (+), $R_f = 80\,\mu m$ rounded edges incompressible (⊙), experimental data (×).

is not altered. The geometrical modification at the orifice edges does not influence the flow path, producing no change for the pressure drop and therefore no change in the resistance either. In the nonlinear regime, one can observe from Fig. 5.12b that even small micro-rounded edges can affect significantly the predicted resistance values. Results for two different rounded edge radii are shown, $R_f = 40\,\mu\text{m}$ and $R_f = 80\,\mu\text{m}$, respectively. These radii represent 1% and 2% of the orifice thickness. From these observations, accounting for rounded edges tends to decrease the resistance, delivering a better agreement with the experimental results. After consideration of the rounded edge radius for the actual test sample, which is found to be close to 80 µm, the extent of this change for seems however to not fully explain the observed discrepancies in resistance between the numerical and experimental approaches for the case HRA. A rounded edge radius larger than 120 µm would indeed be required in the simulations to equal the experimental resonance peak in resistance. No impact on the reactance can be noticed. Additional flow computations have shown that the impact of rounded edges on the impedance is captured in a similar manner for both compressible and incompressible cases, for both rounded edges and straight chamfer situations. The actual micro-scale geometry does, therefore, not change significantly the results.

## 5.4 Conclusions — advantages and limits of the present approach

In this chapter, a method to characterize numerically the aeroacoustic behavior of Helmholtz resonators was investigated and validated for both linear and nonlinear regimes. The procedure to assess the present methodology, by ensuring the same velocities in the orifice as in compressible flow simulations and experiments, was detailed. The numerical results for the resistance in the nonlinear regime, however, show a systematic slight over-prediction with respect to experimental data. The impact of micro-rounded edges on the estimated impedance was investigated. Even if the presence of micro-rounded edges was deemed insufficient to explain alone the discrepancies, such geometrical details were found to affect significantly the computed resonator resistance, and should therefore be included for accurate predictions of the acoustic behavior of Helmholtz resonators in their nonlinear regime.

The proposed methodology was shown, nevertheless, to give satisfying results for the acoustic impedance of Helmholtz resonators. It is an alternative for the study of the nonlinear regime of such acoustic damping systems. The proposed methodology can be applied for the study of both linear and nonlinear regimes of Helmholtz resonators with commercial CFD software with moderate computational costs compared to compressible flow simulations. One of the most significant advantages of this methodology is that it does not rely on

the reflection coefficient to estimate the impedance (as in experiments or compressible simulations) and instead the impedance is directly computed from the pressure and velocity. Impedance curves are therefore valid on a broader frequency range than just around the resonator resonance frequency. This approach can also be extended to the study of an orifice with bias or grazing flow in a straightforward manner following previous works [118,214,224]. In the quiescent case, two possible approaches in the post-processing of the orifice transfer impedance were studied. The difference in concept between these approaches lies on the correction of the pressure losses in the duct segments: in the frequency domain (approach 1) or in the time domain (approach 2). A general conclusion is that both approaches investigated in this work lead to similar impedance prediction but approach 1 was found to be more robust. Finally, the possible impact of 3-D effects on the impedance results presented in this work were investigated and judged minor under the chosen conditions.

# Chapter 6

# Aeroacoustic characterization of nonlinearities at perforates

In this chapter, the methodology proposed and validated in Chapter 5 is further applied to analyze the nonlinearities appearing for structures with orifices at high amplitude sound excitations. The nonlinear character related to the acoustic dissipation by flow separation can be detected by two aspects for a harmonic excitation. On the one hand, the amplitude and phase of the reflected wave may depend on the amplitude of the excitation in a non proportional manner. This was shown in the previous chapter in terms of the acoustic impedance. On the other hand, scattering of acoustic energy to other frequencies, called higher harmonics, may occur. The pattern for these higher harmonics, reported in the literature and characterized by dominating odd harmonics, is investigated by means of the present numerical method.

This chapter aims at giving a global understanding of the nonlinear regime of orifices and resonators by making the link between the local flow field, the global impedance, and the spectrum of the acoustic response. The study of the higher harmonics pattern delivers in-depth information on the local flow field generated by high amplitude acoustic excitation. This constitutes an original investigation of the physics of orifices in the nonlinear regime.

## 6.1 Energy scattering to higher harmonics for orifices

### 6.1.1 Nonlinearities caused by flow separation

In the low Strouhal number region, i.e. $\mathrm{Sr} < 1$, the acoustic velocity amplitude is high enough for the separation of the acoustic boundary layer at the orifice edges to occur. The pressure difference induced by the acoustic losses at the orifice is no longer linearly related to the incident velocity perturbation. The frequency spectrum of the transmitted sound will therefore be distorted towards higher harmonics. For incompressible flow simulations with a mono-harmonic velocity excitation, the nonlinearities related to the creation of vortices can be seen in the distortion of the pressure loss time series from the original sinusoidal shape. This is illustrated in Fig. 6.1 for three different values of $A_u$ at 380 Hz for the Helmholtz resonator geometry HRA detailed in Table 5.1. The appearance of higher harmonics has been demonstrated experimentally by Ingård and Ising [159] and Ingård [158] for a pure tone incident on an orifice plate in a duct terminated by an absorber, and by Cummings [69] using tone-burst signals. The relationship between the pressure and velocity amplitudes of the acoustic fluctuations, which is linear at sufficiently low pressure amplitudes, is found to approach a quadratic relation at larger SPLs. In those works, the frequency content of the response of orifices is analyzed in detail. The spectrum of the orifice response is dominated by the odd higher harmonics. These observations are in good agreement with results obtained by Salikuddin and Plumblee [260] on the measurements of power losses at various types of duct terminations using an acoustic impulse technique. Cummings and Eversman [72] offered a theoretical explanation for those acoustic losses and harmonic patterns based on a quasi-steady flow model. Dedicated flow visualization studies supported these theories and gave a better understanding of the link between nonlinear acoustic losses and the eddies formed at the edges. Whiffen and Ahuja [313] used a schlieren system to study the turbulent structure of an acoustically excited jet and showed periodic perturbations both with and without flow.

Among the mentioned works, the ones dealing specifically with the energy scattering to higher harmonics focus on acoustic losses due to vortex shedding at the edges of very thin orifices (for which $l_o/d_o \ll 1$, see Fig. 6.2a). The effects of vortex propagation and vortex interaction inside the orifice are therefore not present. For example, in the study of Ingård and Ising [159], the plate at the orifice is tapered from 6.0 mm down to 0.1 mm, so that actually only one edge can be seen. Several other studies considered orifices of arbitrary thickness (Fig. 6.2c), e.g. Ingård and Labate [160], Hersh et al. [133] and Temiz et al. [287], but the detailed spectrum of the orifice acoustic response was not in the scope of these works.

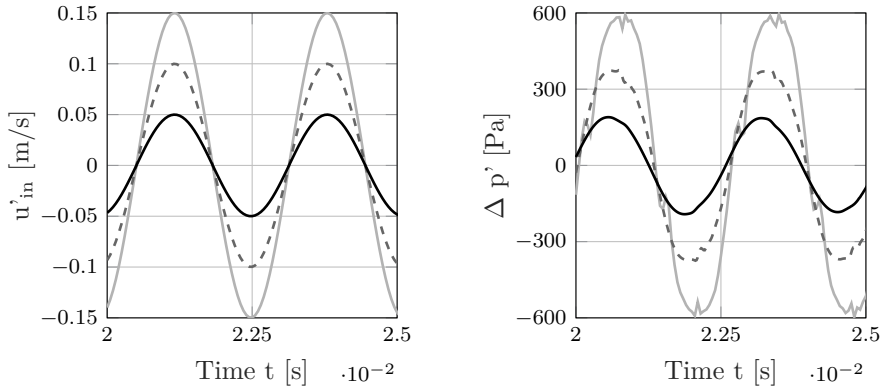


(a) Inlet axial velocity $u'_{\mathrm{in}}(t)$

(b) Pressure loss $\Delta p'(t)$ between the monitored duct sections at $x = \mp 2\, d_{\mathrm{cav}}$

Figure 6.1. Time series of $u'_{\mathrm{in}}$ (left) and $\Delta p'$ (right) for different excitation amplitudes $A_u$ at $f = 380\,\mathrm{Hz}$ for the Helmholtz resonator HRA: Sr = 1.42 ($A_u = 0.5\,\mathrm{m/s}$) (▬), Sr = 0.71 ($A_u = 1\,\mathrm{m/s}$) (▪ ▪), and Sr = 0.47 ($A_u = 1.5\,\mathrm{m/s}$) (▬).

The behavior of thick orifices has been investigated by studies on open end tubes. The main theoretical results for this configuration (illustrated in Fig. 6.2b) can be found in the investigations of Howe [145], Disselhorst and Van Wijngaarden [87], and Peters and Hirschberg [228] on the exit of open pipes in presence of high amplitude pressure waves. In [87], schlieren pictures show that for a sharp edge, vortices are formed during inflow and are shed from the pipe during the outflow. From these observations, a quasi-steady model was derived, in which a formed jet is accounted for. In [228], the vortex shedding process is described by the single panel method, as an alternative to the single vortex model from Howe [145], by accounting for an additional Magnus force to compensate the effect of the time dependence of the circulation of the vortex.

A limited number of numerical studies focused on the sound-excited flow and acoustic nonlinearities at orifices with a look at the response spectrum. In the work by Jing and Sun [165], a potential model is developed to investigate the sound-excited flow field at a circular orifice. The strength of the shed vortices is directly determined by applying a Kutta condition at the orifice edge. In this potential theory, it is assumed that the eddies shed from the orifice edge are simply moved by the fluid slug coming out of the orifice. The slug was considered either cylindrical or in the shape of an inviscid steady jet. A good agreement between this potential theory and measurement data was found. Therefore, the nonlinear behavior depends mainly on the vortex shedding rate at the orifice edges and on the convection speed of the shed eddies, rather than on the fine details of the shed vortices. Similar to the experimental results [69, 159], a

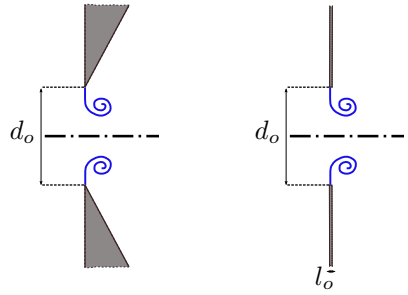


(a) Sharp edge and very thin orifice configurations

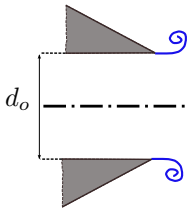


(b) Sharp tube end and very thick orifice

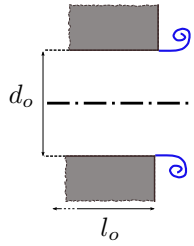


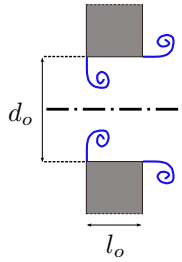


(c) Orifice in this study

Figure 6.2. Different orifice configurations: (a) considered by Ingård and Ising's [159] and Cummings [69], (b) investigated by Disselhorst and van Wijngaarden's [87], and (c) examined in the present work.

harmonic pattern dominated by odd harmonics was found for this geometry with tapered orifice edges (illustrated in Fig. 6.2a).

Recent works aim at describing the acoustic behavior of orifices while accounting for the nonlinear energy transfer between harmonics. In [40], the multi-port characterization method is extended to the case of tonal excitation for nonlinear samples by adding the contribution of the first one or two odd higher harmonic components in the definition of the multi-port. This method assumes the dominance of the odd harmonics and neglects the contribution of even ones. The possibility to apply nonlinear system identification techniques to generalize the impedance concept in the nonlinear regime is also under investigation, e.g. [36, 107].

### 6.1.2 Standard theory for higher harmonics content of orifice acoustic response

When sound of sufficiently high amplitude is transmitted through a sharp-edged orifice in a plate, boundary layer separation occurs at those edges. The vortices formed can substantially increase the acoustic energy dissipation and the transmitted sound spectrum will be distorted with higher harmonics appearing. To analyze these nonlinear mechanisms responsible for the acoustic dissipation at an orifice, the 1-D unsteady Bernoulli equation can be applied to an orifice configuration, see e.g., references [71, 158].

The case of high level amplitude excitations ($\mathrm{Sr} < 1$ and $\mathrm{Sr} \ll 1$), for which the flow separates at the edges of the orifice, is considered here. The velocity in the orifice can be expressed as $u'_o = 1/(C_d\sigma)\, u'$, where the coefficient of contraction $C_d$ accounts for the contraction of the flow due to the separation. It is assumed that the total kinetic energy of the flow in the orifice $1/2\, \rho_0 \left(1/(C_d\sigma)\, u'\right)^2$ is fully dissipated and does not recuperate downstream of the orifice. It follows

$$\Delta p' \approx \rho_0 \frac{1}{\sigma} l_e \frac{\partial u'}{\partial t} + \frac{1}{2} \rho_0 \frac{u'\,|u'|}{C_d^2\,\sigma^2} \ , \tag{6.1}$$

where $l_e$ is the commonly used effective length describing the inertial mass of fluid attached to the orifice. This effective length equals the geometrical length of the orifice $l_o$ with an additional end correction length, as described for example in Ingård [157].

The linear losses caused by friction at the orifice walls can be included by an appropriate real valued constant $R_l$ (see, e.g., Keller and Zauner [174]):

$$\Delta p' \approx \underbrace{\rho_0 \frac{1}{\sigma} l_e \frac{\partial u'}{\partial t}}_{\text{inertia}} + \underbrace{\frac{1}{2} \rho_0 \frac{u'\,|u'|}{C_d^2\,\sigma^2}}_{\text{flow separation}} + \underbrace{R_l\, u'}_{\text{viscosity}} \ . \tag{6.2}$$

In the equation above, it can be seen that the first term accounting for the inertia of the fluid is responsible for the reactive part of the transfer impedance ($\partial u'/\partial t \equiv \mathrm{j}\omega\hat{u}'$). The friction in the orifice and flow separation contribute to the resistive part.

In the nonlinear regime, the frequency response of an orifice is commonly characterized by its dominating odd higher harmonics [158]. This pattern in the spectrum is labeled here as Odd Harmonics Only (OHO) pattern. It can be explained by studying the leading term of the quasi-steady 1-D expression [71] in Eq. (6.2). For high velocities in the neck, the term $C\, u'\,|u'|$ dominates over the reactance contribution and the viscous losses, leading to

$$\Delta p'(t) \approx C\, u'\,|u'| \ , \tag{6.3}$$

where all constants are subsumed in the factor $C = \rho_0/(2C_d^2\,\sigma^2)$. This can be solved analytically for the input velocity $u' = A_u \sin(\omega t)$ chosen in this work as

$$\Delta p'(t) = A_u^2\, C \sum_{k=1}^{\infty} \left( -\frac{8}{\pi} \frac{1}{(2k-1)^3 - 4(2k-1)} \sin[(2k-1)\,\omega t] \right) . \qquad (6.4)$$

The analytic solution contains only the odd harmonics, while the even ones vanish. The OHO pattern originates from the symmetry of the orifice. Regardless of the direction of the flow, the same coefficient of contraction was assumed, so that the nonlinear term can be summarized as $C\,u'\,|u'|$ with $C$ being constant. The impact of asymmetries of the resonator neck on the spectral content of the acoustic response is further detailed in [109].

Figure 6.3 shows the higher harmonics from both incompressible and compressible orifice simulations for the resonator HRA at a SPL of 119.7 dB. The results are given as a function of $\tilde{\omega} = \omega/\omega_{\mathrm{res}}$. The dominance of the odd harmonics is evident with both numerical methods. The agreement of the numerical results with the theoretical values obtained from the quasi-steady model is both qualitatively and quantitatively good. The scattering to higher harmonics takes place close to the eigenfrequency, where the velocities in the orifice are the largest, corresponding to the low Strouhal number region (Sr $< 1$). It should be noticed that the normalization for the spectral content of the orifice response differs between the compressible and incompressible simulations, as the considered input and output variables are different (see Chapter 5). For the incompressible results, the harmonics of $\Delta p'$ are considered and the

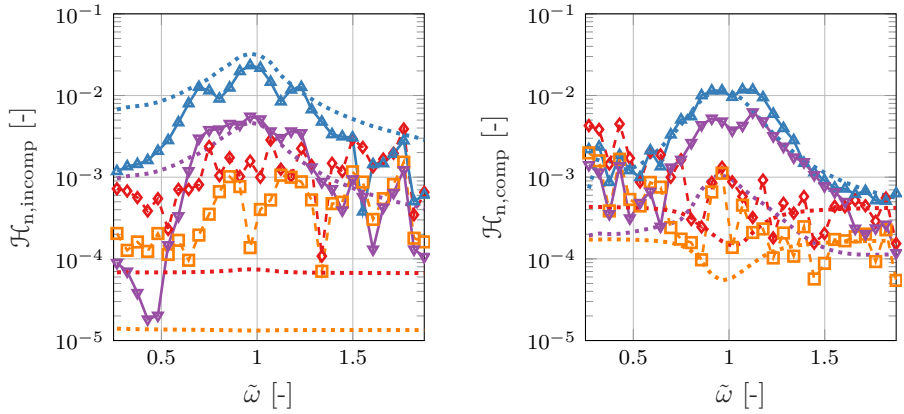


(a) Higher harmonics in $\Delta p'$ from incompressible solution

(b) Higher harmonics in $G_r$ from compressible solution by Förner [108]

Figure 6.3. OHO pattern visualized for the geometry HRA at 119.7 dB: 2nd harmonic (-◆-), 3rd harmonic (-△-), 4th harmonic (-□-), 5th harmonic (-▽-), and with the quasi-steady 1-D analysis (- - -).

normalization is done with respect to the fundamental, such that the relative content of the $n^{\text{th}}$ harmonic $\mathcal{H}_n$ is defined as:

$$\mathcal{H}_{\text{n,incomp}} = \frac{|\Delta\hat{p}'(n\,\omega)|}{|\Delta\hat{p}'(\omega)|}\,. \tag{6.5}$$

For the compressible simulations, the harmonic content $\mathcal{H}_n$ is given by the spectrum of the reflected wave $G_r$ normalized by the harmonic incoming wave $F_r$, i.e.

$$\mathcal{H}_{\text{n,comp}} = \frac{\left|\hat{G}_r(n\,\omega)\right|}{\left|\hat{F}_r(\omega)\right|}\,. \tag{6.6}$$

Figure 6.4 presents the higher harmonics from both incompressible and compressible orifice simulations for the resonator HRB at a SPL of 130 dB. The OHO pattern is in this case also clearly visible but seems to disappear in the frequency range $f \in [550\,\text{Hz} - 610\,\text{Hz}]$, indicated as a gray zone in Fig. 6.4. This behavior is not in agreement with the expected spectrum given by Eq. (6.4) and with previously reported results in the literature [71, 158]. The remainder of this chapter aims at explaining this observed deviation from the standard OHO pattern.

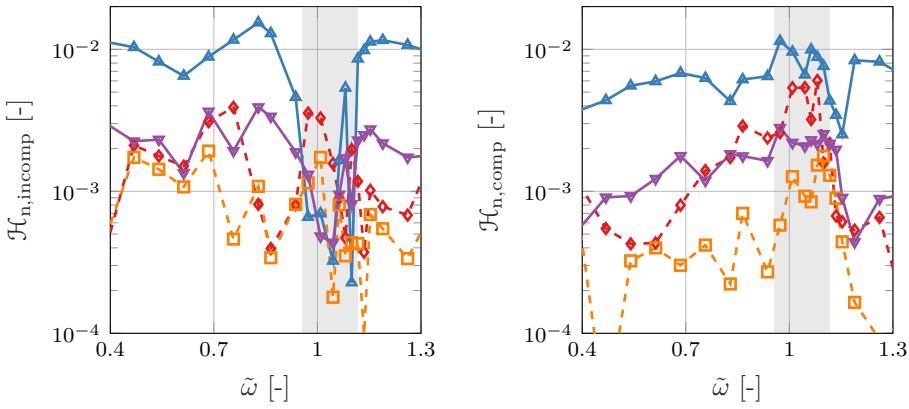


(a) Higher harmonics in $\Delta p'$ from incompressible solution

(b) Higher harmonics in $G_r$ from compressible solution

Figure 6.4. Higher harmonics for the geometry HRB at 130 dB: $2^{\text{nd}}$ harmonic (-◆-), $3^{\text{rd}}$ harmonic (—▲—), $4^{\text{th}}$ harmonic (-□-), $5^{\text{th}}$ harmonic (—▽—).

## 6.2 Vortex disruption phenomenon

### 6.2.1 Model based on vortex convective length

From the observation of the vorticity field in the vicinity of the orifice (see Fig. 6.5), it can be noticed that the vortex formed at the upstream side edge of the orifice is shed through the orifice during half of an excitation cycle. If the convected length $l_c$ traveled by the vortex during a half-cycle is longer than the orifice thickness, the vortex is ejected during the same half-cycle on the other side of the orifice (e.g. Figs. 6.5b, 6.5d and 6.5f). However, if the traveled length is shorter than the orifice thickness, the vortex is "trapped" inside the orifice for the considered half-cycle and it will be ejected during the following half-cycle, on the side where the vortex was first formed (e.g. Figs. 6.5a, 6.5c and 6.5e). This difference in the local vortex path in the orifice vicinity (as illustrated in Fig. 6.6) has been found to impact the higher harmonics content of the nonlinear acoustic response of orifices and will be further illustrated in Section 6.3.

The convection length traveled by a vortex crossing the orifice during half a cycle is defined here as:

$$l_c = \int_{t_s}^{t_e} u_c(t)\,\mathrm{d}t\,, \tag{6.7}$$

where $t_s$ and $t_e$ are the starting and ending times of the convection process for the vortex, $u_c(t)$ is the effective convection speed of the vortex. The considered half-cycle is chosen as $t \in [0 - T/2]$, such that $0 \leq t_s < t_e \leq T/2$. The convection speed is time dependent, as the convection process is not steady. The flow visualization indicates that a vortex is formed at the orifice edge and grows in a first step while its convection is rather limited. Subsequently, this vortex is accelerated and it passes through the orifice. In case the vortex is still inside the orifice approaching the flow inversion, its velocity decreases towards zero.

As the exact determination of the time history of the vortex velocity through the orifice from the CFD data can be cumbersome, requiring integration over the vortex path, some assumptions are made here to simplify the computation of $l_c$. In the present work, the excitation velocity inside the duct sections is given by:

$$u_{\mathrm{duct}}(t) = A_u \sin(\omega t)\,, \tag{6.8}$$

with $A_u$ the amplitude of the excitation velocity. The convection speed of the vortex is assumed equal to the orifice averaged velocity in a 1-D approximation. This choice leads to the following expression for the convection speed:

$$u_c(t) = \frac{A_u}{\sigma} \sin(\omega t)\,, \tag{6.9}$$

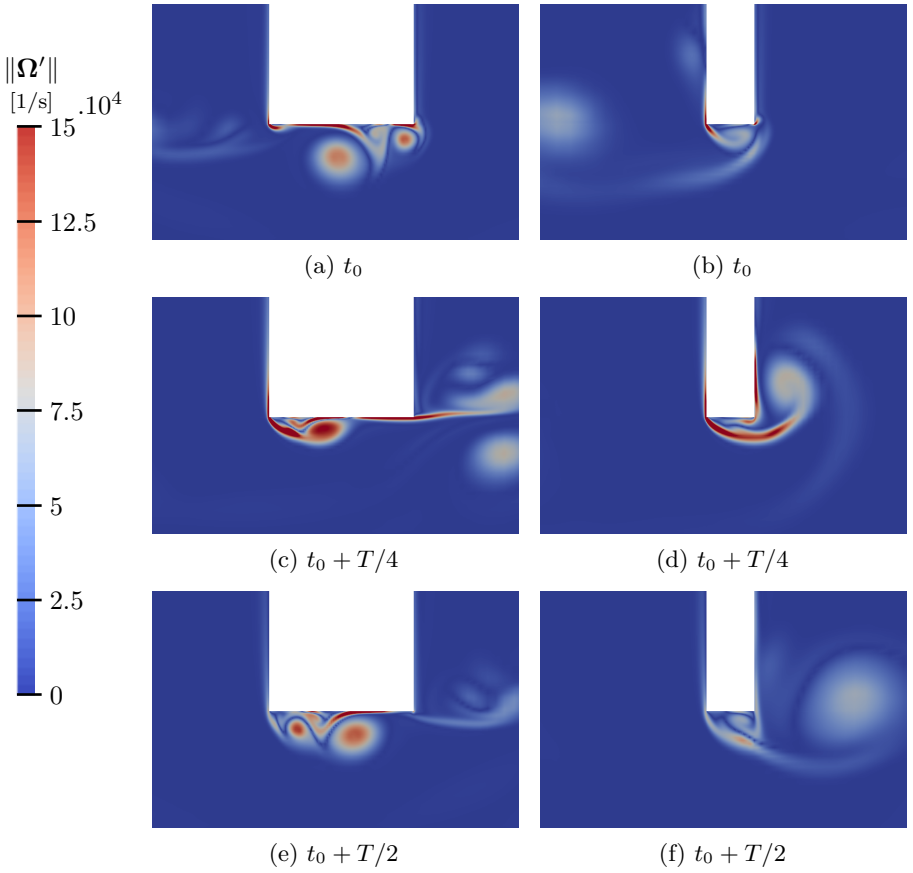


Figure 6.5. Vorticity field $\|\boldsymbol{\Omega}'\|$ history in orifice vicinity during half an excitation cycle: for $l_c < l_o$ with $l_o = 3\,\text{mm}$ (left) and for $l_c > l_o$ with $l_o = 1\,\text{mm}$ (right), all other parameters being kept constant.

where $\sigma$ indicates the open area ratio of the plate. This expression is based on averaged velocity inside the orifice sections instead of effective velocity, which could be taken as the *vena contracta* velocity ($u_{c,vc} = u_c/C_D$). It has the advantage to not rely on a time dependent parameter $C_D$, which is complicated to estimate for such pulsating flow regime. With the previous assumptions on the convection speed, Eq. (6.7) leads to:

$$l_c = (\cos(\omega t_s) - \cos(\omega t_e))\frac{A_u}{\sigma\omega} \leq l_{c,\max} = \frac{2A_u}{\sigma\omega}\,. \tag{6.10}$$

The obtained convection length reaches its maximum value $l_{c,\max}$ when the starting and ending times of the convection process $t_s$ and $t_e$ are assumed to coincide with the start and end of the half-cycle, respectively. This corresponds

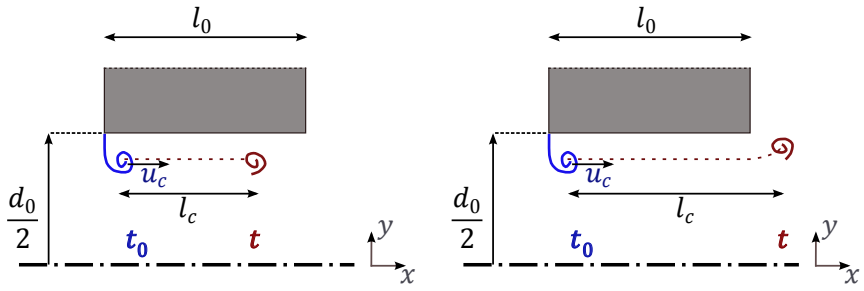


(a) $l_c < l_o$ (b) $l_c > l_o$

Figure 6.6. Convection of the upstream vortex inside the orifice during half of a cycle.

to the maximum length traveled by a vortex during half of an excitation cycle. For convenience, the effective convection length is defined as being proportional to the maximum one $l_{c,\max}$, such that

$$l_c = K_0 \, l_{c,\max} \, . \tag{6.11}$$

Flow observations for different excitation amplitudes, frequencies and geometries showed that the effective convection length $l_{c,\text{eff}}$ of the leading edge vortex is considerably smaller than $l_{c,\max}$ predicted by the formula in Eq. (6.10). As shown in Fig. 6.7, $K_0$ values around 1/4 are found from the performed flow simulations. This shows that the effective convection velocity of the vortex is significantly smaller than the averaged velocity inside an orifice section. This holds predominantly at the beginning and at the end of a half-cycle with stagnation of the vortex, where only roll-up exists and no noticeable spatial convection takes place.

### 6.2.2 Dimensionless parameter to predict this behavior

A criterion can be formulated to distinguish the two vortex paths described previously, and can be related to the higher harmonics content of the orifice acoustic response. To characterize this phenomenon, the dimensionless number $\Lambda_d$ is defined as

$$\Lambda_d = \frac{l_c}{l_o} \, , \tag{6.12}$$

where $l_o$ is the orifice thickness. This criterion states:

$$\begin{cases} (a) \;\; \text{for } \Lambda_d < 1, \quad l_c < l_o \;\; \Rightarrow \;\; \text{Presence of the OHO pattern,} \\ (b) \;\; \text{for } \Lambda_d \geq 1, \quad l_c \geq l_o \;\; \Rightarrow \;\; \text{Loss of the OHO pattern.} \end{cases} \tag{6.13}$$

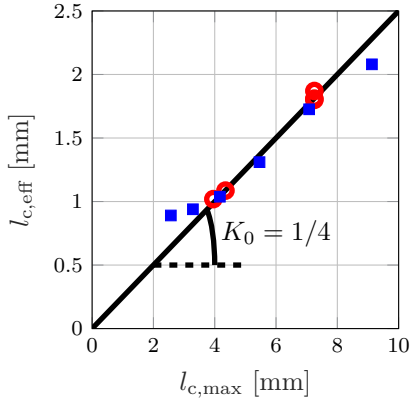


Figure 6.7. Effective vortex convection length $l_{c,\mathrm{eff}}$ from CFD observations in function of $l_{c,\mathrm{max}}$: from geometry HRA (■) and from geometry HRB (○).

Accounting for the numerically found coefficient $K_0 \approx 1/4$, $\Lambda_d$ can be reformulated as $\Lambda_{d,\mathrm{est}}$ with

$$\Lambda_{d,\mathrm{est}} \approx \frac{A_u}{2\sigma\omega l_o}\,. \tag{6.14}$$

Equation (6.14) was found to be valid over the wide range of conditions of this work. The extrapolation to cases out of this range will need to be verified beforehand. This expression, nevertheless, constitutes a practically easy way to determine $\Lambda_d$. It offers an advantage not to require a flow visualization for each simulation to determine $l_c$ unlike the exact definition of $\Lambda_d$ given in Eq. (6.12).

Because Eq. (6.13) is based on the convection process of the vortex from the leading edge to the trailing edge of the orifice (relatively to a particular half-cycle), it describes the interaction phenomena between both sides of the orifice in terms of eddies created at the edges by the acoustic perturbation. When there is no interaction between the vortices of the two sides (for $\Lambda_d < 1$), the flow is perfectly symmetrical from one half-cycle to the following one. This symmetry leads to a strongly marked OHO pattern in the spectrum of the orifice acoustic response as described by the quasi-steady theory (Eq. (6.4)). When the eddies of both sides interact in a direct manner (when $\Lambda_d \geq 1$), the local flow behavior becomes more complex and tends to vary from one half-cycle to another, losing its symmetry. This behavior does not change with the simulation parameters (e.g. time steps, residual thresholds, total length of simulations), the grid refinements tested, nor with the CFD method used. The consequence of this vortex interaction on the spectrum of the orifice response is a loss of the OHO pattern. No clear pattern for the higher harmonics appears under such conditions. Those higher harmonics are still present but their ordering in terms of amplitude follows no specific trend. As this interaction of the eddies is

related to the loss of the OHO pattern, this phenomenon is here called *vortex disruption* for the nonlinear acoustic regime of orifices, and is characterized by the dimensionless number $\Lambda_d$.

The present model is valid only if one can effectively consider a convective process between the two edges of an orifice. This limitation excludes situations where the orifice thickness $l_o$ is much smaller than the vortex size formed at the leading edges $D_v$. Due to the important flow-surface interaction between the vortex structures and the orifice wall at this location, $D_v$ is strongly related to the orifice diameter $d_o$ [86]. As a result, the model does not hold for cases where $l_o/d_o \ll 1$. This corresponds typically to cases where no reattachment of the acoustic boundary layer takes place inside the orifice and where the *vena contracta* is located outside of the orifice. For those cases, the OHO pattern is observed even if $\Lambda_d > 1$, as described in the literature in cases of very thin or/and tapered plates [69,159,165]. As it will be shown in Section 6.3, this limit case is complementary to the vortex disruption theory described previously, and numerical results are in accordance with observations made in the literature.

## 6.3 Observations from incompressible simulations

The theoretical explanation given in Section 6.2 is now evaluated by means of simulations with different orifice geometries and variable excitation amplitudes and frequencies. It allows to cover a large variety of situations for orifices in their nonlinear regime.

### 6.3.1 Assessment via a parametric study

Starting from a reference configuration, one parameter is then varied from its original value while keeping all the others fixed. The reference case is defined by the orifice geometry referred to as HRB given in Table 5.1, with $l_o = 1.59\,\text{mm}$, $d_o = 6.35\,\text{mm}$, and $\sigma = 1.56\,\%$, and at $f = 600\,\text{Hz}$ with an excitation velocity amplitude $A_u = 0.2132\,\text{m/s}$. It corresponds to a frequency close to the resonance frequency of the resonator HRB, for which the OHO pattern is found to disappear. The parameters investigated here are the following: the orifice thickness $l_o$, the averaged velocity amplitude in the orifice $A_u/\sigma$, the frequency $f$, and the orifice diameter $d_o$. The results presented here are obtained with the incompressible solver as the definition of the excitation through prescribed velocity boundary condition enables an easier setup of parameters than with the compressible solver, for which one has to define an incoming acoustic wave (c.f. Section 5.1.4).

### Impact of the orifice thickness

The orifice thickness is taken in the range $l_o \in [0.1\,\text{mm} - 9.0\,\text{mm}]$. The considered geometric ratio $l_o/d_o$ varies, therefore, from very small values (down to $1.5 \times 10^{-2}$) to values larger than 1 (around 1.5).

Figure 6.8 shows the influence of the orifice thickness $l_o$ on both normalized acoustic impedance and spectrum of the pressure drop fluctuation through the orifice. The resistance of the orifice reaches its minimum value around $l_o = 2\,\text{mm}$. Above this value, the resistance increases with increasing thickness as expected: the thicker the orifice is, the more viscous losses are added to the system. The increase in resistance for orifice thickness smaller than 2.0 mm is thought to originate from the sheared flow having no reattachment inside the orifice. The reactance is overall increasing with thicker orifices, as the fluid attached mass increases with the orifice thickness. The change in the slope curve appearing at $l_o = 2\,\text{mm}$ is presumed to be the consequence of the transition between no reattachment and reattachment of the flow inside the orifice. Notice also that the reactance is constant for very thin orifice configurations (where $l_o \leq 1\,\text{mm}$).

Figure 6.8b superimposes the values taken by the vortex disruption number $\Lambda_d \approx \Lambda_{d,\text{est}}$ to the harmonics contents $\mathcal{H}_n$. The OHO pattern is present for any orifice width outside the range $[1.0\,\text{mm} - 1.8\,\text{mm}]$. The disappearance zone of

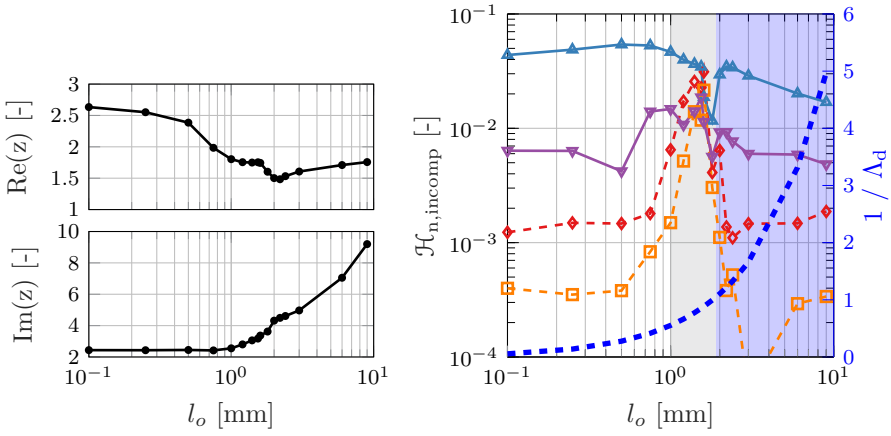


(a) Normalized impedance

(b) Higher harmonics in $\Delta p'$

Figure 6.8. Impact of the orifice thickness $l_o$ on the orifice impedance $z$ (left) and the harmonic content of the orifice response (right): 2nd harmonic (-◆-), 3rd harmonic (-△-), 4th harmonic (-□-), 5th harmonic (-▽-), and $\Lambda_d$-based criterion (▪▪▪).

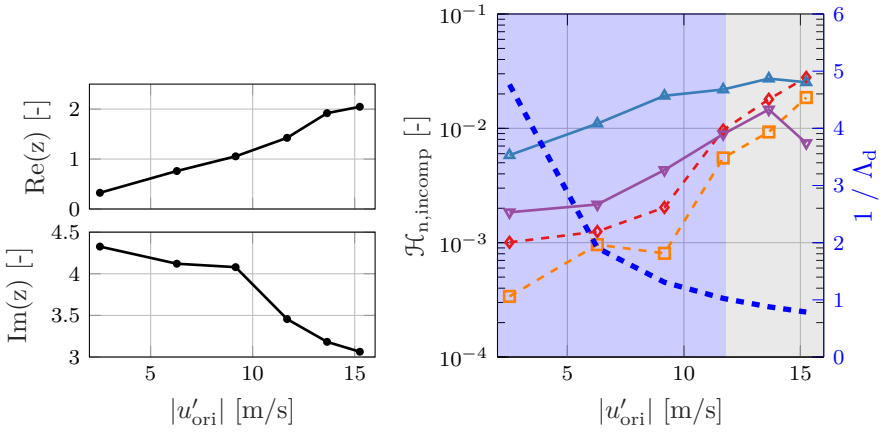


(a) Normalized impedance

(b) Higher harmonics in $\Delta p'$

Figure 6.9. Impact of the excitation amplitude on the orifice impedance $z$ (left) and the harmonic content of the orifice response (right): 2nd harmonic (-◆-), 3rd harmonic (-△-), 4th harmonic (-□-), 5th harmonic (-▽-), and $\Lambda_d$-based criterion (▪▪▪).

the OHO pattern is shown in gray in Fig. 6.8b. The defined criterion based on $\Lambda_d$ is shown to predict correctly the disappearance of the OHO pattern. Starting from the side of the large orifice, i.e. for $1/\Lambda_d \approx 10$, the dimensionless number $\Lambda_d$ crosses indeed the unity value when the OHO pattern disappears. This zone, for which $\Lambda_d \leq 1$, is highlighted in blue in Fig. 6.8b. As explained in Section 6.2, the present theory is not able to predict the lower limit of the zone where the OHO pattern is absent, as this zone corresponds to the limiting case of very thin orifices ($l_o/d_o$), for which no convection of a vortex inside the orifice can be assumed. The OHO pattern appears therefore again for $l_o \leq 1.0\,\text{mm}$ for which $l_o/d_o \approx 0.16 \ll 1$. Those results are in agreement with the experimental results gathered in past references [159] for very thin orifices and orifices made from a tapered plate. For such sharp edge orifice, the OHO pattern in the acoustic response of the orifice in its nonlinear regime is well pronounced and in agreement with the present observations.

### Impact of the averaged velocity amplitude in the orifice

The influence of the velocity amplitude inside the orifice is investigated by varying it in the range $A_u/\sigma \in [2\,\text{m/s} - 15\,\text{m/s}]$, corresponding to Sr values down to $\text{Sr} = \mathcal{O}(1)$. With increasing excitation level, the overall resistance $Re(z)$ increases in a quasi linear manner proportionally to the velocity, as expected in the nonlinear regime [35, 159]. The reactance decreases, as shown

in Fig. 6.9a. A change of slope in the reactance can be observed around $A_u/\sigma \approx 9\,\mathrm{m/s}$. This is related to the alteration of the mass of attached fluid, which is modified depending on whether the core of the leading edge vortex passes through the orifice or not. In Fig. 6.9b, one can see that the global harmonics content increases with growing excitation level. The scattering of energy from the fundamental to the higher harmonics raises with the excitation strengthening. The criterion based on $\Lambda_d$ also turns out here to predict correctly the disappearance of the OHO pattern.

### Impact of frequency

To visualize the impact of frequency on the investigated phenomenon, a frequency sweep is run with all other parameters fixed. The frequencies considered are in the range $f \in [200\,\mathrm{Hz} - 1100\,\mathrm{Hz}]$, leading to $\mathrm{Sr} \in [0.59 - 3.21]$. The resulting impedance and spectrum are shown in Fig. 6.10. The resistance is found to first decrease and then increase for increasing frequencies. The reactance curve is almost linear, with a positive slope regarding the frequency parameter.

From Fig. 6.10b, it is clear that the overall nonlinearity of the orifice grows with decreasing frequencies, as it was experimentally observed. Cummings [69]

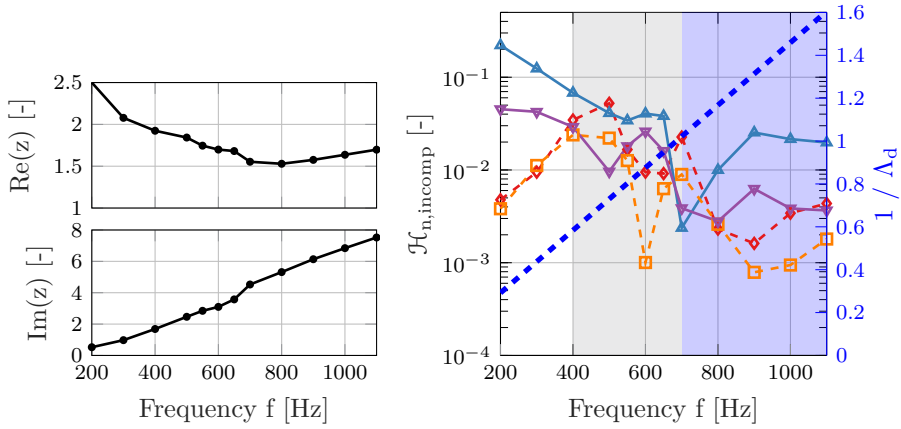


(a) Normalized impedance

(b) Higher harmonics in $\Delta p'$

Figure 6.10. Impact of the frequency $f$ on the orifice impedance $z$ (left) and the harmonic content of the orifice response (right): 2nd harmonic (-◆-), 3rd harmonic (-△-), 4th harmonic (-□-), 5th harmonic (-▽-), and $\Lambda_d$-based criterion (▪▪▪).

documented that "nonlinear transmission effects were observed in all of these[1], although the effects were most marked with the smaller orifices and at the lower frequencies". Nonlinearities tend to dominate for small Strouhal numbers ($\mathrm{Sr} < 1$). The upper limit of the disappearance of the OHO pattern (here around 600 Hz) is correctly predicted by the $\Lambda_d$ number. For the lower frequency limit, the given criterion is not able to predict the appearance of the OHO pattern. This is expected as this low frequency limit corresponds to the vortex path described by the quasi-steady theory [69], similarly to the thin orifice configuration. In this case, the vortex convection process inside the orifice, as characterized in the present model, is not appropriate.

### Role of the orifice diameter

Even if the orifice diameter is not included in the dimensionless number $\Lambda_d$, it is of interest to assess its effect on the observed high harmonics pattern. This parameter is here taken in the range $d_o \in [0.1\,\mathrm{mm} - 9\,\mathrm{mm}]$, corresponding to $\mathrm{Sr} \in [0.03 - 2.63]$. Figure 6.11a shows the impedance curves for varying orifice diameters. As the diameter is reduced, the resistance is strongly increased for sub-millimeter orifice diameters because of the increased viscous losses. The

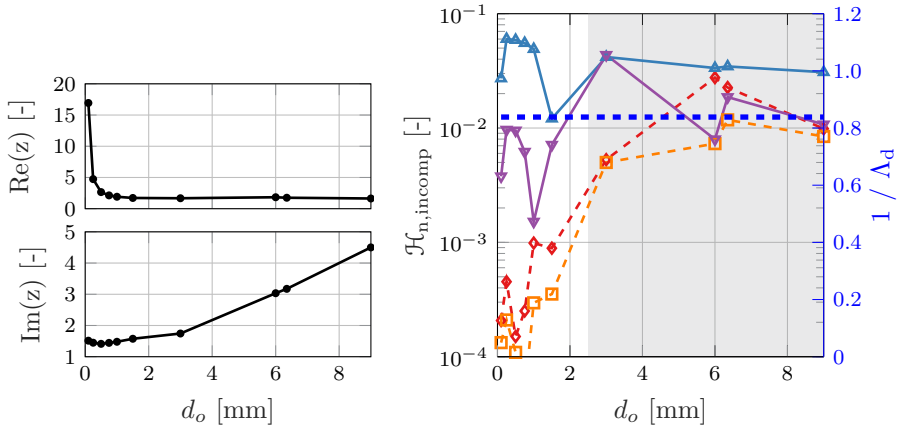


(a) Normalized impedance

(b) Higher harmonics in $\Delta p'$

Figure 6.11. Impact of the orifice diameter $d_o$ on the orifice impedance $z$ (left) and the harmonic content of the orifice response (right): 2nd harmonic (-◇-), 3rd harmonic (-△-), 4th harmonic (-□-), 5th harmonic (-▽-), and $\Lambda_d$-based criterion (▪▪▪).

[1]Six sharp edge orifices were tested in total, with diameters of $1.6 - 25.4$ mm.

reactance is growing with the orifice diameter since the inertia of the fluid in the neck increases.

Concerning the spectrum depicted in Fig. 6.11b, no clear trend is pronounced for orifices wider than 1.5 mm. As the parameter $1/\Lambda_d$ here is constant — i.e. independent of $d_o$ — and takes values slightly smaller than one, it was expected to see no clearly marked OHO pattern. However, the OHO pattern appears for the limit case of very small $d_o$. It is thought that the diameter affects the size of the formed vortex and consequently can modify the ratio $D_v/l_o$, where $D_v$ is the vortex diameter. An outcome of the flow observations is that when $d_o$ becomes smaller than $l_o$, the vortex size stays limited by the diameter dimension. The vortex dimension $D_v$ is therefore reduced by decreasing $d_o$. The OHO pattern can reappear as the situation is shifted from the configuration in Fig. 6.2c to the configuration in Fig. 6.2b. The OHO pattern is thus present for the two limit cases, i.e. for very thin and very thick orifices.

### 6.3.2 Model validation for Helmholtz resonators

Following the previous parametric study, the case of the two Helmholtz resonators HRA and HRB already introduced in Chapter 5 are looked at in the light of Section 6.2. The results are obtained from the incompressible methodology combined with the decomposed model for Helmholtz resonator, as described in Chapter 5. In contrast to the previous parametric study, where only one parameter varies at a time, multiple parameters change here between each operating point of the resonators. For both resonators, the estimated dimensionless number $\Lambda_d \approx \Lambda_{d,\mathrm{est}}$ based on Eq. (6.14) is also added to the figures.

In the HRB case, the OHO pattern disappears only in the frequency range $[550\,\mathrm{Hz} - 610\,\mathrm{Hz}]$ for which the estimated $\Lambda_d$ is very close to unity. For larger values of $1/\Lambda_d$, the OHO pattern is present as expected from the theory. The fact that the $1/\Lambda_d$ curve is not exactly crossing the unity threshold whereas the OHO pattern disappears lets think that the $K_0$ values can change slightly depending on the flow conditions and orifice geometries. It seems, however, that the formula $l_c = K_0\, l_{c,\max}$ with $K_0 \approx 1/4$ gives a satisfying estimation of $l_c$, at least in the treated cases. For the HRA case, the $1/\Lambda_d$ never gets close to the unity threshold (with a minimum value of $\approx 3.1$), and the OHO pattern is expected on the entire frequency range. The spectrum shown in Fig. 6.12a is in very good agreement with this statement.

By studying the results of Fig. 6.12b with the computed acoustic resistance (Fig. 5.8 for 130 dB), a link between these quantities can be seen. It appears that an accurate numerical determination of the impedance is more challenging to obtain in the zone where the OHO pattern disappears, as illustrated by the small fluctuations of the impedance curve in this region. This is explained

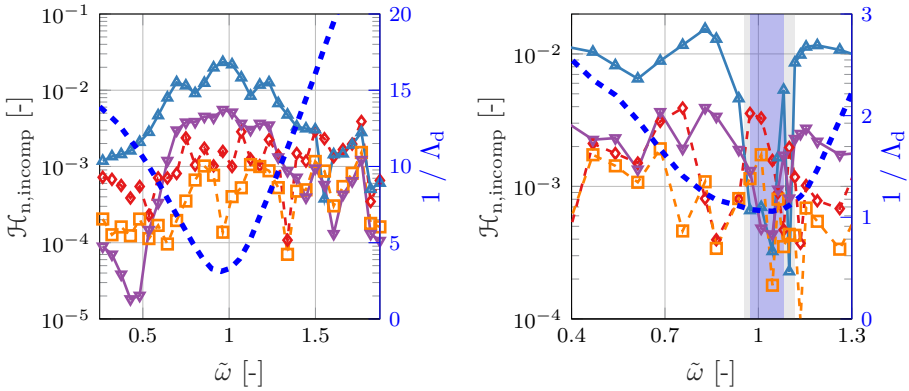


(a) HRA at a SPL of 119 dB

(b) HRB at a SPL of 130 dB

Figure 6.12. Assessment of the defined criterion for the harmonic content of the acoustic response of the resonator HRA (Temiz [287]) at 119 dB and resonator HRB (Hersh [133]) at 130 dB: 2nd harmonic (-◆-), 3rd harmonic (-△-), 4th harmonic (-□-), 5th harmonic (-▽-), and $\Lambda_d$-based criterion (- - -).

by the local flow changes throughout cycles that are observed under those conditions, independently of the numerical setting parameters and meshes. Flow conditions are indeed more complex in the flow regime where eddies from each orifice side interact. In the case of resonator HRA, for which the OHO pattern is clearly present, both compressible and incompressible solvers deliver very smooth impedance curve (see Fig. 5.7). This observation leads to the following conclusion: in the nonlinear regime, even if the energy scattering from the fundamental to the higher harmonics is rather limited (around 1.2 % here), the pattern in the higher harmonics can be important for the numerical determination of the acoustic impedance. The study of the higher harmonics pattern gives a direct information on the local flow field generated by high amplitude acoustic excitations.

Looking at the present observations in the light of the different flow regions defined by Ingård and Labate [160], the zone of evanescence of the OHO pattern happens in the referred region 4. This region was originally defined as "a high sound intensity region in which pulsatory effects are predominant, resulting in the formation of jets and vortex rings." The region where the OHO pattern disappears is therefore a sub-domain of region 4 delimited by the dimensionless $\Lambda_d$ number, linked to convection process of vortices inside the orifice itself. Experimental data documented in [160] give rather small $\Lambda_{d,\text{est}}$ values, where the OHO pattern and perfectly symmetric flow are expected to predominate.

## 6.4 Conclusions

This work investigated the acoustic response of perforated plates and Helmholtz resonators with circular orifices in their nonlinear regime with a particular focus on the scattering of energy from the fundamental to the higher harmonics. The CFD approach presented in the previous chapter, based on the unsteady RANS solution of the incompressible flow equations, is used for the in-depth investigation of the harmonics pattern. The method is shown to be able to correctly evaluate the energy content of the higher harmonics, compared to analytical quasi-steady flow theory and compressible flow simulations. A pattern in the higher harmonics, characterized by its dominating odd harmonics and here referred to as the Odd Harmonics Only (OHO) pattern, is found as documented in the literature.

However, deviations from this pattern are observed under particular conditions. Vortex disruption from the different faces of the orifices is identified as the origin of these observations. A basic theoretical model was proposed, based on the vortex convection length inside the orifice, to predict the disappearance of the standard high harmonics pattern. The present model is valid in cases where vortex convection processes inside the orifice can be defined. Under those conditions, it is shown that the changes in the spectrum pattern can be predicted through a single dimensionless number $\Lambda_d$, defined as the ratio of the vortex convection length inside the orifice to the orifice thickness. For $\Lambda_d < 1$, the standard OHO pattern is present, whereas for $\Lambda_d > 1$ this pattern disappears. The theory is assessed with success through simulations with several orifice configurations and excitation levels. It matches also the experimental studies on higher harmonics for orifice acoustic response found in the literature. Those constitute the limiting cases of very thin orifices ($l_o/d_o \ll 1$).

With all these observations, this work contributes to a global understanding of the nonlinear regime of orifices by making the link between the local flow field, the global impedance, and the spectrum of the acoustic response. It is shown that the study of the higher harmonics pattern delivers in-depth information on the local flow field generated by high amplitude acoustic excitations. The numerical determination of the impedance is found to be more challenging in cases where the OHO pattern is absent due to the presence of more complex flow structures. Therefore, the understanding of this particular behavior and its prediction are of importance, even if the energy content at the high harmonics is small compared to the overall energy at the fundamental frequency.

# Part IV

# A vibro-acoustic model for perforates

# Chapter 7

# Coupled vibro-acoustic FEM model of perforated plates

In the previous chapters, the plates and walls constituting the investigated passive acoustic dampers were assumed to be rigid. The effect of vibrations was then completely disregarded. In this chapter, a FEM-based numerical model of the vibro-acoustic coupling in flexible perforated plates is presented. Each perforation is described as an imposed transfer impedance boundary condition (uniform impedance patch) on the plate. Depending on the material and the dimensions of the problem, the acoustical modes in the medium (air) can now interact with the structural modes of the plate. This coupling leads to changes in the number of absorption peaks, frequency and amplitude of the Helmholtz resonance of the system. The numerical approach adopted here, assuming perforations as discrete impedance patches that can be considered independently, opens the possibility of predicting the influence of perforation distribution on the acoustic performance of perforated plates. The coupled vibro-acoustic model is applied here to the case of flexible Micro-Perforated Plates (f-MPPs) for validation and further investigations, as the effect of vibrations on the acoustic response of MPPs was shown to be of major importance [276].

The present study is limited to the amplitude range for which the MPP behavior can be described by a linear model. This excludes damping due to vortex shedding as detailed in Chapters 5 and 6. The linear sound absorption mechanism in MPPs is then based on the conversion of the kinetic energy of the fluid particles into heat energy due to the viscous resistance in the perforations. The viscous resistance increases with the relative velocity between the plate and the fluid. For a rigid MPP, the relative particle velocity of the air is the same for each perforation when excited by a planar acoustic wave at a given frequency. When the plate flexibility is accounted for, the plate vibrates according to its

mode shapes, which depend on its geometry, excitation frequency, boundary conditions and material. Due to these particular mode shapes, even under acoustic plane wave excitation, the relative air particle velocity with respect to the plate depends on the position of the perforation within the plate. Therefore, the perforation position is potentially a design parameter in flexible micro-perforated plates (f-MPPs). Compared to the commonly used "fully coupled modal" theoretical model [47, 48, 193, 259], the presented FEM model offers an additional flexibility in terms of design estimation for f-MPP, as no analytical expressions for the structural modes are required, allowing the use of more complex geometry and boundary conditions for the plate structure. It gives as well a handy investigation tool for the overall positioning of the orifices for design optimization.

The work presented in Part IV has been partially published in [288] and is the result of a collaboration with researchers of the Eindhoven University of Technology, Muttalip Aşkın Temiz, Ines Lopez Arteaga, and Avraham Hirschberg.

## 7.1 Modeling vibro-acoustic coupling in flexible perforated plates by a patch-impedance approach

The configuration investigated in this chapter consists of a flexible micro-perforated plate placed inside a cylindrical impedance tube to mimic the experimental setup used for comparison. The considered setup is drawn schematically in Fig. 7.1. The numerical model will therefore be composed of two parts: a structural domain (the perforated plate) and an acoustic one (split between the impedance duct ① and the back cavity ②). The following section provides the governing equations used for modeling these domains in the context of the Finite Element Method.

### 7.1.1 FEM model for the coupled vibro-acoustic system

#### Description of the numerical model

The discretized problem is solved through a FEM formulation in the frequency domain. The numerical model is built here in 3-D within LMS Virtual.Lab® [1]. The schematic description of the problem is illustrated in Fig. 7.2. Assuming a quiescent medium (air) and neglecting the thermo-viscous losses in the bulk and at the sound-hard boundaries of the acoustic domains ① and ②, the propagation of acoustic waves is simply governed by the Helmholtz equation in the frequency domain:

$$\omega^2 \hat{p}_n(z) + c_0^2 \nabla^2 \hat{p}_n(z) = 0, \tag{7.1}$$

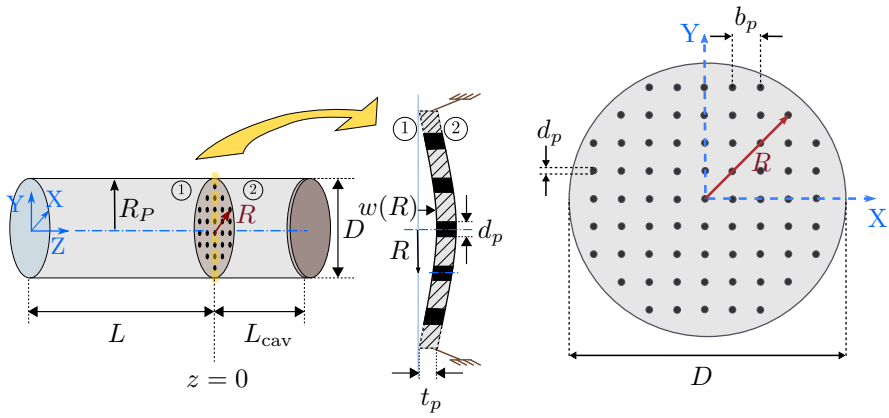


(a) f-MPP mounted inside an impedance tube

(b) Front view of a f-MPP geometry with uniformly distributed perforations

Figure 7.1. Configuration for the circular MPP clamped inside an impedance tube. The plate displacement $w(R)$ is also illustrated on the cross-sectional view of the f-MPP.

where $\omega = 2\pi f$ is the radial frequency, $c_0$ is the speed of sound, $\nabla^2$ is the *Laplacian* operator, and $\hat{p}_n$ is the acoustic pressure in medium on the side $n$. High-order Lobatto shape functions are used to describe the discrete pressure field. The inlet $\Gamma_V$ is defined by an imposed velocity boundary $V_{in}$, with a chosen velocity amplitude $|V_{in}| = 1\,\text{m/s}$, to represent harmonic plane wave excitations. The two acoustic domains ① and ② are connected through the perforations which are here modeled as independent *uniform impedance patches*. Each patch is defined as imposed transfer impedance boundary $\Gamma_{Z_t}$. A mathematical expression for this transfer impedance of a single perforation $z_p$ is given by Maa's classical model [209], developed as an extension of Crandall's theory [68] for the intermediate Sh region. It reads

$$z_{p,\text{Maa}} = \frac{\Delta\hat{p}}{\hat{u}_p \rho_0 c_0} = \underbrace{\frac{32\mu t_p}{\rho_0 c_0 d_p^2}\left[\sqrt{1+\frac{\text{Sh}^2}{32}}\right] + \text{j}\omega\frac{t_p}{c_0}\left[1+\left(9+\frac{\text{Sh}^2}{2}\right)^{-1/2}\right]}_{z_{p,\text{Maa}-\text{inner}}} + \underbrace{\frac{\sqrt{2}}{\rho_0 c_0}\frac{\mu}{d_p}\text{Sh} + \text{j}\frac{8}{6\pi}\omega\frac{r_p}{c_0}}_{z_{p,\text{Maa}-\text{outer}}}, \tag{7.2}$$

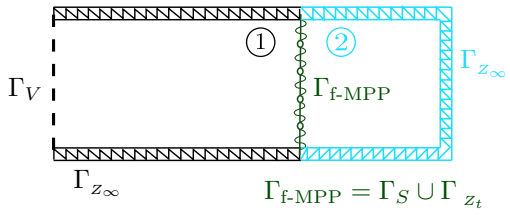


Figure 7.2. Schematic representation of the coupled vibro-acoustic numerical model for the configuration of a f-MPP inside an impedance tube.

for circular holes of diameter $d_p = 2r_p$ and thickness $t_p$, both small compared to the acoustic wavelength $\lambda_a$. An alternative expression for the transfer impedance of a single perforation $z_p$, with an improved representation of the end-correction effects, was also recently proposed by Temiz et al. [286]:

$$z_{p,\text{Temiz}} = \underbrace{\frac{\mathrm{j}\omega t_p}{c_0}\left[1 - \frac{2}{\text{Sh}\sqrt{-\mathrm{j}}}\frac{J_1(\text{Sh}\sqrt{-\mathrm{j}})}{J_0(\text{Sh}\sqrt{-\mathrm{j}})}\right]^{-1}}_{z_{p,\text{Temiz}-\text{inner}}} + \underbrace{\frac{2}{c_0\rho_0}\alpha_s R_s + j\delta_s\omega\frac{r_p}{c_0}}_{z_{p,\text{Temiz}-\text{outer}}}, \tag{7.3}$$

where $\Delta\hat{p} = \hat{p}_1 - \hat{p}_2$ is the sound pressure difference between the two ends of the orifice tube, $\hat{u}_p$ is the averaged acoustic particle velocity in the perforation, and $J_n$ is the Bessel function of the first kind of order $n$. The term $z_{p,\bullet-\text{inner}}$ represents only the inertial and damping effects happening inside the orifice length. The contribution of the end-corrections $z_{p,\bullet-\text{outer}}$ to the total normalized orifice impedance $z_{p,\bullet}$ is defined by the surface resistance $R_s = 0.5\sqrt{2\mu\rho_0\omega}$, and by both resistive and reactive end-correction coefficients $\alpha_s$ and $\delta_s$. An expression for these end-correction coefficients can be found in Temiz et al. [286], for the case of circular perforations with square-edges:

$$\alpha_s = 5.08\,\text{Sh}^{-1.45} + 1.70\,, \tag{7.4a}$$

$$\delta_s = 0.97\exp(-0.20\,\text{Sh}) + 1.54\,. \tag{7.4b}$$

These coefficients are functions of the Shear number only. $\delta_s$ takes into account the effect of viscosity on the inertia of the attached mass of fluid. The expressions given in Eqs. (7.2) and (7.3) are valid as long as the perforations are not too close to each other so that interaction effects can be neglected [284]. This is being taken care of in this work as the distance between perforations $b_p$ is chosen larger than several orifice diameters with $b_p \geq 5d_p$ for all cases.

Due to the small thickness of the considered MPPs, it is appropriate to assume that the displacement field $w(R)$ can be characterized in terms of the displacement components of the shell middle surface. The thin MPP is therefore modeled as a combination of 2-D elastic shell elements and imposed

transfer impedance boundaries $\Gamma_{Z_t}$. The former solve for the plate structural displacement field, while the latter describe the acoustic behavior of each perforation. The vibro-acoustic coupling boundary $\Gamma_S$, between the surfaces of the acoustic domain and the structural shell elements, is defined by the following relations:

$$\hat{F} = \hat{p}_1(Z = 0^-) - \hat{p}_2(Z = 0^+)\,, \tag{7.5a}$$

$$\hat{v}_{1,2}(R, 0) = j\omega w(R)\,, \tag{7.5b}$$

where $F$ is the force acting on the plate surface and $v$ is the velocity. $R$ is the radial position in the plate's plane. Equation (7.5b) ensures the continuity of the normal shell velocities and the normal fluid velocities at the fluid-structure coupling interface. The remaining boundaries are defined as hard-wall boundary, $\Gamma_{Z_\infty}$.

The resulting finite element model for the unconstrained degrees of freedom $\{\mathbf{w}_u, \mathbf{p}_u\}^T$ of the coupled vibro-acoustic problem takes the form:

$$\left\{ \begin{bmatrix} \mathbf{K}_s & \mathbf{K}_c \\ \mathbf{0} & \mathbf{K}_a \end{bmatrix} + j\omega \begin{bmatrix} \mathbf{C}_s & \mathbf{0} \\ \mathbf{0} & \mathbf{C}_a \end{bmatrix} - \omega^2 \begin{bmatrix} \mathbf{M}_s & \mathbf{0} \\ \mathbf{M}_c & \mathbf{M}_a \end{bmatrix} \right\} \begin{Bmatrix} \mathbf{w}_u \\ \mathbf{p}_u \end{Bmatrix} = \begin{Bmatrix} \mathbf{F}_{si} \\ \mathbf{F}_{ai} \end{Bmatrix}, \tag{7.6}$$

where $\mathbf{K}$ is the stiffness, $\mathbf{M}$ is the mass, $\mathbf{C}$ is the dissipation, and $\mathbf{F}$ is the forcing matrix. The subscripts 'a', 's' and 'c' represent the words *acoustic*, *structural* and *coupling*. The vectors $\mathbf{w}_u$ and $\mathbf{p}_u$ represent the degrees of freedom for the plate displacement and acoustic pressure vectors that need to be solved for. The stiffness coupling matrix $\mathbf{K}_c$ represents the force loading of the fluid on the structure, which is proportional to the pressure. The coupled mass matrix $\mathbf{M}_c$ expresses the structural force applied on the fluid, which is proportional to the plate acceleration. The forcing terms $\mathbf{F}_{ai}$ and $\mathbf{F}_{si}$ introduce the prescribed pressure and displacement vectors into the set of equations.

The experimental results serving as reference for this work are taken from the study by Toyoda et al. [298]. Three different geometries of MPPs, referred to as case $\mathcal{P}i$, $i \in \{1, 2, 3\}$, are considered here. The plates have all a diameter $D = 100\,\text{mm}$ and a thickness $t_p = 0.5\,\text{mm}$. Each MPP contains $n_p = 69$ perforations. The orifices' diameters are $d_p = 0.5\,\text{mm}$ for the case $\mathcal{P}1$, $d_p = 1\,\text{mm}$ for the case $\mathcal{P}2$, and $d_p = 2\,\text{mm}$ for the case $\mathcal{P}3$. The configuration of a plate without perforation (referred to as the case $\mathcal{NP}$) is included in this work as well, for the analysis of the impact of perforation size on the plate impedance. The geometric and structural characteristics are summarized in Table 7.1 and illustrated in Fig. 7.1. In Table 7.1, $E_P$ denotes the Young's modulus, $\eta_P$ is the loss factor, and $\nu_P$ is the Poisson ratio of the MPP material. The values of these parameters correspond to MPPs made of PVC (polyvinyl chloride). The comparison between the proposed numerical model and the experimental data is done in terms of absorption coefficient $\alpha$ of the complete perforated plate. The latter is computed as $\alpha = 1 - |p^-/p^+|^2$, where $p^+$ and $p^-$ are the

| **Parameter** | **Case** $\mathcal{NP}$ | **Case** $\mathcal{P}1$ | **Case** $\mathcal{P}2$ | **Case** $\mathcal{P}3$ |
|---|---|---|---|---|
| $d_p$ [mm] | N/A | 0.50 | 1 | 2.0 |
| $t_p$ [mm] | N/A | 0.50 | 0.50 | 0.50 |
| $b$ [mm] | N/A | 10 | 10 | 10 |
| $n_p$ [-] | 0 | 69 | 69 | 69 |
| $\sigma$ [-] | 0 % | 0.2 % | 0.7 % | 2.8 % |
| $D$ [mm] | 100 | | | |
| $L$ [mm] | 300 | | | |
| $L_{\text{cav}}$ [mm] | 50 | | | |
| $E_P$ [N/m$^2$] | $3 \times 10^9$ | | | |
| $\eta_P$ [-] | 0.03 | | | |
| $\nu_P$ [-] | 0.3 | | | |

Table 7.1. Properties of the MMPs from Toyoda et al. [298] used for validation of the proposed FEM model. See Fig. 7.1 for the definition of the geometric parameters.

complex amplitudes of the left and right traveling pressure waves in domain ①. These amplitudes of the pressure waves are calculated by using the standard multi-microphone method [2] in the plane wave regime. The frequency range considered in this work, defined by $f \in [125\,\text{Hz} - 2000\,\text{Hz}]$, satisfies the acoustic plane wave assumption for the chosen dimensions of the impedance tube.

### Compensation for inviscid reactance

The numerical method described in this chapter will be referred to as *discrete* model as it allows to model each perforation separately. Considering now the case of a rigid plate, the results of the discrete model are expected to match the ones obtained from the lumped formulation of the entire perforated plate using Eq. (7.2) or Eq. (7.3)[1]. However, a frequency shift is observed by directly taking these expressions, as shown in Fig. 7.3.

This frequency shift is related to the reactance end-correction $\delta_s$ which already accounts for the inertia of the non-uniform acoustic flow around the opening of the perforations. The solution of the Helmholtz equation should therefore disregard this contribution. To eliminate this inviscid reactance contribution by the Helmholtz equation, noted $Im(Z_{t,H})$, its value is estimated from several simulations [288] with different porosity $\sigma$ and orifice diameter $d_p$ values, and then subtracted from Eqs. (7.2) and (7.3). This new expression $z_p^\star$ is used at the imposed transfer impedance boundaries in the proposed numerical model.

[1] As long as no interactions between the perforations take place, as expected in the considered cases.

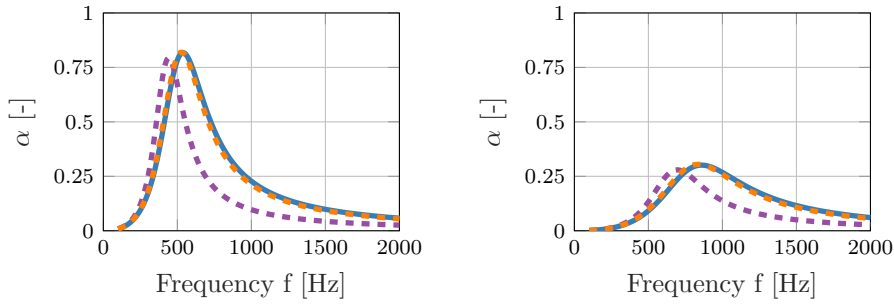


(a) $d_p = 1\,\text{mm}$ (b) $d_p = 2\,\text{mm}$

Figure 7.3. Absorption coefficient $\alpha$ calculated with the lumped model of the complete MPP ( ) compared with the ones obtained by means of the FEM model with geometrical representation of the perforations using $z_{p,\text{Maa}}$ ( ) and using the modified transfer impedance $z^{\star}_{p,\text{Maa}}$ ( ).

Similarly to the reactance end-correction, the inviscid reactance contribution is expressed as a non-dimensionalized parameter $\delta_H$ by normalizing it as proposed by Ingard [157]:

$$\delta_H = \frac{2Im(Z_{t,H})}{\rho_0 \omega d_p} \tag{7.7}$$

The inviscid reactive end-correction $\delta_H$ is found in Fig. 7.4 to only depend on the porosity $\sigma$. An expression for the non-dimensional inviscid reactance is proposed by Temiz [288] as

$$\delta_H = 0.85\sigma - 2.40\sqrt{\sigma} + 1.54, \qquad 0 \leq \sigma \leq 1\,. \tag{7.8}$$

This expression for $\delta_H$ is derived by the fitting[2] of the data shown in Fig. 7.4 and constraining its value for the limit cases:

- When the porosity is unity, i.e. $\sigma = 1$, $\delta_H = 0$ is satisfied.
- When the porosity becomes very small, i.e. $\sigma \to 0$, the value of $\delta_H$ tends to 1.54, limit value of $\delta_s$ in Eq. (7.4b). This value is also very close to the theoretical limit value calculated by Pierce [231] who obtains the analytical value $\pi/2 \approx 1.57$ for the quasi-steady limit ($f \to 0\,\text{Hz}$) of the length of the oscillating fluid mass at a circular orifice in an infinite (thin) baffle plate.

[2]The quality of the fit for the expression in Eq. (7.8) is given by a coefficient of determination $r^2_{\text{fit}} = 0.9998$.

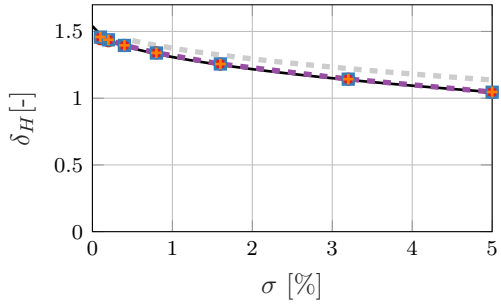


Figure 7.4. Non-dimensional inviscid reactance $\delta_H$ as function of the porosity $\sigma$: simulations with $d_p = 0.5\,\text{mm}$ (O), $d_p = 1\,\text{mm}$ (□), $d_p = 2\,\text{mm}$ (+), and $d_p = 4.0\,\text{mm}$ (- - -), fitted function in Eq. (7.8) by Temiz (—) and $\delta_{\text{FOK}}$ given by Tayong et al. [284] (- - -).

The expression of $\delta_H$ in Eq. (7.8) can further be compared to the expression $\delta_{\text{FOK}}$ given by Tayong et al. [284] by means of the Fok's function [254] to account for the orifice interaction effects on the acoustic reactance. This expression, also depending on the porosity, shows a similar trend as given by Eq. (7.8). The later expression of $\delta_H$ to compensate the excess reactance is therefore thought to be reasonable. The expressions in Eqs. (7.2) and (7.3) are then adjusted to be used in the proposed FEM model. It follows:

$$z^{\star}_{p,\text{Maa}} = z_{p,\text{Maa}-\text{inner}} + \frac{\sqrt{2}}{\rho_0 c_0}\frac{\mu}{d_p}\text{Sh} + \text{j}\left(\frac{8}{6\pi} - \delta_H\right)\omega\frac{r_p}{c_0}, \tag{7.9}$$

and

$$z^{\star}_{p,\text{Temiz}} = z_{p,\text{Temiz}-\text{inner}} + \frac{2}{c_0\rho_0}\alpha_s R_s + \text{j}\left(\delta_s - \delta_H\right)\omega\frac{r_p}{c_0}. \tag{7.10}$$

The predicted absorption coefficient using the modified transfer impedance $z^{\star}_{p,\text{Maa}}$ in the FEM model is shown in Fig. 7.3. The discrepancy with the lumped model is found to be drastically reduced once the correction for the inviscid reactance is accounted for.

### 7.1.2 Validation of the numerical model

To validate the numerical model in terms of vibro-acoustic coupling for MPPs, the test cases from Toyoda et al. [298] are used, with the parameters listed in Table 7.1. A density of $\rho_{\text{PVC}} = 1300\,\text{kg/m}^3$ is taken for the MPPs which are made of PVC.

### Structural behavior of thin MPPs

To start this results section, a closer look is taken at the structural response of the investigated MPPs and the related plate displacement field $w(R)$. Figure 7.5 presents the computed absorption coefficient $\alpha$ over the frequency range $f \in [125\,\text{Hz} - 2000\,\text{Hz}]$, for the case $\mathcal{NP}$ without perforation. The absorption curve obtained with the FEM model is in good agreement with the experimental results.

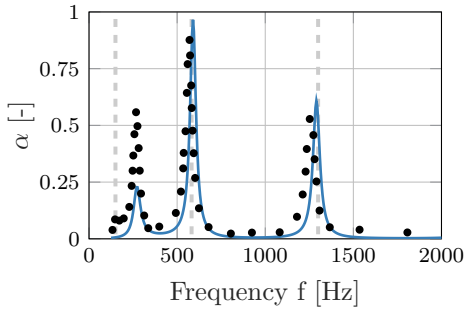


Figure 7.5. Absorption coefficient obtained by means of the FEM model (—) compared to measurement data by Toyoda et al. [298] (•) and analytical model (- - -) for the case $\mathcal{NP}$.

For the simple geometry considered in this work, an analytical treatment of the structural behavior of the MPPs is often applied in the literature [298]. The flexible MPP is assumed to behave as a thin, homogeneous plate of radius $R_P = D/2$. This implies that the hole diameters and the open surface ratios are considered sufficiently small for their effect on the plate motion to be neglected. The structural analysis will therefore be limited here to the symmetric vibrations of a uniform circular diaphragm, with the local displacement $w(R)$ of the plate only depending on the radial position $R$ from the plate center (see Fig. 7.1). The equation of motion for the thin plate, whose restoring force results from its stiffness, is given by [179]:

$$D_P \nabla^4 \hat{w}(R) - \rho_P t_p \omega^2 \hat{w}(R) = \Delta\hat{p}\,, \tag{7.11}$$

where $\rho_P$ is the volume density of the material and $\Delta\hat{p}$ is the external pressure difference acting as driving force on the plate surface. The term $D_P = E_P(1 + \mathrm{j}\eta_P)t_p^3/[12(1-\nu_P^2)]$ is the flexural rigidity where $E_P$ is the Young's modulus, $\eta_P$ is the loss factor, and $\nu_P$ is the Poisson ratio of the MPP material. Applied oscillatory forces are assumed. The steady-state solution for the local plate displacement $\hat{w}(R)$ has thus the form $\hat{w}(R) = \Psi(R)e^{\mathrm{j}\omega t}$. For this particular circular symmetry case, and by further assuming perfectly clamped condition at the boundary in contact with the duct wall, i.e. $\Psi(R_P) = 0$ and $\partial\Psi/\partial r(R_P) = 0$,

the complete solution of Eq. (7.11) is given by

$$\Psi(R) = \frac{\Delta\hat{p}}{\rho_P t_p \omega^2} \left[ \frac{J_0(\frac{\gamma_m}{R_P}R) - \frac{J_1(\gamma_m)}{I_1(\gamma_m)} I_0(\frac{\gamma_m}{R_P}R)}{J_0(\gamma_m) - \frac{J_1(\gamma_m)}{I_1(\gamma_m)} I_0(\gamma_m)} - 1 \right], \tag{7.12}$$

with $J_j$ and $I_j$ the $j^{\text{th}}$ order Bessel functions and modified Bessel functions of the first kind, respectively. For a given $m^{\text{th}}$ modal vibration, the parameter $\gamma_m$, which is a constant for the present clamped condition, is defined by the following transcendental equation

$$\frac{J_0(\gamma_m)}{J_1(\gamma_m)} = -\frac{I_0(\gamma_m)}{I_1(\gamma_m)}\,. \tag{7.13}$$

From the value of $\gamma_m$ given by Eq. (7.13), the natural frequencies of the clamped thin plate can be computed by

$$f_{n,m} = \frac{t_p \gamma_m^2}{2\pi R_P^2} \sqrt{\left( \frac{E_P(1+\mathrm{j}\eta_P)}{12\rho_P(1-\nu_P^2)} \right)}\,. \tag{7.14}$$

The solutions obtained from Eq. (7.14) are represented as dashed lines in Fig. 7.5 and further summarized in Table 7.2.

| Plate structural mode $i$ | 1 | 2 | 3 | 4 |
|---|---|---|---|---|
| Analytical natural frequency $f_{n,i}$ [Hz] | 149.5 | 582 | 1304 | 2315 |
| FEM resonance frequency $f_{n,i}^{\text{num}}$ [Hz] | 272 | 590 | 1291 | |

Table 7.2: Summary of the peak frequencies obtained for the vibro-acoustic response of the investigated plates.

Under normal incidence condition, the non-axisymmetric modes do not contribute to the simulated plate response, as expected. Only the axisymmetric modes are observed in Fig. 7.5 and the resonance frequencies obtained with the FEM model coincide well with the analytical ones, at the exception of the first eigenfrequency. The first resonance peak in the simulation appears indeed at a significantly higher frequency compared to the analytical calculations. This is the consequence of the additional stiffness added by the air volume in the back cavity. The peak at $f_{\text{PC, num}} \approx 270\,\text{Hz}$ originates from the panel-cavity resonance due to the mass-spring system formed with the cavity, whereas the analytical resonance frequency at $f_{n,1} = 150\,\text{Hz}$ can be regarded as the first *in vacuo* plate natural frequency [47, 288]. The panel-cavity resonance frequency found is in accordance with its analytical expression [47, 92] given by

$$\omega_{\text{PC}}^2 = \omega_{n,1}^2 + \frac{k_{\text{cav}}}{m_P} \geq \omega_{n,1}^2\,, \tag{7.15}$$

with $\omega_{n,1}^2$ the angular natural frequency, $k_{\text{cav}} = \rho_0 c_0^2 / L_{\text{cav}}$ the acoustic equivalent stiffness of the cavity and $m_P$ the modal mass of the first plate mode[3].

To assess the impact of the perforation size on the structural behavior of the plate, the velocity field $v_{\text{plate}}(R)$ can be derived from the computed displacement field $\Psi_{num}$. The pressure fields on both sides of the MPP are further extracted to obtain the averaged pressure difference $\Delta p$ through the plate. This allows to compute the local values of the plate impedance

$$z_{\text{plate}}(R) = \frac{\Delta \hat{p}}{\hat{v}_{\text{plate}}(R)} \,. \tag{7.16}$$

The plate impedance $z_{\text{plate}}(R)$ for the different perforation sizes is compared to the no-perforation case. The values of the plate impedance at the center of the plate $z_{\text{plate}}(0)$ are shown in Figs. 7.6a and 7.6b, as well as the absolute changes compared to the no-perforation reference case in Fig. 7.6c. It appears that the effect on the plate impedance due to the presence of perforations is rather limited. The impedance curves divert further from the reference case as the orifice size increases, but nevertheless the impact is kept small for the investigated cases, as the porosity values are also small ($\sigma \leq 2.7\,\%$). The eigenfrequencies predicted by the analytical model in Eq. (7.14) match very well the zeros of the plate reactance curves. The absolute changes in terms of impedance appear predominant in-between the natural frequencies $f_{n,2}$ and $f_{n,3}$ over the frequency range considered. The maximum relative deviations of $z_{\text{plate}}$, indicated as $\epsilon_{\text{plate,max}}$, from the impedance of the non-perforated plate[4] are summarized in Table 7.3.

| Case | $\mathcal{P}1$ | $\mathcal{P}2$ | $\mathcal{P}3$ |
|---|---|---|---|
| $\epsilon_{\text{plate,max}}$ [%] | 3.5 | 9.5 | 19 |

Table 7.3: Maximum relative change in plate impedance $z_{\text{plate}}$ in respect to the impedance of the non-perforated plate $z_{\text{plate},\mathcal{NP}}$ over the frequency range [125 - 2000] Hz.

Figure 7.7 shows the absolute value of the numerically computed plate displacement $|\Psi_{num}|$ at frequencies close to the first three natural frequencies of the plate $f_{n,1/2/3}$. The displacement fields observed match with the shapes of the normal axisymmetric modes for a plate with fixed rim, as expressed in Eq. (7.12). The modes (0,1), (0,2) and (0,3) are shown for the case $d_p = 2\,\text{mm}$ in Fig. 7.7a, Fig. 7.7b and Fig. 7.7c, respectively.

[3]The modal mass of the first panel mode is defined [47, 92] as $m_p = M_P N_1 / C_{01}^2$ with $N_m = \iint_S |\Psi_m(x)|^2 \, dx^2$ and coupling term $C_{nm} = \iint_S \Psi_m(x) \phi_n^*(x) \, dx^2$, where $\phi_n$ is the $n^{\text{th}}$ cross-sectional mode of the rigid walled cavity.

[4]excluding the values around the eigenfrequencies for which $Im(z_{\text{plate}}) = 0$

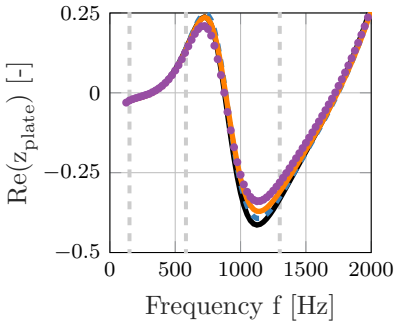


(a) Normalized plate resistance

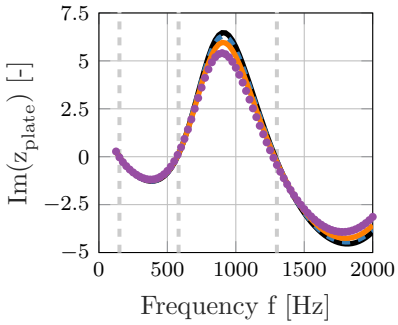


(b) Normalized plate reactance

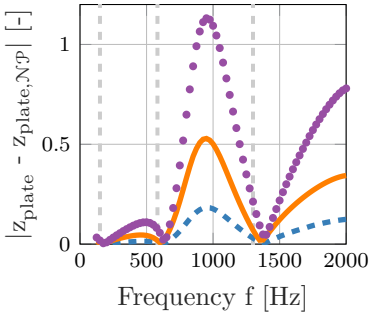


(c) Absolute change in plate impedance $z_{\text{plate}}$ compared to the case without perforation $\mathcal{NP}$.

Figure 7.6. Impact of the orifices on the normalized plate impedance $z_{\text{plate}}$ at the center of the duct (R=0): case with no perforation (—) and cases with orifices of diameter $d_p = 0.5\,\text{mm}$ (- - -), $d_p = 1\,\text{mm}$ (—), and $d_p = 2\,\text{mm}$ (•).

The previous results show that the perforation ratios used in this work are not significantly impacting the plate density, rigidity, and overall its structural behavior.

### Vibro-acoustic response of the MPPs

The absorption curves obtained by means of the FEM approach with impedance patches are displayed in Fig. 7.8 for the cases $\mathcal{P}1$, $\mathcal{P}2$, and $\mathcal{P}3$. These results are compared to the measurement data from Toyoda et al. [298] and the numerical computation for the rigid wall plate. From Fig. 7.8, it is clear that the plate vibrations can drastically modify the absorption curves, especially for small values of the perforation ratio. The observed absorption peaks

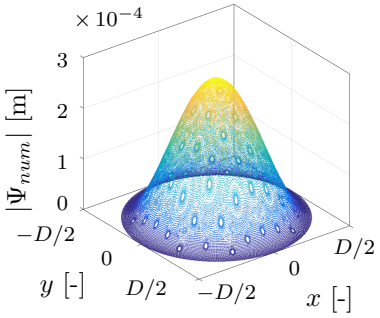


(a) At $f = 150\,\text{Hz} \approx f_{n,1}$

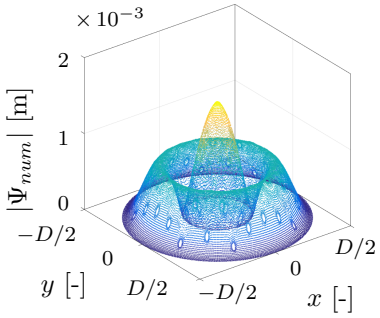


(b) At $f = 575\,\text{Hz} \approx f_{n,2}$

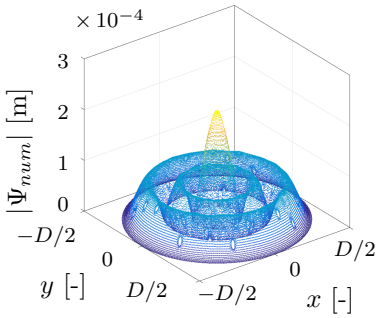


(c) At $f = 1300\,\text{Hz} \approx f_{n,3}$

Figure 7.7. Magnitude of the plate displacement field obtained numerically $|\Psi_{num}|$ for frequencies near $f_{n,1}$ (a), $f_{n,2}$ (b), and $f_{n,3}$ (c) for the case $\mathcal{P}3$ (i.e. $d_p = 2\,\text{mm}$).

are either panel-type absorption due to eigen-mode vibrations (also called panel-controlled resonances) or Helmholtz resonance absorption (hole-controlled resonances) [47]. The sharpness of the peaks is strongly related to the nature of the physical mechanisms involved in the damping of the acoustic energy. The absorption peaks originating from structural vibrations are much sharper, limited to very narrow bands for which the plate vibrates. The peaks related to the Helmholtz resonance, originating from the viscous damping of the air particles passing through the perforations, expand over a wider frequency band. The Helmholtz resonance frequencies $f_{\text{HR}}$ obtained from the semi-empirical expression in Eq. (2.2) for the rigid system are indicated in Fig. 7.8. They are in good agreement with the numerical FEM results.

The numerically obtained absorption coefficients are overall lower than the ones measured experimentally. As shown by Toyoda et al. [298], this difference is mainly due to the surface admittances of the PVC perforated plate and backing impedance tube wall which are neglected in the numerical model (by

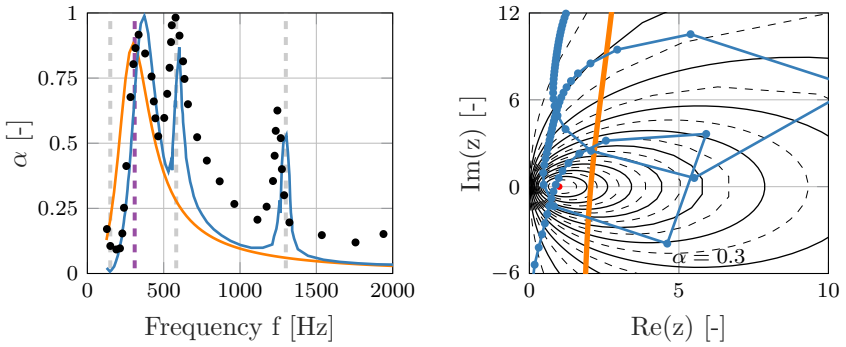


(a) Case $\mathcal{P}1$

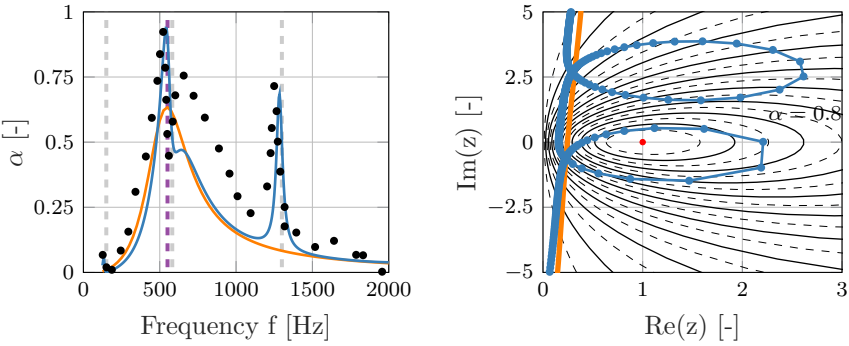


(b) Case $\mathcal{P}2$

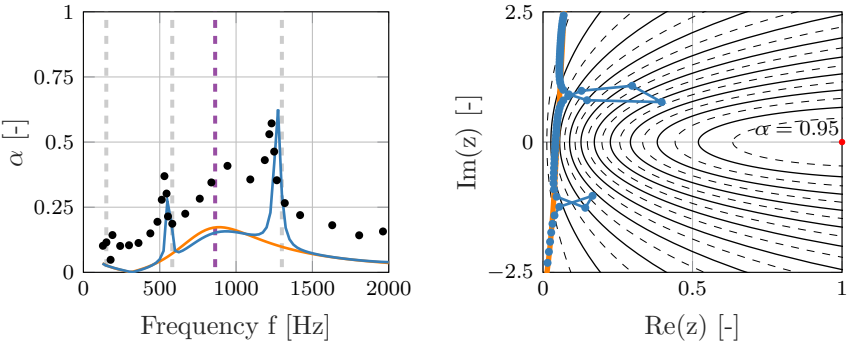


(c) Case $\mathcal{P}3$

Figure 7.8. Absorption coefficient $\alpha$ (left) and phasor representation of the normalized impedance (right) obtained for the f-MPP by means of the FEM model with impedance patches (— and —●—) compared to measurement data by Toyoda et al. (•) and numerical results for the rigid case (—).

assuming the surface admittances equal to zero on the plate boundary $\Gamma_S$). The exact values of these surface admittances being unknown, they have been

excluded from the model. The absorption coefficients for the PVC surface and the back wall surface were measured in [298] and estimated to be less than 0.1 for the frequency range investigated. These surface admittances mostly affect the calculated peak value due to the mass–spring resonance absorption in the $\mathcal{NP}$ case, as seen around 270 Hz in Fig. 7.5, and become of importance with increasing porosity, as the absorption coefficient decreases.

With the previous observations, the proposed FEM model is judged to correctly predict the influence of the plate elastic behavior on the acoustic absorption characteristics of a thin MPP. The following discussion aims at clarifying the underlying mechanisms involved in f-MPP. The main observations are now listed in the form of a bullet list:

- No peak is observed near the first natural frequency $f_{n,1}$ in all cases. This is caused by the merging of the panel-type absorption due to mass-spring resonance of the system "plate and air in cavity" (as observed at 270 HZ in Fig. 7.5) with the Helmholtz-resonance absorption[5]. It is referred as the first cavity resonance frequency.

- The panel-type absorption peaks appear to be very close to the natural frequencies of the plate, $f_{n,2}$ and $f_{n,3}$, for both cases $\mathcal{P}1$ and $\mathcal{P}3$. The situation differs greatly for the case $\mathcal{P}2$, for which the Helmholtz-type resonance frequency $f_{\mathrm{HR}}$ and the first uncoupled panel natural frequency $f_{n,2}$ are very close. It leads to a strong coupling between the individual panel-type and Helmholtz-type resonances which produces two resonance peaks for the elastic MPP whose frequencies are symmetric with respect to the Helmholtz resonance of the rigid case, as explained analytically by Bravo et al. [47]. They define a critical porosity $\sigma_c$, for a given cavity depth $L_{\mathrm{cav}}$, for which the coupling between the Helmholtz-type resonance and the structural motion is maximal. This value of porosity corresponds to the matching of the panel-cavity frequency $\omega_{\mathrm{PC}}$ with the Helmholtz resonance frequency $\omega_{\mathrm{HR}}$. They define

$$\sigma_c = \frac{M_h}{k_{\mathrm{cav}}}\omega_{\mathrm{PC}}, \ , \tag{7.17}$$

  where $k_{\mathrm{cav}}$ is the acoustic equivalent stiffness of the cavity and $M_h$ the effective mass of the perforations, which is weakly frequency dependent. $M_h$ can be defined from the rigid cases. The value of $\sigma_c$ estimated for the present work is $\sigma_c \approx 0.14\%$, which is lower than the smallest porosity treated here. This value seems reasonable since even for the case $\mathcal{P}1$, the $\omega_{\mathrm{HR}}$ is still higher than $\omega_{\mathrm{PC}}$. Nevertheless, a strong coupling between panel-controlled and Helmholtz resonance phenomena

[5] due to mass-spring resonance of the system "air in holes and cavity"

can happen if $\omega_{\mathrm{HR}}$ matches a higher eigenfrequency of the plate, like $f_{n,2}$ for the case $\mathcal{P}2$. These phenomena are caused by a phase jump at the structural eigenfrequencies [47] and can be utilized to widen the absorption bandwidth of such MPP-based resonators, as suggested by Lee et al. [192, 193]. At these frequencies, the plate vibrates at a velocity out of phase with the air particle velocity at the holes. This difference in phase induces an increased air-frame relative velocity and therefore enhances the sound absorption. These phase jumps are illustrated in Fig. 7.9b.

- The higher the order of the plate mode, the less coupling happens with the Helmholtz-type resonance. It appears that mostly the two first plate vibration modes are relevant for the vibro-acoustic coupling in the present MPP configuration. The panel-controlled resonance peaks around $f_{n,3}$ are very similar for all three cases presented.

The previous observations are supported by the phasor representation of the acoustic impedance. Such a description, as suggested by Bravo et al. [47], is of particular relevance when dealing with flexible MPPs. It illustrates the path of the impedance along a phasor curve in the complex plane as the frequency increases (traveling from the bottom to the top). The comparison between the rigid and the elastic MPP models are represented in the complex impedance plane together with circles of constant absorption coefficient (for $\alpha \in \{0.05 : 0.05 : 0.95\}$). For the rigid cases, the shortest distance to the point of maximum absorption (•) is achieved at the Helmholtz resonance, when the $Im(z) = 0$. For the flexible MPPs, the phasor curves show significant differences from the rigid case with two clearly identified modal loops due to the panel-controlled resonances. When sweeping around these modal loops, the panel-controlled resonances occur precisely at the frequencies for which the impedance has the smallest imaginary part in absolute value. As shown in Fig. 7.8, the panel resonances can increase the acoustic resistance of the MPP towards higher absorption, corresponding to the sharp peaks already discussed. Out of these panel-controlled resonances, the resistance of the flexible MPP is found systematically lowered by the structural vibrations. This trend appears to be strengthened with decreasing perforation diameters. The decrease in orifice size is also found to enlarge the loops from the panel-controlled resonances. For the case $\mathcal{P}1$, the loops are even crossing. For the highest porosity investigated here, the loops appear to be well separated, with the hole-controlled resonance clearly in-between. The situation is more complex for lower open surface ratios, as the modal loops for the panel-controlled resonance can encircle the point of maximum absorption $z = (1, 0)$ (marked by a red point). In these cases, the first cavity resonance frequency can happen at a higher (case $\mathcal{P}2$) or lower (case $\mathcal{P}1$) frequency than the first panel-controlled resonance frequency.

The amplitude and phase of the ratio of the plate average velocity $\bar{v}$ to the air particle velocity in the plate perforations $u_p$ are drawn in Fig. 7.9 for the cases $\mathcal{P}i$, $i \in \{1, 2, 3\}$. The phase jumps at the panel-controlled resonances,

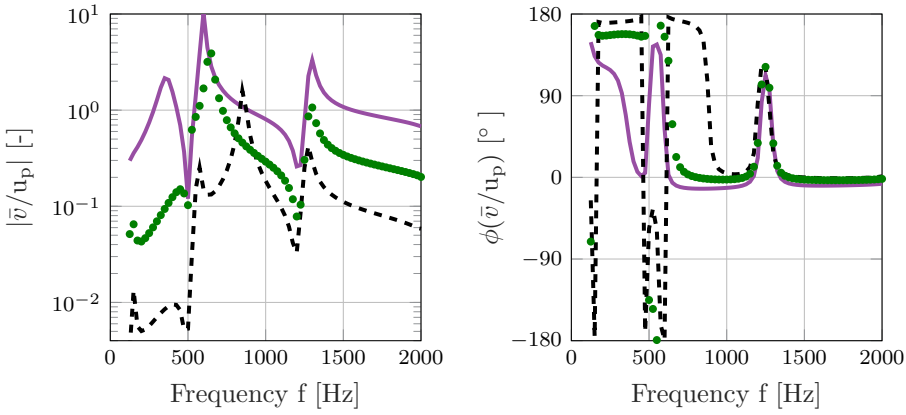


(a) Amplitude ratio of the panel averaged velocity to the air particle velocity in the MPP holes

(b) Phase difference between the plate averaged velocity $\bar{v}$ and the air particle velocity induced by the incident wave in the MPP holes $u_p$

Figure 7.9. Impedance influence factor ($\bar{v}/u_p$) over the investigated frequency range for the cases $\mathcal{P}1$ (—), $\mathcal{P}2$ (•), and $\mathcal{P}3$ (- - -).

mentioned earlier, are clearly visible in Fig. 7.9b. It also appears that the phase behavior at the frequency $f_{n,3}$ is similar in the three cases. It supports the observations that this panel-type resonance is only very weakly coupled to the hole-controlled resonance. The amplitude $|\bar{v}/u_p|$ is found overall to increase with decreasing perforation diameters and strong peaks can be seen near the structural eigenfrequencies. The values of the air-frame velocity can therefore vary significantly in amplitude depending on the frequency. This can result, in combination with the phase difference at the considered frequency, in a local improvement or deterioration of the absorption properties of the MPP compared to the rigid case.

The results presented previously were obtained by using the Maa model (see Eq. (7.9)) to describe the acoustic behavior of the perforations. Figure 7.10 illustrates the absorption curves computed with the Temiz model instead and shows the normalized orifice impedance $z_p$ given by both models. Both impedance models deliver overall similar results in terms of $\alpha$. The $\alpha$-curves are quasi-identical for the case $\mathcal{P}1$, whereas more discrepancy is observed for the cases $\mathcal{P}2$ and $\mathcal{P}3$. The larger resistance values given by the Temiz model (Eq. (7.10)) lead to an overall higher absorption coefficient linked to the Helmholtz-type resonance. In the context of this study on flexible MPPs, it is particularly relevant to note that, when the coupling between panel- and hole-controlled resonance is strong, even a slight change in orifice impedance can have a tangible impact on the absorption curves. This is visible for the case $\mathcal{P}2$

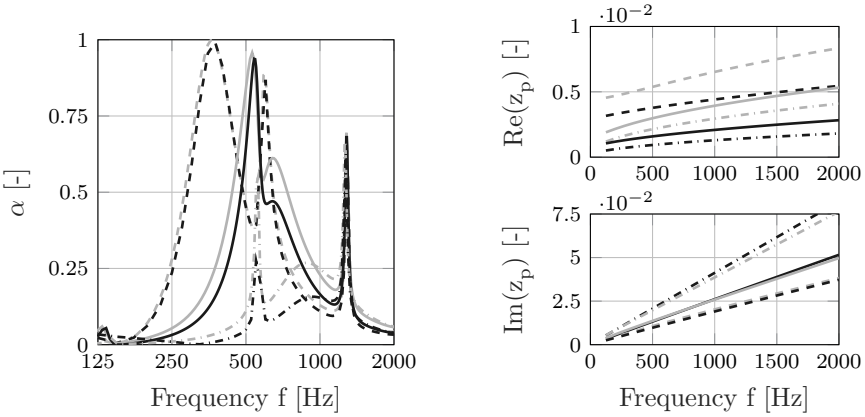


(a) Absorption coefficient (b) Orifice impedance

Figure 7.10. Absorption coefficient $\alpha$ (left) obtained with the FEM model with geometrical representation of the perforations using $z^{\star}_{p,\mathrm{Maa}}$ (■) and using $z^{\star}_{p,\mathrm{Temiz}}$ (▭), and the corresponding orifice impedance (right): for $d_p = 0.5\,\mathrm{mm}$ (- - -), $d_p = 1\,\mathrm{mm}$ (——), and $d_p = 2\,\mathrm{mm}$ (—·—).

with the two-peaks around $\omega_{\mathrm{HR}}$ of the rigid case, which are more pronounced using the Temiz model.

## 7.2 Impact of the vibrations on the local orifice impedance

In Section 7.1, the proposed FEM approach has been successfully compared to literature data for the investigation of f-MPPs. The present section aims at introducing the additional impact of the plate vibration on the local orifice acoustic impedance. The influence of accounting for this phenomenon is evaluated for the global acoustic absorption characteristic of the previously introduced f-MPP geometries (see Table 7.1).

### 7.2.1 Modified impedance model accounting for the local displacement of the plate

In most of the studies on the vibro-acoustic response of micro-perforated plates/panels in the literature [46,47,298], the impedance chosen to describe the acoustic behavior of the perforations is based on Maa's classical model. This model is derived assuming a rigid plate [208], for which $v_{\mathrm{plate}} = 0$. As illustrated

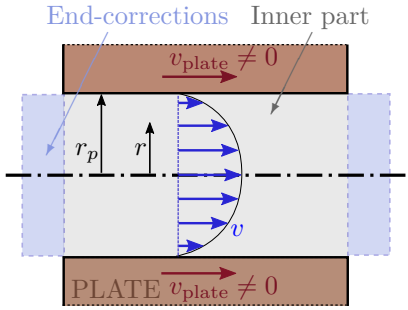


Figure 7.11. Description of the velocity field $v(r)$ in the local coordinate system for each single perforation.

in Fig. 7.11, the fluid particle velocity at the hole wall $v(r = r_p)$ is then taken equal to zero, and the effect of the plate vibration on the acoustic impedance of the perforations is neglected. Under these assumptions, the normalized acoustic transfer impedance for a single perforation $z_p$ is given by $z_{p,\text{Maa}}$ [210], expressed previously in Eq. (7.2).

Li et al. [195], in a work on the acoustic behavior of perforated membranes, recently proposed an alternative to the classical Maa's model by modifying the boundary condition at the wall inside a perforation to account for a non-zero plate velocity. The fluid particles adhere at the moving hole wall boundary due to the no-slip boundary condition, and therefore, their velocity is supposed to be equal to the panel/membrane velocity. The proposed velocity boundary condition, expressed as a function of the distance $r$ from the perforation axis in the local coordinate of an orifice of radius $r_p$, is expressed as

$$v(r = r_p) = v_{\text{plate}} \neq 0\,. \tag{7.18}$$

Applying the boundary condition Eq. (7.18) to the general solution of the equation of motion for the fluid particles inside a cylindrical (axisymmetric) orifice [68], considered short compared to the acoustic wavelength, leads to the following expression for the particle velocity inside a perforation:

$$v(r) = v_{\text{plate}} \frac{J_0(k_{\text{a}} r)}{J_0(k_{\text{a}} r_p)} - \frac{\Delta p}{t_p \mu k_{\text{a}}^2} \left[ 1 - \frac{J_0(k_{\text{a}} r)}{J_0(k_{\text{a}} r_p)} \right] , \tag{7.19}$$

where $k_{\text{a}}^2 = -\text{j}\rho_0\omega/\mu = -\text{j}(\text{Sh}/r_p)^2$, with Sh the Shear number.

The expression in Eq. (7.19) can be integrated over the area of the orifice section to compute an averaged particle velocity $\bar{v}$, and the following formula can be

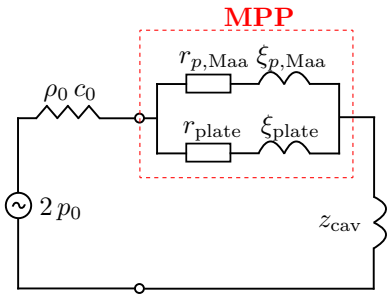


(a) Standard representation of the complete system constituted of the MPP and the backing cavity - case with no effect of the plate vibrations on the impedance of the orifices: $z \equiv$ impedance, $r \equiv$ resistance, and $\xi \equiv$ reactance.

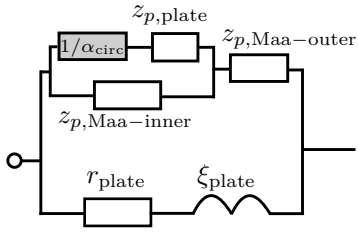


(b) Case with only impact of the vibrations on the inner part of the orifice impedance.

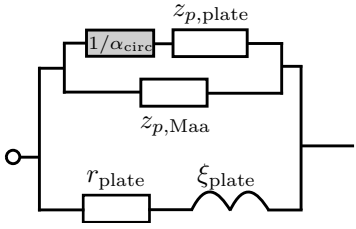


(c) Case with the correction due to plate vibrations applied to the complete orifice impedance.

Figure 7.12. Electrical analogy for the perforated plate.

derived [195] for the normalized acoustic impedance of a single orifice:

$$z_p^{\star\star} = \frac{\Delta\hat{p}}{\bar{v}\rho_0 c_0} = \frac{1}{\rho_0 c_0 \dfrac{\hat{v}_{\mathrm{plate}}}{\Delta\hat{p}} \dfrac{2}{k_{\mathrm{a}} r_p} \dfrac{J_1(k_{\mathrm{a}} r_p)}{J_0(k_{\mathrm{a}} r_p)} + \dfrac{c_0}{\mathrm{j}\omega t_p}\left[1 - \dfrac{2}{k_{\mathrm{a}} r_p} \dfrac{J_1(k_{\mathrm{a}} r_p)}{J_0(k_{\mathrm{a}} r_p)}\right]}. \tag{7.20}$$

The second term of the denominator in Eq. (7.20) corresponds to the internal part of the hole acoustic impedance under Maa's rigid wall assumption $z_{p,\mathrm{Maa-inner}}$.

The term $z_{\mathrm{plate}} = \Delta\hat{p}/(\rho_0 c_0 \hat{v}_{\mathrm{plate}})$ in Eq. (7.20) can be defined as the local normalized impedance of the plate. Equation (7.20) describes the direct effect of the plate vibration on the local orifice acoustic impedance. This correction of the orifice impedance at a position $R$ from the center of the plate is thus given by

$$z_p^{\star\star}(R) = \frac{1}{\dfrac{\alpha_{\mathrm{circ}}}{z_{\mathrm{plate}}(R)} + \dfrac{1}{z_{p,\mathrm{Maa-inner}}}}, \tag{7.21}$$

where

$$\alpha_{\mathrm{circ}} = \frac{2}{\mathrm{Sh}\sqrt{-j}} \frac{J_1(\mathrm{Sh}\sqrt{-j})}{J_0(\mathrm{Sh}\sqrt{-j})} \tag{7.22}$$

is a weighting factor linked to the orifice circular shape, and depending only on the Shear number Sh for the given circular geometry. As it is highlighted in Eq. (7.21), the analytical expression of the correction to be applied on the orifice acoustic impedance is derived only for the internal part, and neglects the effect of vibration on the end-corrections. No evidence has yet been found that this correction can be applied similarly to the resistive and reactive contributions related to the attached mass of air outside of the orifice. The precise answer to this question is beyond the scope of the presented work and cannot be treated with the numerical model used here. It is, nevertheless, possible to assess the relevance of this consideration for the acoustic behavior of vibrating MPPs. For this purpose, the two following limit cases will be investigated:

- applying the correction to only the internal part of the orifice impedance and keeping the end-corrections unaltered by the vibration — Eq. (7.23a),
- applying the correction to the complete orifice impedance — Eq. (7.23b).

The impedance $z^{\star\star}_{p,B}$ in Eq. (7.23b) corresponds to the case where the plate vibration is considered affecting both the orifice inner part and the attached mass of air on the sides in a similar manner. The expression $z^{\star\star}_{p,A}$ in Eq. (7.23a), however, entirely disregards the effect of the vibration on the outer air mass. The final expressions used for the acoustic impedance of one perforation at the location $R$ are thus the following:

$$z^{\star\star}_p(R) = \begin{cases} z^{\star\star}_{p,A}(R) = \dfrac{1}{\dfrac{\alpha_{\text{circ}}}{z_{\text{plate}}(R)} + \dfrac{1}{z_{p,\text{Maa}-\text{inner}}}} + z_{p,\text{Maa}-\text{outer}}\,, & \text{(7.23a)} \\ z^{\star\star}_{p,B}(R) = \dfrac{1}{\dfrac{\alpha_{\text{circ}}}{z_{\text{plate}}(R)} + \dfrac{1}{z_{p,\text{Maa}}}}\,. & \text{(7.23b)} \end{cases}$$

In the work of Li [195], the expression in Eq. (7.23b) is applied. We will quantify here the differences between the previous two assumptions for the case of f-MPPs, both in terms of local acoustic impedance and global acoustic response. Figure 7.12 illustrates, through an electrical analogy, the different modeling options for an MPP compared in this study. As the plate impedance is a complex number, the vibration can be expected to affect both resistive and reactive parts of the orifice impedance (see Eq. (7.21)).

In order to compute the local value of the orifice impedance accounting for the plate vibration, it is necessary to know the value of the plate impedance $z_{\text{plate}}$ at the orifice position. The results in Section 7.1.2 have proved that the analytical

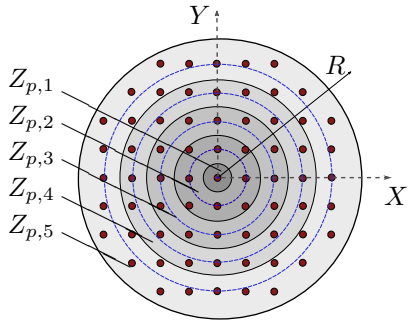


Figure 7.13. Zonal splitting of the plate surface to define the local values for the orifice impedance, depending on the distance $R$ from the plate center: orifice surface area, impedance zones, (---) position chosen for impedance estimation.

displacement fields predicted from thin plate theory are acceptable for the cases of this work. Nevertheless, as they are directly accessible in the presented frequency domain Finite Element Method framework, the displacements of the plate are numerically computed from a first coupled vibro-acoustic simulation, where an homogeneous orifice impedance is imposed for all orifices over the plate. From this step, the plate impedance $z_{\text{plate}}(R)$ is retrieved applying Eq. (7.16). The corrected impedance value for an orifice at the position $R$ is then obtained using Eq. (7.23). The fully coupled vibro-acoustic problem is finally run again with, this time, the locally modified orifice impedance values.

### 7.2.2 Case study of a circular MPP in an impedance tube

The same configuration as in Section 7.1 is chosen. It consists of a perforated plate of diameter $D = 100\,\text{mm}$ and thickness $t_p = 0.5\,\text{mm}$ placed in an impedance tube, as represented in Fig. 7.1. To study the effect of the modified boundary condition applied to the orifice impedance, different orifice sizes are considered: $d_p = 0.5\,\text{mm}$ for the case $\mathcal{P}1$, $d_p = 1\,\text{mm}$ for the case $\mathcal{P}2$, and $d_p = 2\,\text{mm}$ for the case $\mathcal{P}3$. The structural parameters such as the Young's modulus $E_P$, Poisson ratio $\nu_P$ and the loss factor $\eta_P$ of the MPPs are listed in Table 7.1.

The modified orifice impedance, as defined in Eq. (7.23), is spatially varying over the plate, depending on the position of the orifice considered. The FEM representation allows to define the exact acoustic impedance for each of the orifices. Nevertheless, for practical reasons, orifices have been grouped in zones depending on their distance to the plate center in the present axisymmetric configuration. This is illustrated in Fig. 7.13. An averaged impedance value is assigned for all the orifices inside one specific zone. In the presented case, the

plate area is divided into five zones with respective orifice impedance $Z_{p,i}$, for $i \in \{1, .., 5\}$.

### 7.2.3 Results and discussions

#### Impact of vibration on single orifice impedance

This section presents the corrected orifice impedance accounting for the local velocity of the MPP, as given by the two expressions of Eq. (7.23a) and Eq. (7.23b). Results are shown here for a single orifice, at a given location $R$ from the plate center.

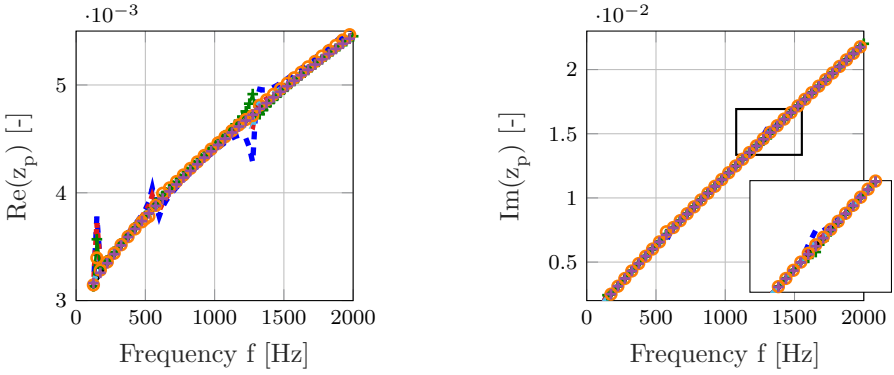


(a) Orifice diameter $d_p = 0.5\,\text{mm}$

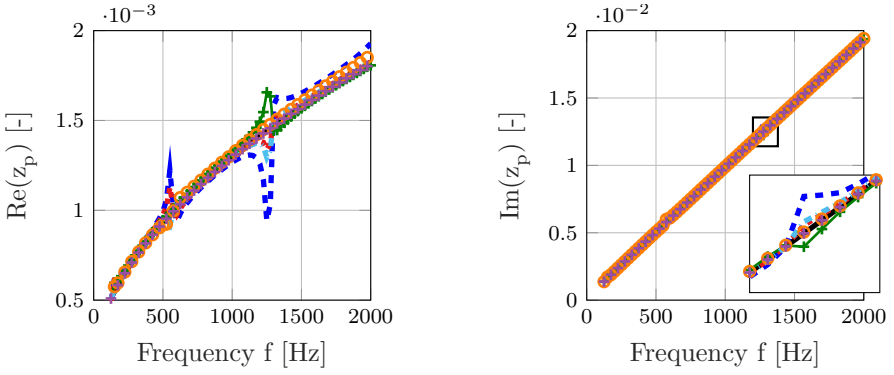


(b) Orifice diameter $d_p = 2\,\text{mm}$

Figure 7.14. Normalized resistance $\text{Re}(z_p)$ (left) and reactance $\text{Im}(z_p)$ (right) of a single orifice, depending on its location: classical Maa impedance (—) compared to the corrected impedance of an orifice at $R = 0\,\text{m}$ (- - -), $R = 0.01\,\text{m}$ (- - -), $R = 0.02\,\text{m}$ (—+—), $R = 0.03\,\text{m}$ (—○—), $R = 0.04\,\text{m}$ (- - -), and $R = 0.05\,\text{m}$ (—+—).

Figure 7.14 illustrates, for the case of orifice diameters $d_p = 0.5\,\text{mm}$ and $d_p = 2\,\text{mm}$, the corrected orifice impedance computed from Eq. (7.23b) at different locations on the plate. The correction accounting for the plate impedance influences the orifice impedance predominantly near the plate natural frequencies. Over the remaining of the frequency range, the impedance is very close to the value obtained under rigid-wall assumption. Unlike the results for membranes presented in [195], the impact on the orifice reactance is observed to be negligible (see Figs. 7.14a and 7.14b) for the considered perforated plates. The impedance correction mostly impacts the resistive part. The change appears to be of the same magnitude for both orifice sizes. This is mainly due to the plate impedance, which is roughly independent of the orifice size here (see Section 7.1.2). Nevertheless, as the resistance is higher for the smallest diameter dimension, the relative change is found to be lower for small orifices. The impedance correction due to vibrations is therefore expected to have more impact for larger orifices. This conclusion will be discussed further in Section 7.2.3 for the absorption coefficient $\alpha$. Comparing the values at different radial locations on the plate, it turns out that, the closer to the center the orifice is, the more effective the vibrations are on its local impedance. This is consistent with the clamped condition applied on the rim of the plate, limiting the plate motion closeby. As expected, the impedance values computed at $R = 0.05\,\text{m}$, i.e. on the plate edge, give a similar result as the standard impedance model neglecting vibration effects, as $\Psi(R = 0.05) = 0$ is imposed.

Figure 7.15 compares the impedance values obtained from the two proposed corrections — see Eq. (7.23) — for an orifice placed at the center of the plate. The same trend for the corrected impedance is observed for both corrections.

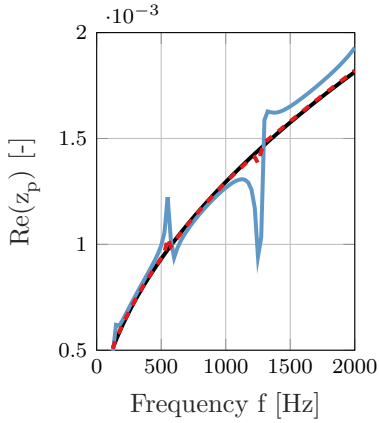


Figure 7.15. Modified normalized resistance $\text{Re}(z_p)$ for an orifice of $d_p = 2\,\text{mm}$ at the center of the plate ($R = 0$): $z^{\star\star}_{p,A}$ (- - -), $z^{\star\star}_{p,B}$ (——), and reference Maa model (——).

Including the end-correction part to the correction as defined by Eq. (7.23b) delivers, however, significantly more deviation from the standard impedance values.

### Global effect on MPP absorption coefficient

After having observed the local changes in impedance which ensue from the modified boundary condition at the inner wall of the orifices, the global impact on the acoustic behavior of the MPP is analyzed and quantified in the following. Results are presented here in terms of MPP absorption coefficient $\alpha$. These absorption curves have been obtained from the numerically computed pressure fields by a standard multi-microphone approach with different probes placed inside the duct domain, as mentioned in Section 7.1.1. The absorption coefficient obtained with an orifice impedance under Maa's rigid wall assumption ($\alpha$) will be compared to the corrected ones ($\alpha^{\star\star}_{A/B}$), resulting from the modified boundary conditions at the orifice wall $z^{\star\star}_{p,A/B}$.

Figure 7.16 shows, for two different sizes of orifice ($d_p = 0.5\,\text{mm}$ in Fig. 7.16a and $d_p = 2\,\text{mm}$ in Fig. 7.16b), the relative changes in terms of absorption coefficient. The impact on the absorption curve by accounting for the vibration effect on the orifice impedance is overall of limited magnitude for the investigated cases. It is only of significance for the low frequency range, and predominantly near the first MPP natural frequency. For the rest of the spectrum, the changes are kept below

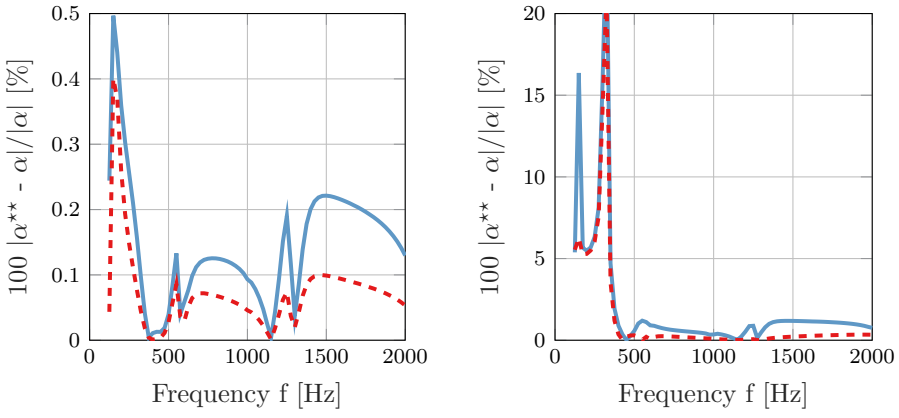


(a) Orifices with a diameter $d_p = 0.5\,\text{mm}$ (b) Orifices with a diameter $d_p = 2\,\text{mm}$

Figure 7.16. Relative change in the MPP absorption coefficient $\alpha^{\star\star}$ due to the modified orifice impedance, compared to absorption coefficient obtained with the standard Maa Model case $\alpha$: impedance correction done on the complete impedance (——), correction on the internal part only (- - -).

1 %. Note that the 2$^{\text{nd}}$ peak in Fig. 7.16b, appearing at 325 Hz, is not relevant because the absorption coefficient itself is very close to zero. This does not appear for the case with $d_p = 0.5$ mm. We only get one peak in relative change of $\alpha^{\star\star}$ which matches with a natural frequency, i.e. the 1$^{\text{st}}$ one. Considering the absolute changes (not represented here), the impedance modification has an impact 4 times larger on the absorption coefficient for $d_p = 2$ mm than for $d_p = 0.5$ mm. Another trend is that the absorption coefficient is not modified the most, in relative consideration, at the natural frequency but to the left and right of this natural frequency. It is important to remember that the correction on the orifice impedance is only affecting the numerical model on the surface related to the orifices. Therefore, the impact of the modified boundary condition at the orifice inner wall is weighted by the porosity of the plate. As the porosities of the investigated plate samples are rather low (max. 2.8 %), the influence on the MPP absorption curve is limited.

The effect of vibration on the orifice impedance appears to be more important for the case with the largest orifice diameter. This can stem from two facts. Firstly, the relative change in resistance due to the vibration is found to be larger for larger orifices, because the resistance is overall lower. Secondly, the increase in orifice size leads, in the present case of a fixed number of perforations in the plate, to larger porosity values. This larger porosity delivers more weight to the modified orifice impedance.

Applying the correction to the complete orifice impedance leads, as expected from the local impedance curves, e.g. Fig. 7.15, to larger relative changes in terms of absorption coefficient. The trends between the curves are very similar, but extending the correction to the end-correction part of the Maa impedance model appears to considerably strengthen its effect over the entire frequency range. Following what has been stated before, this is again mostly of importance for the low frequency and the lowest plate natural frequency.

## 7.3 Conclusions

A novel coupled vibro-acoustic FEM model for estimating the absorption characteristics of flexible perforated plates is presented. The model conjugates the linear acoustics with the thin plate theory. The perforations are defined separately as imposed transfer impedance boundaries on the shell domain defining the flexible plate, in a patch-impedance approach. The transfer impedance value of a single orifice is first chosen as given by Maa [210] and Temiz et al. [286], i.e. assuming the plate to be rigid. In a second part, the orifice impedance is modified to account for the local displacement of the plate. Due to the actual representation of the orifices, a correction to the transfer impedance expression is required, for the reactive part, due to the Helmholtz solver already accounting for the area changes. This correction is proposed

here as a part of the numerical model. The validation of the discrete numerical model is performed by comparing it to the experimental results from Toyoda et al. [298]. Good agreement is achieved between the experimental and numerical results.

The results further show that vibrations can significantly affect the absorption properties of micro-perforated plates and should also be considered in the design process. Allowing the treatment of each perforation independently, the proposed FEM model enables one to consider perforation location as an additional design parameter. As a result, the effect of non-uniform perforation distributions on flexible MPPs can be investigated. An example can be found in [285]. The numerical model also has the advantage of being generally applicable to all kinds of plate geometries and fixation conditions.

The second part of this chapter explores the impact of the vibrations on the orifice acoustic impedance and the consequences for the absorption performance of MPPs. The numerical vibro-acoustic FEM model, in which each orifice can be modeled independently, allows to define a local value for the impedance of each orifice depending on the plate impedance. Unlike the case of membranes, vibrations are found to only alter the resistive part of the orifice impedance. Two expressions for the modified local orifice impedance have been compared. Including the effect of vibrations on the end-corrections appears to be as important as on the orifice inner part. Applying the correction to the total attached mass of fluid at the orifice is, nevertheless, not entirely justified by the theory and results are presented here as a limit case to show the implications linked to this particular phenomenon. An exact answer would require to solve the coupled vibro-acoustic problem for a moving orifice considering the viscous-thermal losses, which lies beyond the scope of this work.

The results for the absorption curves of MPPs with different orifice sizes have shown that accounting for the orifice impedance alteration through the structural motion is more important for larger orifice diameters and at low frequency. This effect is rather limited for the investigated micro-perforated plates. It is expected to be more significant for perforates with a higher porosity. For the presented configurations, this effect can be neglected without it leading to significant error on the absorption characteristics of the MPPs.

# Part V

# Conclusions

# Chapter 8

# Conclusion and future perspectives

In this chapter, the key contributions of the doctoral work, which have been introduced in Section 1.3 and covered throughout this dissertation, are first summarized. Some insights on future perspectives are given in a second section.

## 8.1 Summary and achievements

As introduced in Chapter 1, passive noise control solutions based on perforates play an important role in many engineering applications for the damping of unwanted acoustic waves — e.g. in building acoustics, combustion engines, aircraft nacelles, or mufflers. Due to their robustness, their absorption performances, and their relative elementary structures, passive silencers with perforations remain the most common solution. However, even if these systems are rather simple devices and have already been studied for many decades [157, 174, 208, 240], there are still several aspects requiring further studies in order to maximize their efficiency.

As discussed in Chapter 2, the absorption properties of such silencers can be drastically altered by the presence of flow [96, 166, 186], by the amplitude of the incoming acoustic excitation [69, 133, 159], or by structural vibrations [47, 190, 193]. Understanding the mechanisms, responsible for the damping of the acoustic energy occurring at perforates, is key for the proper design and modeling of these systems under complex conditions. Available impedance models, describing the acoustic behavior of perforates, originate mostly from analytical studies or experimental works. However, these valuable models can

suffer from limitations in their application validity ranges. In order to better understand the complex physics involved in sound wave absorption at perforates and to improve the design of future passive sound absorbers, the need for efficient numerical prediction methods and characterization techniques comes to the fore.

In this context, the present research pursued the dual goal of:

- developing novel and efficient numerical methods to characterize the acoustic behavior of perforated silencers in complex working conditions.
- applying these numerical methods to a selected set of resonators and orifices in order to characterize the damping mechanisms involved and identify potential parameters that can be included in the modeling and design of future passive silencers.

The achievements related to each of these aspects are summarized in the following sections.

### 8.1.1 Numerical methods for aeroacoustic characterization of passive silencers

#### High-order finite element methods to solve the linearized Navier-Stokes equations

In this work, novel high-order finite element models have been developed to solve the linearized Navier-Stokes equations for perforates. Such hybrid methodology with linear solvers is valid at low SPLs and relies on the separation of the global flow quantities between small perturbations and mean flow contributions. This approach allows to compute the propagation of acoustic waves through non-uniform and non-isentropic flow regions, accounting for all dissipative and convective effects. Thus, it constitutes an appealing alternative to direct methods [9, 216, 278, 279, 319] to characterize and to analyze the linear phenomena involved in acoustic wave damping and flow-acoustic interactions. Different variants of the LNSE have been investigated during the research activities: isentropic and non-isentropic versions of the LNSE, the standard double-decomposed (also called quasi-laminar) and the triple-decomposed (i.e. turbulent) forms of the LNSE. This allows to investigate the impact of modeling assumptions on the obtained acoustic results for the case of orifices and resonators.

Two implementations of the linearized Navier-Stokes equations have been considered in Chapters 3 and 4 of this work: a frequency-domain high-order continuous Finite Element Method ($p$-FEM) approach and a time-domain Runge-Kutta Discontinuous Galerkin (RKDG) solver. These high-order techniques

present an improved accuracy and lower memory requirement for a given problem compared to classical methods. By increasing the polynomial order representing the field variables, the pollution effects linked to dispersion errors remains low, even for large elements. This is particularly interesting for the chosen applications due to the large scale disparity between boundary layer effects — $\mathcal{O}(\delta_v)$ — and microphone spacing — $\mathcal{O}(\lambda_a)$ — for the impedance eduction methods that can be applied to quantify the acoustic absorption properties of silencers.

In frequency domain, the numerical method combines a high-order FEM associated with a Galerkin/Least-Squares stabilization technique to avoid convection-related spurious oscillations. Formulations have been implemented in two and three dimensions even if most of the application cases considered in Chapter 4 are performed on 2-D configurations. The boundary conditions have been imposed through the method of characteristics. Perfectly Matched Layers have been applied to inject an acoustic excitation at the inlet of the computational domain and absorb the outgoing waves at the outlet.

In time domain, the existing parallelized Runge-Kutta Discontinuous Galerkin code originally developed at the KU Leuven by Reymen [242], Toulorge and coworkers [83,120,293,295], based on the work of Hesthaven and Warburton [138, 139], is extended to deal with non-isentropic conditions and to account for the mean flow turbulence via an eddy-viscosity model.

Some validation cases are treated in Section 3.4, for which results of both linearized Navier-Stokes solvers are compared to reference solutions. Both non-uniform flow effects — for the case of a monopole source radiating in a plate boundary layer — and visco-thermal dissipation effects — for a closed-end waveguide of small dimensions and a slit MPP — are examined in the context of high-order methods.

### Unsteady incompressible flow simulations

As discussed in Chapter 2, the acoustic dissipation mechanisms involved in passive acoustic dampers significantly differ depending on the amplitude of the incoming acoustic excitation. For low excitation amplitudes, the numerical methods based on linearized equations, as detailed in Chapters 3 and 4, allow for an efficient treatment of the linear regime with limited computational costs. By increasing the excitation amplitudes, nonlinear effects related to the boundary layer separation and vortex shedding appear and become progressively dominant. Therefore, nonlinear time-domain solvers are needed at medium and high excitation amplitudes.

In Chapter 5, a methodology based on unsteady incompressible flow simulations has been proposed to study the acoustic behavior of Helmholtz resonators

and orifices under a large range of excitation amplitudes. Its assessment has been performed in a quiescent environment but the general formulation given in Section 5.1.1 enables a straightforward extension to cases for which $M_0 \neq 0$ [214,224]. It constitutes an alternative approach to the more widespread methodology based on compressible flow simulations to analyze the non-linear regime of perforates. Acoustic impedance results, obtained from incompressible simulations, have been successfully compared to both numerical results of the full compressible equations and experimental data for two resonator geometries at different SPLs. A good agreement in terms of both impedance values and patterns in the scattering of acoustic energy towards higher harmonics has been found. The procedure to assure the same acoustic velocity at the orifice between the incompressible approach and the references has been detailed in Section 5.1.4. In the linear regime, combining broadband excitation with a system identification technique [104] has shown to accurately predict the impedance curves with a single simulation. Causal filters were found to behave best for the considered set of primitive variables.

The proposed methodology has been applied for the study of both linear and nonlinear regimes of Helmholtz resonators with a commercial CFD software for moderate computational costs compared to compressible flow simulations. It allows to run extended parametric studies, as performed in Chapter 6. Additionally, the obtained impedance curves do not rely on the reflection coefficient but directly on the pressure and velocity. As such, they are valid over the complete frequency range under consideration and not only near the resonance frequency of the resonator.

### Coupled vibro-acoustic FEM model with a patch-impedance approach

In Chapter 7, a novel coupled vibro-acoustic FEM model for estimating the absorption characteristics of flexible perforated plates has been presented. The model conjugates linear potential acoustics with the shell elements theory. The problem is solved in the frequency domain via a commercial software for the complete 3-D configuration. The numerical model presents the advantage of being generally applicable to all kinds of plate geometries and fixation conditions. The plate perforations are described individually and each of them is defined independently as an imposed transfer impedance boundary on the shell domain defining the flexible plate. Due to the geometric representation of the orifices, a correction of the transfer reactance expression is required. This adjustment originates from the Helmholtz solver, which already accounts for the effect of area changes on potential flows. A correction has been proposed as part of the numerical methodology via a single parameter $\delta_H$ function of the porosity $\sigma$. The validation of the FEM model has been performed by comparison with experimental results from Toyoda et al. [298]. The validation case consists of a plate with squared-edge circular orifices placed in a cylindrical impedance tube.

A satisfying agreement was found between numerical and experimental results. Vibro-acoustic effects are captured correctly by the numerical model.

The impact of the plate vibrations on the local orifice acoustic impedance has been explored in Section 7.2. In most of the studies on the vibro-acoustic response of micro-perforated plates/panels in the literature [46, 47, 298], the impedance chosen to describe the acoustic behavior of the perforations is based on Maa's classical model [208, 210] or equivalent [287]. These models assume a rigid plate, with the fluid particle velocity at the hole wall being zero, and the effect of the plate vibration on the acoustic impedance of the perforations is neglected. A modified impedance model accounting for the local displacement of the plate, based on the velocity continuity condition at the perforation boundary by Li [195], is included in the present FEM modeling in an iterative manner. The influence of accounting for this phenomenon is evaluated for both local impedance values and global acoustic absorption characteristics of MPPs.

### 8.1.2 Application to perforated passive silencers and orifices

The developed methods allow an original investigation of sound-flow interactions, nonlinearities, and vibro-acoustic coupling happening at perforates and passive acoustic dampers. This section regroups the main observations made on the acoustic behavior of perforates throughout this dissertation.

#### Sound-flow interactions at perforates in their linear regime

In Part II, treating of linear acoustic problems in non-homogeneous flow/medium, the application cases have focused on the influence of grazing and bias flows at low Mach numbers for orifices and resonators, the effect of flow turbulence on these predictions, and temperature effects in resonators.

A flow grazing over a SDOF silencer is a very common situation met in applications, such as aircraft liners [5, 27]. For such cases, an increase in the flow speed is known to augment the resistance and decrease the reactance of the system [96, 178, 278, 318]. The case of a slit resonator with grazing flow has been examined in Section 4.1. Considering the modeling assumptions compared to the real test object, it has been concluded that the LNSE approach is able to capture correctly the complex interactions between acoustic waves and the shear layer over the orifice. The isentropic formulation, applied to the resonator in Section 4.1, predicts the correct trends and presents a good qualitative agreement. This section has also given the opportunity to compare quantitatively in-situ measurements and impedance eduction techniques (lumped and distributed) in the framework of linearized acoustic solvers.

Temperature effects can be responsible for detuning the designed resonance frequency of perforated silencers [39, 97, 306]. In Section 4.2, the LNS $p$-FEM solver has been applied to the cases of Helmholtz resonators in homogeneous hot environments (Section 4.2.2) and in presence of given temperature profiles inside their neck and cavity (Section 4.2.3). The results from the numerical linearized approach are qualitatively in agreement with previous experimental observations. The validity of the traditional scaling of an equivalent cold flow impedance model was found to have some limits with respect to the resistance. The different mechanisms involved in the acoustic energy dissipation in presence of temperature gradients have been further quantified by integrating numerically the energy balance for the acoustically perturbed field based on [222]. This offers an interesting insight into the mechanisms responsible for acoustic wave damping. A parametric study on the resonator neck length, the backing cavity depth and the temperature jump across the facing sheet has been performed. For the considered set of geometries and thermal conditions, the isentropic and non-isentropic versions of the linearized Navier-Stokes equations can deliver divergent results in terms of absorption peak amplitude, with a relative deviation which can reach up to 7%. Entropy and thermal effects have been found relevant at low Helmholtz numbers in the presence of temperature gradients through the resonator neck. In this context, the length of the resonator neck was identified as an important factor to consider.

When sound waves propagate within a turbulent flow, turbulent mixing can result in extra acoustic attenuation due to the turbulent stress acting on them [243]. The mechanisms of sound-flow and sound-turbulence interactions at low Mach number for perforates have been examined in Section 4.3. Numerical results from the turbulent set of LNS equations with an eddy-viscosity model (Section 3.1.2) have been compared to the standard quasi-laminar (Section 3.1.1) version of the LNSE for the cases of an orifice with bias flow (Section 4.3.1) and of a resonator with grazing flow (Section 4.3.2). The results have shown that accounting for the turbulent character of the mean flow inside the acoustic solver can drastically change the interpretation of the numerically predicted acoustic behavior when the diameter of the orifice increases. It is mostly relevant for the determination of the onset of hydrodynamic instabilities like the whistling phenomenon for duct flow components. The configuration with bias flow appears to be affected more strongly by the turbulence than the grazing flow one. For small orifices (e.g. $\mathrm{Sh} \leq 30$) with grazing flow, both solvers tend to yield the same results. For such configurations, both the flow turbulence level and the shear layer profile are found to have a small impact on the acoustic results.

### Characterization of the nonlinear effects at medium and high amplitudes

Along with the two Helmholtz resonator geometries used for validation of the unsteady incompressible flow simulations detailed in Chapter 5, some specificities

of the nonlinear regime of these resonators have been observed. The impedance results from the 2-D and 3-D models have shown that the overall impact of 3-D effects remains secondary, although it increases with increasing velocity at the orifice. Similar conclusions have been made for the turbulence modeling. This demonstrates that the separation process itself, responsible for the nonlinear acoustic dissipation, is almost not influenced by the shed vortices. Accounting for micro-rounded or micro-chamfered edges tends to decrease the resistance, leading to better agreement with the experimental results. Even for very small chamfered sizes, their impact on the boundary layer separation, and therefore on the predicted resistance was found important for high amplitude excitations. Such geometrical details should therefore be included for accurate predictions of the acoustic behavior of Helmholtz resonators in their nonlinear regime.

In Chapter 6, the unsteady incompressible approach has been further applied to investigate the scattering of acoustic energy from the excitation frequency towards higher harmonics at orifices. The method has been shown to correctly determine the energy content of the higher harmonics compared to analytical quasi-steady flow theory and compressible flow simulations. A pattern in the higher harmonics, characterized by its dominating odd harmonics — referred to as OHO pattern — was found in accordance with previous works [69, 72].

Deviations from this classical pattern have been observed under particular conditions. Vortex disruption from the different faces of the orifices was identified as the cause. A theoretical model has been proposed, based on the vortex convection length inside the orifice, to predict the disappearance of the standard high harmonics pattern. This model is intrinsically valid only in cases where vortex convection processes can be defined inside the orifice. When this condition is fulfilled, it is shown that the changes in the spectrum pattern can be predicted through a single dimensionless number $\Lambda_d$, defined as the ratio of the vortex convection length inside the orifice to the orifice thickness. For $\Lambda_d < 1$, the standard OHO pattern is present, whereas for $\Lambda_d > 1$ this pattern disappears. The theory was successfully assessed by means of a parametric study with several orifice geometries and excitation amplitudes. This theory is also in accordance with former experimental works on higher harmonics of orifice responses.

Combining local flow visualizations with impedance results and spectral content of the acoustic responses, this work contributes to a global understanding of the nonlinear regime of orifices. It has been shown that the study of the higher harmonics pattern delivers in-depth information on the local flow field generated by high amplitude acoustic excitations. The numerical determination of the impedance has been found to be more challenging in cases where the OHO pattern is absent due to the more complex flow structures present. Therefore, the understanding of this particular behavior and its prediction are of importance, even if the energy content at the high harmonics is small compared to the overall energy contained at the fundamental frequency.

### Impact of vibrations on passive silencers

Additionally to the absorption curves obtained for validation in Part IV, the proposed FEM model with impedance patches has proven to offer great insights into the coupling between the acoustic field and the structural response of perforated plates. The influence of the perforations on the plate structural impedance has been precisely quantified and found limited in the case of the MPPs considered. Results further showed that vibrations can significantly affect the absorption properties of micro-perforated plates when a strong coupling between panel-controlled and hole-controlled resonance phenomena exists. The phasor representation of the results has also revealed that the panel resonances can increase the acoustic resistance of the MPP, leading to higher absorption. However, the resistance of the flexible MPP is found systematically lowered by the structural vibrations. This trend appears to be strengthened with decreasing perforation diameters. The decrease in orifice size is also found to enlarge the phasor loops from the panel-controlled resonances, showing an increased sensibility of the MPP's absorption properties to the plate motion. The amplitude ratio of the panel averaged velocity to the air particle velocity in the MPP holes is found to increase with decreasing perforation diameters and strong peaks can be seen near the structural eigenfrequencies. Therefore, the values of the air-frame velocity can vary significantly in amplitude depending on the frequency. This can result, combined with the phase difference at the considered frequency, in a local improvement or deterioration of the absorption properties of the MPP compared to the rigid case.

The impact of vibrations on the orifice impedance itself and the consequences for the absorption performance of MPPs have been explored in the second part of Chapter 7. Unlike the case of membranes, vibrations are found to only affect significantly the resistive part of the orifice impedance. Noticeable differences arise when including the effect of vibrations on the total attached mass of fluid at the orifice rather than solely on the inner part. Applying the correction to the total attached mass is, nevertheless, not entirely justified by the theory and results are presented here as a limit case to show the implications linked to this particular phenomenon. An exact answer would require to solve the coupled vibro-acoustic problem for a moving orifice considering the viscous-thermal losses, which lies beyond the scope of this work.

The absorption curves, obtained for the considered MPPs with different orifice sizes, show that accounting for the orifice impedance alteration through the structural motion is more important for larger orifice diameters and at low frequencies. This effect is, however, rather limited for the investigated micro-perforated plates. It is expected to be more significant for perforates with a higher porosity. For the examined configurations, this sophistication of the model can be simply neglected without significantly impacting the prediction of the MPP's absorption characteristics.

## 8.2 Future perspectives

Based on the major contributions presented in Parts II to IV of this work and supported by the experience gained throughout the research activities, some suggestions for further research can be formulated. These future perspectives are shortly presented in this section.

### Further improvements on the efficiency of the LNSE solvers

The linear solvers described in Part II, combined with global and local characterization techniques (e.g. two-port model, energy balance), have shown their potential for studying and modeling the acoustic behavior of perforated silencers. Being able to account for all visco-thermal and non-uniform flow effects comes, however, with a computation cost. For silencer applications, it is mainly related to the proper resolution of wall boundary layers. Even if the high-order methods developed in this work allow faster problem resolution and lower memory requirements than classical approaches, some further improvements should be made in order to perform extended parametric studies on 3-D configurations of perforates.

A possibility to reduce the overall computational cost of the LNSE approach is to spatially separate the numerical domain between a region where complex sheared-flow and dissipative effects are important (modeled with LNSE) and an inviscid, irrotational flow region modeled with a potential acoustic operator. Examples of this approach can be found in the frequency domain for the coupling of LNSE with the Helmholtz equation in [223] and for the coupling LEE/LPE in [124]. For frequency solvers, an alternative solution for the memory limits could be found in the Domain Decomposition Methods [75, 103, 211].

In time domain, the parallelization of the developed RKDG solver for the LNSE already allows to deal with large problems. However, the presence of locally refined mesh elements, to resolve the visco-thermal boundary layers, forces the effective time step to be drastically smaller to respect the CFL conditions. It results in vastly increasing the computational effort over the whole domain. In this context, the implementation of a locally varying time stepping scheme appears as an appealing solution [138, 204, 217, 299].

### Turbulence modeling for large orifices

It was observed in Section 4.3 that including the base flow turbulence in the acoustic solver was required to correctly predict the acoustic behavior of the largest orifices considered in this work. The turbulence model, used for the description of the perturbation Reynolds stress $\tilde{\tau}_{ij}^{R}$, was the Newtonian eddy

model [114, 142, 243], based on the Boussinesq turbulent viscosity hypothesis. Such model has already shown limitations at low frequencies in previous studies on duct acoustics with turbulent low Mach number flows [311]. Alternatives, like the frequency-dependent eddy-viscosity models and non-equilibrium models of the turbulent diffusion [235, 311], could be investigated in the framework of the LNSE solvers.

### Application of the unsteady incompressible CFD approach for cases with grazing flow

Part III thoroughly details the nonlinear phenomena happening at orifices and resonators under medium and high amplitude excitations in a quiescent medium. It would be interesting to apply the proposed unsteady incompressible flow approach to the case of resonators under grazing flow conditions to review the existing semi-empirical impedance models. Additionally, the dissertation focuses on resonators made with a single orifice in Parts II and III and, therefore, disregards any Hole Interaction Effects. As indicated by direct numerical simulations of resonators with grazing flow [278], vortices can be convected downstream for a relatively long distance. This observation suggests that fluid mechanical interactions between neighboring resonators of an acoustic liner could happen due to interferences with this traveling vortices. Quantifying and modeling these HIE in presence of grazing flow would be of importance for the design of locally reacting acoustic liners.

A further extension of this work on the nonlinear regime of orifices and resonators could be to use the pressure and velocity information obtained by the unsteady incompressible flow simulation to feed data-based reduced-order models. This would deliver an efficient and robust approach to generate accurate models to describe the dynamics of arbitrary resonator geometries under various operating conditions. Such nonlinear models, based on system identification techniques [233], have been recently applied with compressible flow simulations for the characterization of Helmholtz resonators with a local-linear neuro-fuzzy network model [107].

### Optimized design of flexible MPPs

Concerning Part IV on the vibro-acoustic behavior of MPPs, the proposed FEM model, due to its individual treatment of the perforations, enables to consider the perforation locations as an additional design parameter. As a consequence, the non-uniform perforation distributions on flexible MPPs could be investigated to assess the potential of this design parameter for specific applications. An example of such changes in perforation distribution is given by

Temiz [285], related to the present FEM model, but no clear design guidelines have been stated yet.

# Part VI

# Addenda

# Appendix A

# Matrix formulation for Linearized Navier-Stokes equations solvers

The acoustic matrix operator defined by the linearized Navier-Stokes equations is given by:

$$\mathcal{L}_{\mathrm{LNSE}}(\mathbf{q}) = 0 \Leftrightarrow \frac{\partial \mathbf{q}}{\partial t} + \frac{\partial \mathbf{A}_i \mathbf{q}}{\partial x_i} + \mathbf{C}\mathbf{q} + \frac{\partial}{\partial x_i}\left(\frac{\partial \mathbf{C}_{ij}\mathbf{q}}{\partial x_j}\right) = \mathbf{0}\,, \tag{A.1}$$

with $\mathbf{q} = \{\rho', \rho_0 u_1', \rho_0 u_2', p'\}^T$ for a 2-D problem defined with the Cartesian coordinates $\mathbf{x} = (x_1, x_2)$. The expressions for the matrices $\mathbf{A}_i$, $\mathbf{C}$, and $\mathbf{C}_{ij}$ are given in this appendix.

## A.1 Quasi-laminar isentropic LNSE

$$\mathbf{A}_i = \begin{bmatrix} u_{0i} & \delta_{1i} & \delta_{2i} & 0 \\ 0 & u_{0i} & 0 & \delta_{1i} \\ 0 & 0 & u_{0i} & \delta_{2i} \\ 0 & c_0^2\delta_{1i} & c_0^2\delta_{2i} & u_{0i} \end{bmatrix},$$

$$\mathbf{C} = \begin{bmatrix} 0 & 0 & 0 & 0 \\ u_{0i}\frac{\partial u_{01}}{\partial x_i} & \frac{\partial u_{01}}{\partial x_1} & \frac{\partial u_{01}}{\partial x_2} & 0 \\ u_{0i}\frac{\partial u_{02}}{\partial x_i} & \frac{\partial u_{02}}{\partial x_1} & \frac{\partial u_{02}}{\partial x_2} & 0 \\ 0 & \frac{1-\gamma}{\rho_0}\frac{\partial p_0}{\partial x_1} & \frac{1-\gamma}{\rho_0}\frac{\partial p_0}{\partial x_2} & (\gamma-1)\frac{\partial u_{0i}}{\partial x_i} \end{bmatrix},$$

and

$$\mathbf{C}_{ij} = \frac{\mu}{\rho_0}\begin{bmatrix} 0 & 0 & 0 & 0 \\ 0 & -\frac{4}{3}\delta_{1i}\delta_{1j} - \delta_{2i}\delta_{2j} & \frac{2}{3}\delta_{1i}\delta_{2j} - \delta_{2i}\delta_{1j} & 0 \\ 0 & \frac{2}{3}\delta_{2i}\delta_{1j} - \delta_{1i}\delta_{2j} & -\delta_{1i}\delta_{1j} - \frac{4}{3}\delta_{2i}\delta_{2j} & 0 \\ 0 & 0 & 0 & 0 \end{bmatrix}.$$

## A.2 Quasi-laminar non-isentropic LNSE operator

Only the matrix row related to the energy equation is explicitly given, as the other terms are not affected by the non-isentropic assumption and stay the same as in Appendix A.1.

$$\mathbf{A}_1(4,:) = \Big[0, \quad \frac{\gamma p_0}{\rho_0} + (\gamma-1)\frac{\mu}{\rho_0}\left(\frac{4}{3}\frac{\partial u_{o2}}{\partial x_2} - \frac{8}{3}\frac{\partial u_{o1}}{\partial x_1}\right), \quad 2(1-\gamma)\frac{\mu}{\rho_0}\left(\frac{\partial u_{o2}}{\partial x_1} + \frac{\partial u_{o1}}{\partial x_2}\right), \quad u_{01}\Big],$$

$$\mathbf{A}_2(4,:) = \Big[0, \quad 2(1-\gamma)\frac{\mu}{\rho_0}\left(\frac{\partial u_{o2}}{\partial x_1} + \frac{\partial u_{o1}}{\partial x_2}\right), \quad \frac{\gamma p_0}{\rho_0} + (\gamma-1)\frac{\mu}{\rho_0}\left(\frac{4}{3}\frac{\partial u_{o1}}{\partial x_1} - \frac{8}{3}\frac{\partial u_{o2}}{\partial x_2}\right), \quad u_{02}\Big],$$

$$\mathbf{C}(4,:) = \Big[0, \quad \frac{1-\gamma}{\rho_0}\frac{\partial p_0}{\partial x_1} + (\gamma-1)\frac{\mu}{\rho_0}\left(\frac{8}{3}\frac{\partial^2 u_{01}}{\partial x_1 x_1^2} + \frac{2}{3}\frac{\partial^2 u_{02}}{\partial x_1 x_2^2} + 2\frac{\partial^2 u_{01}}{\partial x_2 x_2^2}\right), \quad \frac{1-\gamma}{\rho_0}\frac{\partial p_0}{\partial x_2} + (\gamma-1)\frac{\mu}{\rho_0}\left(\frac{8}{3}\frac{\partial^2 u_{02}}{\partial x_2 x_2^2} + \frac{2}{3}\frac{\partial^2 u_{01}}{\partial x_1 x_2^2} + 2\frac{\partial^2 u_{02}}{\partial x_1 x_1^2}\right), \quad (\gamma-1)\frac{\partial u_{0i}}{\partial x_i}\Big],$$

$$\mathbf{C}_{ii}(4,:) = \left[(\gamma-1)\frac{\lambda_t}{R\rho_0} \quad 0 \quad 0 \quad -(\gamma-1)\lambda_t\frac{p_0}{R\rho_0^2}\right].$$

## A.3 Turbulent homentropic LNSE

In this work, the modeling of the perturbation Reynolds stress tensor $\tilde{\tau}_{ij}^R$ is done by means of the Newtonian eddy model based on the Boussinesq turbulent viscosity hypothesis. Considering this hypothesis, the matrices can be expressed as:

$$\mathbf{A}_i = \begin{bmatrix} u_{0i} & \delta_{1i} & \delta_{2i} \\ \frac{\gamma p_0}{\rho_0}\delta_{1i} & u_{0i} + \frac{4}{3\rho_0}\frac{\partial \mu_t}{\partial x_1}\delta_{1i} + \frac{1}{\rho_0}\frac{\partial \mu_t}{\partial x_2}\delta_{2i} & -\frac{2}{3\rho_0}\frac{\partial \mu_t}{\partial x_1}\delta_{1i} + \frac{1}{\rho_0}\frac{\partial \mu_t}{\partial x_1}\delta_{2i} \\ \frac{\gamma p_0}{\rho_0}\delta_{2i} & \frac{1}{\rho_0}\frac{\partial \mu_t}{\partial x_2}\delta_{1i} - \frac{2}{3\rho_0}\frac{\partial \mu_t}{\partial x_1}\delta_{2i} & u_{0i} + \frac{1}{\rho_0}\frac{\partial \mu_t}{\partial x_1}\delta_{1i} + \frac{4}{3\rho_0}\frac{\partial \mu_t}{\partial x_2}\delta_{2i} \end{bmatrix},$$

$$\mathbf{C} = \begin{bmatrix} 0 & 0 & 0 \\ u_{0i}\frac{\partial u_{01}}{\partial x_i} - \gamma(\frac{1}{\rho_0}\frac{\partial p_0}{\partial x_1} - \frac{1}{\rho_0^2}\frac{\partial \rho_0}{\partial x_1}p_0) & -\frac{\partial u_{02}}{\partial x_2} - \frac{1}{\rho_0}(u_{0i}\frac{\partial \rho_0}{\partial x_i}) & \frac{\partial u_{01}}{\partial x_2} \\ u_{0i}\frac{\partial u_{02}}{\partial x_i} - \gamma(\frac{1}{\rho_0}\frac{\partial p_0}{\partial x_2} - \frac{1}{\rho_0^2}\frac{\partial \rho_0}{\partial x_2}p_0) & \frac{\partial u_{02}}{\partial x_1} & -\frac{\partial u_{01}}{\partial x_1} - \frac{1}{\rho_0}(u_{0i}\frac{\partial \rho_0}{\partial x_i}) \end{bmatrix},$$

and

$$\mathbf{C}_{ij} = \frac{\mu + \mu_t}{\rho_0} \begin{bmatrix} 0 & 0 & 0 \\ 0 & -\frac{4}{3}\delta_{1j}\delta_{1i} - \delta_{2j}\delta_{2i} & \frac{2}{3}\delta_{1j}\delta_{2i} - \delta_{2j}\delta_{1i} \\ 0 & \frac{2}{3}\delta_{2j}\delta_{1i} - \delta_{1j}\delta_{2i} & -\delta_{1j}\delta_{1i} - \frac{4}{3}\delta_{2j}\delta_{2i} \\ 0 & 0 & 0 \end{bmatrix}.$$

# Appendix B

# Waveguide case in time domain

In this appendix, some specificities of the time-domain RKDG simulations are reviewed in the light of the waveguide case discussed in Section 3.4.2. According to the configuration in Fig. 3.8, two different types of inlet velocity excitation are investigated:

- Mono-frequency excitation: the velocity at the inlet boundary is prescribed as function of a single frequency $\omega_{\text{ex}}$, defined as

$$\mathbf{u}'_{\mathbf{in}} \cdot \mathbf{n} = V_{\text{in}} \sin\left(\omega_{\text{ex}} t\right), \tag{B.1}$$

  where the term $V_{\text{in}}$ is the normalized inlet axial velocity to be prescribed on the boundary, taken here as $V_{\text{in}} = 1\,\text{m/s}$.

- Multiple-frequency excitation: the previous expression is extended to a finite set of $N_f$ discrete frequencies:

$$\mathbf{u}'_{\mathbf{in}} \cdot \mathbf{n} = \sum_{k=1}^{N_f} V_{in}^k \sin\left(\omega_{\text{ex}}^k t + \phi_k\right), \tag{B.2}$$

  where $V_{\text{in}}^k$ is the desired velocity amplitude for the $k^{\text{th}}$ excitation frequency $\omega_{\text{ex}}^k$, with initial phase $\phi_k$. No difference in phase between the input excitation at different frequencies has been accounted for in the current case, which reads $\phi_k = 0, \forall\, k \in \{1 \dots N_f\}$. The pressure amplitude is further chosen as $V_{\text{in}}^k = 1\,\text{m/s}, \forall\, k \in \{1 \dots N_f\}$ to match mono- and multiple-frequency simulations.

The simulations are performed assuming $\mu = 0$ and $\lambda_t = 0$. Polynomial shape functions of order $p = 7$ and a non-dimensional time step $\Delta t^\star = c_0 \, \Delta t = 1.5 \times 10^{-4}$ are chosen. The simulations are run until non-dimensional time $t^\star = 100$ or 200. The fluctuating pressure is monitored at the backing wall at a frequency corresponding to the sampling time step $\Delta t_s^\star = 1.5 \times 10^{-3}$.

Figure B.1 illustrates the evolution in time of the pressure fluctuation at the monitoring point placed at the backing wall of the waveguide, from a single frequency excitation at the resonance frequency $f_{\text{res}} = 1000\,\text{Hz}$ and two near frequencies $f_{\text{ex}} = \{975\,\text{Hz}, 1050\,\text{Hz}\}$. The low frequency pattern observed in Fig. B.1, which envelops the pressure time signal, is given by the difference between the resonance frequency and the actual excitation frequency, i.e. $f_{\text{low}} = |f_{\text{ex}} - f_{\text{res}}|$. This explains the phenomenon of resonance observed on Fig. B.1b where the low frequency envelop does not exist and the amplitude of the pressure is growing endlessly in the absence of dissipative mechanisms. From the spectrum of the pressure signal, it appears that the resonance frequency of the system is always present for time-domain simulations. It also requires rather long time series to perform the FFT on the signal to be able to have accurate results near the resonance frequency.

Figure B.2 shows the results obtained from the time-domain simulations for the inviscid waveguide case considering both excitation types — Eqs. (B.1) and (B.2). The numerical results are in good agreement with the theoretical solution. It is observed, nevertheless, that it is more challenging to get accurate pressure amplitude by means of fast Fourier transforms compared to the direct frequency-domain computations. The quality of the computed pressure values at the backing wall depends significantly on the type of inlet excitation applied. As shown in Fig. B.2, mono-frequency excitations require the shortest simulation length (in terms of $t^\star$) for a specific frequency. For simulations with multiple-frequency inlet excitation, including the system resonance frequency to the excitation is found to have a negative effect on the determination of the pressure amplitudes. The time series of the computed pressure amplitude is drastically different with and without the excitation at the resonance frequency considered, as illustrated in Fig. B.3. Multiple-frequency and mono-frequency excitations are found to give similar results but multiple-frequency excitations require much longer time data to perform the Fourier treatment.

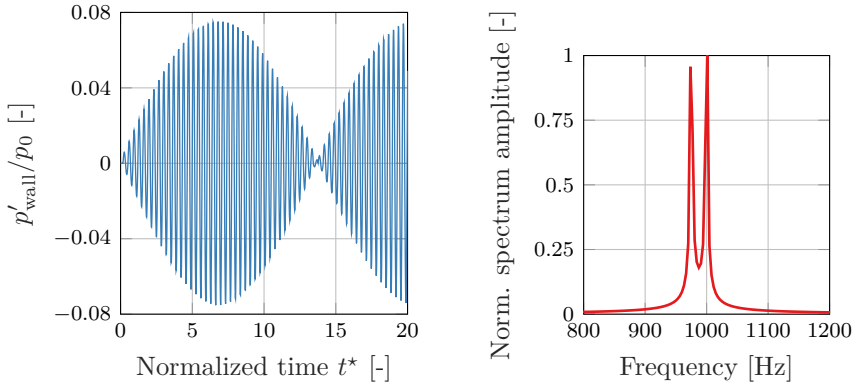


(a) At $f = 975\,\text{Hz}$, i.e. $f_{\text{ex}} < f_{\text{res}}$

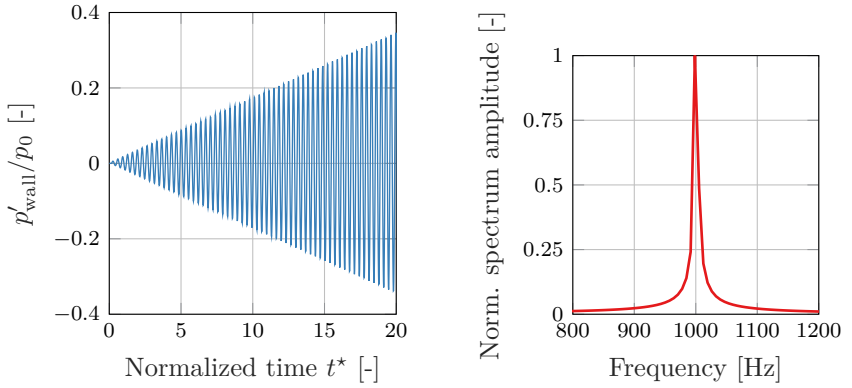


(b) At $f = 1000\,\text{Hz}$, i.e. $f_{\text{ex}} \approx f_{\text{res}}$

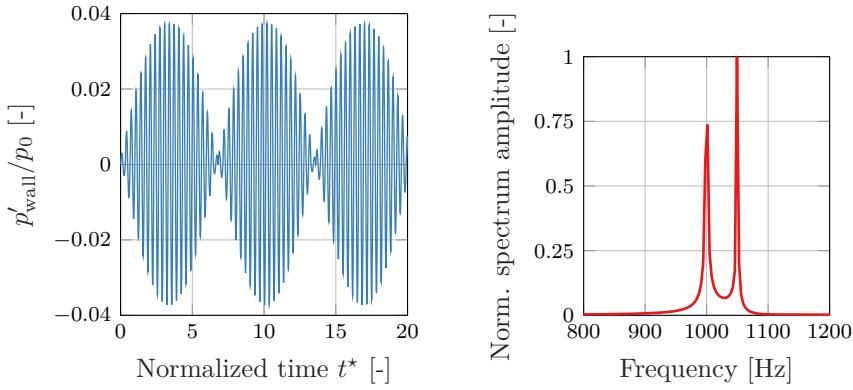


(c) At $f = 1050\,\text{Hz}$, i.e. $f_{\text{ex}} > f_{\text{res}}$

Figure B.1. Time series of the normalized pressure $p'$ at the backing wall (left) and the corresponding pressure spectrum (right) at three different frequencies.

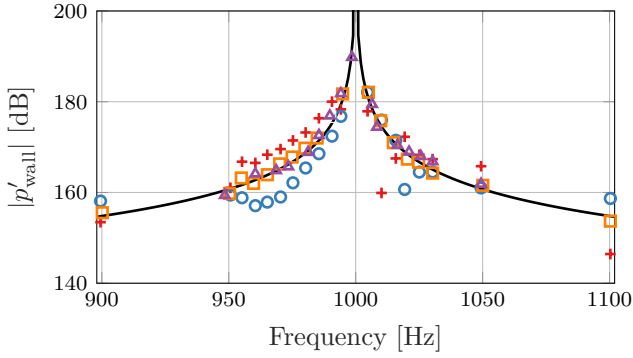


Figure B.2. Comparison of the backing wall pressure amplitude $|p'_{\text{wall}}|$ obtained with the time-domain LNS RKDG solver with the analytic solution (—) for the no-dissipative case ($\mu = 0$, $\lambda_t = 0$): for a multiple-frequency excitation including $f_{\text{res}}$ and $t^\star = 0 \dots 200$ (+), for a multiple-frequency excitation excluding $f_{\text{res}}$ and $t^\star = 0 \dots 200$ (○), for a multiple-frequency excitation excluding $f_{\text{res}}$ and $t^\star = 0 \dots 500$ (□), and for a mono-frequency input velocity and $t^\star = 0 \dots 100$ (△).

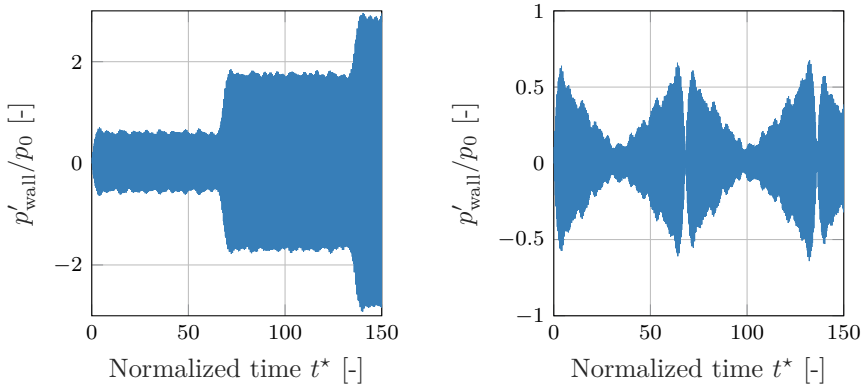


(a) Including the resonance frequency (b) Without the resonance frequency

Figure B.3. Time series of the normalized pressure at the backing wall for a multiple-frequency input velocity excitation.

# Appendix C

# Polynomial shape functions, first and second derivatives for the LNSE-RKDG solver

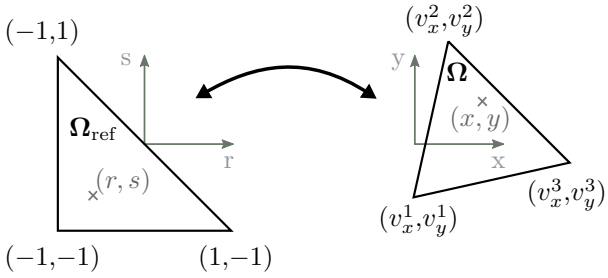


Figure C.1. Mapping of triangular element from physical domain $\Omega$ to reference domain $\Omega_{\text{ref}}$ to define the basis of polynomial shape functions $\phi_{nm}^{\Omega_{\text{ref}}}$.

For a two-dimensional problem, the following orthonormal basis is chosen [138], defined on the reference element $\Omega_{\text{ref}}$ depicted in Fig. C.1, for the Discontinuous Galerkin representation of variables. The transformation from an arbitrary element $\Omega$ to the reference triangular element $\Omega_{\text{ref}}$ is given by the Lagrange expansion of the physical coordinates in terms of vertex shape functions such that

$$\begin{pmatrix} x \\ y \end{pmatrix} = -\left(\frac{r+s}{2}\right)\begin{pmatrix} v_x^1 \\ v_y^1 \end{pmatrix} + \left(\frac{1+r}{2}\right)\begin{pmatrix} v_x^2 \\ v_y^2 \end{pmatrix} + \left(\frac{1+s}{2}\right)\begin{pmatrix} v_x^3 \\ v_y^3 \end{pmatrix}. \tag{C.1}$$

**Shape functions:**

$$\phi_{nm}^{\Omega_{\text{ref}}}(r,s) = P_n^{0,0}(\frac{2(1+r)}{(1-s)} - 1)\left(\frac{1-b}{2}\right)^n P_m^{2n+1,0}(s)\ ,\ \forall(n,m) \in \mathbb{N}^2\,, \quad \text{(C.2)}$$

where $P_k^{\alpha,\beta}$ are the Jacobi polynomials of order $k$ and real parameters $\alpha$ and $\beta$.

Concerning the 1st and 2nd derivatives of the shape functions $\phi_{nm}^{\Omega_{\text{ref}}}(r,s)$, specific conditions on $(n,m)$, e.g. $(n,m) \geq 1$ or 2, may be required for some terms in the following expressions to ensure the existence of the Jacobi polynomials.

**1st derivatives:**

$$\frac{\partial \phi_{nm}^{\Omega_{\text{ref}}}}{\partial r}(r,s) = \left(\frac{2}{1-s}\right)\left(\frac{n+1}{2}\right) P_{n-1}^{1,1}\left(\frac{2(1+r)}{(1-s)} - 1\right)\left(\frac{1-s}{2}\right)^n P_m^{2n+1,0}(s) \quad \text{(C.3)}$$

$$\begin{aligned}\frac{\partial \phi_{nm}^{\Omega_{\text{ref}}}}{\partial s}(r,s) = &\left[\frac{2(1+r)}{(1-s)^2}\left(\frac{n+1}{2}\right) P_{n-1}^{1,1}\left(\frac{2(1+r)}{(1-s)} - 1\right)\right]\left(\frac{1-s}{2}\right)^n P_m^{2n+1,0}(s) \\ &+ P_n^{0,0}\left(\frac{2(1+r)}{(1-s)} - 1\right)\left[-\frac{n}{2}\left(\frac{1-s}{2}\right)^{n-1}\right] P_m^{2n+1,0}(s) \\ &+ P_n^{0,0}\left(\frac{2(1+r)}{(1-s)} - 1\right)\left(\frac{1-s}{2}\right)^n \left[\left(\frac{m+2n+2}{2}\right) P_{m-1}^{2n+2,1}(s)\right]\end{aligned} \quad \text{(C.4)}$$

**2nd derivatives:**

$$\frac{\partial^2 \phi_{nm}^{\Omega_{\text{ref}}}}{\partial r^2}(r,s) = \left(\frac{n+2}{2}\right)\left(\frac{n+1}{2}\right) P_{n-2}^{2,2}\left(\frac{2(1+r)}{(1-s)} - 1\right)\left(\frac{1-s}{2}\right)^{n-2} P_m^{2n+1,0}(s) \quad \text{(C.5)}$$

$$\begin{aligned}\frac{\partial^2 \phi_{nm}^{\Omega_{\text{ref}}}}{\partial s \partial r}(r,s) = &\frac{1}{1-s}\left(\frac{n+1}{2}\right) P_{n-1}^{1,1}\left(\frac{2(1+r)}{(1-s)} - 1\right)\left(\frac{1-s}{2}\right)^{n-1} P_m^{2n+1,0}(s) \\ &+ \left(\frac{n+1}{2}\right)\frac{2(1+r)}{(1-s)^2}\left(\frac{n+2}{2}\right) P_{n-2}^{2,2}\left(\frac{2(1+r)}{(1-s)} - 1\right)\left(\frac{1-s}{2}\right)^{n-1} P_m^{2n+1,0}(s) \\ &- \frac{n}{2}\left(\frac{n+1}{2}\right) P_{n-1}^{1,1}\left(\frac{2(1+r)}{(1-s)} - 1\right)\left(\frac{1-s}{2}\right)^{n-2} P_m^{2n+1,0}(s) \\ &+ \left(\frac{n+1}{2}\right) P_{n-1}^{1,1}\left(\frac{2(1+r)}{(1-s)} - 1\right)\left(\frac{1-s}{2}\right)^{n-1}\left(\frac{m+2n+2}{2}\right) P_{m-1}^{2n+2,1}(s)\end{aligned} \quad \text{(C.6)}$$

$$\frac{\partial^2 \phi_{nm}^{\Omega_{\text{ref}}}}{\partial s^2}(r,s) = \left[\frac{1+r}{1-s}\left(\frac{n+1}{2}\right) P_{n-1}^{1,1}\left(\frac{2(1+r)}{(1-s)}-1\right) + \left(\frac{1+r}{1-s}\right)^2 \left(\frac{n+1}{2}\right)\right.$$

$$\left(\frac{n+2}{2}\right) P_{n-2}^{2,2}\left(\frac{2(1+r)}{(1-s)}-1\right) - n\frac{1+r}{1-s}\left(\frac{n+1}{2}\right) P_{n-1}^{1,1}\left(\frac{2(1+r)}{(1-s)}-1\right)$$

$$\left. + \frac{n(n-1)}{4} P_n^{0,0}\left(\frac{2(1+r)}{(1-s)}-1\right)\right]\left(\frac{1-s}{2}\right)^{n-2} P_m^{2n+1,0}(s)$$

$$+ \left[2\frac{1+r}{1-s}\left(\frac{n+1}{2}\right) P_{n-1}^{1,1}\left(\frac{2(1+r)}{(1-s)}-1\right)\left(\frac{1-s}{2}\right)^{n-1} - n\left(\frac{1-s}{2}\right)^{n-1}\right.$$

$$\left. P_n^{0,0}\left(\frac{2(1+r)}{(1-s)}-1\right)\right]\left(\frac{m+2n+2}{2}\right) P_{m-1}^{2n+2,1}(s)$$

$$+ \left[P_n^{0,0}\left(\frac{2(1+r)}{(1-s)}-1\right)\left(\frac{1-s}{2}\right)^n\right]\left(\frac{m+2n+2}{2}\right)\left(\frac{m+2n+3}{2}\right) P_{m-2}^{2n+3,2}(s) \tag{C.7}$$

# Appendix D

# Resonator in hot environment: $p$- and grid-independent test for the LNSE $p$-FEM solver

In this appendix, the accuracy of the numerical results for the work on Helmholtz resonators in hot environment, presented in Section 4.2, is shown through two representative simulation cases on two different grids. These FEM meshes are referred to as $M_1$ and $M_2$, respectively. The mesh $M_1$ corresponds to a mixed structured/unstructured mesh (see Fig. D.1a) of 4800 triangular elements. The orifice zone, which involves the smallest elements, is here meshed on a structured grid to limit the number of those elements. The mesh $M_2$, represented in Fig. D.1b, is fully unstructured and is composed of 26000 triangular elements. Both grids have a minimum element size $h_{min} \approx 1.5 \times 10^{-5}\,\mathrm{m}$ which is similar to the viscous and thermal boundary layers minimal thickness ($\delta_{v/t,min} \approx 3.5 \times 10^{-5}\,\mathrm{m}$). The case geometry is considered fixed here, with $l_o = 1.0\,\mathrm{mm}$, $d_o = 1.5\,\mathrm{mm}$, and $l_{\mathrm{cav}} = 0.0175\,\mathrm{m}$. The temperature outside the resonator is taken as $T_0 = 500\,\mathrm{K}$. The first case represents a situation with homogeneous temperature (i.e. $\Delta T_{0,\,\mathrm{orifice}} = 0\,\mathrm{K}$), whereas the second one illustrates situations in presence of a temperature gradient through the resonator neck with $\Delta T_{0,\mathrm{orifice}} = 40\,\mathrm{K}$. Two particular features differentiate the meshes used: the large size jump for the structured/unstructured transition in $M_1$ and the better refinement of $M_2$ on the wall of the resonator facing sheets.

The peak values of the absorption coefficient obtained from the LNS simulations for the two situations described above are listed in Table D.1. It shows that the difference in terms of predicted absorption coefficient is very small between $M_1$ and $M_2$, with $\epsilon_M \approx 0.25\,\%$. This is verified both in presence of the temperature gradient and without.

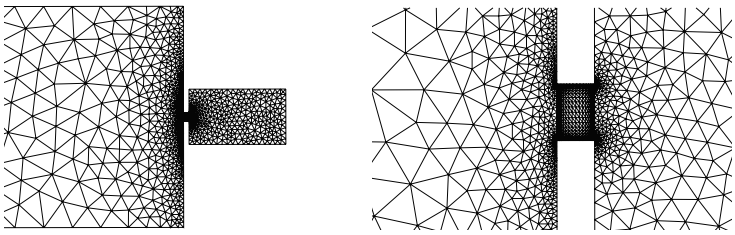

(a) Mesh $M_1$: Mixed mesh used for FEM simulations.

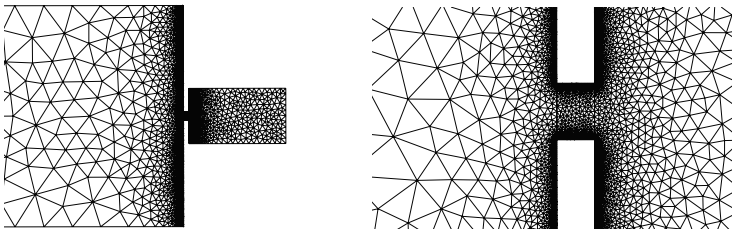

(b) Mesh $M_2$: Unstructured mesh used for FEM simulations.

Figure D.1. Discretization of the two-dimensional numerical domain for the Helmholtz resonator case with $l_o = 1.0\,\text{mm}$ and $d_o = 1.5\,\text{mm}$: global view of the mesh (left) and close-up in the orifice vicinity (right).

| $\Delta T_{0,\,\text{orifice}}$ [K] | $M_1$ | $M_2$ | $\epsilon_M$ [%] |
|---|---|---|---|
| 0 | 0.5571 | 0.5584 | 0.23 |
| 40 | 0.5468 | 0.5482 | 0.26 |

Table D.1: Absorption coefficient $\alpha$ [−] at resonance frequency obtained with the non-isentropic LNS solver for the two investigated cases, as well as the corresponding relative variations $\epsilon_M$; $p = 3$.

The integral formulation of the energy balance over the complete computational domain, given by Eq. (3.75), reduces to $\mathbb{W}' = \mathbb{D}'$ for the present case with harmonic perturbations in frequency domain. Figures D.2a and D.2b show that the energy balance for the two particular cases discussed in this appendix section is close to being satisfied. The substitution of mesh only leads to small changes on the overall energy balance fulfillment, and predominantly away from the resonance frequency. In both cases, $M_1$ and $M_2$ give similar results at the resonance. Nevertheless, for the case where $\Delta T_0 = 0\,\text{K}$, the more refined mesh $M_2$ delivers improved fulfillment of the energy balance at low frequency, probably due to the smoother transition between inner and outer zones of the orifice. The situation is different in presence of a temperature gradient inside the orifice. In this case, $M_2$ does not give improved energy balance quality.

This can originate to some extent from the discontinuities in the temperature profiles at the locations $\pm l_o/2$ along the duct axis, for which $M_2$ presents less spatial element refinement.

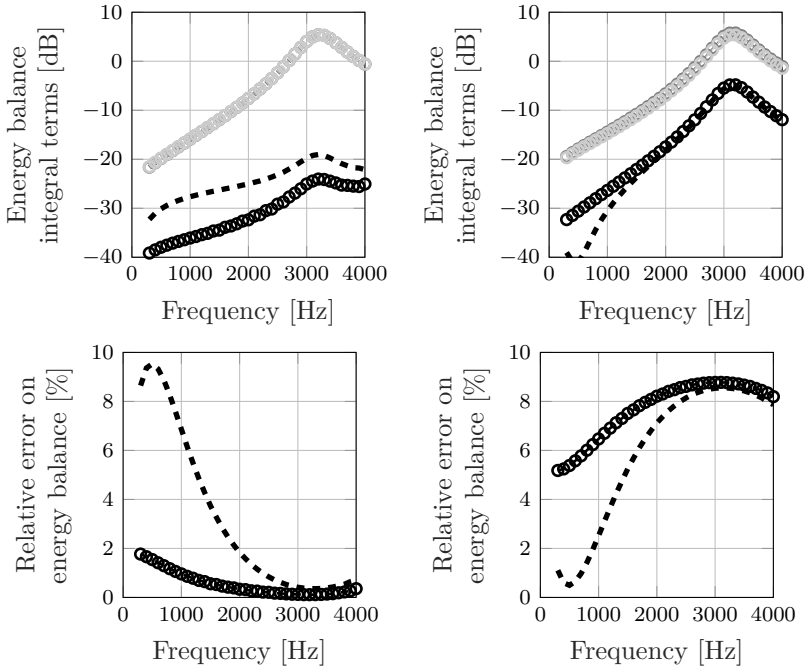


(a) $T_0 = 500\,\mathrm{K}$ and $\Delta T_{0,\,\mathrm{orifice}} = 0\,\mathrm{K}$

(b) $T_0 = 500\,\mathrm{K}$ and $\Delta T_{0,\,\mathrm{orifice}} = 40\,\mathrm{K}$

Figure D.2. Global energy balance over the complete numerical domain obtained with mesh $M_1$ (▪ ▪ ▪) and mesh $M_2$ (○), and its related relative error: $l_{\mathrm{cav}} = 0.0175\,\mathrm{m}$, $T_0 = 500\,\mathrm{K}$ for the case with homogeneous temperature $\Delta T_{0,\,\mathrm{orifice}} = 0\,\mathrm{K}$ (left) and in the presence of a temperature gradient $\Delta T_{0,\,\mathrm{orifice}} = 40\,\mathrm{K}$ (right) — $\mathbb{D}'$ (▭), $\mathbb{W}'$ (▬), and balance (■).

Figure D.3 displays how the choice of order $p$ for the polynomial shape functions impacts the results' accuracy. This is checked on the mesh $M_1$. As expected, taking $p = 1$ delivers very poor results when accounting for no-slip wall boundary conditions, due to the zero first-order derivatives of the shape functions not suitable for the LNSE operator. For higher orders $p$, the relative error on the energy balance is found to decrease with increasing orders $p$. This is predominantly visible at high frequencies. For the low frequency part, the accuracy on the energy balance is limited due to the mesh size and boundary layer resolution on the walls of the facing sheet. It appears that already taking $p = 3$ delivers sufficient accuracy in the results for the present work, due to the highly refined meshes involved.

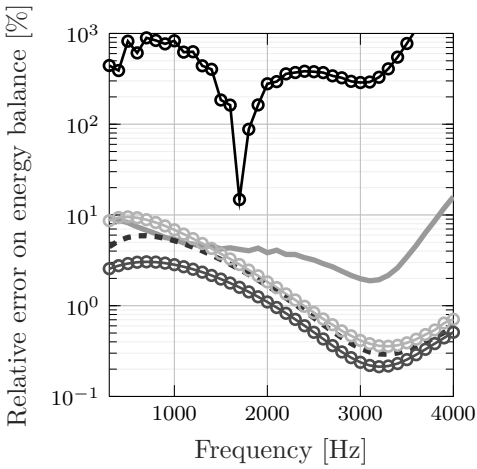


Figure D.3. Effect of shape functions order $p$ on the energy balance, computed over the complete numerical domain on mesh $M_1$ for the case $T_0 = 500\,\mathrm{K}$ and $\Delta T_0 = 0\,\mathrm{K}$: $p = 1$ (—●—), $p = 2$ (——), $p = 3$ (—●—), $p = 4$ (- - -), $p = 5$ (—●—).

Table D.2 reveals that the changes in maximum absorption coefficient $\alpha$ are as well not significant for $p \geq 3$. This observation holds for both cases with and without a temperature gradient.

| $\Delta T_{0,\,\mathrm{orifice}}$ [K] | $p = 1$ | $p = 2$ | $p = 3$ | $p = 4$ |
|---|---|---|---|---|
| 0 | 39.601 | 0.883 | 0.258 | 0.015 |
| 40 | 43.677 | 1.148 | 0.327 | 0.0346 |

Table D.2: Variations $\epsilon_p$ [%] of the absorption coefficient at resonance frequency depending on the polynomial order of the shape functions used $p$, compared to case $p = 5$.

The previous observations ensure the convergence and the good accuracy of the results obtained with the LNS $p$-FEM numerical method for the investigation done on the acoustic behavior of resonator in hot conditions. It guarantees that the trends observed in the parametric study performed in Section 4.2 originate from physical phenomena and not from numeric artifacts.

# Bibliography


[1] Siemens PLM Software LMS Virtual.Lab, 2015. Version 13.5 [software] https://www.plm.automation.siemens.com.

[2] Åbom, M. Measurement of the scattering-matrix of acoustical two-ports. *Mechanical Systems and Signal Processing 5*, 2 (1991), 89–104.

[3] Åbom, M., and Allam, S. On the use of micro-perforates for machinery and vehicle noise control. *The Journal of the Acoustical Society of America 132*, 3 (2012), 1887.

[4] Åbom, M., and Bodén, H. Error analysis of two-microphone measurements in ducts with flow. *The Journal of the Acoustical Society of America 83*, 6 (1988), 2429–2438.

[5] Åbom, M., Sack, S., and Kabral, R. Optimum duct liners and modal filters. *The Journal of the Acoustical Society of America 140*, 4 (2016), 2992.

[6] Agarwal, A., Morris, P. J., and Mani, R. Calculation of sound propagation in nonuniform flows: suppression of instability waves. *AIAA journal 42*, 1 (2004), 80–88.

[7] Ajello, G. Mesures acoustiques dans les guides d'ondes en présence d'écoulement: Mise au point d'un banc de mesure, application à des discontinuités. *Mémoire de Thèse de Doctorat, Université du Maine, soutenue en* (1997).

[8] Alenius, E. *Flow Duct Acoustics: An LES Approach*. PhD thesis, KTH Royal Institute of Technology, 2012.

[9] Alenius, E., Åbom, M., and Fuchs, L. Large eddy simulations of acoustic-flow interaction at an orifice plate. *Journal of Sound and Vibration 345*, Supplement C (2015), 162–177.

[10] Allam, S., and Åbom, M. A new type of muffler based on microperforated tubes. *Journal of Vibration and Acoustics 133*, 3 (2011), 1–8.

[11] Allard, J.-F., and Atalla, N. *Propagation of sound in porous media: modelling sound absorbing materials*. John Wiley & Sons, 2009. Second Edition.

[12] Angeloski, A., Discacciati, M., Legendre, C., Lielens, G., and Huerta, A. Challenges for time and frequency domain aeroacoustic solvers. In *11th World Congress on Computational Mechanics* (2014), pp. 1–12.

[13] Arina, R. Validation of a Discontinuous Galerkin implementation of the time-domain linearized Navier–Stokes equations for aeroacoustics. *Aerospace 3*, 1 (2016), 1–22.

[14] Arnold, D. N. An Interior Penalty Finite Element Method with Discontinuous Elements. *SIAM Journal on Numerical Analysis 19*, 4 (1982), 742–760.

[15] Arnold, D. N., Brezzi, F., Cockburn, B., and Marini, L. D. Unified analysis of Discontinuous Galerkin Methods for elliptic problems. *SIAM Journal on Numerical Analysis 39*, 5 (2002), 1749–1779.

[16] Astley, R., and Eversman, W. The finite element duct eigenvalue problem: An improved formulation with hermitian elements and no-flow condensation. *Journal of Sound and Vibration 69*, 1 (1980), 13–25.

[17] Atalla, N., and Sgard, F. Modeling of perforated plates and screens using rigid frame porous models. *Journal of Sound and Vibration 303*, 1 (2007), 195–208.

[18] Aurégan, Y., Leroux, M., and Pagneux, V. Measurement of liner impedance with flow by an inverse method. In *Proceedings of the 10th AIAA/CEAS Aeroacoustics Conference* (2004), 2004-2838.

[19] Aurégan, Y., and Starobinski, R. Determination of acoustical energy dissipation/production potentiality from the acoustical transfer functions of a multiport. *Acta Acustica united with Acustica 85*, 6 (1999), 788–792.

[20] Aurégan, Y., Starobinski, R., and Pagneux, V. Influence of grazing flow and dissipation effects on the acoustic boundary conditions at a lined wall. *The Journal of the Acoustical Society of America 109*, 1 (2001), 59–64.

[21] Bailly, C., and Juve, D. A stochastic approach to compute subsonic noise using linearized Euler's equations. In *Proceedings of the 5th AIAA/CEAS Aeroacoustics Conference and Exhibit* (1999), 1999-1872.

[22] Bake, F., Richter, C., Mühlbauer, B., Kings, N., Röhle, I., Thiele, F., and Noll, B. The Entropy Wave Generator (EWG): A reference case on entropy noise. *Journal of Sound and Vibration 326*, 3 (2009), 574–598.

[23] Bassi, F., Crivellini, A., Rebay, S., and Savini, M. Discontinuous Galerkin solution of the Reynolds-averaged Navier–Stokes and $k$–$\omega$ turbulence model equations. *Computers & Fluids 34*, 4 (2005), 507–540. Residual Distribution Schemes, Discontinuous Galerkin Schemes and Adaptation.

[24] Bassi, F., and Rebay, S. A high-order accurate Discontinuous Finite Element Method for the numerical solution of the compressible Navier–Stokes equations. *Journal of Computational Physics 131*, 2 (1997), 267–279.

[25] Bassi, F., Rebay, S., Mariotti, G., Pedinotti, S., and Savini, M. A high-order accurate Discontinuous Finite Element Method for inviscid and viscous turbomachinery flows. In *Proceedings of the 2nd European Conference on Turbomachinery Fluid Dynamics and Thermodynamics* (1997), Technologisch Instituut Antwerpen, pp. 99–109.

[26] Batchelor, G. K. *An introduction to fluid dynamics*. Cambridge University Press, 1967.

[27] Bauer, A. B. Impedance theory and measurements on porous acoustic liners. *Journal of Aircraft 14*, 8 (1977), 720–728.

[28] Bauer, M., Dierke, J., and Ewert, R. Application of a Discontinuous Galerkin Method to predict airframe noise. In *Proceedings of the 15th AIAA/CEAS Aeroacoustics Conference* (2009), 2009-3175.

[29] Bécache, E., Bonnet-Ben Dhia, A. S., and Legendre, G. Perfectly matched layers for the convected Helmholtz equation. *SIAM Journal on Numerical Analysis 42*, 1 (2004), 409–433.

[30] Bellucci, V., Flohr, P., Paschereit, C. O., and Magni, F. On the use of Helmholtz resonators for damping acoustic pulsations in industrial gas turbines. *Journal of Engineering for Gas Turbines and Power 126*, 2 (2004), 271–275.

[31] Bériot, H., Gabard, G., and Perrey-Debain, E. Analysis of high-order finite elements for convected wave propagation. *International Journal for Numerical Methods in Engineering 96*, 11 (2013), 665–688.

[32] Bériot, H., Prinn, A., and Gabard, G. Efficient implementation of high-order finite elements for Helmholtz problems. *International Journal for Numerical Methods in Engineering 106*, 3 (2016), 213–240.

[33] Bermúdez, A., Hervella-Nieto, L., Prieto, A., and Rodríguez, R. An optimal perfectly matched layer with unbounded absorbing function for time-harmonic acoustic scattering problems. *Journal of Computational Physics 223*, 2 (2007), 469–488.

[34] Betgen, B., Galland, M.-A., Piot, E., and Simon, F. Implementation and non-intrusive characterization of a hybrid active–passive liner with grazing flow. *Applied Acoustics 73*, 6 (2012), 624–638.

[35] Bodén, H. Experimental investigation of harmonic interaction effects for perforates. In *Proceedings of the 11th AIAA/CEAS Aeroacoustics Conference* (2005), 2005-2896.

[36] Bodén, H. Acoustic characterisation of perforates using non-linear system identification techniques. In *Proceedings of the 13th AIAA/CEAS Aeroacoustics Conference* (2007), 2007-3530.

[37] Bodén, H. Acoustic properties of perforates under high level multitone excitation. In *Proceedings of the 19th AIAA/CEAS Aeroacoustics Conference* (2013), 2013-2175.

[38] Bodén, H., and Åbom, M. Influence of errors on the two-microphone method for measuring acoustic properties in ducts. *The Journal of the Acoustical Society of America 79*, 2 (1986), 541–549.

[39] Bodén, H., and Kabral, R. The effect of high temperatures and grazing flow on the acoustic properties of liners. In *Proceedings of the 10th European Congress and Exposition on Noise Control Engineering* (2015), pp. 2261–2266.

[40] Bodén, H. One-sided multi-port techniques for characterisation of in-duct samples with nonlinear acoustic properties. *Journal of Sound and Vibration 331*, 13 (2012), 3050–3067.

[41] Bogey, C., Bailly, C., and Juvé, D. Computation of flow noise using source terms in linearized Euler's equations. *AIAA journal 40*, 2 (2002), 235–243.

[42] Bossart, R., Joly, N., and Bruneau, M. Hybrid numerical and analytical solutions for acoustic boundary problems in thermo-viscous fluids. *Journal of Sound and Vibration 263*, 1 (2003), 69–84.

[43] Bothien, M. R., and Wassmer, D. Impact of density discontinuities on the resonance frequency of Helmholtz resonators. *AIAA journal 53*, 4 (2015), 877–887.

[44] Boutin, C. Acoustics of porous media with inner resonators. *The Journal of the Acoustical Society of America 134*, 6 (2013), 4717–4729.

[45] Brambley, E. J. Well-posed boundary condition for acoustic liners in straight ducts with flow. *AIAA journal 49*, 6 (2011), 1272–1282.

[46] Bravo, T., Maury, C., and Pinhède, C. Sound absorption and transmission through flexible micro-perforated panels backed by an air layer and a thin plate. *The Journal of the Acoustical Society of America 131*, 5 (2012), 3853–3863.

[47] Bravo, T., Maury, C., and Pinhède, C. Vibroacoustic properties of thin micro-perforated panel absorbers. *The Journal of the Acoustical Society of America 132*, 2 (2012), 789–798.

[48] Bravo, T., Maury, C., and Pinhède, C. Enhancing sound absorption and transmission through flexible multi-layer micro-perforated structures. *The Journal of the Acoustical Society of America 134*, 5 (2013), 3663–3673.

[49] Brezzi, F., Manzini, G., Marini, D., Pietra, P., and Russo, A. Discontinuous Galerkin approximations for elliptic problems. *Numerical Methods for Partial Differential Equations 16*, 4 (2000), 365–378.

[50] Burman, E., Quarteroni, A., and Stamm, B. Stabilization strategies for high order methods for transport dominated problems. *Bollettino della Unione Mate matica Italiana. Serie 9*, 1 (2008), 57–77.

[51] Busse, S., Richter, C., Nitsch, S., Thiele, F., Bake, F., Enghardt, L., Kückens, C., and Müller, U. Acoustic investigation of a specially manufactured non-locally reacting liner for aircraft application. In *Proceedings of the 16th AIAA/CEAS Aeroacoustics Conference* (2010), 2010-3830.

[52] Busse, S., Richter, C., Thiele, F. H., Heuwinkel, C., Enghardt, L., Röhle, I., Michel, U., Ferrante, P., and Scofano, A. Impedance deduction based on insertion loss measurements of liners under grazing flow conditions. In *Proceedings of the 14th AIAA/CEAS Aeroacoustics Conference* (2008), 2008-3014.

[53] Cai, Q., Kollmannsberger, S., Sala-Lardies, E., Huerta, A., and Rank, E. On the natural stabilization of convection dominated problems using high order Bubnov-Galerkin finite elements. *Comput. Math. Appl. 66*, 12 (Jan. 2014), 2545–2558.

[54] Carbajo, J., Ramis, J., Godinho, L., Amado-Mendes, P., and Alba, J. A finite element model of perforated panel absorbers including viscothermal effects. *Applied Acoustics 90*, Supplement C (2015), 1–8.

[55] Carette, J.-C., Deconinck, H., Paillere, H., and Roe, P. Multidimensional upwinding: its relation to finite elements. *International Journal for Numerical Methods in Fluids 20*, 8–9 (1995), 935–955.

[56] Champoux, Y., and Allard, J.-F. Dynamic tortuosity and bulk modulus in air-saturated porous media. *Journal of Applied Physics 70*, 4 (1991), 1975–1979.

[57] Chevaugeon, N., Remacle, J.-F., Gallez, X., Ploumhans, P., and Caro, S. Efficient discontinuous Galerkin methods for solving acoustic problems. In *Proceedings of the 11th AIAA/CEAS Aeroacoustics Conference* (2005), 2005-2823.

[58] Chu, B.-T. On the energy transfer to small disturbances in fluid flow (Part I). *Acta Mechanica 1*, 3 (Sep 1995), 215–234.

[59] Chu, B.-T., and Apfel, R. E. Are acoustic intensity and potential energy density first- or second-order quantities? *American Journal of Physics 51*, 10 (1983), 916–918.

[60] Chu, B.-T., and Kovásznay, L. S. Non-linear interactions in a viscous heat-conducting compressible gas. *Journal of Fluid Mechanics 3*, 05 (1958), 494–514.

[61] Cockburn, B., Kanschat, G., Perugia, I., and Schötzau, D. Superconvergence of the local Discontinuous Galerkin Method for elliptic problems on Cartesian grids. *SIAM Journal on Numerical Analysis 39*, 1 (2001), 264–285.

[62] Cockburn, B., and Shu, C.-W. TVB Runge-Kutta local projection Discontinuous Galerkin Finite Element Method for conservation laws II: General framework. *Mathematics of Computation 52*, 186 (1989), 411–435.

[63] Cockburn, B., and Shu, C.-W. The local Discontinuous Galerkin Method for time-dependent convection-diffusion systems. *SIAM Journal on Numerical Analysis 35*, 6 (1998), 2440–2463.

[64] Cockburn, B., and Shu, C.-W. Runge-Kutta Discontinuous Galerkin Methods for convection-dominated problems. *Journal of Scientific Computing 16*, 3 (Sep 2001), 173–261.

[65] Codina, R. Comparison of some finite element methods for solving the diffusion-convection-reaction equation. *Computer Methods in Applied Mechanics and Engineering 156*, 1-4 (1998), 185–210.

[66] Codina, R. On stabilized finite element methods for linear systems of convection–diffusion-reaction equations. *Computer Methods in Applied Mechanics and Engineering 188*, 1 (2000), 61–82.

[67] Ćosić, B., Wassmer, D., Terhaar, S., and Paschereit, C. Acoustic response of Helmholtz dampers in the presence of hot grazing flow. *Journal of Sound and Vibration 335*, Supplement C (2015), 1–18.

[68] Crandall, I. B. *Theory of vibrating systems and sound*. D. Van Nostrand Company, 1954.

[69] Cummings, A. Acoustic nonlinearities and power losses at orifices. *AIAA journal 22*, 6 (1984), 786–792.

[70] Cummings, A. The effects of grazing turbulent pipe-flow on the impedance of an orifice. *Acta Acustica united with Acustica 61*, 4 (1986), 233–242.

[71] Cummings, A. Transient and multiple frequency sound transmission through perforated plates at high amplitude. *The Journal of the Acoustical Society of America 79*, 4 (1986), 942–951.

[72] Cummings, A., and Eversman, W. High amplitude acoustic transmission through duct terminations: Theory. *Journal of Sound and Vibration 91*, 4 (1983), 503–518.

[73] Dassé, J., Mendez, S., and Nicoud, F. Large-eddy simulation of the acoustic response of a perforated plate. In *Proceedings of the 14th AIAA/CEAS Aeroacoustics Conference* (2008), 2008-3007.

[74] Davies, P. Practical flow duct acoustics. *Journal of Sound and Vibration 124*, 1 (1988), 91–115.

[75] de La Bourdonnaye, A., Farhat, C., Macedo, A., Magoules, F., Roux, F.-X., et al. A non-overlapping Domain Decomposition Method for the exterior Helmholtz problem. *Contemporary Mathematics 218* (1998), 42–66.

[76] De Roeck, W., and Desmet, W. Indirect acoustic impedance determination in flow ducts using a two-port formulation. In *Proceedings of the 15th AIAA/CEAS Aeroacoustics Conference* (2009), 2009-3302.

[77] Dean, P. An in situ method of wall acoustic impedance measurement in flow ducts. *Journal of Sound and Vibration 34*, 1 (1974), 97–130.

[78] Denayer, H., De Roeck, W., and Desmet, W. Iterative procedure for accurate plane wave decomposition in flow ducts. In *Proceedings of the 26th International Conference on Noise and Vibration Engineering* (2014), pp. 279–288.

[79] Denayer, H., De Roeck, W., and Desmet, W. Impedance eduction in the presence of grazing flow based on an analytical multi-port model. In *Proceedings of the 44th International Congress on Noise Control Engineering* (2015), art.nr. 590.

[80] Denayer, H., De Roeck, W., and Desmet, W. Active multi-port characterization of a butterfly valve. In *Proceedings of the International Conference on Noise and Vibration Engineering* (2016), pp. 317–330.

[81] Denayer, H., De Roeck, W., Desmet, W., and Toulorge, T. Acoustic characterization of a Helmholtz resonator under grazing flow conditions using a hybrid methodology. In *Proceedings of the 19th AIAA/CEAS Aeroacoustics Conference* (2013), 2013-2076.

[82] Denayer, H., Gracia, M. M., Desmet, W., Orselli, R. M., and De Roeck, W. Numerical investigation of the acoustic scattering behavior of a butterfly valve. In *Proceeding of the 24th International Congress on Sound and Vibration* (2017), art.nr. 381.

[83] Denayer, H., Korchagin, V., De Roeck, W., and Desmet, W. Multi-port characterization of a modal filter containing micro-perforated panels. In *Proceedings of the 22nd AIAA/CEAS Aeroacoustics Conference* (2016), 2016-2850.

[84] Denayer, H., Tournadre, J., De Roeck, W., Desmet, W., and Martínez-Lera, P. Combined numerical and experimental study of a slit resonator under grazing flow. In *Proceedings of the 20th AIAA/CEAS Aeroacoustics Conference* (2014), 2014-2959.

[85] Dickey, N. S., Selamet, A., and Ciray, M. S. An experimental study of the impedance of perforated plates with grazing flow. *The Journal of the Acoustical Society of America 110*, 5 (2001), 2360–2370.

[86] Didden, N. On the formation of vortex rings: Rolling-up and production of circulation. *Zeitschrift für angewandte Mathematik und Physik ZAMP 30*, 1 (Jan 1979), 101–116.

[87] Disselhorst, J. H. M., and Wijngaarden, L. V. Flow in the exit of open pipes during acoustic resonance. *Journal of Fluid Mechanics 99*, 2 (1980), 293–319.

[88] Dokumaci, E. A note on transmission of sound in a wide pipe with mean flow and viscothermal attenuation. *Journal of Sound and Vibration 208*, 4 (1997), 653–655.

[89] Dokumaci, E. On attenuation of plane sound waves in turbulent mean flow. *Journal of Sound and Vibration 320*, 4 (2009), 1131–1136.

[90] Donea, J., and Huerta, A. *Finite element methods for flow problems.* John Wiley & Sons, Chichester, United-Kingdom, 2003.

[91] Douglas, J., and Dupont, T. *Interior Penalty Procedures for Elliptic and Parabolic Galerkin Methods.* Springer Berlin Heidelberg, Berlin, Heidelberg, 1976, pp. 207–216.

[92] Dowell, E., Gorman, G., and Smith, D. Acoustoelasticity: General theory, acoustic natural modes and forced response to sinusoidal excitation, including comparisons with experiment. *Journal of Sound and Vibration 52*, 4 (1977), 519–542.

[93] Dupère, I. D. J., and Dowling, A. P. The use of Helmholtz resonators in a practical combustor. *Journal of Engineering for Gas Turbines and Power 127*, 2 (2005), 268–275.

[94] Ehrenfried, K., Meyer, C., and Dillmann, A. Simulation of sound propagation in boundary layers based on Möhring's acoustic analogy. In *Proceedings of the 9th AIAA/CEAS Aeroacoustics Conference* (2003), 2003-3272.

[95] Eldredge, J. D., and Dowling, A. P. The absorption of axial acoustic waves by a perforated liner with bias flow. *Journal of Fluid Mechanics 485* (2003), 307–35.

[96] Elnady, T., and Boden, H. On semi-empirical liner impedance modeling with grazing flow. In *Proceedings of the 9th AIAA/CEAS Aeroacoustics Conference* (2003), 2003-3304.

[97] Elnady, T., Bodén, H., and Kontio, T. Impedance of SDOF perforated liners at high temperatures. In *Proceedings of the 10th AIAA/CEAS Aeroacoustics Conference* (2004), 2004-2842.

[98] Elnady, T., Musharrof, M., Bodén, H., and Elhadidi, B. Validation of an inverse analytical technique to educe liner impedance with grazing flow. In *Proceedings of the 12th AIAA/CEAS Aeroacoustics Conference* (2006), 2006-2639.

[99] European Environment Agency. Noise in Europe 2014. In *EEA Report, 10/2014*. 2014.

[100] Ewert, R., Dierke, J., Siebert, J., Neifeld, A., Appel, C., Siefert, M., and Kornow, O. CAA broadband noise prediction for aeroacoustic design. *Journal of Sound and Vibration 330*, 17 (2011), 4139–4160.

[101] Ewert, R., and Schröder, W. Acoustic perturbation equations based on flow decomposition via source filtering. *J. Comput. Phys. 188*, 2 (2003), 365–398.

[102] Falsafi, I., and Ohadi, A. Improving absorption bandwidth of microperforated panel by stepping the cavity. In *Proceedings of the 22nd International Congress on Sound and Vibration* (2015), art.nr. 203.

[103] Farhat, C., Macedo, A., Lesoinne, M., Roux, F.-X., Magoulès, F., and de La Bourdonnaie, A. Two-level domain decomposition methods with Lagrange multipliers for the fast iterative solution of acoustic scattering problems. *Computer Methods in Applied Mechanics and Engineering 184*, 2 (2000), 213–239.

[104] Föller, S., and Polifke, W. Identification of aero-acoustic scattering matrices from large eddy simulation. application to a sudden area expansion of a duct. *Journal of Sound and Vibration 331*, 13 (2012), 3096–3113.

[105] Föller, S., Polifke, W., and Tonon, D. Aeroacoustic characterization of T-junctions based on large eddy simulation and system identification. In *Proceedings of the 16th AIAA/CEAS Aeroacoustics Conference* (2010), 2010-3985.

[106] Förner, K., and Polifke, W. Aero-acoustic characterization of Helmholtz resonators in the linear regime with system identification. In *Proceedings of the 22th International Congress on Sound and Vibration* (2015), art.nr. 596.

[107] Förner, K., and Polifke, W. Nonlinear aeroacoustic characterization of Helmholtz resonators with a local-linear neuro-fuzzy network model. *Journal of Sound and Vibration 407* (2017), 170–190.

[108] Förner, K., Temiz, M. A., Polifke, W., Lopez Arteaga, I., and Hirschberg, A. On the non-linear influence of the edge geometry on vortex shedding in Helmholtz resonators. In *Proceedings of the 22nd International Congress on Sound and Vibration* (2015), art.nr. 1341.

[109] Förner, K., Tournadre, J., Martínez-Lera, P., and Polifke, W. Scattering to higher harmonics for quarter-wave and Helmholtz resonators. *AIAA Journal 55*, 4 (2017), 1194–1204.

[110] Foundation, O. OpenFOAM (Open Field Operation and Manipulation), February 2014. Version 2.3.0 [software].

[111] Gabard, G. Mode-matching techniques for sound propagation in lined ducts with flow. In *Proceedings of the 16th AIAA/CEAS Aeroacoustics Conference* (2010), 2010-3940.

[112] Gabard, G., Bériot, H., Prinn, A., and Kucukcoskun, K. An adaptive, high-order finite element method for aeroengine acoustics. In *Proceedings of the 22nd AIAA/CEAS Aeroacoustics Conference* (2016), 2016-2970.

[113] Geuzaine, C., and Remacle, J.-F. Gmsh: A 3-D finite element mesh generator with built-in pre- and post-processing facilities. *International Journal for Numerical Methods in Engineering 79*, 11 (2009), 1309–1331.

[114] Gikadi, J., Föller, S., and Sattelmayer, T. Impact of turbulence on the prediction of linear aeroacoustic interactions: Acoustic response of a turbulent shear layer. *Journal of Sound and Vibration 333*, 24 (2014), 6548–6559.

[115] Gikadi, J., Schulze, M., Schwing, J., Föller, S., and Sattelmayer, T. Linearized Navier-Stokes and Euler equations for the determination of the acoustic scattering behaviour of an area expansion. In *Proceedings of the 18th AIAA/CEAS Aeroacoustics Conference* (2012), 2012-2292.

[116] Goldman, A. L., and Panton, R. L. Measurement of the acoustic impedance of an orifice under a turbulent boundary layer. *The Journal of the Acoustical Society of America 60*, 6 (1976), 1397–1405.

[117] Golliard, J. *Noise of Helmholtz-resonator like cavities excited by a low Mach-number turbulent flow.* PhD thesis, University of Poitiers, 2002.

[118] Golliard, J., González-Díez, N., Belfroid, S., Nakiboğlu, G., and Hirschberg, A. U-RANS model for the prediction of the acoustic sound power generated in a whistling corrugated pipe. In *Proceedings of the ASME Pressure Vessels and Piping Conference* (2013), PVP2013-97385.

[119] Grace, S., Horan, K., and Howe, M. The influence of shape on the Rayleigh conductivity of a wall aperture in the presence of grazing flow. *Journal of Fluids and Structures 12*, 3 (1998), 335–351.

[120] Gracia, M. M., Vanelderen, B., De Roeck, W., and Desmet, W. Accurate interfacing schemes for the coupling of CFD data with high order DG methods for aeroacoustic propagation. *Proceedings of the 26th Conference on Noise and Vibration Engineering* (2014), 1333–1346.

[121] Groby, J.-P., Lagarrigue, C., Brouard, B., Dazel, O., Tournat, V., and Nennig, B. Enhancing the absorption properties of acoustic porous plates by periodically embedding Helmholtz resonators. *The Journal of the Acoustical Society of America 137*, 1 (2015), 273–280.

[122] Guess, A. Calculation of perforated plate liner parameters from specified acoustic resistance and reactance. *Journal of Sound and Vibration 40*, 1 (1975), 119–137.

[123] Gysling, D. L., Copeland, G. S., McCormick, D. C., and Proscia, W. M. Combustion system damping augmentation with Helmholtz resonators. *Journal of Engineering for Gas Turbines and Power 122*, 2 (1999), 269–274.

[124] Hamiche, K. *A high-order finite element model for acoustic propagation.* PhD thesis, University of Southampton, 2016.

[125] Hamiche, K., Gabard, G., and Bériot, H. A higher-order finite element method for the linearised Euler equations. In *Proceedings of the 26th Conference on Noise and Vibration Engineering* (2014), pp. 1311–1325.

[126] Hamiche, K., Gabard, G., and Bériot, H. Application of a high-order FEM solver to realistic aeroengine exhaust noise radiation. In *Proceeding of the 22nd International Congress on Sound and Vibration* (2015), art.nr. 113.

[127] Hamiche, K., Gabard, G., and Bériot, H. A high-order Finite Element Method for the linearised Euler equations. *Acta Acustica united with Acustica 102*, 5 (2016), 813–823.

[128] Hamilton, J., and Astley, R. Acoustic propagation on irrotational mean flows using time-domain finite and infinite elements. In *Proceedings of the 9th AIAA/CEAS Aeroacoustics Conference* (2003), 2003-3208.

[129] Hamlington, P. E., and Dahm, W. J. A. Reynolds stress closure for nonequilibrium effects in turbulent flows. *Physics of Fluids 20*, 11 (2008), 1–18.

[130] Harari, I. A survey of finite element methods for time-harmonic acoustics. *Computer Methods in Applied Mechanics and Engineering 195*, 13 (2006), 1594–1607. A Tribute to Thomas J.R. Hughes on the Occasion of his 60th Birthday.

[131] Hersch, A., and Walker, B. Effect of grazing flow on the acoustic impedance of Helmholtz resonators consisting of single and clustered orifices. *The Journal of the Acoustical Society of America 72*, 2 (1982), 642–642.

[132] Hersh, A., Walker, B., and Celano, J. Semi-empirical Helmholtz resonator impedance model. In *Proceedings of the 5th AIAA/CEAS Aeroacoustics Conference and Exhibit* (1999), 1999-1825.

[133] Hersh, A., Walker, B., and Celano, J. Helmholtz resonator impedance model, part 1: Nonlinear behavior. *AIAA journal 41*, 5 (2003), 795–808.

[134] Hersh, A. S., and Rogers, T. Fluid mechanical model of the acoustic impedance of small orifices. Tech. Rep. CR-2682, NASA, 1976.

[135] Hersh, A. S., and Walker, B. Fluid mechanical model of the Helmholtz resonator. Tech. Rep. CR-2904, NASA, 1977.

[136] Hesthaven, J. From electrostatics to almost optimal nodal sets for polynomial interpolation in a simplex. *SIAM J. Numer. Anal 35* (1998), 655–676.

[137] Hesthaven, J. S., and Teng, C. H. Stable spectral methods on tetrahedral elements. *SIAM Journal on Scientific Computing 21*, 6 (2000), 2352–2380.

[138] Hesthaven, J. S., and Warburton, T. Nodal high-order methods on unstructured grids. *J. Comput. Phys. 181*, 1 (2002), 186–221.

[139] Hesthaven, J. S., and Warburton, T. *Nodal Discontinuous Galerkin Methods: Algorithms, Analysis, and Applications*, vol. 54 of *Texts in Applied Mathematics*. Springer New York, 2008.

[140] Higdon, R. L. Initial-boundary value problems for linear hyperbolic system. *SIAM Review 28*, 2 (1986), 177–217.

[141] Holmberg, A., Karlsson, M., and Åbom, M. Aeroacoustics of rectangular T-junctions subject to combined grazing and bias flows – An experimental investigation. *Journal of Sound and Vibration 340* (2015), 152–166.

[142] Holmberg, A., Kierkegaard, A., and Weng, C. A frequency domain linearized Navier–Stokes method including acoustic damping by eddy viscosity using RANS. *Journal of Sound and Vibration 346* (2015), 229–247.

[143] Hou, K., and Bolton, J. S. Finite element models for micro-perforated panels. In *Proceedings of the 38th International Congress on Noise Control Engineering* (2009), art.nr. 4, pp. 2420–2428.

[144] Howe, M. Influence of wall thickness on Rayleigh conductivity and flow-induced aperture tones. *Journal of Fluids and Structures 11*, 4 (1997), 351–366.

[145] Howe, M. S. Contributions to the theory of aerodynamic sound, with application to excess jet noise and the theory of the flute. *Journal of Fluid Mechanics 71*, 4 (1975), 625–673.

[146] Howe, M. S. On the theory of unsteady high Reynolds number flow through a circular aperture. *Proceedings of the Royal Society of London A: Mathematical, Physical and Engineering Sciences 366*, 1725 (1979), 205–223.

[147] Howe, M. S. On the absorption of sound by turbulence and other hydrodynamic flows. *IMA Journal of Applied Mathematics 32*, 1–3 (1984), 187–209.

[148] Howe, M. S. Edge, cavity and aperture tones at very low mach numbers. *Journal of Fluid Mechanics 330* (1997), 61–84.

[149] Howe, M. S. Low strouhal number instabilities of flow over apertures and wall cavities. *The Journal of the Acoustical Society of America 102*, 2 (1997), 772–780.

[150] Howe, M. S. *Theory of vortex sound*, vol. 33. Cambridge texts in Applied Mathematics, Cambridge University Press, 2003.

[151] Howe, M. S., Scott, M. I., and Sipcic, S. R. The influence of tangential mean flow on the Rayleigh conductivity of an aperture. *Proceedings of the Royal Society of London A: Mathematical, Physical and Engineering Sciences 452*, 1953 (1996), 2303–2317.

[152] Hu, F. Q. On absorbing boundary conditions for Linearized Euler Equations by a Perfectly Matched Layer. *Journal of Computational Physics 129*, 1 (1996), 201–219.

[153] Hu, F. Q. A Perfectly Matched Layer absorbing boundary condition for linearized Euler equations with a non-uniform mean flow. *Journal of Computational Physics 208*, 2 (2005), 469–492.

[154] Hughes, T. J. R., Franca, L. P., and Hulbert, G. M. A new finite element formulation for computational fluid dynamics: VIII. the Galerkin/Least-Squares method for advective-diffusive equations. *Computer Methods in Applied Mechanics and Engineering 73*, 2 (1989), 173–189.

[155] Hughes, T. J. R., and Mallet, M. A new finite element formulation for computational fluid dynamics: III. the generalized streamline operator for multidimensional advective-diffusive systems. *Computer Methods in Applied Mechanics and Engineering 58*, 3 (1986), 305–328.

[156] Hunt, J., Wray, A., and Moin, P. Eddies, stream, and convergence zones in turbulent flows. Report CTR-S88. *Center for Turbulence Research, Stanford University, USA* (1988), 193–208.

[157] Ingård, U. On the theory and design of acoustic resonators. *The Journal of the Acoustical Society of America 25*, 6 (1953), 1037–1061.

[158] Ingård, U. Nonlinear distortion of sound transmitted through an orifice. *The Journal of the Acoustical Society of America 48*, 1A (1970), 32–33.

[159] Ingård, U., and Ising, H. Acoustic nonlinearity of an orifice. *The Journal of the Acoustical Society of America 42*, 1 (1967), 6–17.

[160] Ingård, U., and Labate, S. Acoustic circulation effects and the nonlinear impedance of orifices. *The Journal of the Acoustical Society of America 22*, 2 (1950), 211–218.

[161] Iob, A., Arina, R., and Schipani, C. Frequency-domain linearized Euler model for turbomachinery noise radiation through engine exhaust. *AIAA journal 48*, 4 (2010), 848–858.

[162] Ji, C., and Zhao, D. Lattice boltzmann investigation of acoustic damping mechanism and performance of an in-duct circular orifice. *The Journal of the Acoustical Society of America 135*, 6 (2014), 3243–3251.

[163] Jing, X., Peng, S., and Sun, X. A straightforward method for wall impedance eduction in a flow duct. *The Journal of the Acoustical Society of America 124*, 1 (2008), 227–234.

[164] Jing, X., and Sun, X. Experimental investigations of perforated liners with bias flow. *The Journal of the Acoustical Society of America 106*, 5 (1999), 2436–2441.

[165] Jing, X., and Sun, X. Sound-excited flow and acoustic nonlinearity at an orifice. *Physics of Fluids 14*, 1 (2002), 268–276.

[166] Jing, X., Sun, X., Wu, J., and Meng, K. Effect of grazing flow on the acoustic impedance of an orifice. *AIAA journal 39*, 8 (2001).

[167] Johnson, D. L., Koplik, J., and Dashen, R. Theory of dynamic permeability and tortuosity in fluid-saturated porous media. *Journal of Fluid Mechanics 176* (1987), 379–402.

[168] Kabral, R., Du, L., Åbom, M., and Knutsson, M. A compact silencer for the control of compressor noise. *SAE Int. J. Engines 7* (06 2014), 1572–1578.

[169] Kampinga, W. R., Wijnant, Y. H., and de Boer, A. Performance of several viscothermal acoustic finite elements. *Acta Acustica united with Acustica 96*, 1 (2010), 115–124.

[170] Kang, J., and Brocklesby, M. Feasibility of applying micro-perforated absorbers in acoustic window systems. *Applied Acoustics 66*, 6 (2005), 669–689.

[171] Kang, J., and Fuchs, H. Predicting the absorption of open weave textiles and micro-perforated membranes backed by an air space. *Journal of Sound and Vibration 220*, 5 (1999), 905–920.

[172] Karlsson, M., and Åbom, M. Aeroacoustics of T-junctions — An experimental investigation. *Journal of Sound and Vibration 329*, 10 (2010), 1793–1808.

[173] Karlsson, M., and Åbom, M. On the use of linear acoustic multiports to predict whistling in confined flows. *Acta Acustica united with Acustica 97*, 1 (2011), 24–33.

[174] Keller, J. J., and Zauner, E. On the use of Helmholtz resonators as sound attenuators. *Zeitschrift für angewandte Mathematik und Physik ZAMP 46*, 3 (May 1995), 297–327.

[175] Kierkegaard, A., Allam, S., Efraimsson, G., and Åbom, M. Simulations of whistling and the whistling potentiality of an in-duct orifice with linear aeroacoustics. *Journal of Sound and Vibration 331*, 5 (2012), 1084–1096.

[176] Kierkegaard, A., Boij, S., and Efraimsson, G. A frequency domain linearized Navier–Stokes equations approach to acoustic propagation in flow ducts with sharp edges. *The Journal of the Acoustical Society of America 127*, 2 (2010), 710–719.

[177] Kierkegaard, A., Boij, S., and Efraimsson, G. Simulations of the scattering of sound waves at a sudden area expansion. *Journal of Sound and Vibration 331*, 5 (2012), 1068–1083.

[178] Kirby, R., and Cummings, A. The impedance of perforated plates subjected to grazing gas flow and backed by porous media. *Journal of Sound and Vibration 217*, 4 (1998), 619–636.

[179] Kirchhoff, G. Über das Gleichgewicht und die Bewegung einer elastischen Scheibe. *Journal für die reine und angewandte Mathematik 40* (1850), 51–88.

[180] Kirchhoff, G. Über den Einfluss der Wärmeleitung in einem Gase auf die Schallbewegung. *Annalen der Physik 210*, 6 (1868), 177–193.

[181] Kooi, J., and Sarin, S. An experimental study of the acoustic impedance of Helmholtz resonator arrays under a turbulent boundary layer. In *AIAA, Astrodynamics Specialist Conference* (1981).

[182] Kooijman, G., Hirschberg, A., and Golliard, J. Acoustical response of orifices under grazing flow: Effect of boundary layer profile and edge geometry. *Journal of Sound and Vibration 315*, 4 (2008), 849–874.

[183] Kovasznay, L. S. G. Turbulence in supersonic flow. *Journal of the Aeronautical Sciences 20*, 10 (1953), 657–674.

[184] Lacombe, R., Föller, S., Jasor, G., Polifke, W., Aurégan, Y., and Moussou, P. Identification of aero-acoustic scattering matrices from large eddy simulation: Application to whistling orifices in duct. *Journal of Sound and Vibration 332*, 20 (2013), 5059–5067.

[185] Lacombe, R., Moussou, P., and Aurégan, Y. Identification of whistling ability of a single hole orifice from an incompressible flow simulation. In *Proceedings of the ASME Pressure Vessels and Piping Conference* (2011), PVP2011-57355, pp. 261–267.

[186] Lahiri, C., and Bake, F. A review of bias flow liners for acoustic damping in gas turbine combustors. *Journal of Sound and Vibration 400*, Supplement C (2017), 564–605.

[187] Lahiri, C., Knobloch, K., Bake, F., and Enghardt, L. Acoustic measurements of perforated liners in hot and pressurized flow. In *Proceedings of ASME Turbo Expo* (2013), GT2013-94674, pp. 1–12.

[188] Laudien, E., Pongratz, R., Pierro, R., and Preclik, D. Experimental procedures aiding the design of acoustic cavities. *Progress in Astronautics and Aeronautics 169* (1995), 377–402.

[189] Lavrentjev, J., Åbom, M., and Bodén, H. A measurement method for determining the source data of acoustic two-port sources. *Journal of Sound and Vibration 183*, 3 (1995), 517–531.

[190] Lee, J., and Swenson, G. W. Compact sound absorbers for low frequencies. *Noise Control Engineering Journal 38*, 5 (1992), 109–117.

[191] Lee, S.-H., and Ih, J.-G. Empirical model of the acoustic impedance of a circular orifice in grazing mean flow. *The Journal of the Acoustical Society of America 114*, 1 (2003), 98–113.

[192] Lee, Y., and Lee, E. Widening the sound absorption bandwidths of flexible micro-perforated curved absorbers using structural and acoustic resonances. *International Journal of Mechanical Sciences 49*, 8 (2007), 925–934.

[193] Lee, Y., Lee, E., and Ng, C. Sound absorption of a finite flexible micro-perforated panel backed by an air cavity. *Journal of Sound and Vibration 287*, 1 (2005), 227–243.

[194] Leung, R., So, R., Wang, M., and Li, X. In-duct orifice and its effect on sound absorption. *Journal of Sound and Vibration 299*, 4 (2007), 990–1004.

[195] Li, C., Cazzolato, B., and Zander, A. Acoustic impedance of micro perforated membranes: Velocity continuity condition at the perforation boundary. *The Journal of the Acoustical Society of America 139*, 1 (2016), 93–103.

[196] Li, D., Chang, D., Liu, B., and Tian, J. Improving sound absorption bandwidth of micro-perforated panel by adding porous materials. In *Proceedings of the 43rd International Congress on Noise Control Engineering* (2014), art.nr. 249, pp. 1877–1882.

[197] Li, Y., Wang, X., and Zhang, D. Control strategies for aircraft airframe noise reduction. *Chinese Journal of Aeronautics 26*, 2 (2013), 249–260.

[198] Lieuwen, T. C. *Unsteady combustor physics*. Cambridge University Press, 2012.

[199] Lighthill, J., and Lighthill, M. *Waves in fluids*. Cambridge university press, 2001.

[200] Lighthill, M. J. On sound generated aerodynamically. I. general theory. In *Proceedings of the Royal Society of London A: Mathematical, Physical and Engineering Sciences* (1952), vol. 211, The Royal Society, pp. 564–587.

[201] Lighthill, M. J. On sound generated aerodynamically. II. turbulence as a source of sound. In *Proceedings of the Royal Society of London A: Mathematical, Physical and Engineering Sciences* (1954), vol. 222, The Royal Society, pp. 1–32.

[202] Lilley, G. M., Plumblee, H. E., Strahle, W. C., Ruo, S.-Y., and Doak, P. E. The generation and radiation of supersonic jet noise. Volume IV. theory of turbulence generated jet noise, noise radiation from upstream sources, and combustion noise. Tech. rep., DTIC Document, 1972.

[203] Liu, J., and Herrin, D. Enhancing micro-perforated panel attenuation by partitioning the adjoining cavity. *Applied Acoustics 71*, 2 (2010), 120–127.

[204] Liu, L., Li, X., and Hu, F. Q. Nonuniform time-step Runge-Kutta Discontinuous Galerkin Method for computational aeroacoustics. *J. Comput. Phys. 229*, 19 (Sept. 2010), 6874–6897.

[205] Lörstad, D., Pettersson, J., and Lindholm, A. Emission reduction and cooling improvements due to the introduction of passive acoustic damping in an existing SGT-800 combustor. In *Proceedings of the ASME Turbo Expo* (2009), GT2009-59313, pp. 1355–1362.

[206] Lung, T. Y., and Doige, A. G. A time-averaging transient testing method for acoustic properties of piping systems and mufflers with flow. *The Journal of the Acoustical Society of America 73*, 3 (1983), 867–876.

[207] Luong, T., Howe, M., and McGowan, R. On the Rayleigh conductivity of a bias-flow aperture. *Journal of Fluids and Structures 21*, 8 (2005), 769–778.

[208] Maa, D.-Y. Theory and design of microperforated panel sound-absorbing constructions. *SCIENCE CHINA Mathematics 18*, 1 (1975), 55–71.

[209] Maa, D.-Y. Microperforated panel wide-band absorber. *Noise Control Engineering Journal 29*, 3 (1987), 77–84.

[210] Maa, D.-Y. Potential of microperforated panel absorber. *The Journal of the Acoustical Society of America 104*, 5 (1998), 2861–2866.

[211] Magoulès, F., Meerbergen, K., and Coyette, J.-P. Application of a domain decomposition method with Lagrange multipliers to acoustic problems arising from the automotive industry. *Journal of Computational Acoustics 08*, 03 (2000), 503–521.

[212] Mankbadi, R. R., and Liu, J. T. C. Near-wall response in turbulent shear flows subjected to imposed unsteadiness. *Journal of Fluid Mechanics 238* (1992), 55–71.

[213] Marié, S., Ricot, D., and Sagaut, P. Comparison between lattice Boltzmann method and Navier–Stokes high order schemes for computational aeroacoustics. *Journal of Computational Physics 228*, 4 (2009), 1056–1070.

[214] Martínez-Lera, P., Schram, C., Föller, S., Kaess, R., and Polifke, W. Identification of the aeroacoustic response of a low Mach number flow through a T-joint. *The Journal of the Acoustical Society of America 126*, 2 (2009), 582–586.

[215] Melling, T. The acoustic impendance of perforates at medium and high sound pressure levels. *Journal of Sound and Vibration 29*, 1 (1973), 1–65.

[216] Mendez, S., and Eldredge, J. Acoustic modeling of perforated plates with bias flow for Large-Eddy Simulations. *Journal of Computational Physics 228*, 13 (2009), 4757–4772.

[217] Minisini, S., Zhebel, E., Kononov, A., and Mulder, W. A. Local time stepping with the discontinuous Galerkin method for wave propagation in 3D heterogeneous media. *GEOPHYSICS 78*, 3 (2013), T67–T77.

[218] Möhring, W., Müller, E.-A., and Obermeier, F. Problems in flow acoustics. *Rev. Mod. Phys. 55* (1983), 707–724.

[219] Morse, P. M., and Ingård, U. *Theoretical acoustics.* New York : McGraw-Hill, 1968. Bibliography: p. 886-887.

[220] Munjal, M. L. *Acoustics of ducts and mufflers with application to exhaust and ventilation system design.* John Wiley & Sons, 1987.

[221] Myers, M. On the acoustic boundary condition in the presence of flow. *Journal of Sound and Vibration 71*, 3 (1980), 429–434.

[222] Myers, M. K. Transport of energy by disturbances in arbitrary steady flows. *Journal of Fluid Mechanics 226* (1991), 383–400.

[223] Na, W., Boij, S., and Efraimsson, G. Acoustic characterization of a hybrid liner consisting of porous material by using a unified linearized Navier-Stokes approach. In *Proceedings of the 22nd AIAA/CEAS Aeroacoustics Conference* (2016), 2016-1101.

[224] Nakiboğlu, G., Belfroid, S. P. C., Golliard, J., and Hirschberg, A. On the whistling of corrugated pipes: effect of pipe length and flow profile. *Journal of Fluid Mechanics 672* (2011), 78–108.

[225] Okuzono, T., and Sakagami, K. A finite-element formulation for room acoustics simulation with microperforated panel sound absorbing structures: Verification with electro-acoustical equivalent circuit theory and wave theory. *Applied Acoustics 95*, Supplement C (2015), 20–26.

[226] Park, S.-H. A design method of micro-perforated panel absorber at high sound pressure environment in launcher fairings. *Journal of Sound and Vibration 332*, 3 (2013), 521–535.

[227] Peat, K. S., Ih, J.-G., and Lee, S.-H. The acoustic impedance of a circular orifice in grazing mean flow: Comparison with theory. *The Journal of the Acoustical Society of America 114*, 6 (2003), 3076–3086.

[228] Peters, M., and Hirschberg, A. Acoustically induced periodic vortex shedding at sharp edged open channel ends: Simple vortex models. *Journal of Sound and Vibration 161*, 2 (1993), 281–299.

[229] Pierce, A. D. *Acoustics: An Introduction to Its Physical Principles and Applications*, 2 ed. In [230], 1989, ch. 7, pp. 110–113.

[230] Pierce, A. D. *Acoustics: An Introduction to Its Physical Principles and Applications*, 2 ed. McGraw-Hill, New York, 1989.

[231] Pierce, A. D. *Acoustics: An Introduction to Its Physical Principles and Applications*, 2 ed. In [230], 1989, ch. 7, pp. 339–341.

[232] Poinsot, T., and Lele, S. Boundary conditions for direct simulations of compressible viscous flows. *Journal of Computational Physics 101*, 1 (1992), 104–129.

[233] Polifke, W. System identification for aero- and thermo-acoustic applications. In *VKI Lecture Series* (2010), von Karman Institute for Fluid Dynamics, Brussels.

[234] Polifke, W., and Gentemann, A. Order and realizability of impulse response filters for accurate identification of acoustic multi-ports from transient CFD. *International Journal of Acoustics and Vibration 9*, 3 (2004), 139–148.

[235] Pope, S. B. A more general effective-viscosity hypothesis. *Journal of Fluid Mechanics 72*, 2 (1975), 331–340.

[236] Powell, A. Theory of vortex sound. *The Journal of the Acoustical Society of America 36*, 1 (1964), 177–195.

[237] Quarteroni, A. *Numerical models for differential problems*, vol. 2. Springer Science & Business Media, 2010.

[238] Rademaker, E. R., van der Wal, H. M., and Geurts, E. G. Hot-stream in-situ acoustic impedance measurements on various air-filled cavity and porous liners. Tech. Rep. NLR-TP-2009-142, National Aerospace Laboratory NLR, 2009.

[239] Rao, P. P., and Morris, P. J. Use of finite element methods in frequency domain aeroacoustics. *AIAA journal 44*, 7 (2006), 1643–1652.

[240] Rayleigh, J. W. S. *Theory of Sound*, vol. 2. Dover, 1945. revised ed.

[241] Renou, Y., and Aurégan, Y. Failure of the Ingard–Myers boundary condition for a lined duct: An experimental investigation. *The Journal of the Acoustical Society of America 130*, 1 (2011), 52–60.

[242] Reymen, Y. *3D High-order Discontinuous Galerkin Methods for time-domain simulation of flow noise propagation.* PhD thesis, KU Leuven, 2008.

[243] Reynolds, W. C., and Hussain, A. K. M. F. The mechanics of an organized wave in turbulent shear flow. Part 3. Theoretical models and comparisons with experiments. *Journal of Fluid Mechanics 54*, 2 (1972), 263–288.

[244] Rice, E. J. Theoretical study of the acoustic impedance of orifices in the presence of a steady grazing flow. *The Journal of the Acoustical Society of America 59*, S1 (1976), 1–23.

[245] Rienstra, S. 1-D reflection at an impedance wall. *Journal of Sound and Vibration 125*, 1 (1988), 43–51.

[246] Rienstra, S. W., and Hirschberg, A. *An introduction to acoustics*, vol. 18. 2004. https://www.win.tue.nl/ sjoerdr/papers/boek.pdf.

[247] Rivière, B., Wheeler, M. F., and Girault, V. Improved energy estimates for interior penalty, constrained and discontinuous Galerkin methods for elliptic problems. Part I. *Computational Geosciences 3*, 3 (1999), 337–360.

[248] Roche, J.-M., Leylekian, L., and Vuillot, F. Acoustic and aerodynamic dissipations induced by a sound wave-impacted Helmholtz resonator. *The Journal of the Acoustical Society of America 123*, 5 (2008), 3250–3250.

[249] Roche, J.-M., Vuillot, F., Leylekian, L., Delattre, G., Simon, F., and Piot, E. Numerical and experimental study of resonant liners aeroacoustic absorption under grazing flow. In *Proceedings of the 16th AIAA/CEAS Aeroacoustics Conference* (2010), 2010-3767.

[250] Rolls-Royce Ltd. *The Jet Engine*, 5th ed. Derby, U.K., 1996.

[251] Ronneberger, D. The acoustical impedance of holes in the wall of flow ducts. *Journal of Sound and Vibration 24*, 1 (1972), 133–150.

[252] Ruiz, H., Claeys, C., Deckers, E., and Desmet, W. Numerical and experimental study of the effect of microslits on the normal absorption of structural metamaterials. *Mechanical Systems and Signal Processing 70*, Supplement C (2016), 904–918.

[253] Rupp, J., Carrotte, J., and Spencer, A. Interaction between the acoustic pressure fluctuations and the unsteady flow field through circular holes. *Journal of Engineering for Gas Turbines and Power 132*, 6 (2010), 1–9.

[254] Rzhevkin, S. N. *A course of lectures on the theory of sound*. Pergamon Press;[distributed in the Western Hemisphere by Macmillan, New York], 1963.

[255] Sack, S., and Åbom, M. Investigation of orifice aeroacoustics by means of multi-port methods. *Journal of Sound and Vibration 407* (2017), 32–45.

[256] Sack, S., Åbom, M., and Efraimsson. On acoustic multi-port characterisation including higher order modes. *Acta Acustica united with Acustica 102*, 5 (2016), 834–850.

[257] Sakagami, K., Matsutani, K., and Morimoto, M. Sound absorption of a double-leaf micro-perforated panel with an air-back cavity and a rigid-back wall: Detailed analysis with a Helmholtz–Kirchhoff integral formulation. *Applied Acoustics 71*, 5 (2010), 411–417.

[258] Sakagami, K., Nagayama, Y., Morimoto, M., and Yairi, M. Pilot study on wideband sound absorber obtained by combination of two different microperforated panel (MPP) absorbers. *Acoustical Science and Technology 30*, 2 (2009), 154–156.

[259] Sakagami, K., Takahashi, D., Gen, H., and Morimoto, M. Acoustic properties of an infinite elastic plate with a back cavity. *Acta Acustica united with Acustica 78*, 5 (1993), 288–295.

[260] Salikuddin, M., and Ahuja, K. Acoustic power dissipation on radiation through duct terminations: Experiments. *Journal of Sound and Vibration 91*, 4 (1983), 479–502.

[261] Santana, L. D., De Roeck, W., and Desmet, W. Indirect acoustic impedance eduction in presence of flow based on an analytical two-port formulation. *Mechanical Systems and Signal Processing 48*, 1 (2014), 388–403.

[262] Scarpato, A., Ducruix, S., and Schuller, T. A LES based sound absorption analysis of high-amplitude waves through an orifice with bias flow. In *Proceedings of ASME Turbo Expo* (2011), GT2011-4563, pp. 613–622.

[263] Schuster, B. A comparison of ensemble averaging methods using Dean's method for in-situ impedance measurements. In *Proceedings of the 18th AIAA/CEAS Aeroacoustics Conference* (2012), 2012-2244.

[264] Science Communication Unit, University of the West of England (UWE), Bristol. Science for environment policy - thematic issue: Noise impacts on health. In *European Commission, Directorate-General for the Environment, Issue 47*. January 2015.

[265] Scofano, A., Murray, P. B., and Ferrante, P. Back-calculation of liner impedance using duct insertion loss measurements and FEM predictions. In *Proceedings of the 13th AIAA/CEAS Aeroacoustics Conference* (2007), 2007-3534.

[266] Selamet, A., Xu, M. B., Lee, I.-J., and Huff, N. T. Helmholtz resonator lined with absorbing material. *The Journal of the Acoustical Society of America 117*, 2 (2005), 725–733.

[267] Sijtsma, P., and van der Wal, H. Modelling a spiralling type of non-locally reacting liner. In *Proceedings of the 9th AIAA/CEAS Aeroacoustics Conference* (2003), 2003-3308.

[268] Sivian, L. J. Acoustic impedance of small orifices. *The Journal of the Acoustical Society of America 7*, 2 (1935), 94–101.

[269] Sohn, C. H., and Park, J. H. A comparative study on acoustic damping induced by half-wave, quarter-wave, and Helmholtz resonators. *Aerospace Science and Technology 15*, 8 (2011), 606–614.

[270] Sovardi, C., Jaensch, S., and Polifke, W. Concurrent identification of aero-acoustic scattering and noise sources at a flow duct singularity in low Mach number flow. *Journal of Sound and Vibration 377* (2016), 90–105.

[271] Stinson, M. R. The propagation of plane sound waves in narrow and wide circular tubes, and generalization to uniform tubes of arbitrary cross-sectional shape. *The Journal of the Acoustical Society of America 89*, 2 (1991), 550–558.

[272] Sun, X., Jing, X., Zhang, H., and Shi, Y. Effect of grazing–bias flow interaction on acoustic impedance of perforated plates. *Journal of Sound and Vibration 254*, 3 (2002), 557–573.

[273] Suzuki, T., and Lele, S. K. Green's functions in a boundary layer: Low and high frequency asymptotes. In *Proceedings of the 6th AIAA/CEAS Aeroacoustics Conference, Hawaii* (2000), 2000-2071.

[274] Suzuki, T., and Lele, S. K. Green's functions for a source in a boundary layer: direct waves, channelled waves and diffracted waves. *Journal of Fluid Mechanics 477* (2003), 129–173.

[275] Takahashi, D. A new method for predicting the sound absorption of perforated absorber systems. *Applied Acoustics 51*, 1 (1997), 71–84.

[276] Takahashi, D., and Tanaka, M. Flexural vibration of perforated plates and porous elastic materials under acoustic loading. *The Journal of the Acoustical Society of America 112*, 4 (2002), 1456–1464.

[277] Tam, C., Ju, H., Jones, M., Watson, W., and Parrott, T. A computational and experimental study of slit resonators. *Journal of Sound and Vibration 284*, 3 (2005), 947–984.

[278] Tam, C. K., Ju, H., and Walker, B. E. Numerical simulation of a slit resonator in a grazing flow under acoustic excitation. *Journal of Sound and Vibration 313*, 3 (2008), 449–471.

[279] Tam, C. K., and Kurbatskii, K. A. Microfluid dynamics and acoustics of resonant liners. *AIAA journal 38*, 8 (2000), 1331–1339.

[280] Tam, C. K. W. Computational aeroacoustics: An overview of computational challenges and applications. *International Journal of Computational Fluid Dynamics 18*, 6 (2004), 547–567.

[281] Tam, C. K. W., Ju, H., Jones, M., Watson, W., and Parrott, T. A computational and experimental study of resonators in three dimensions. *Journal of Sound and Vibration 329*, 24 (2010), 5164–5193.

[282] Tam, C. K. W., Kurbatskii, K. A., Ahuja, K., and Gaeta, R. A numerical and experimental investigation of the dissipation mechanisms of resonant acoustic liners. *Journal of Sound and Vibration 245*, 3 (2001), 545–557.

[283] Tang, S. K. On sound transmission loss across a Helmholtz resonator in a low Mach number flow duct. *The Journal of the Acoustical Society of America 127*, 6 (2010), 3519–3525.

[284] Tayong, R., Dupont, T., and Leclaire, P. Experimental investigation of holes interaction effect on the sound absorption coefficient of micro-perforated panels under high and medium sound levels. *Applied Acoustics 72*, 10 (2011), 777–784.

[285] Temiz, M. A. *Passive noise control by means of micro-perforated plates: developing tools for an optimal design.* PhD thesis, Eindhoven University of Technology, 2017.

[286] Temiz, M. A., Lopez Arteaga, I., Efraimsson, G., Åbom, M., and Hirschberg, A. The influence of edge geometry on end-correction coefficients in micro perforated plates. *The Journal of the Acoustical Society of America 138*, 6 (2015), 3668–3677.

[287] Temiz, M. A., Tournadre, J., Lopez Arteaga, I., and Hirschberg, A. Non-linear acoustic transfer impedance of micro-perforated plates with circular orifices. *Journal of Sound and Vibration 366* (2016), 418–428.

[288] Temiz, M. A., Tournadre, J., Lopez Arteaga, I., and Hirschberg, A. Modelling vibro-acoustic coupling in flexible micro-perforated plates by a patch-impedance approach. *Applied Acoustics 125* (2017), 80–90.

[289] Temiz, M. A., Tournadre, J., Lopez Arteaga, I., Martínez-Lera, P., and Hirschberg, A. Effect of orifice geometry on the non-linear acoustic resistance of perforated plates in the transition regime. In *Proceedings of the 22nd International Congress on Sound and Vibration* (2015), art.nr. 1014.

[290] Testud, P., Aurégan, Y., Moussou, P., and Hirschberg, A. The whistling potentiality of an orifice in a confined flow using an energetic criterion. *Journal of Sound and Vibration 325*, 4 (2009), 769–780.

[291] Tijdeman, H. On the propagation of sound waves in cylindrical tubes. *Journal of Sound and Vibration 39*, 1 (1975), 1–33.

[292] Tonon, D., Moers, E., and Hirschberg, A. Quasi-steady acoustic response of wall perforations subject to a grazing-bias flow combination. *Journal of Sound and Vibration 332*, 7 (2013), 1654–1673.

[293] Toulorge, T. *Efficient Runge-Kutta discontinuous Galerkin methods applied to aeroacoustics.* PhD thesis, KU Leuven, 2012.

[294] Toulorge, T., De Roeck, W., Denayer, H., and Desmet, W. Computational aeroacoustic characterization of different orifice geometries under grazing flow conditions. In *Proceedings of the 25th Conference on Noise and Vibration Engineering* (2012), pp. 617–631.

[295] Toulorge, T., and Desmet, W. Optimal Runge–Kutta schemes for discontinuous Galerkin space discretizations applied to wave propagation problems. *Journal of Computational Physics 231*, 4 (2012), 2067–2091.

[296] Tournadre, J., Desmet, W., and Martínez-Lera, P. Evaluation of temperature effects on passive acoustic dampers with a frequency-domain linearized Navier-Stokes equations solver. In *Proceedings of the 23rd International Congress on Sound and Vibration* (2016), art.nr. 857.

[297] Tournadre, J., Förner, K., Polifke, W., Martínez-Lera, P., and Desmet, W. Determination of acoustic impedance for Helmholtz resonators through incompressible unsteady flow simulations. *AIAA Journal 55*, 3 (2017), 790–798.

[298] Toyoda, M., Mu, R. L., and Takahashi, D. Relationship between Helmholtz-resonance absorption and panel-type absorption in finite flexible microperforated-panel absorbers. *Applied Acoustics 71*, 4 (2010), 315–320.

[299] Trahan, C. J., and Dawson, C. Local time-stepping in Runge–Kutta discontinuous Galerkin finite element methods applied to the shallow-water equations. *Computer Methods in Applied Mechanics and Engineering 217d* (2012), 139–152.

[300] Tritton, D. J. *Physical fluid dynamics*. Springer Science & Business Media, 2012. Section 22.7, pp. 284–286.

[301] Ullrich, W. C., Gikadi, J., Jörg, C., and Sattelmayer, T. Acoustic-entropy coupling behavior and acoustic scattering properties of a laval nozzle. In *Proceedings of the 20th AIAA/CEAS Aeroacoustics Conference* (2014), 2014-3193.

[302] Ullrich, W. C., Schulze, M., and Sattelmayer, T. Fundamental indirect noise generation by interactions between entropy, vorticity and acoustic waves in the context of aero engine applications. In *Proceedings of the 43rd International Congress on Noise Control Engineering* (2014).

[303] Šolín, P., Segeth, K., and Doležel, I. *Higher-order finite element methods*. CRC Press, 2003.

[304] Walker, B. E., and Charwat, A. F. Correlation of the effects of grazing flow on the impedance of Helmholtz resonators. *The Journal of the Acoustical Society of America 72*, 2 (1982), 550–555.

[305] Wang, C., and Huang, L. On the acoustic properties of parallel arrangement of multiple micro-perforated panel absorbers with different cavity depths. *The Journal of the Acoustical Society of America 130*, 1 (2011), 208–218.

[306] Wassmer, D., Ćosić, B., and Paschereit, C. O. Resonance frequency of Helmholtz dampers in the presence of high-temperature grazing flows. In *Proceedings of the 20th AIAA/CEAS Aeroacoustics Conference* (2014), 2014-3179.

[307] Watson, W. R. A new method for determining acoustic-liner admittance in a rectangular duct with grazing flow from experimental data. Tech. Rep. Paper 2310, NASA, 1984.

[308] Watson, W. R. A method for determining acoustic-liner admittance in ducts with sheared flow in two-cross-sectional directions. Tech. Rep. Paper 2518, NASA, 1985.

[309] Watson, W. R., and Jones, M. G. Impedance eduction in ducts with higher-order modes and flow. In *Proceedings of the 15th AIAA/CEAS Aeroacoustics Conference* (2009), 2009-3236.

[310] Watson, W. R., Tracy, M. B., Jones, M. G., and Parrott, T. L. Impedance eduction in the presence of shear flow. In *Proceedings of the 7th AIAA/CEAS Aeroacoustics Conference* (2001), 2001-2263.

[311] Weng, C., Boij, S., and Hanifi, A. The attenuation of sound by turbulence in internal flows. *The Journal of the Acoustical Society of America 133*, 6 (2013), 3764–3776.

[312] Wheeler, M. F. An elliptic collocation-finite element method with interior penalties. *SIAM Journal on Numerical Analysis 15*, 1 (1978), 152–161.

[313] Whiffen, M., and Ahuja, K. An improved schlieren system and some new results on acoustically excited jets. *Journal of Sound and Vibration 86*, 1 (1983), 99–105.

[314] Williams, J. F., and Hawkings, D. L. Sound generation by turbulence and surfaces in arbitrary motion. *Philosophical Transactions of the Royal Society of London A: Mathematical, Physical and Engineering Sciences 264*, 1151 (1969), 321–342.

[315] Wong, D., Ireland, P., Neely, A., Mullender, A., and Derby, U. Preliminary experimental investigation of acoustic liner heat passing capacity. In *Proceedings of the 5th AIAA/CEAS Aeroacoustics Conference and Exhibit* (1999), 1999-1950.

[316] World Health Organization and others. Burden of disease from environmental noise: Quantification of healthy life years lost in europe. In *Burden of disease from environmental noise: quantification of healthy life years lost in Europe*. 2011, pp. 1–126.

[317] Zalluhoglu, U., and Olgac, N. A study of Helmholtz resonators to stabilize thermoacoustically driven pressure oscillations. *The Journal of the Acoustical Society of America 139*, 4 (2016), 1962–1973.

[318] Zhang, Q., and Bodony, D. J. Numerical simulation of two-dimensional acoustic liners with high-speed grazing flow. *AIAA journal 49*, 2 (2011), 365–382.

[319] Zhang, Q., and Bodony, D. J. Numerical investigation and modelling of acoustically excited flow through a circular orifice backed by a hexagonal cavity. *Journal of Fluid Mechanics 693* (2012), 367–401.

[320] Zhang, Q., and Bodony, D. J. Impedance prediction of three-dimensional honeycomb liners with laminar/turbulent boundary layers using DNS. In *Proceedings of the 19th AIAA/CEAS Aeroacoustics Conference* (2013), 2013-2268.

[321] Zhang, Q., and Bodony, D. J. Numerical investigation of a honeycomb liner grazed by laminar and turbulent boundary layers. *Journal of Fluid Mechanics 792* (2016), 936–980.

[322] Zhou, L., and Bodén, H. Experimental investigation of an in-duct orifice with bias flow under medium and high level acoustic excitation. *International Journal of Spray and Combustion Dynamics 6*, 3 (2014), 267–292.

[323] Zienkiewicz, O. C., Taylor, R. L., and Zhu, J. Z. Chapter 4 - Variational forms and finite element approximation: 1-D problems. In *The Finite Element Method: its Basis and Fundamentals (Seventh Edition)*. Butterworth-Heinemann, Oxford, 2013, pp. 93–113.

[324] Zinn, B. A theoretical study of non-linear damping by Helmholtz resonators. *Journal of Sound and Vibration 13*, 3 (1970), 347–356.

[325] Zlavog, G., Breard, C., and Diamond, J. Non-locally reacting liner modeling and validation. In *Proceedings of the 15th AIAA/CEAS Aeroacoustics Conference* (2009), 2009-3111.

[326] Zorumski, W. E., and Tester, B. J. Prediction of the acoustic impedance of duct liners. Tech. rep., NASA Langley Research Center, Hampton, VA, 1976.

# List of publications

## Articles in international refereed journals

- J. Tournadre, P. Martínez-Lera, W. Desmet. Study of thermal effects on passive silencers with a Linearized Navier-Stokes equations solver. International Journal of Spray and Combustion Dynamics (2017). *Manuscript submitted for publication*
- J. Tournadre, K. Förner, W. Polifke, P. Martínez-Lera, W. Polifke, W. Desmet. Influence of vortex disruption on the nonlinear acoustic response of orifices, Journal of Sound and Vibration (2017). *Manuscript submitted for publication*
- K. Förner, J. Tournadre, P. Martínez-Lera, W. Polifke. Scattering to higher harmonics for quarter wave and Helmholtz resonators, AIAA Journal 55(4), pp. 1194–1240 (2017).
- J. Tournadre, K. Förner, W. Polifke, P. Martínez-Lera, W. Desmet. Determination of acoustic impedance for Helmholtz resonators through incompressible unsteady flow simulations, AIAA Journal 55(3), pp. 790–798 (2017).
- M. A. Temiz, J. Tournadre, I. Lopez Arteaga, A. Hirschberg. Modelling vibro-acoustic coupling in flexible micro-perforated plates by a patch-impedance approach, Journal of Applied Acoustics 125, pp. 80–90 (2017).
- M. A. Temiz, J. Tournadre, I. Lopez Arteaga, A. Hirschberg. Non-linear Acoustic Transfer Impedance of Micro-Perforated Plates with Circular Orifices, Journal of Sound and Vibration 366, pp. 418–428 (2016).

## Articles at international scientific conferences

- Denayer, H., Tournadre, J., De Roeck, W., Desmet, W., Martínez-Lera, P. (2014). Combined Numerical and Experimental Study of a Slit

Resonator Under Grazing Flow. In Proceedings of the 20th AIAA/CEAS Aeroacoustics Conference. Atlanta (GA), USA, 16-20 June 2014 (art.nr. AIAA 2014-2959).

- Tournadre, J., Martínez-Lera, P., Desmet, W. (2015). Numerical study of the acoustic response of a single orifice with turbulent mean flow. In Proceedings of the 22nd International Congress on Sound and Vibration. Florence, Italy, 12-16 July 2015 (art.nr. 1103).

- Temiz, M. A., Tournadre, J., Lopez Arteaga, I., Martínez-Lera, P., Hirschberg, A. (2015). Effect of orifice geometry on the non-linear acoustic resistance of perforated plates in the transition regime. In Proceedings of the 22nd International Congress on Sound and Vibration. Florence, Italy, 12-16 July 2015 (art.nr. 1014).

- Tournadre, J., Förner, K., Polifke, W., Martínez-Lera, P. (2016). Determination of acoustic impedance for Helmholtz resonators through incompressible unsteady flow simulations. In Proceedings of the 22th AIAA/CEAS Aeroacoustics Conference. Lyon, France, 30 May-1 June 2016 (art.nr. AIAA 2016-2917).

- Förner, K., Tournadre, J., Martínez-Lera, P., Polifke, W. (2016). Scattering to higher harmonics for quarter wave and Helmholtz resonators. In Proceedings of the 22th AIAA/CEAS Aeroacoustics Conference. Lyon, France, 30 May-1 June 2016 (art.nr. AIAA 2016-2968).

- Tournadre, J., Martínez-Lera, P., Desmet, W. (2016). Evaluation of temperature effects on passive acoustic dampers with a frequency-domain Linearized Navier-Stokes equations solver. In Proceedings of the 23rd International Congress on Sound and Vibration. Athens, Greece, 10-14 July 2016 (art.nr. 857).

- Temiz, M. A., Tournadre, J., Lopez Arteaga, I., Martínez-Lera, P., Hirschberg, H. (2016). Numerical estimation of the absorption coefficient of flexible micro-perforated plates in an impedance tube. In Proceedings of the 23rd International Congress on Sound and Vibration. Athens, Greece, 10-14 July 2016 (art.nr. 803).

- Tournadre, J., Temiz, M. A., Martínez-Lera, P., De Roeck, W., Desmet, W. (2016). Vibro-acoustic response of flexible Micro-Perforated Plates: impact of the boundary condition at the perforation walls. In Proceedings of the International Conference on Noise and Vibration Engineering ISMA 2016. Leuven, Belgium, 19-21 September 2016 (art.nr. 505).

## Chapers in academic books

- Förner, K., Tournadre, J., Martínez-Lera, P., Polifke, W. (2015). Characterization of the nonlinear response of Helmholtz resonator. In Annual Report TRR40, Sonderforschungs-bereich/Transregio 40, pp. 33-45 (December 2015).

FACULTY OF ENGINEERING SCIENCE
DEPARTMENT OF MECHANICAL ENGINEERING
NOISE & VIBRATION RESEARCH GROUP
Celestijnenlaan 300 box 2420
B-3001 Leuven
https://www.mech.kuleuven.be/en/research/mod